To Mum and Dad with love,

UNIVERSITY OF SOUTHAMPTON

FACULTY OF ENGINEERING, SCIENCE & MATHEMATICS

School of Chemistry

Nanostructured Electrodes for Battery Applications

by

Kenneth Helmut Reiman BSc (Hons)

Thesis for the degree of Doctor of Philosophy

DATE 29/09/2008

ABSTRACT

Nanostructured materials have attracted attention for application in energy storage devices, especially for those which require high charge/discharge current rates such as lithium ion batteries. Initial work in this thesis focused on finding a nanostructured electrode pair capable of performing as a high rate device. Previously, mesoporous nickel demonstrated high rate performance in alkaline electrolyte, but attempts to ion-exchange H^+ for Li^+ and import in to aprotic lithium electrolytes proved futile; due to the corrosion of the active NiOOH by anions of the lithium salt. Both Nickel-Phosphorous (NiP) and Mesoporous Nickel Phosphorous Alloys (MNiP) were electrodeposited and displayed an increased corrosion resistance in aprotic electrolytes compared to pure Ni; characterised by a shift in pitting potential (E_P) from ~3.2V to 4.75 V $vs.$ Li for $Ni_{0.78}P_{0.22}$. MiNiP ion-exchanged in warm aqueous lithium hydroxide yielded significantly higher electrochemical activity than MNi when subsequently cycled in aprotic electrolytes, however, the ion exchange reaction was only 22 % complete.

The search for a nanostructured electrode pair moved toward finding a high rate aqueous negative electrode to partner the MNi electrode. Nanostructured titanium dioxide films, (formed by the sol-gel surfactant template method) unlike non-templated, have been found to be reduced when cathodically polarised in aqueous lithium hydroxide. The result is attributed to accelerated lithium ion diffusion within the porous nanostructure, allowing a rapidly reversible insertion of lithium ions forming Li_xTiO_2 with x as high as 0.25 in a 1.3 μm thick film. An open circuit potential of 1.75 V is observed for the charged $NiOOH_{2-x}/Li_xTiO_2$ device with an average cell potential of 1.6 V, well in excess of Ni/MH and Ni/Cd systems; which discharge between 1.0 and 1.3 V. A specific energy of 90 Wh kg^{-1} whilst impressive for a supercapacitor is not comparable to batteries. Synthesising films of a thickness great enough to be utilised in a battery or ultra capacitor device was ultimately unsuccessful, due to cracking and exfoliation of the film from the underlying FTO substrate.

To achieve higher material loadings internally nanostructured TiO_2 powders (100-220 m^{2}g^{-1}) also prepared by the sol-gel technique, were investigated in composite electrode films. An extra capacity for lithium insertion at low voltage and an impressive rate performance, characteristic of high surface area titanates was observed. A correlation between the observed rate performance and electrode thickness was discovered. Further study revealed that the diffusion of ions through the electrode matrix was the limiting factor for nanomaterials in thick composite electrodes rather than solid state diffusion, contrary to conventional wisdom. Nanostructured TiO_2 as has been optimised such that particle relaxation time is of the order of a few minutes, therefore the composite or microstructure of the battery must also operate on this time scale. If characteristic electrode thickness > 100 μm for commercial application are to facilitate high rates, significant efforts must now focus on optimisation of the microstructure of batteries, in tandem with continued efforts on the preparation of more uniform nanostructured materials.

Acknowledgements

So many people to thank who have helped me in so many different ways over the long journey as, finally, I sit here having finished the corrections! There were some stages when I thought it couldn't be done, and it wouldn't have without all the great people I have around me. Not just for help with the thesis, or the general moral support but, for the football, the staff club, the coffee breaks, the chats in the lift and all the laughs along the way:

In particular order:

John,

Girts, Matt,

Thierry,

Toby, Karen, Phil,

Doug, Maciej, Alex,

Ailsa, Alan, Hannah, Phil J, James M, Steve K, The Waki, Alistair,

Chrissy V, Timmy G, Stevo, Pete B, Hanne, Katie, Mat Cheets, Rich, Jason, Sergio.

Stop press: special mention to Joanne and Guy for such a good job reading the thesis!

On the home front I'd like to thank my fantastic friends and family for all their encouragement and understanding and generally for the interest in my progress (mostly to tease me).

Especially I'd like to thank my Mum and Dad who have lived and breathed the write-up with me, thanks for all the sacrifices you have made and the inspiration and guidance you have given me in every stage of my life; and lastly to my sister Lucy who is my all-time favourite person in the world.

Symbols

A	electrode area	cm^2
AM	active material in pellet	g
C	Concentration	$mol\ dm^{-3}$
C	C-rate	h^{-1}
C_v	Pseudocapacitance	$F\ cm^{-3}$
D	Diffusion coefficient	$cm^2\ s^{-1}$
d	Electrode thickness	cm
E	potential	V
E^o	Standard Electrode Potential	V
E_a	Activation Energy	eV
E_{corr}	Corrosion potential at open circuit	V
E_p	The pitting potential	V
F	faradays number (96487)	$C\ mol^{-1}$
I	current	A
i_a	current per area	$mA\ cm^{-2}$
i_m	current per mass	$mA\ g^{-1}$
ir	Current resistance drop	V
j	Current density	$mA\ cm^{-2}$
L	propagation distance of the diffusion front	m
m	mass	g
μ	Chemical Potential	$J\ mol^{-1}$
n	number of electrons	
η	overpotential	V
Q	charge	C
q.i	capacity current product	$C^2 g^{-2} s^{-1}$
q_a	Capacity per area	$mC\ cm^{-2}$
q_m	Capacity per mass	$mA\ h\ g^{-1}$
r	Particle radius	m
R	resistance	Ω
t	time	s
τ	time constant	s
Vm	Molar volume	$cm^3\ mol^{-1}$
ΔG	change in free energy	$J\ mol^{-1}$
θ	X-ray beam angle of incidence	degrees
ρ	density	$g\ cm^{-3}$
σ	conductivity	$S\ cm^{-1}$

Abbreviations

AC	Alternating current
ACB	Acetylene carbon black
AM	Active material
B56	Brij 56
B78	Brij 78
CP	cyclopentanone
CV	cyclic voltammetry
DEC	diethyl carbonate
DMC	dimethyl carbonate
DME	dimethoxyethane
EC	ethylene carbonate
EDX	Energy Dispersive X-ray
F127	Pluronics 127
FEG SEM	Field emission gun scanning electron microscope
FTO	Fluorine doped Tin Oxide
H_I	Hexagonal liquid crystal phase
I_I	Micellar Cubic liquid crystal phase
IPA	isopropanol
LiTFSI	lithium bis(trifluoromethane sulfone imide)
MNi	Mesoporous Nickel
MNiP	Mesoporous Nickel Phosphorous
OCV	Open Circuit Voltage
P123	Pluronics 123
PC	propylene carbonate
PTFE	poly(tetrafluoroethylene)
PVdF	polyvinylidene difluoride
PVdF_HFP	polyvinylidene difluoride hexafluropropylene
SEI	solid electrolyte interface
SEM	scanning electron microscope
TGA	thermo gravimetric analysis
VMP2	variable multi-channel potentiostat
XRD	X-ray diffraction
SAXS	Small angle x-ray scattering
WAXS	Wide angle x-ray scattering
NS	Nanostructured
NP	Nanoparticulate
CCE	Constant Current Cycling with Equilibration
CC	Constant Current Cycling
BET	Brunauer-Emmett-Teller
CMC	Critical Micelle Concentration
EISA	Evaporation Induced Self-Assembly
DLCT	Direct Liquid Crystal Templating

Table of Contents

Chapter 1

Introduction to Mesoporous Materials and

Power Source Applications

1.1 Increasing Demand for High Performance Electrodes

Nanomaterials have been widely applied in the life sciences, information technology, the environment, and other related fields. Recently, nanostructured materials have also attracted attention for application in energy storage devices[1], especially for those with high charge/discharge current rates such as lithium ion batteries.[2, 3] The development of next-generation energy storage devices with high power and high energy density is key to the success of electric and hybrid electric vehicles (EVs and HEVs, respectively)[4], which are expected to at least partially replace conventional vehicles and help solve the problems of air pollution and climate change. These energy storage technologies will rely on innovative materials science, i.e. developing electrode materials capable of being charged and discharged at high current rates.

1.2 The Role of Porous Materials

In many electrochemical systems, particularly those of industrial importance, it is desirable for reaction processes to occur as rapidly as possible. High reaction rates in reactions such as the electrochemical reduction of species O to R in *Eq. 1.2.1* are demonstrated by high currents since the degree of reactant conversion is proportional to the current, *Eq. 1.2.2*.

$$O + e- \rightarrow R$$

Eq. 1.2.1

$$-\frac{d[O]}{dt} \propto I$$

Eq. 1.2.2

Improving the reaction rate can be achieved in a number of ways. One of the easiest ways of increasing current in a cell is to increase the overpotential at the electrode. The overpotential is defined as the deviation from the equilibrium potential, $\eta = E\text{-}E^\circ$. The result is an exponential increase in the current, (that is where the reaction is not mass transport limited) as dictated by the general form of the Tafel equation, *Eq. 1.2.3*:

$$\eta = a + b\log I$$

Eq. 1.2.3

where η is the overpotential and *I* is current. This method is generally acceptable in electrolytic cells, however in energy producing galvanic cells, an increase in the cell overpotential results in a decrease in the cell output voltage. To avoid this problem, in certain systems such as fuel cells the overpotential needed for a reaction may be reduced, such that the same cell potential yields a higher current. This is achieved by selecting an electrode material of higher catalytic activity, thus reducing the activation energy for the process and consequently the overpotential needed to drive the reaction at significant rates. This approach constitutes the first of the two methodologies used in optimisation of electrode performance, that is, optimisation of electrode composition. Very much an empirical art, optimisation of electrode performance by tuning electrode composition is now the focus of combinatorial investigations.

Another means of increasing cell current is to increase the area of an electrode. This is achieved by simply extending the geometric area of the electrode (as in a dielectric capacitor), or less crudely, by increasing the roughness of the electrode such that the current density per unit geometric area is increased. The latter approach is the basis of the second methodology used in enhancing electrode performance, that is, optimisation of electrode structure and the effect on its properties are the topic of discussion in this thesis, where reaction rates can bee seen to improve, or even permit new reaction to take place, which are not possible with regular electrode structures.

1.2.1   Porous Materials

Porous materials have attracted the attention of chemists and materials scientists due to commercial interest in not only their electrochemical application but also their function in chemical separation and heterogeneous catalysis; as well as scientific interest in the challenge posed by their synthesis, processing, and characterisation. Application of basic scientific principles to the key technological issues involved has been difficult; however, more progress has been achieved in tailoring porous materials through manipulation of processing parameters than through understanding of the chemical and physical mechanisms that influence porosity. As a result, the tailoring of porous materials has proceeded largely in an empirical fashion rather than by design.

1.2.1.1   Sol-Gel Chemistry

Most glasses or ceramics are produced by melting their component oxides and cooling faster than the rate of crystallisation; another route to glasses and ceramics is the sol-gel process.   The sol-gel process involves the transition of a system from a liquid (the colloidal "sol") into a solid (the "gel") phase, as in Scheme 1.2.1.
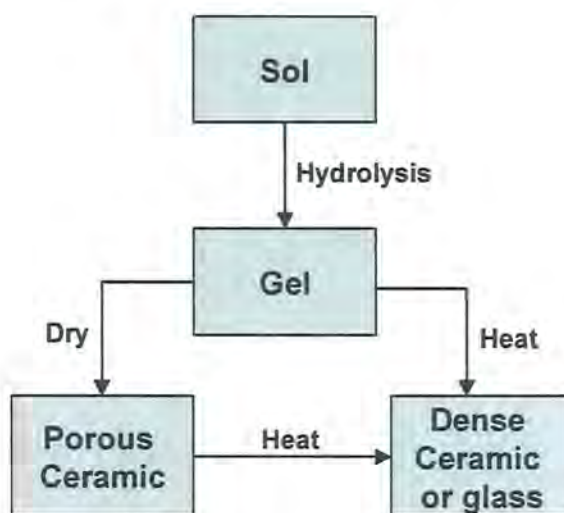
Scheme 1.2.1: Diagram of the sol-gel process.

A typical process involves the addition of a metal alkoxide precursor e.g silicon [5, 6]to an alcohol, followed by the addition of water to hydrolyse the reactants. The thus formed acids then undergo self-condensation polymerisation to form soluble, high molecular mass polysilicates (a sol). These polysilicates then polymerise to form a three-dimensional network, the pores of which are filled with solvent molecules. This hydrolysis and subsequent condensation leads to a thick gel that can be dehydrated and sintered (heated below its meting point) to form a compact solid.   For example, ceramics such as TiO_2 and Al_2O_3 can be prepared in this way at much lower temperatures than from simple oxides.   Sol-gel chemistry is a remarkably versatile approach for fabricating materials and allows the fabrication of a huge variety of materials; fine powders, monolithic ceramics and glasses, ceramic fibres, inorganic membranes, and thin film coatings for example.

1.2.1.2   Nanoparticles, Aerogels and Xerogels

Different types of porous structure can be obtained by altering the methods of ageing/drying/heating the gel. Nanoparticles can be obtained by the sol-gel process[7], the oxide particles are obtained after filtering the solvent from the suspended solid particles and sintering The sintering step removes excess water from the sol and converts the usually amorphous hydrated mass into a crystalline oxide. The electrode itself is usually fabricated by tape casting or doctor blading a paste.[8]

Aerogels are high surface area nanoporous materials composed of a network of interconnected solid species. Aerogels differ from nanoparticulate materials in that the former have significantly lower densities and higher porosities as illustrated in Figure 1.2.1

50 nm **supercritically dried**
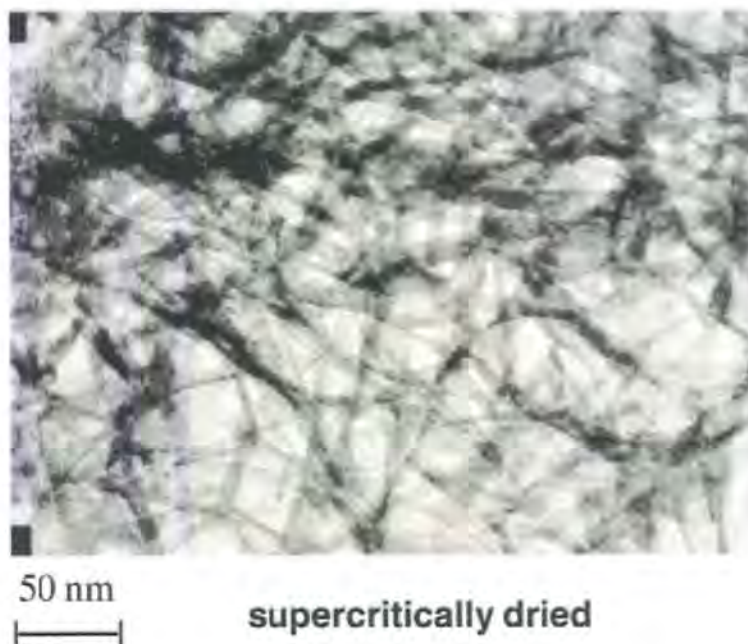
Figure 1.2.1: Transmission electron micrograph of vanadium oxide gels produced by supercritical drying from CO_2 to form an aerogel.[9]

The morphology of Aerogels is best understood when considering the method of their synthesis. Synthesis of Aerogels is carried out by using an adaptation of sol-gel processing with the formation of a wet gel, using a network-forming precursor such as a metal alkoxide. The similarity ends here however, since instead of separating the solid components from the gel by a method such as filtration as for the nanoparticles, the gel is allowed to undergo further polycondensation forming a cohesive but fragile network.

The gel is then carefully dried, preserving the condensed network. The manner in which the liquid phase is removed from the wet gel determines whether the dried solid is a highly porous Aerogel or a denser Xerogel. The latter is formed as a result of collapse of the structure of the wet gel, as the pore liquid is removed relatively quickly by evaporation. By drying the wet gel under supercritical CO_2 stresses associated with capillary pressure induced by evaporation of the pore water are removed, allowing the wet gel network structure to remain intact.[9] Unlike the older and more established technology of nanoparticulate electrodes, Aerogels and Xerogels have found only limited commercial application. Aerogels of silica are used as high surface area catalysts, catalyst supports and chromatographic stationary phases.[10] However, Aerogels and Xerogels are receiving increasing attention in the technical literature, particularly in the development of electrochemical applications such as supercapacitors and lithium ion secondary batteries.[11]

1.2.2   Templated Structures.

1.2.2.1   Zeolites – early templated structures.

Zeolites are porous aluminosilicate based materials consisting of a crystalline anionic cage framework, charge balanced by cations residing within the cavities or channels created by the framework. The composition of the framework oxide is represented by the general formula, $[(Al_aM_bSi_c) Od]$ where M may be any of the elements P, Ga, Ge, B, Be, Zn, Ti, Fe, Co, Cr, Mn, V or Mg. The zeolite framework is constructed from TO_4 ($SiO_4$for example) tetrahedra such that each apical O atom is shared between two adjacent tetrahedra giving a framework O/T ratio of two. Pure silicates with this structure do not contain framework charge since Si is tetravalent. However, due to the variation in charge of the framework atoms in aluminosilicates from +4, zeolites have negatively charged frameworks (1 negative charge per Al^{3+} framework atom). Consequently, zeolite frameworks require charge balancing by extra-framework positive ions. In naturally occurring zeolites, these cations are either alkali metal (e.g. Na^+) or alkaline earth (eg. Ca^{2+}) ions. Synthetic zeolite frameworks are capable of hosting a larger range of cationic species such as H^+ and organic cations such as quaternary ammonium ions.

The porosity of zeolites varies greatly, with pores of either circular or elliptical geometry forming one- two- or three-dimensional networks of channels or cages. Pore

size distributions are extremely narrow since pore dimensions are defined by the bond lengths and angles between the framework atoms and the volume of the voids is usually less than 50 %. Approximately 60 naturally occurring zeolites are known, however many of the more industrially important examples such as ZSM-5 (Zeolite Socony Mobil material number 5) illustrated in Figure 1.2.2 are synthetic. Pores sizes generally range from 2.5 to 8 Å[*12*], however diameters up to 14 Å have been reported.[*13*]

The industrial importance of zeolites and zeolitic materials is difficult to overstate. They have found use in a number of catalytic and separation applications including adsorptive separation of hydrocarbons, purification of gases and liquids and catalytic cracking of long chain hydrocarbons to form more valuable short chain homologues. Calcined zeolites such as ZSM-5 are capable of carrying out protonation reactions on usually unreactive organic molecules because of the presence of super-acid sites within the channel structure, and modification of reaction energetics due to the electronic confinement of guest species.[*14*]
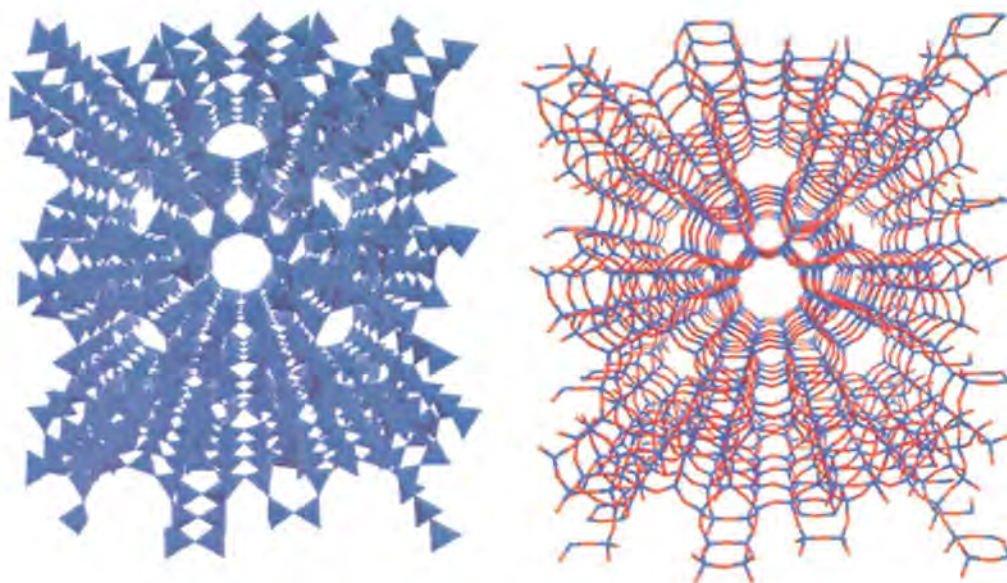
Figure 1.2.2: Zeolite ZSM-5, made up of SiO_4 and AlO_4 tetrahedra shown left, the atomic structure right reveals more clearly the open channels and resultant porosity.

Here, the negative charge of the framework is balanced only by extremely reactive unsolvated protons such that even very weak bases like *n*-alkanes form reactive carbocations. Zeolites are also used in ion exchange and act as molecular sieves for dehydration of organic solvents. The utility of zeolites arises as a consequence of their channel/cavity structures which host metal cations, water and a vast range of potential

guest species. Since the aluminosilicate cages are sufficiently robust, guest species may move in and out of the channels without disruption of the host framework. This utility is limited however by the small channel diameters of zeolitic materials, making operations such as sieving of biomolecules and cracking of the heavier fractions of crude oil impossible.

Zeolite formation is a kinetically controlled process, where zeolites are reaction intermediates during the formation of dense phases from silica precursors. Provided the reaction time is long enough (up to some million years in nature) or the reaction rate is enhanced, e.g. due to high temperature, dense silica or silicon oxide phases are the thermodynamically stable products. In zeolite synthesis, the reaction is stopped when the thermodynamically meta-stable zeolite has formed. Extended reaction time at high temperature and/or high pressure usually results in dense phases. Most aluminosilicate zeolites probably could be obtained at temperatures below 100°C in alkaline solutions. This is generally the case for zeolites with a low Si/Al ratio. However, in order to reduce the reaction time (especially for zeolites with a high Si/Al ratio) and to control crystallite sizes, morphologies, and compositions, some syntheses are performed at temperatures above 100°C under pressure in autoclaves. For the synthesis of some materials, an organic template molecule has to be added to the reaction mixture. These structure-directing agents (usually amines, alkylammonium salts or alcohols) are essential for the formation of a large number of zeolitic materials. However, the role of the template molecules during the crystallization is not absolutely clear and a number of possible mechanisms for its interaction with the forming zeolite are discussed. The two most generally accepted are:

1) The true template effect, where the zeolite is formed around the organic molecule (= template) which determines the pore topology due to its own shape.

2) A pore filling effect, where the template stabilises the micropores of the zeolite by filling them and, thus, preventing a collapse of the pores.

Many attempts to rationally design zeolite synthesis were made but up to now, the synthesis of new zeolite structures is usually still a matter of serendipity. If template molecules are used during the synthesis, a calcination process has to follow the

synthesis. By that step the template is removed from the micropores of the zeolite which makes them accessible. Usually, temperatures in the range of 450 - 600°C are applied to remove the organic components, which is not critical for the stability of the zeolites since they are usually stable to much higher temperatures.

1.3 Self Assembly of Lyotropic Liquid Crystalline Phases

1.3.1   Surfactants and formation of Micelles

Surface-active agents or surfactants are molecular entities composed of both lyophilic (solvent loving) and lyophobic (solvent fearing) components. In those cases in which water is the solvent, these components are referred to as hydrophilic and hydrophobic respectively.
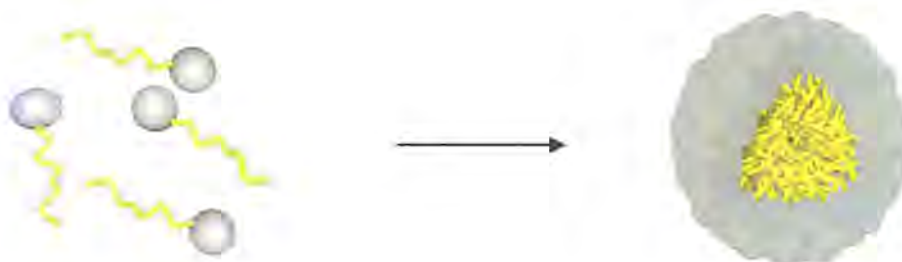
Figure 1.3.1 At the cmc surfactants in solution self-assembled into spherical structures called Micelles. This is driven by a gain in entropy; minimising contact between the surfactant's hydrophobic component and water by sequestering the hydrophobic (non-polar) component within the interior of the structure and shielding it with an exterior shell composed of the hydrophilic (polar) component.

In aqueous solution, surfactants exhibit characteristics of both hydrophilicity and hydrophobicity and as such surfactants are referred to as amphiphilic (loving both kinds) molecules. In an aqueous solution containing surfactant molecules the system will seek to adopt a minimum energy configuration as dictated by the laws of thermodynamics. At very low surfactant concentrations this configuration is one in which the surfactant moves to the air-water interface (if one is present) and orients itself such that the hydrophobic component is protruding through the interface into the hydrophobic air side and the hydrophilic component remains within the water side of the interface.[15] As the concentration of dissolved surfactant increases in the solution, surfactant accumulates at the air-water interface until a complete monolayer forms corresponding to saturation of the interface. The surfactant concentration at this saturation point is known as the critical micelle concentration (cmc), and can be measured by withdrawing at Pt ring from solution. The force applied to break the

resultant meniscus is related to the surface tension. Once the cmc is reached, the saturated interface forces the subsequently dissolving surfactant molecules to remain completely within the aqueous environment. At this point, the surfactants will aggregate to form structures known as Micelles, one of which is displayed in Figure 1.3.1.

The aggregation of amphiphiles to form micelles and lyotropic liquid crystal phases is driven by entropy, and occurs due to the hydrophobic effect, manifest in the non-miscibility of oil and water. The enthalpy of formation of micelles is considered to be an endothermic process with ΔH approximately 1-2 kJ mol^{-1} of surfactant. Since micelles form readily above the cmc, then the entropy of formation (ΔS) of micelles must also be positive. This must be the case because the change in Gibbs free energy for any spontaneously occurring process must be negative. The Gibbs free energy change is related to the enthalpy and entropy of formation in accordance with *Eq. 1.3.1*.

$$\Delta G = \Delta H - T \Delta S$$

Eq. 1.3.1

Therefore, if ΔH is positive then ΔS must also be positive if ΔG is to be negative. Experimentally the entropy of formation of micelles has been determined to be ~140 J K^{-1} mol^{-1}. This can be rationalised by considering the interaction between monomeric amphiphiles and the bulk aqueous environment. When water molecules surround a hydrocarbon, the water forms an ordered clathrate cage (one type of molecule trapping and containing a second type of molecule). In this configuration each water molecule is, on average, hydrogen bonded to 3.5 - 4 neighbours, greater than the average hydrogen bonding in bulk water (3 – 3.5 hydrogen bonds per water molecule), and hence greater order than in the bulk liquid water due to the directional nature of hydrogen bonds. When micelles are formed, there is a net increase in disorder due to the loss of the clathrate cage surrounding the hydrocarbon/hydrophobic segments of the amphiphiles. This is the origin of the hydrophobic effect.

1.3.2 Phase Behaviour

At relatively low surfactant concentration the self assembled micelles exist in a non-uniform arrangement, known simply as the Micellar phase (denoted L_1). Further increases in surfactant concentration are accommodated by the formation of more micelles which results in an increase in the viscosity of the solution. As the density of micelles in solution increases, the micellar packing geometry is forced to take on less random configurations and ultimately the cubic micellar phase (I_1) forms. The I_1 phase consists of spherical micelles packed on a body-centred cubic (bcc) lattice as illustrated in Figure 1.3.2, and is the first of the lyotropic liquid crystalline phases observed in surfactant-water systems. At higher surfactant concentrations spherical micelles coalesce to form rod-like structures in which the surfactant's hydrophobic segments are located within the centre of the rod. Self-assembly of these cylindrical rods in a hexagonal array constitutes the hexagonal phase (H_1), where surfactant rods are separated by a continuous aqueous phase. As the quantity of water in solution decreases further, another cubic morphology forms, composed of short surfactant rods, which intersect to form a continuous network.[16] This is the bicontinuous cubic phase denoted V_1.[17] The V_1 phase, unlike the H_1 phase is structurally isotropic and possesses three axes of symmetry rather than one. Under different conditions a sheet like structure called the lamellar phase (L_α) forms, consisting of surfactant molecules arranged in bilayers separated by layers of aqueous solution. These different lyotropic liquid crystalline phases are most easily recognised based on their texture under polarising light microscopy.[18]

One of the essential characteristics to consider in defining and characterising the phase behaviour of lyotropic liquid crystalline phases is the curvature of the mesophase surface. The curvature (and therefore the structure) of liquid crystalline phases may be understood and predicted to a greater extent if the surfactant packing parameter, (ζ) is considered, *Eq. 1.3.2*:

$$\zeta = \frac{v}{a_o l} \qquad \qquad \text{*Eq. 1.3.2*}$$

where a_0 is the interfacial area occupied by the head group and l and v are the alkyl chain (or more generally, the hydrophobic segment) length and volume respectively[19]. The surfactant packing parameter is inversely proportional to

curvature in a liquid crystalline phase. For example, by increasing the head group size whilst keeping the hydrophobic portion of the molecule constant, the surfactant packing parameter decreases and the curvature of the phase increases. Consequently, the phase behaviour of surfactants with large head groups tends to be dominated by spherical or highly curved phases. This concept may be expressed in a more instinctive manner by noting that as the size and hence packing area occupied by the hydrophilic group is increased, surfactant packing considerations favour curved interfaces (spheres and cylinders) over planar ones (bilayers). The surfactant packing parameter also considers surfactant concentration effects; since increasing surfactant concentration decreases a_0 due to the lower activity of water, and hence the reduced hydration of each chain. Despite its apparent simplicity, the surfactant packing parameter has been successfully applied to explain the phase behaviour of polyoxyethylene surfactants.[20]

Name   Phase Structure

Micellar solution
(L_I)

Cubic micellar
phase (I_I)

Hexagonal phase
(H_I)

Bicontinuous cubic
phase (V_I)

Lamellar phase
(L_α)

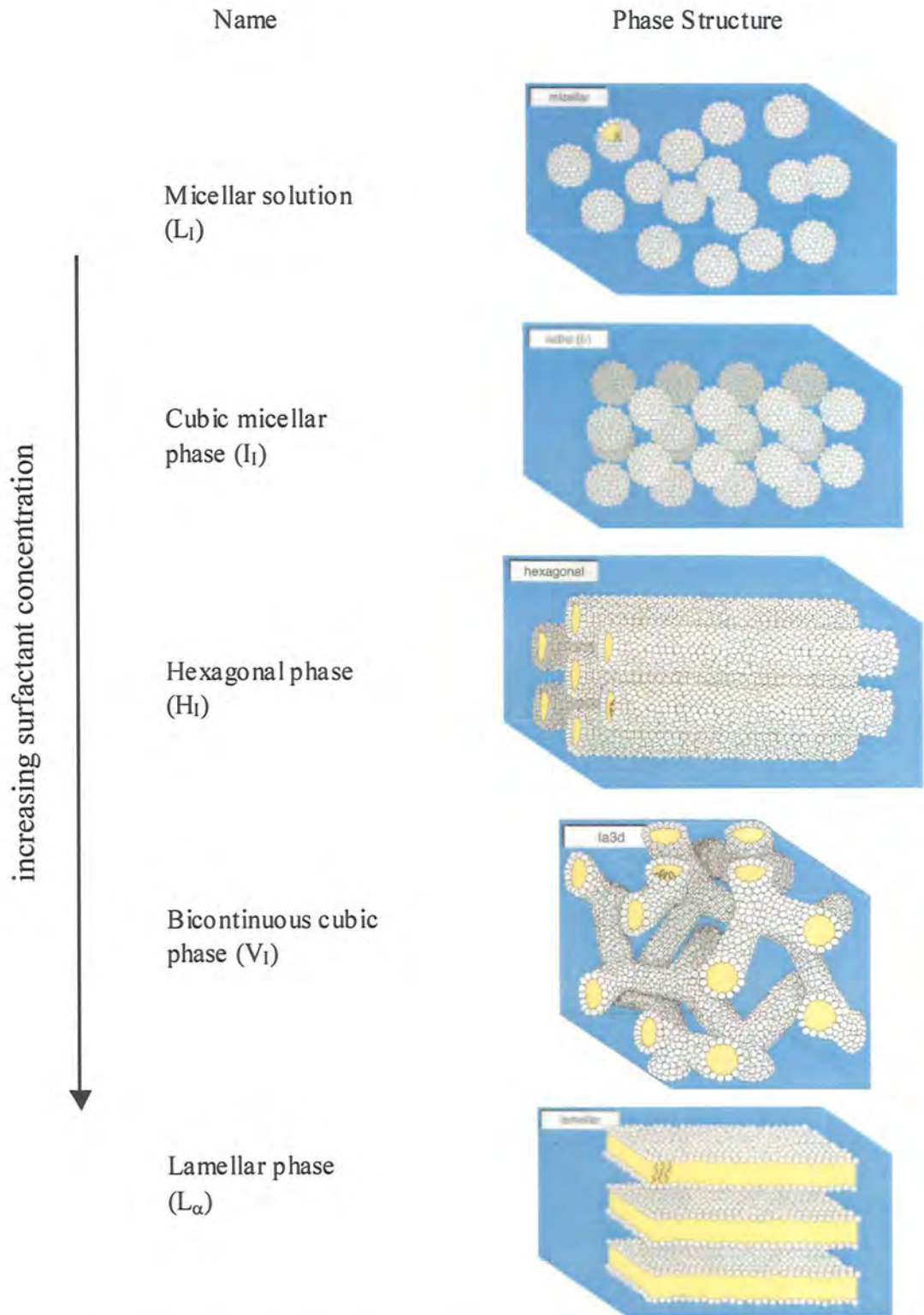increasing surfactant concentration

Figure 1.3.2: The generalised structural progression of liquid crystalline phases with increasing surfactant concentration.[21]

1.3.3   Different Types of Surfactants

There exists a vast array of surfactant species that are capable of self-assembling into liquid crystalline phases when mixed with water.[22] Of these, only selected non-ionic surfactants will be discussed here, that is, the polyoxyethylene family (with general formula C_xEO_y) and the tri-block copolymers. In the case of the former, the hydrophilic component of the surfactant is composed of polyethylene oxide (PEO) and the hydrophobic component of a hydrocarbon tail. The non-ionic triblock copolymers discussed here also possess PEO as their hydrophilic components but utilise polypropylene oxide (PPO) to provide the hydrophobicity. The family of tri-block copolymers consisting of the basic structural formula $(PEO)_x(PPO)_y(PEO)_x$, are commercially available (under the generic name poloxamers and the trade names Pluronics® and Synperonics®) and form micellar and lyotropic liquid crystalline phases in aqueous and other solvent systems. Where the solvent is relatively hydrophilic, micellar structure generally consists of a central dense core of PPO and an outer corona of hydrated PEO[23] as illustrated in Figure 1.3.3.
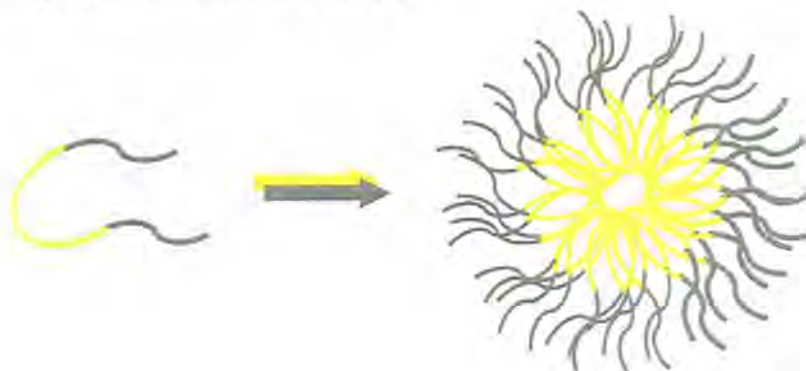
Figure 1.3.3: The shielding of a hydrophobic polymer core (yellow) from an aqueous solution by hydrophilic segments of a Pluronic® triblock copolymer (grey).

The Pluronic® surfactants have significantly more ideal lyotropic behaviour than the polyoxyethylene surfactants in that their phase behaviour is almost entirely dependent on interactions with the solvent[24] and almost independent of temperature, as indicated by the phase diagrams of Figure 1.3.4. Here it can be seen that trends in the phase behaviour of the triblock copolymer P105 are accurately modelled by trends in the surfactant packing parameter. As P105 concentration and surfactant packing density are

increased, the area at the surfactant/water interface occupied by the head group is forced to decrease, and interfacial curvature in turn decreases, resulting in phase transitions from the spherical curvature of micelles to the lower planar curvature of the lamellar phase.
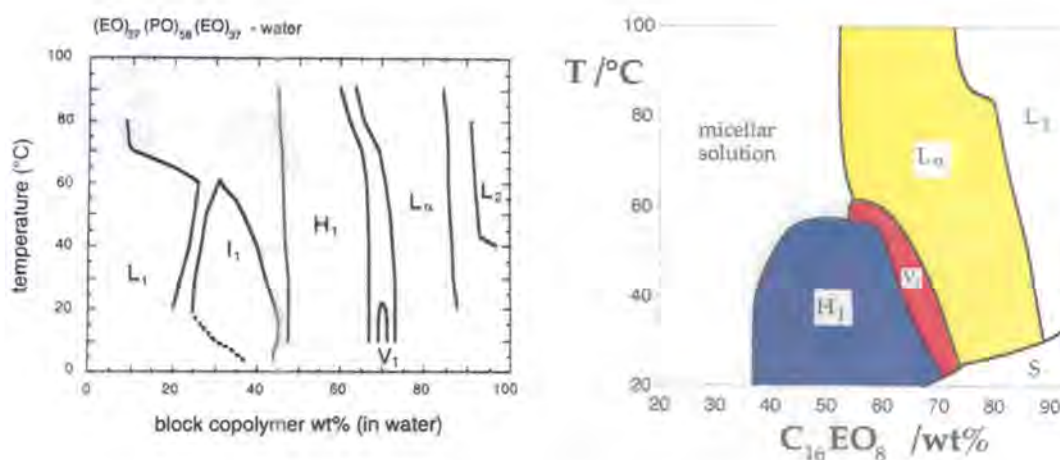
Figure 1.3.4: The phase behaviour of the triblock copolymer $(EO)_{37}(PO)_{58}(EO)_{37}$ (Pluronic® P105)[25](left) and $C_{16}EO_8$ (right) in water. [21]

Polyoxyethylene/water surfactant systems also follow this trend[21], however it is noted that phase structure may also be changed significantly by variation in temperature at a constant mixture composition. In addition, the aqueous phase behaviour of Pluronic® surfactants is influenced to a much greater degree by the addition of polar solvents to aqueous surfactant mixtures[26, 27] than are additions of polar solvents to non-ionic polyoxyethylene surfactant-aqueous systems[28, 29]. One of the principal reasons for this difference in behaviour is the relative difference in polarity between each of the hydrophilic and hydrophobic surfactant components. Unlike in the polyoxyethylene surfactant-water systems in which even relatively hydrophilic species such as large primary alcohols locate preferably in the hydrophobic phase, organic solvents in Pluronic® systems show a much greater tendency to partition in the hydrophilic phase[30]. Some solvents (for example ethanol) show amphiphilic behaviour and act as co surfactants by positioning themselves at the hydrophilic/hydrophobic interface. This variation in phase behaviour with co solvent addition has led the Pluronic® surfactants to possess the richest structural polymorphism of lyotropic liquid crystal forming species.[28, 31]

This relative instability of the liquid crystalline phases of Pluronics® to co-solvent addition can be appreciated in knowing that the hydrophobicity of CH_2 groups in polyoxyethylene surfactants is 4-5 times greater than that of a propylene oxide group as reported by Wanka *et al[32]*. As a result, there is less lyotropic contrast between hydrophilic and hydrophobic segments in the Pluronic® surfactants and therefore less stabilisation of aggregate structures. As such, the addition of species of different polarity than those of the surfactant molecules may serve to lower the polarity difference across the interface even further, causing a phase change.

1.4 Templated Materials

The application of porous materials such as those discussed in 1.2.1 is of considerable commercial interest particularly in separation, catalysis and power sources, in addition to the fundamental scientific interest in their synthesis and properties.[*33*] Despite this interest however, the application of basic scientific principles to the technological issues impeding the development of porous materials has been slow. Significant progress has been achieved in improving porous materials, however this has been accomplished largely by manipulation of processing parameters, rather than understanding of the chemical and physical mechanisms that influence porosity. As such, the development of porous materials has progressed largely by empirical means rather than by design.

1.4.1   Mobil synthesis – low surfactant concentrations

The discovery and synthesis of zeolites (1.2.2.1) first aroused inquiry into the possibilities of designing the structure of porous materials for specific applications, however the pore sizes available in zeolitic materials do not penetrate the meso- range (2 to 50 nm). This deficiency was addressed by Kresge *et al.[34]* of Mobil Research and Development Corporation, in a now much cited paper reporting the synthesis of mesoporous aluminosilicates using a self-assembled liquid crystalline template. The materials with variable pore diameters of 16 to 100 Å and a hexagonal pore arrangement (designated MCM-41) were synthesised by mixing a quaternary ammonium surfactant (< 20 wt. % of the total mixture) with alumina and a solution of silica precursor, Figure 1.4.1. The pore size can be directly correlated to the length of the alkyl chain lengths of 8-18 carbon atoms. Larger pores can be synthesised if an additional hydrophobic

organic species, such as 1,3,5 trimethyl benzene, is added to swell the self-assembled structures.[35]
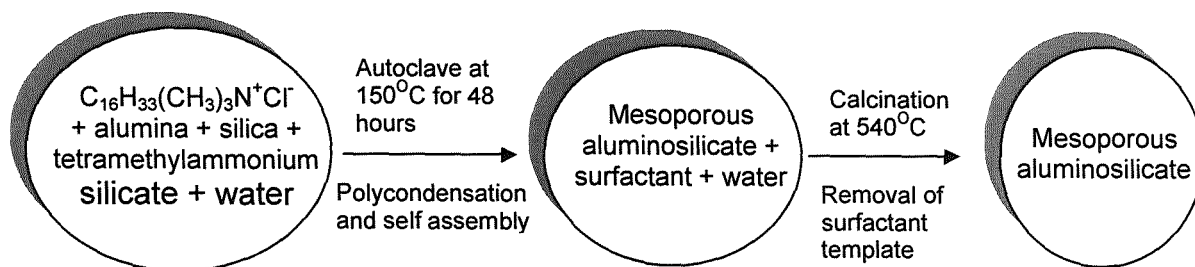
Figure 1.4.1: Mobil synthesis of mesoporous materials employing low surfactant concentrations[34, 35].

The authors suggested a 'liquid-crystal templating' synthesis mechanism in which hexagonal arrays of cylindrical micelles formed as a result of electrostatic interactions between the cationic surfactant and anionic silicate species with subsequent condensation of the silica precursor within the aqueous domains of the liquid crystal. This seemed an obvious conclusion as suggested by the clear resemblance between the MCM-41 structure and the H_I liquid crystalline phase found in surfactant-water mixtures. Davis *et al.*[36, 37] supported by in situ ^{14}N NMR data proposed an alternative mechanism however, in which the synthesis mixture phase separates into a biphasic mixture of largely surfactant free aqueous solution and a small region rich in silicate encapsulated cylindrical micelles. The liquid crystalline phase is not present in the synthesis medium prior to or during formation of MCM-41. It was suggested that phase separation occurs because the surfactant concentration is too low to permit formation of bulk liquid crystalline phases throughout the entire mixture. Stucky and co-workers supported this mechanism in which initially randomly ordered micelles interact with the silicate species, resulting in the condensation of 2 or 3 monolayers of silica around the external surface of the micelles.[38] These composite species were proposed to subsequently aggregate with further condensation as represented schematically in Figure 1.4.2[39] to give the characteristic long-range order of MCM-41 materials.

H_2O $Si(OH)_3O^-$

Rod-like
micelles

silicate

Phase separation and assembly
to a hexagonal structure

condensation
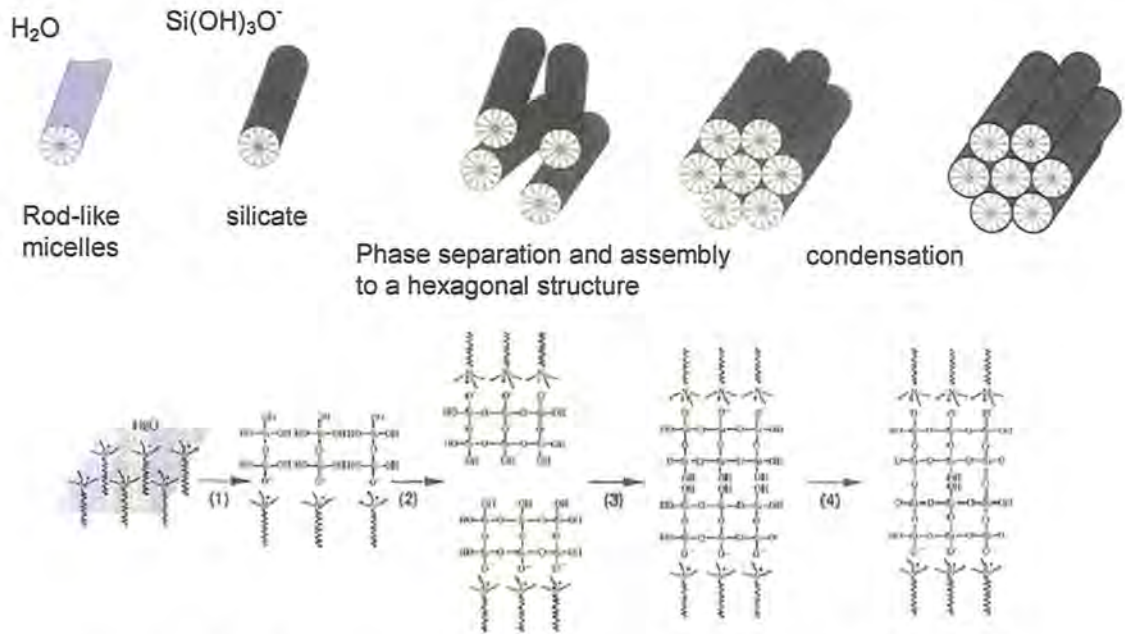
Figure 1.4.2: Proposed mechanism for the formation of MCM-41 via silicate
encapsulated rod-like micelles.[*39*]

There is a large number of variations on the Mobil method, but they all rely on self-assembly of micelles at low surfactant concentration. Critical to the method is the charge interaction between the surfactant head group and the forming material.

Use of non-ionic templates has used hydrogen bonding interactions (rather than electrostatic interactions) between non-ionic template forming species such as primary amine[*40*] and polyoxyethylene[*38*] and allows the templating of a wider range of materials than do electrostatic templating methods using ionic surfactants. In addition, the thicker pore walls obtained using non-ionic templates marginally improve the poor thermal and hydrothermal stability of the mesopore framework.[*41*] Stucky and co-workers[*42, 43*] extended the use of non-ionic surfactant templates to the synthesis of a range of mesoporous transition metal oxides using the Pluronic® block copolymer surfactants with the general formula $(PEO)_x(PPO)_y(PEO)_x$. This method, which exploits block copolymer assembly, induced by complexation of the inorganic metal species and hydrophilic copolymer moieties, has produced materials with pore diameters as large as 14 nm.

1.4.2 Direct Liquid Crystal Templating

An alternative surfactant templating route devised by Attard *et al.* used template mixtures with high surfactant concentrations (typically > 30 wt.% surfactant) to produce mesopore morphologies identical to the M41S family structures.[38] However, unlike the previously mentioned routes, Attard and co-workers demonstrated the ability to fabricate monolithic structures. This method is termed 'direct liquid crystal templating' (DLCT) because unlike previously mentioned routes in which the formation of the mesoporous material is directed by micellar aggregates, deposition of the mesoporous material occurs within a preformed, ordered liquid crystalline mesophase. As a result of the existence of the template prior to deposition of the material, the formation of the template does not rely on hydrogen bonding or electrostatic interactions between the surfactant and inorganic precursor or polymerisation of inorganic species on micellar aggregates. Therefore, the DLCT route could possibly tolerate a greater range of deposition chemistries than the low surfactant concentration routes. In addition, the presence of the template prior to deposition introduces a greater degree of predictability into the deposition process, since the mesopore morphology of the deposited material has been shown to reflect that of the surfactant template.

1. condensation of silica precursor in aqueous domain

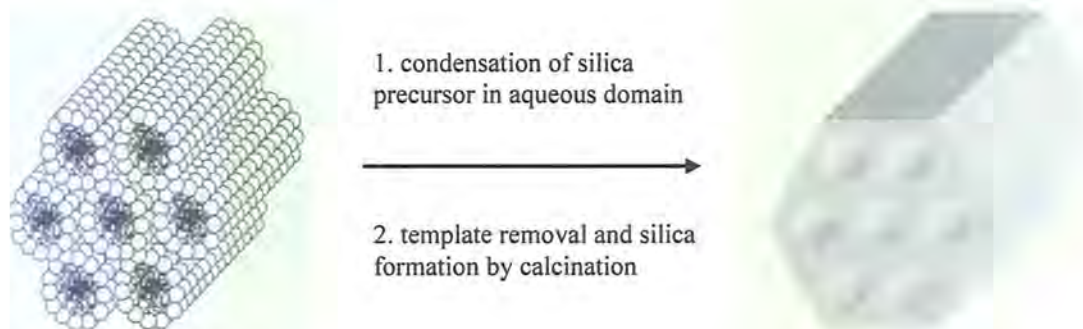2. template removal and silica formation by calcination

Figure 1.4.3: Silica condensation is preceded here by the formation of a liquid crystalline phase of H_1 morphology.[21]

Deposition of mesoporous silica by Attard *et al.* was carried out using a sol-gel reaction localised in the aqueous domains of the liquid crystal phases of polyoxyethylene

surfactants, as represented schematically in Figure 1.4.3. After condensation of the silica phase, the template was removed by calcination. This type of preparation has been used extensivly to prepare and study mesoporous forms of Silica and Titania and will be discussed in detail in chapter three.[44-50]

The versatility of the DLCT route was shown by Templer and co-workers with the demonstration of the synthesis of high surface area platinum powder by reduction of hexachloroplatinic acid with the aqueous domains of a H_I liquid crystalline phase.[51] The templated platinum powder was characterised by a specific surface area of ~ 60 m^2 g^{-1} as compared to 35 m^2 g^{-1} characteristic of platinum black materials. Attard *et al.* reported an extension of the DLCT route; hexachloroplatinic acid confined within the aqueous domains of a polyoxyethylene surfactant was electrochemically reduced to platinum metal at the surface of an electrode immersed in the mixture.[52, 53] During this process a thin monolithic platinum film was deposited in regions occupied by the aqueous domains of the surfactant with the same morphology as materials produced by the chemical reduction route.[54] This process and subsequent removal of the surfactant template to produce a porous structure is represented schematically in Figure 1.4.4.
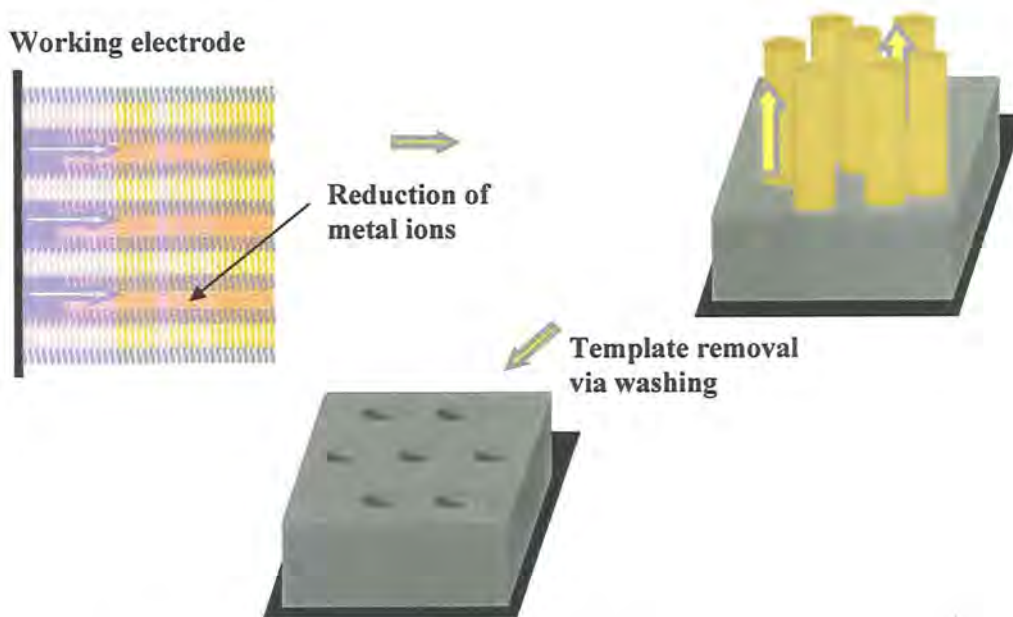

Figure 1.4.4: Illustrates the electrodeposition of metal films (grey) within the aqueous domains of an H_I liquid crystal. Mesoporosity is created on removal of the surfactant template (yellow).

These electrodeposited films were shown to possess high surface areas and more importantly, high electrochemically accessible surface areas as demonstrated by surface activity in sulphuric acid and toward methanol oxidation.[*53, 55*]

Since these reports, a number of studies have been conducted concerning the electrodeposition of mesoporous materials using liquid crystalline templates. Bartlett *et al.* deposited mesoporous palladium[*56*] and cobalt[*57, 58*] with H_I morphologies from the corresponding phase of a polyoxyethylene surfactant. Nandhakumar *et al.* electrodeposited H_I selenium also using a template mixture based on polyoxyethylene surfactant and selenium dioxide.[*59, 60*]

Huang and co-workers obtained cuprite (Cu_2O) nanowires by electrodeposition within the aqueous domains of a reverse hexagonal phase liquid crystal.[*61*] Nanowires tens of micrometers in length were grown, assisted by electric field alignment of the ionic surfactant template between the electrodes. Elliott and co-workers electropolymerised poly(1,2-diaminobenzene) within the aqueous domains of a polyoxyethylene surfactant template.[*62*] Cheng *et al.* used a Pluronic® surfactant based template to synthesise mesoporous tungsten oxide for possible application as an electrochromic material.[*63-65*] Although the mesoporous material compared favourably with its sol-gel derived counterpart in applications testing, the mesoporosity of the templated material was shown to be disordered, and the mesopore structure collapsed during calcination at 400 °C due to crystallisation of the framework walls. Ozin and co-workers reported the fabrication of mesoporous nickel-yttria-zirconia composites deposited using a quaternary ammonium surfactant for fuel cell applications.[*66, 67*] An impressive thermal stability threshold of 800 °C was reported.

1.5 The Lithium Ion Battery.

Lithium batteries have found wide application as energy storage devices because of their ability to reversibly store lithium with high energy densities. There reliance on non-aqueous rather than aqueous electrolytes enables operating voltages greater than 3 V to be achieved, so that energy densities are greater than in aqueous batteries. Lithium batteries function by storage of lithium ions in an electrode material either by intercalation, alloying or the formation of ionic bonds. Figure 1.5.1 shows the movement of Li^+ ions (pink) through an electrolyte (green) between two electrode materials (yellow) capable of hosting such ions in their interlayer cavities.
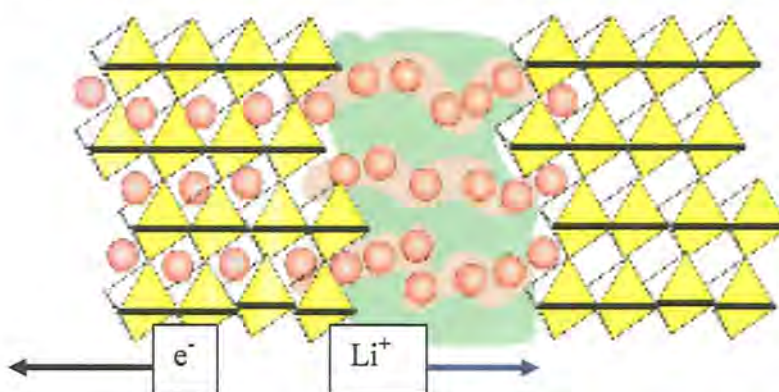
Figure 1.5.1 Lithium batteries accommodate guest lithium ions between layers or within cavities in the electrode structure as indicated here and in doing so provide a means of store charge.

1.5.1   Positive Electrodes

Lithium batteries function by reversible storage of lithium ions in the electrode materials by intercalation, alloying, or formation of ionic bonds. Positive electrode materials usually consisting of lithiated transition metal oxides, of which $LiCoO_2$, $LiNiO_2$, and $LiMnO_2$ have received the most interest. Although $LiNiO_2$ exhibits the highest energy density, its commercialisation has been outstripped by others. This is a consequence of the difficulties in obtaining the desired β- phase from conventional synthetic routes such as high temperature solid state reactions. Problems arise due to the instability of trivalent nickel species, as well as disordering of cationic distribution at lithium sites within the structure. Energy friendly low temperature syntheses are

therefore sought after to reduce this structural disordering that can occur at high temperatures.   Soft chemistry techniques such as hydrothermal techniques or ion exchange reactions have been proposed.

1.5.2   Negative Electrodes

Commercially graphitic carbon (first introduced by SONY) is widely used, with insertion of 1 Li per 6 carbons to form LiC_6. A capacity of ~320 mA h g^{-1}, and an insertion voltage of 0.25 V *vs* Li means the cell voltage remains acceptably high. Other negative electrode materials include alloys with Si, Al and Sn which offer much larger capacities (> 600 mA h g^{-1}); however, the retention of capacity on cycling was poor.

Rutile and many other forms of TiO_2 have exhibited reversible insertion and extraction of lithium up to a stoichiometry of about $Li_{0.5}TiO_2$, which is sufficient for applications in lithium batteries.[*68, 69*]   Nanotubes and nanowires can be prepared from methods including hydrothermal synthesis; such as the high density polymorph $TiO_2(B)$.[*70*] TiO_2-(B) has a discharge potential of 1.4 V *vs.* Li and a capacity of approximately 200 mA h g^{-1}.   One significant advantage of this material is its high discharge potential removes the threat of dendrite formation and subsequent cell failure from Li plating; with a graphitic electrode this can still sometimes be a problem, especially at high rates. Mesoporous forms have also been used for lithium storage, and an additional pseudo capacitance has been found as a result of the high internal surface area.[*2, 71, 72*] (these are discussed in more detail in the chapters on TiO_2).

1.5.3   Electrolytes

Electrolytes used in most lithium ion batteries comprise lithium salts dissolved in an organic solvent. Most lithium ion batteries however, operate well outside the stability window of such solvents. This problem is resolved as a passivation layer known as the solid electrolyte interface (SEI) forms on the surface of the negative electrode and protects against decomposition, whilst also permiting ion conduction from the electrode to the electrolyte. Many different salts have been used during the development of the Li ion battery, however, recently $LiPF_6$, and LiTFSI appear most commonly within the literature. Various different organic solvents have also been examined; with ethylene carbonate (EC) and dimethyl carbonate mixtures (DMC) being the most widely used.

Several different polymer electrolytes have also been trialled, such as polyethylene oxide (PEO). The use of such electrolytes has several advantages compared with the organic solvents; the increased strength over the porous separator forms a physical barrier to dendrites reducing the possibility of short circuits. The low vapour pressure also reduces the chance of the cell drying out which is often a problem with liquid electrolytes. Another recent approach has been the use of ionic liquids which have extremely low vapour pressure and are resistant to fire. However, problems due to extremely low diffusion coefficients significantly limit their practical application.[73]

1.6 Electrode structures

1.6.1 The composite structure of battery electrodes

Most battery electrodes are composite electrodes with porous structures (Figure 1.6.1). Many electrode materials are inherently poor electronic conductors, therefore a conductive additive (typically acetylene carbon black, ACB) is added to provide electronic 'wires' through the electrode matrix. A polymer binder is added to hold the powder together in a film; typically, this material is PVdF but sometimes PTFE. Negative electrodes have higher electronic conductivity but often a similar structure used; the binder to provide structure and carbon to provide an electronic pathway through the binder. This structure is porous to the electrolyte so the Li ions can easily diffuse to the surface of the active material particles. When the electrodes are poor electronic conductors the electrochemical reaction can only occur at those points where the active material, binder and electrolyte meet.
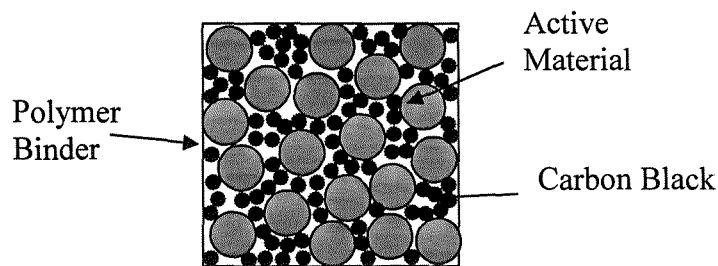
Figure 1.6.1: Schematic of battery electrode comprising: active material (grey circles); conductive additive (black); white regions represent binder.

Electronic electrode resistance is manifest as a voltage drop during operation, and in high power devices such as supercapacitors, this limits the maximum attainable power output. Ionic resistance limitations are equally important for high power operation in devices such as lithium-ion batteries, which function by insertion processes. Ions must diffuse through the electrode structure to undergo reaction and as such resistance to this diffusion results in power and energy losses.

1.6.2   Nanostructures to improve electrode performance.

High power capability in electrochemical devices require large electrode surface areas providing high current densities.   The benefits of large surface areas are negated however, if those species in solution facilitating the reaction are not able to move rapidly to the reaction sites within a high surface area electrode. Therefore, in addition to possessing a high roughness factor, high power porous electrodes must also have a structure capable of facilitating rapid diffusion.   Another requirement for both high power and energy density is low electronic and ionic resistance in the electrode structure itself.

Porous electrodes composed of nanoparticles attempt to address these requirements. Such materials possess high surface areas by virtue of their finely divided nature as illustrated in Figure 1.6.2. Since the particles are of nanometre dimensions, the distance ions must diffuse through the bulk to the interface is extremely small, as depicted schematically in Figure 1.6.3. The time constant for bulk diffusion is low, and therefore reactions can be carried out rapidly. Although these materials may induce a high rate electrode performance, the inherent problem with all such high porosity/low density materials is that they have a lower volumetric energy density and are often difficult to process. For example for a composite battery electrode, it may be envisaged that a larger amount of binder and carbon would be needed to ensure adequate mechanical properties and electronic percolation, resulting in a reduction in the gravimetric energy density. Further negative attributes of the nanoparticulate electrode concern the aggregate structure; a high density of grain boundaries and consequently, high ionic and electronic electrode resistance.   Secondly, the random nature of nanoparticle packing in the electrode means the pore structure is not uniform, and consists of non-linear channels of varying diameter with necking at particle-particle boundaries. Consequently, species moving within the electrode encounter significant tortuosity.
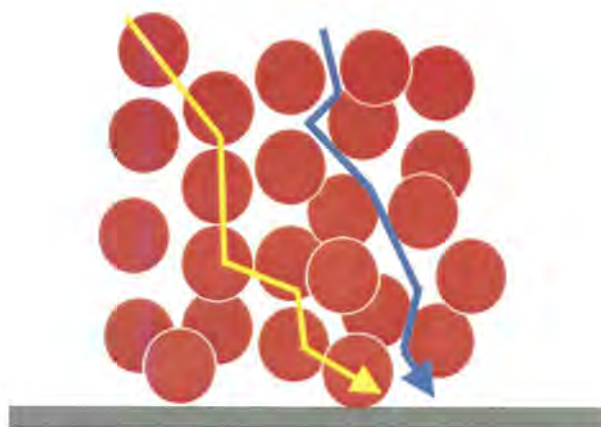
Figure 1.6.2: Intercalated ions and electrons (yellow) and solution bound species (blue) must traverse a considerably tortuous path in order to move through a nanoparticulate electrode.
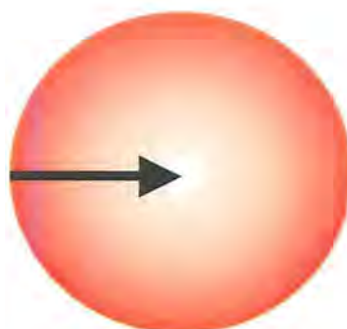
Figure 1.6.3: For complete utilisation of an active material an ion may have to diffuse a distance equal to the particle radius.

Templated materials offer high surface areas, moreover their pore structures offer a number of advantages over nanoparticulate electrodes as illustrated in Figure 1.6.4. The ordered pore system conveyed by the self-assembly of the template facilitates faster diffusion through the pore network such that the inherent capability of high current density which comes with high surface area is realised by high rates of mass transfer. This non-tortuous pore network works in concert with the monolithic electrode structure, the absence of grain boundaries also reduce power losses. Ionic and electronic movement within the templated electrode would encounter relatively low impedance due to the uniformity of the structure.[74] Mesoporous Ni templated by

Nelson *et al.* demonsrated the advantages of such a structure; yielded impressive rate capability and high power in an alkaline solution.[75] Templated electrodes may also offer increased resistance to decrepitation associated with stresses induced by electrode volume expansion and contraction in comparison to nanoparticulate systems because of their more uniform structure. Whitehead *et al.* deposited mesoporous tin from the H_I phase of a polyoxyethylene surfactant.[74, 76] Sn rapidly expands on alloying with Li meaning the useful capacity obtained falls dramatically on cycling due to mechanic decrepitation. The structures obtained in this work appeared to possess some mesoporosity, however, this porosity was disordered and although initially cyclability improved over bulk materials, the capacity still exhibited significant fade after 8-10 cycles.[76]
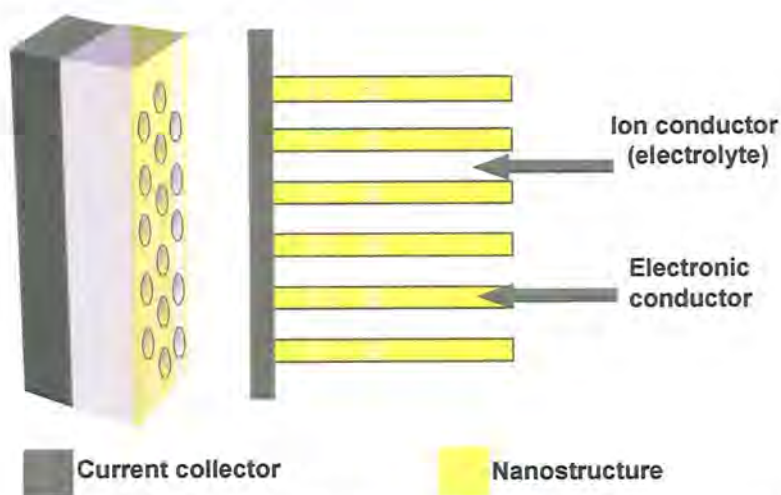
Figure 1.6.4: Schematic of the ideal nanostructured electrode.

1.7 Thesis aims

The aim at the onset of this thesis was to use the design of Nanostructured materials to improve energy storage devices, especially for those which require high charge/discharge current rates such as lithium ion batteries. Investigation of both electrodes operating as monolithic thin films as well as nano scale materials in a composite electrode structures will be carried out. Electrodes will be studied for their suitability in aqueous and non-aqueous battery systems. Initial work in this thesis focuses on finding a nanostructured electrode pair capable of performing as a high rate device.

Chapter 2

Corrosion resistance of a Nanostructured Ni-P alloy.

2.1 Background and Objectives

2.1.1 Mesoporous Nickel the story so far

Prior to this work, successful preparation of Mesoporous Ni (MNi) with an ordered nanostructure has been undertaken.[75, 77]   High rate electrode performance for the $Ni^{2+/3+}$ redox couple $Ni(OH)_2/NiOOH$ was demonstrated, where protons were reversibly stored in alkaline electrolyte.

2.1.1.1   Low Temperature Preparation of Lithiated Transition Metal Oxides

Of the transition metal oxides, $LiCO_2$, $LiNiO_2$ and $LiMn_2O_4$ have received the most attention as possible positive electrode materials in lithium ion batteries. $LiNiO_2$ exhibits the highest energy density of these candidates and has an innate advantage over $LiCoO_2$ because of the lower cost of nickel. Despite this, $LiNiO_2$ has not to date been commercially successful, since the desired β-phase is difficult to prepare using popular synthetic routes such as high temperature solid state reaction. Oxygen atmospheres or partial substitution with cobalt (forming $LiNi_{1-y+}Co_yO_2$) are required to stabilise Ni(III) against the more stable Ni(II) at the temperatures of synthesis (~700 °C). $LiNiO_2$ is also susceptible to cationic disordering and as such, its formula is often written as $Li_xNi_{2-x}O_2$ (with $0 \leq x \leq 1$) where NiO is formed at the lower extreme of lithiation. Here, as x decreases an increasing amount of Ni^{2+} is resident within the van der Waals gap between the NiO_2 layers. This decreases the capacity of the electrode for lithium storage and decreases lithium ion mobility since the amount of lithium ions in the structure is reduced. Electrochemical performance is further reduced as a consequence of cationic disorder because the lower diffusion rates in a disordered electrode increase polarisation.

Low temperature synthetic routes in inorganic chemistry[78] are receiving increasing attention in the technical literature because they offer access to meta-stable compositions and structures as well as to thermodynamically stable low temperature phases that otherwise decompose at higher temperatures. Commercial issues have also driven this interest since high temperature fabrication processes require high capital cost

outlays for fabrication equipment in addition to significant ongoing expense in terms of energy usage.

The structure of $LiNiO_2$ consists of edge sharing NiO_6 octahedra connected to form NiO_2 sheets. On complete delithiation $LiNiO_2$ forms NiO_2. Due to its high open circuit voltage, NiO_2 immediately oxidises atmospheric moisture to form the reduced phase NiOOH. Recognising the close structural relationship that couples NiOOH and NiO_2 (β-NiOOH and $LiNiO_2$ are isostructural with the rock-salt α-$NaFeO_2$)[79] has enabled investigators to pursue low temperature routes to $LiNiO_2$. The majority of these efforts have proceeded with attempts to exchange H^+ with Li^+ ions in a NiOOH structure. The interlayer spacing in γ-NiOOH is 7.2 Å while in β-NiOOH and $LiNiO_2$ this spacing is 4.7 Å. As a result, while the only species resident between the layers of β-NiOOH are protons, γ-NiOOH is capable of accommodating a range of species such as H^+, H_2O and alkali metal ions. Consequently in low temperature ion exchange reactions, the well ordered β-phase of NiOOH is preferred, rather than the disordered impurity containing γ-phase as the starting material.

2.1.1.2   Ion Exchange reaction

$LiMO_2$ layered compounds (where M is a transition metal) are widely known to exchange H^+ for Li^+ in acidic media. However, until recently, no investigations had achieved the reverse reaction:

$$MOOH + Li^+ \rightarrow LiMO_2 + H^+$$ Eq. 2.1.1
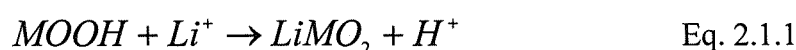
Dahn and co-workers in 1993 were perhaps the first to demonstrate the synthesis of positive electrode materials using an ion exchange process[80], where they successfully lithiated MnOOH using $LiOH.H_2O$ at low temperatures. Amatucci *et al.* ion exchanged the protons in CoOOH to form $LiCoO_2$ using $LiOH.H_2O$ at 100 °C. However the resulting materials contained impurities whose presence severely retarded lithium storage capacity and reversibility.[81] Only on heating the powders to 250 °C were the impurities removed and electrochemical performance improved.

Using a modification of the ion exchange syntheses discussed above, Murata *et al.*[82] reported the low temperature synthesis of lithium nickelate positive electrodes

by chemical oxidation of $Ni(OH)_2$ in an aqueous solution containing an oxidising agent and LiOH at temperatures close to 100 °C. In their 'direct oxidation method' the oxidation of $Ni(OH)_2$ and a subsequent ion exchange reaction took place in the same medium, allowing the authors to obtain almost pure β-phase material. Capacities as high as 310 mAh g^{-1} were reported which was attributed to storage capacity derived from both the Ni^{2+}/Ni^{3+} and Ni^{3+}/Ni^{4+} redox couples. This impressive capacity was attributed to the potential difference between these two couples which was shown to be significantly less than in materials synthesised at high temperature, while the capacity of the Ni^{2+}/Ni^{3+} redox couple was also much greater. The oxidised product NiOOH is said to ion exchange H^+ for Li^+ to form the isostructural $LiNiO_2$. If such high rate performance was reproduced in aprotic lithium electrotyles for Li^+ cycling, then the extended voltage stability window could be utilised to produce the ultimate high power device. However on the electrochemical cycling of the proposed ion exchanged product $LiNiO_2$ in aprotic electrolytes, the capacity was seen to decay rapidly. This was attributed to the corrosion of the structure in particular the Ni-O bonds, if this corrosion process were to be eradicated extended cycling could be possible. Therefore a Ni alloy with corrosion resistant properties is desirable.

This chapter seeks to demonstrate the fabrication of both non-templated and nanostructured nickel phosphorus (Ni-P) alloy film electrodes. A quantitative investigation of corrosion resistance versus phosphorous content in both aqueous and non-aqueous environments will be reported. The ion exchange product $LiNiO_2$ will be compared for both mesoporous Ni and NiP.

2.2 Deposition Ni-P alloys

Nickel-phosphorus deposits are important surface finishes for industrial materials owing to their electrocatalytic activity for hydrogen evolution, special paramagnetic characteristics, excellent microhardness and corrosion resistance.[83] Nickel-phosphorus is a relatively complex system and can form a number of stable compounds. Two mechanisms for the incorporation of phosphorus during electrodeposition of Ni-P have been proposed; a direct and an indirect mechanism.[84] In the direct mechanism, the oxyacid in the bath, i.e. phosphorous acid (H_3PO_3), is reduced solely to the elemental state. In the indirect mechanism, phosphine (PH_3) is an intermediate in the

formation of the Ni-P alloy.[85] Electrodeposition of nickel takes place with co-deposition of phosphorus in octahedral interstitial sites. The pH of the plating solutions is an important consideration for the electrodeposition of phosphorus alloys. It is well known that above a critical phosphorous content, the Ni-P alloy becomes amorphous; amorphous alloys tend to be harder and have higher contact resistance than their crystalline counterparts.[86] Amorphous alloys prepared by electrodeposition are generally brittle or of low ductility.

2.2.1 Corrosion Parameters

Corrosion resistance can be measured thermodynamically by determining any shift in the equilibrium potential of corrosion (E_{corr}). It can also be measured kinetically by studying the ability of a material to form a passivation layer to impede corrosion. The point where passivation ceases to be effective is accompanied by an exponential rise in corrosion current; this point is often referred to as the Pitting Potential (E_p).

2.3 Experimental

2.3.1 Deposition Baths

Nickel(II) acetate tetrahydrate (>99%) and sodium acetate trihydrate (>99.5%) were obtained from Fluka. Boric acid (>99.5%) was obtained from BDH chemicals. Phosphorous acid (>99% Aldrich) and sodium hypophosphite (>98% Fisons) were obtained from Aldrich and used as received. All solutions were prepared using deionised water. The initial deposition bath was made up of 0.2 M nickel (II) acetate (Ni(Ac)$_2$) as the nickel salt, 0.2 M boric acid (H$_3$BO$_3$) to buffer against pH changes at the electrode surface and to act as a surface stabilising agent, and finally 0.5 M sodium acetate (NaAc) as a supporting electrolyte. Nelson *et al* initially used a bath of this nature, and it is known to be compatible with the surfactant, and to form stable liquid crystalline phases.[87] It is understood that some components of typical Ni-P alloy baths, such as nickel sulphate or sulphamate produce inhomogeneous bi-phasic liquid crystal phases rendering them useless for the fabrication of nanostructured films. To the initial Ni deposition bath a range of 0.2 M to 1.0 M of phosphorus acid or sodium hypophosphite was added as the phosphorous source. The amount being dependent on the desired P content in the alloy.[88]

2.3.2 Electrodeposition

Electrochemical experiments were carried out using a purpose built potentiostat and potential ramp generator, or alternatively a varied multi-channel potentiostat, (VMP, Perkin Elmer). A three-electrode cell was used consisting of a gold working electrode, a saturated calomel reference electrode (SCE), and a platinum gauze counter electrode, all potentials given are with reference to SCE. Electrodeposition and characterisation was carried out in Pyrex water- jacketed cells, with temperature maintained at 25°C with an accuracy of $^+$/.0.1 °C using a Grant ZD thermostatted water bath. All glassware was washed in a solution of 5 % Decon 90(Hogg) for 24 hours before soaking in dilute HCl, rinsing in deionised water and drying in an oven. The Ni-P alloys prepared for electrochemical characterisation were deposited onto 1 mm diameter gold disc electrodes set in an epoxy insulator. Electrodes were first cleaned by polishing sequentially with 25 μm, 1 μm, and 0.3 μm alumina-embedded microcloths.

The electrodes were then cycled between –0.6 V and 1.4 V *vs.* SMSE at 200 mVs^{-1} for 5 min. in a 2 M H$_2$SO$_4$ solution. With each cycle a layer of gold oxide was formed and subsequently removed from the electrode surface. The cycling was suspended in the reduced oxidation state such that the gold was a clean deposition ready surface.
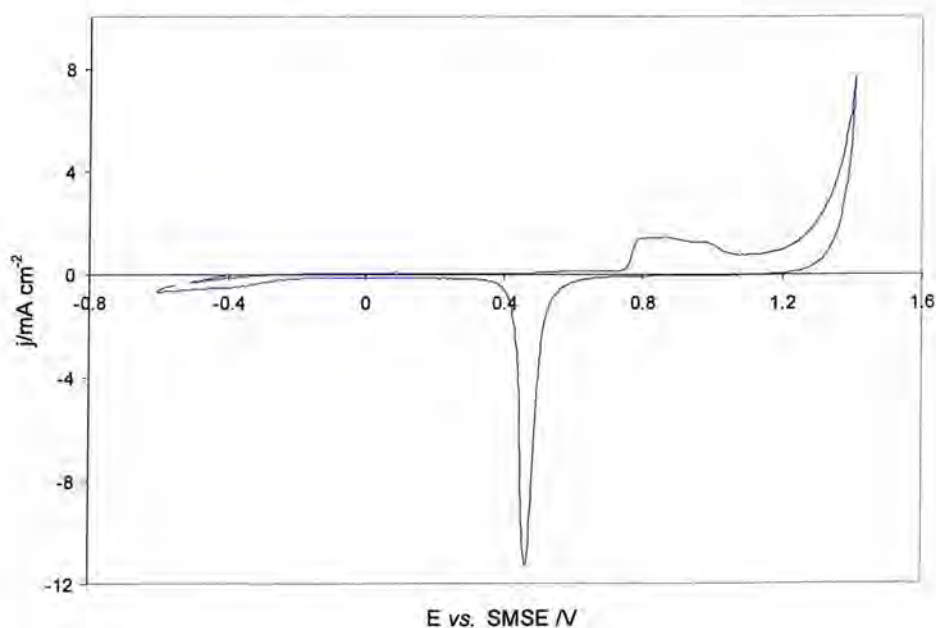

Figure 2.3.1: Voltammetry of a polished Au disc electrode cycled in 2 M H$_2$SO$_{4(aq)}$ at 200 mV s^{-1}.

Films grown for scanning electron microscopy (SEM) and energy dispersive X-ray analysis (EDX), as well as small angle x-ray scattering (SAXS) were deposited on ~0.25-1 cm^2 thin film gold electrodes made by evaporation of gold on to chromium-coated glass microscope slides. Prior to deposition electrodes were cleaned in an ultrasonic bath of 2-propanol for 30 minutes and left to dry under ambient conditions.

2.3.3 Liquid Crystal Templating mixtures

The non-ionic surfactants Brij® 56 ($C_{16}EO_n$ where n~10) and Brij® 78 ($C_{18}EO_n$ where n~20) were obtained from Aldrich and used as received. The templating media used in the electrodeposition of mesoporous nickel were binary systems comprising either Brij® 56 or Brij® 78 surfactants and an aqueous precursor solution consisting of 0.2 M nickel acetate, 0.5 M sodium acetate and 0.2 M boric acid and 0.5 M phosphorous acid. In preparing the mixtures the surfactant was heated to ~60 ° C (above its melting point) in a glass vial, and mixed manually using a glass rod on addition of the aqueous solution. Mixing times of ~10 minutes were required to obtain a homogeneous mixture. Complete mixing was confirmed by homogeneity of the liquid crystal's color and by the absence of macroscopic surfactant particles under the non-polarizing light of an optical microscope. An Olympus BH-2 polarizing microscope equipped with a Linkam TMS 90 heating/cooling stage accurate to ±0.1°C was used to investigate phase behavior. Here, thin films of the liquid crystals were prepared by sandwiching the mixture between a glass microscope slide and cover slip. Liquid crystalline phases were identified based on their optical texture, viscosity and the shape of the air bubbles present in the mixture.[51, 52] Templated Ni-P films were deposited initially from a 55/45 wt.% Brij® 56/precursor solution. Prior to the commencement of electrodeposition, the liquid crystalline electrolyte was heated to approximately 50 °C (into the less viscous micellar solution or lamellar phase regions) and then allowed to cool without assistance for 15 min. followed by a further 15 min. cooling period assisted by a water bath held at the deposition temperature.[87] This process essentially annealed the liquid crystal, allowing internal stresses in the mesophase to be relieved. In combination with the 30 min. cooling period, this annealing resulted in the formation of a more continuous and ordered phase structure, as well as allowing larger air bubbles to be removed from the solution by virtue of their buoyancy in the less viscous

electrolyte at 50 °C. The removal of air bubbles ensures that the deposition of metal films is homogeneous over the entire electrode surface. During this annealing process the liquid crystal solutions were covered with parafilm to limit water loss. All templated Ni-P films were deposited at -800 mV *vs.* SCE before washing in isopropanol for 24 h.
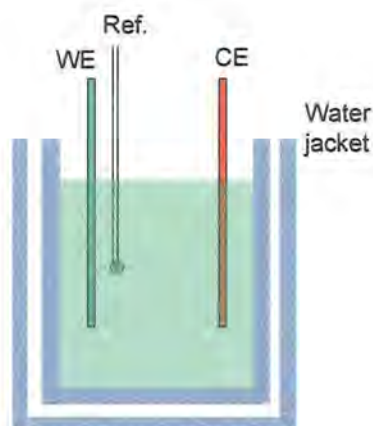

Figure 2.3.2: This schematic shows the electrodeposition cell consisting of a three electrode cell contained within a glass water jacket used in the deposition of nickel phosphorous alloys, as well as liquid crystal template depositions.

2.3.4   Characterisation

The electrochemically accessible surface area of the prepared films was investigated by examination of the charge associated with the Ni $^{2+/3+}$ redox peaks in 6 M KOH. Cycling was between -1250 mV and 500 mV *vs.* SCE at a scan rate 20 mVs^{-1} and temperature 25 °C. Electrochemical corrosion testing was carried out using linear sweep voltammetry (LSV) in 0.1 M HCl from -0.6 to $+2.0$ V *vs.* SCE to determine the corrosion resistance using a Tafel type analysis, at a rate of 1 mVs^{-1}, 25 °C. The charge associated with the Ni $\rightarrow$ Ni^{2+} peak was also utilised to calculate the efficiency of deposition reactions from aqueous solution and liquid crystal templates. Testing in a Lithium battery electrolyte 1M LiPF$_6$ in propylene carbonate (PC) was used and cycled over the range 2.0 to 5.0 V Li/Li$^+$, also at 1 mVs^{-1}, 25°C. Cell assembly was carried out in air free conditions under argon. A newly scratched Aluminium wire 1 mm diameter (>99.99%, Aldrich) was encapsulated in epoxy , and tested for comparison with the Ni-P alloys produced.

2.3.5   Structural Characterisation

Both low resolution SEM and EDX analysis was performed using a JEOL JSM 6400 field emission microscope operating at an accelerating voltage of 20 kV.   X-ray diffraction was carried out using a Siemens D-5000 diffractometer (Cu-K$_\alpha$ radiation) with a 2θ range of 1-5° and a scan rate of 12° min^{-1}.

2.3.6   Ion Exchange

Ion exchange reactions were by either direct transfer to the aprotic lithium electrolyte, or by cycling in saturated lithium hydroxide solutions. The latter was carried out in 1.5 M LiOH$_{(aq)}$ at 50 $^\circ$C, by cycling at 1 mVs^{-1}, for 24 hours to promote the exchange reaction. The direct transfer method was simply to cycle the as prepared film, to the oxidised NiOOH form, before ion exchanging.

2.4 Results and Discussion

2.4.1 Investigation of Precursor Solution

Prior to depositing nanostructured NiP a precursor solution had to be identified and tested for varied P content and properties. Deposition baths of both phosphorous acid and sodium hypophosphite were studied to determine the most suitable for liquid crystal templating.

Figure 2.4.1: Cyclic voltammograms of 0.2 M Ni(Ac)$_2$, 0.5 M Na(Ac) 0.2 M H$_3$BO$_3$,(Blue) with 0.2 M NaH$_2$PO$_2$ (Pink) on 1 mm gold disc at 50 mVs^{-1} at 25 ^{o}C.
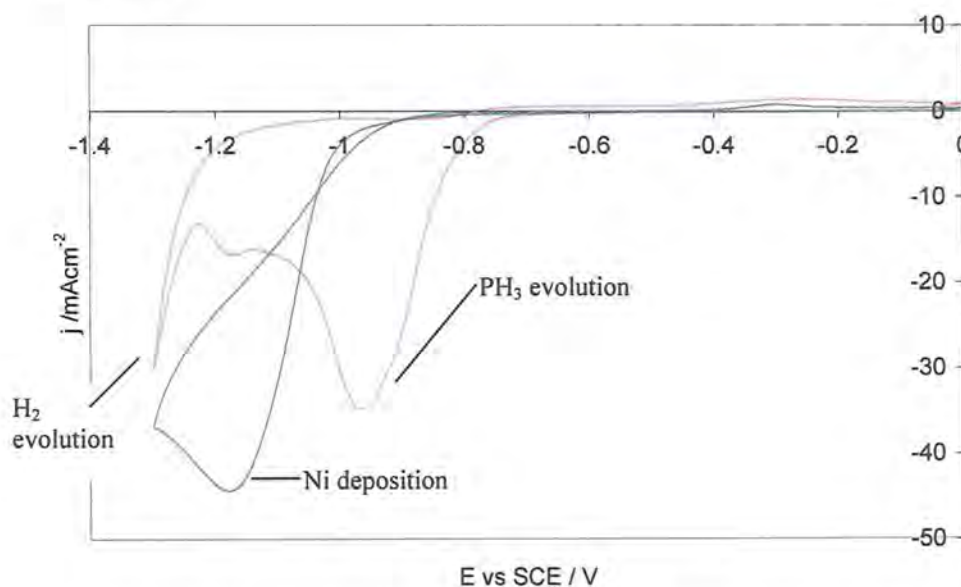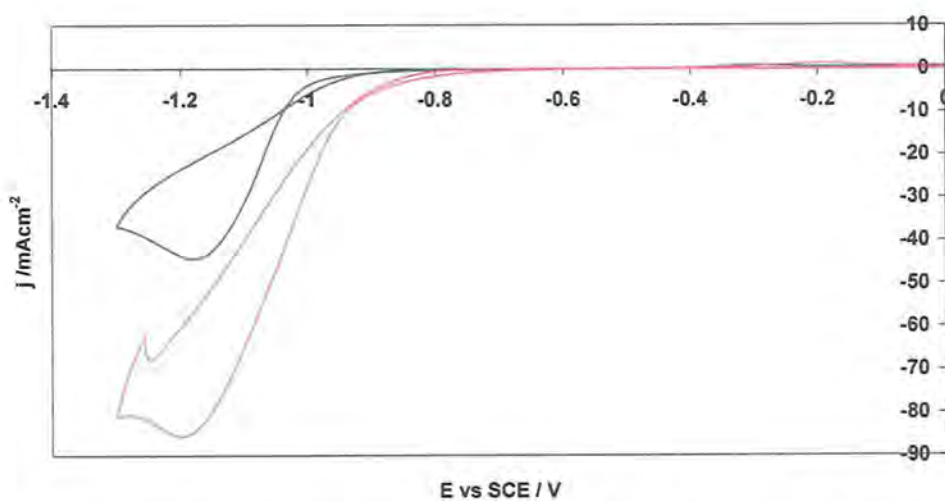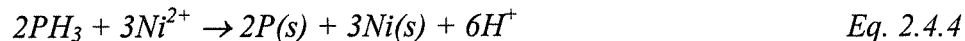

Figure 2.4.2: Cyclic voltammogram of 0.2 M Ni(Ac)$_2$, 0.5 M Na(Ac) 0.2 M H$_3$BO$_3$,(Blue) with 0.2 M H$_3$PO$_3$ (Pink) on 1 mm gold disc at 50 mVs^{-1} at 25 ^{o}C.

45

Initial cyclic voltammograms are displayed in Figure 2.4.1 and Figure 2.4.2 respectively, (pure nickel is displayed as a background). From the voltammetry of the hypophosphite deposition solution Figure 2.4.1, three peaks can clearly be identified. The first broad peak, *ca.* -0.9 V corresponds to the production of the $PH_3(g)$ intermediate, confirmed by formation of tiny bubbles on the electrode surface.(*Eq. 2.4.3*) The detection of $PH_3(g)$ has been confirmed by spectroscopy.[85] A second wave at peak current *ca* -1.15 V corresponds to direct deposition of nickel (*Eq. 2.4.2*), a lower intensity is observed than for nickel deposition from the background solution as some Ni is being used in the chemical reduction step. (*Eq. 2.4.4*) The onset of hydrogen evolution (*Eq. 2.4.1*) is clearly identified at −1.3 V. Proposed mechanism for Ni-P electrodeposition[89]:

$$2H^+ + 2\,e^- \rightarrow H_2 \qquad\qquad Eq.\ 2.4.1$$

$$Ni^{2+} + 2e^- \rightarrow Ni \qquad\qquad Eq.\ 2.4.2$$

$$H_3PO_3 + 6H^+ + 6e^- \rightarrow PH_3 + 3H_2O \qquad\qquad Eq.\ 2.4.3$$

$$2PH_3 + 3Ni^{2+} \rightarrow 2P(s) + 3Ni(s) + 6H^+ \qquad\qquad Eq.\ 2.4.4$$

In Figure 2.4.2 the three electrode processes are super-imposed as one peak, consequently higher currents are observed when comparing with the background of Ni deposition. Hydrogen evolution has been shifted more positive (lower over potential) as the solution is more acidic, while the formation of PH_3 has been shifted more negative as the reduction is from oxidation state (OS) +3 in phosphorous acid as compared to OS +1 in the hypophosphite.

2.4.2   Characterisation

Investigation of P content was studied by variation of over-potential for deposition from the phosphorous acid bath. The Ni-P alloys were deposited potentiostatically, ranging from 650-1200 mV *vs.* SCE. The results are displayed in Figure 2.4.3.
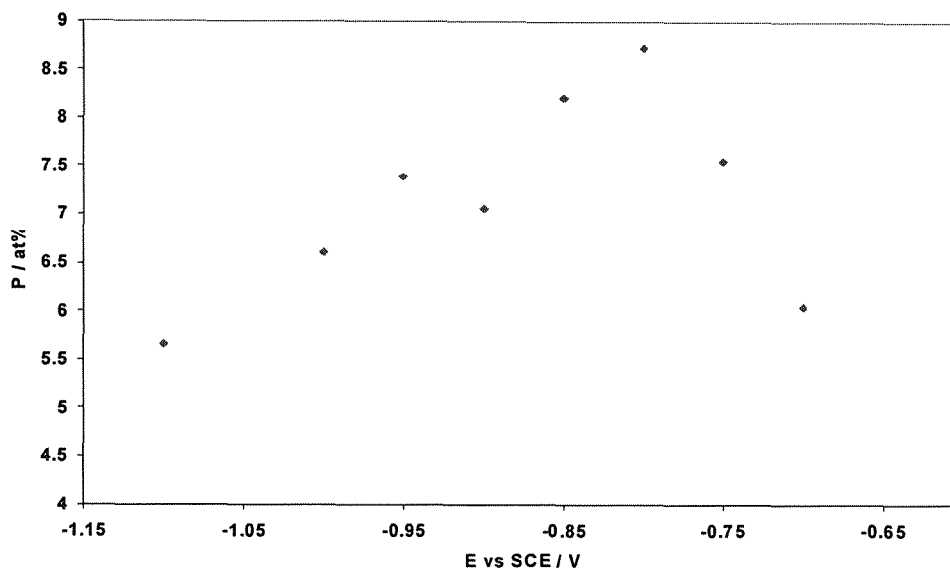
Figure 2.4.3: The affect of overpotential on the amount of phosphorus in atom percent (at %) in the nickel phosphorus alloy, deposited from 0.2 M Ni (Ac)$_2$, 0.2 M H$_3$BO$_3$, 0.2 M H$_3$PO$_3$, 0.2 M Na(Ac) at 25 ^{0}C.

P content was maximized from deposition at −800 mV *vs*. SCE. This could be due to the competing reactions of direct Ni deposition (eq.2), and the chemical reaction step, since P cannot be directly electrodeposited from aqueous solutions.[*85*] Therefore at a voltage of -800 mV PH$_3$ is being produced and the chemical reaction step (*Eq. 2.4.4*) is able to occur, whilst the overpotential for direct Ni deposition is not enough to increase the Ni:P significantly. At more negative overpotentials the P content in the deposit is reduced, as the direct deposition of Ni would become more prominent. At less negative overpotentials it is possible that little amounts of PH$_3$ would be produced so less phosphorus would be incorporated as a result. The investigation of overpotential from films produced from hypophosphite as the P source were also examined, however the films were characteristically brittle, with cracks throughout the structure. The voids in the deposit can be attributed to tiny PH$_3$ bubbles trapped on the surface. Deposits obtained from the phosphorous acid containing solutions were characteristically smooth and uniform over a range of over-potentials with cracks, voids and some surface inclusions only occurring at high over-potentials. A typical deposit from both phosphorous acid and hypophosphite can be seen from SEM in Figure 2.4.4.

(a)
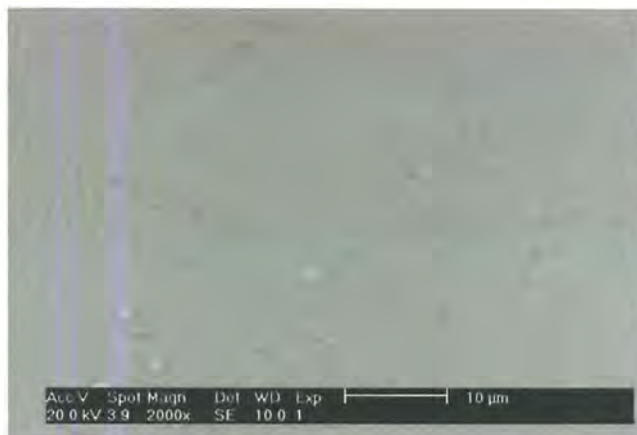
(b)
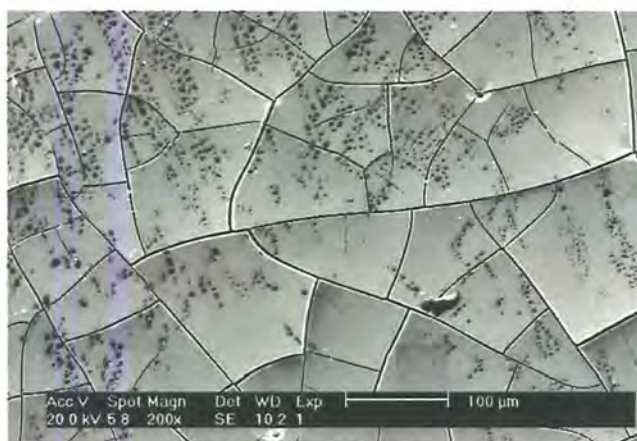
Figure 2.4.4: SEM micrographs of typical deposits from 0.2 M $Ni(Ac)_2$, 0.5 M Na(Ac) 0.2 M H_3BO_3, with 0.2 M H_3PO_3 (a) and 0.2 M NaH_2PO_2 (b), deposited at -800mV *vs*. SCE at 25 $^{\circ}$C.

The focus of the study was consequently directed on phosphorous acid as the phosphorous source in the deposition bath. EDX elemental analysis was used to determine P content, a typical spectrum is included in Figure 2.4.5. An EDX map is also included in Figure 2.4.6, which shows the elemental distribution of both Ni and P from a sample of one of the alloys produced.
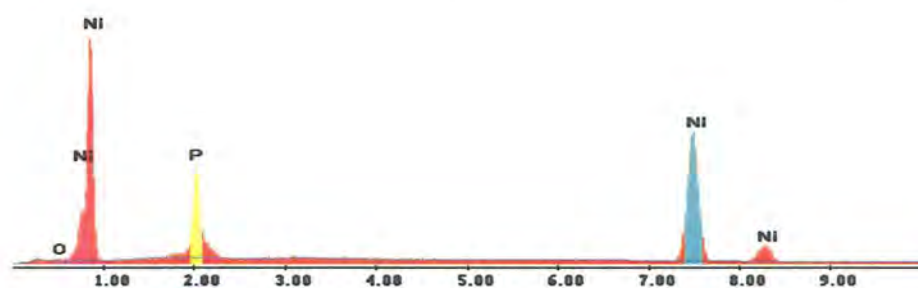
Figure 2.4.5: A typical EDX analysis of film deposited from 0.2 M Ni (Ac)$_2$, 0.2 M H$_3$BO$_3$, 0.9 M H$_3$PO$_3$, 0.2 M Na(Ac) at −800 mV, 25^{0}C.

(a)   (b)

(c)   (d)
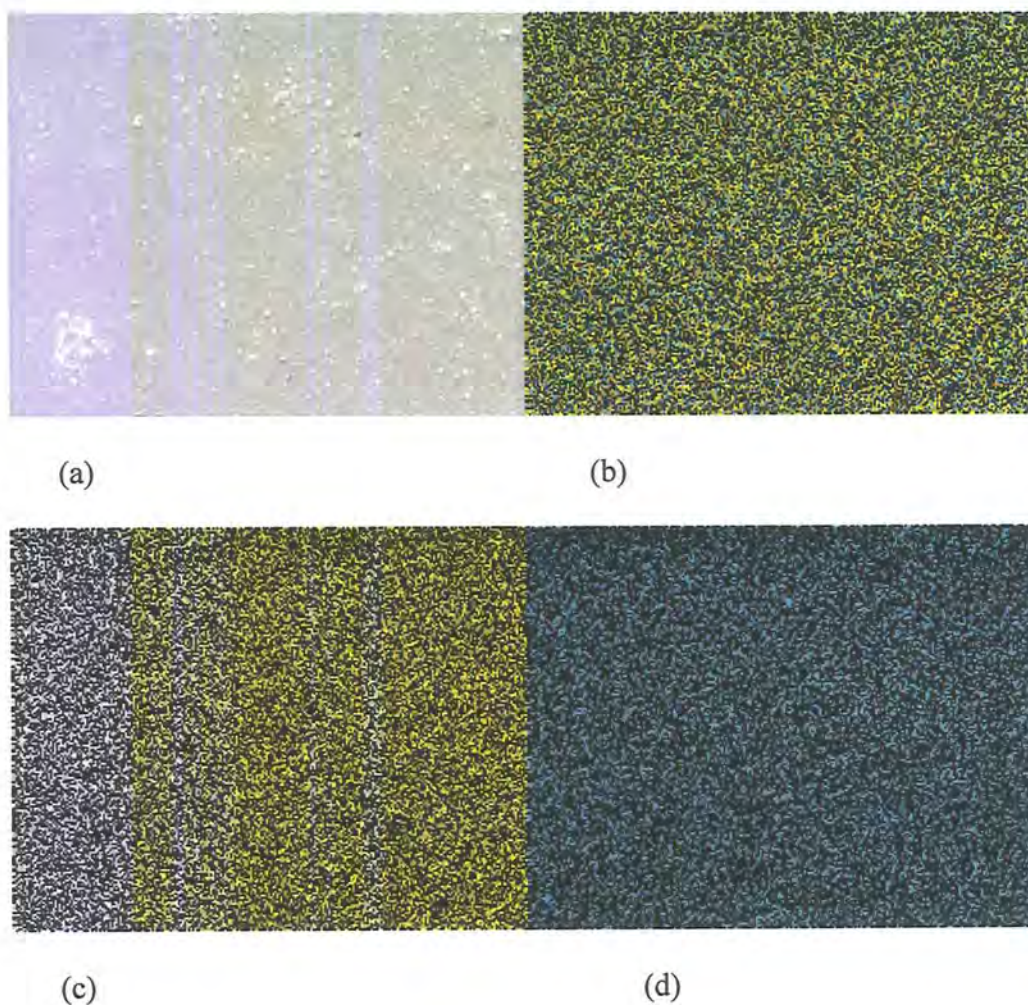
Figure 2.4.6: EDX map of Ni-P alloy deposited from 0.2 M Ni (Ac)$_2$, 0.2 M H$_3$BO$_3$, 0.9 M H$_3$PO$_3$, 0.2 M Na(Ac) at −800 mV, 25 ^{o}C. (a) region of film from which map was recorded, (b) an overlay of the nickel and phosphorus regions; nickel map (c) and phosphorus map (d). Sample size is ~300 μm across.

From the EDX map it can be observed that the deposition of the alloy is generally uniform with no P or Ni rich regions. This is important, as the corrosion resistant nature of the alloy must remain constant throughout the film.
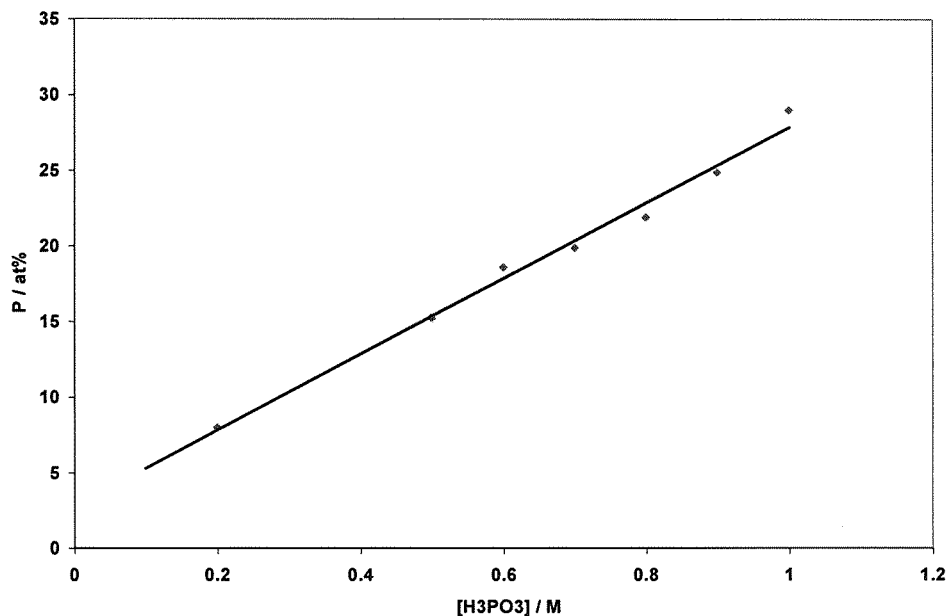
Figure 2.4.7: P content in atomic % for increasing concentrations of phosphorous acid at -800 mV *vs*. SCE.

Varying the amount of P in the alloy was achieved by changing the concentration of phosphorous acid in the deposition bath as seen in Figure 2.4.7. The pH was not adjusted and the deposition bath becomes more acidic as more H_3PO_3 is added. The result is that a linear distribution of P is observed i.e. as more phosphorous acid is added to the bath a steady increase in the P content is observed which is in accordance with literature values.[*88*]

2.4.3 Corrosion in HCl

Films of differing P content were tested for their corrosion resistance in HCl, a Tafel plot appears in Figure 2.4.8 e.g. $Ni_{90}P_{10}$ refers to 10 atom percent phosphorus.
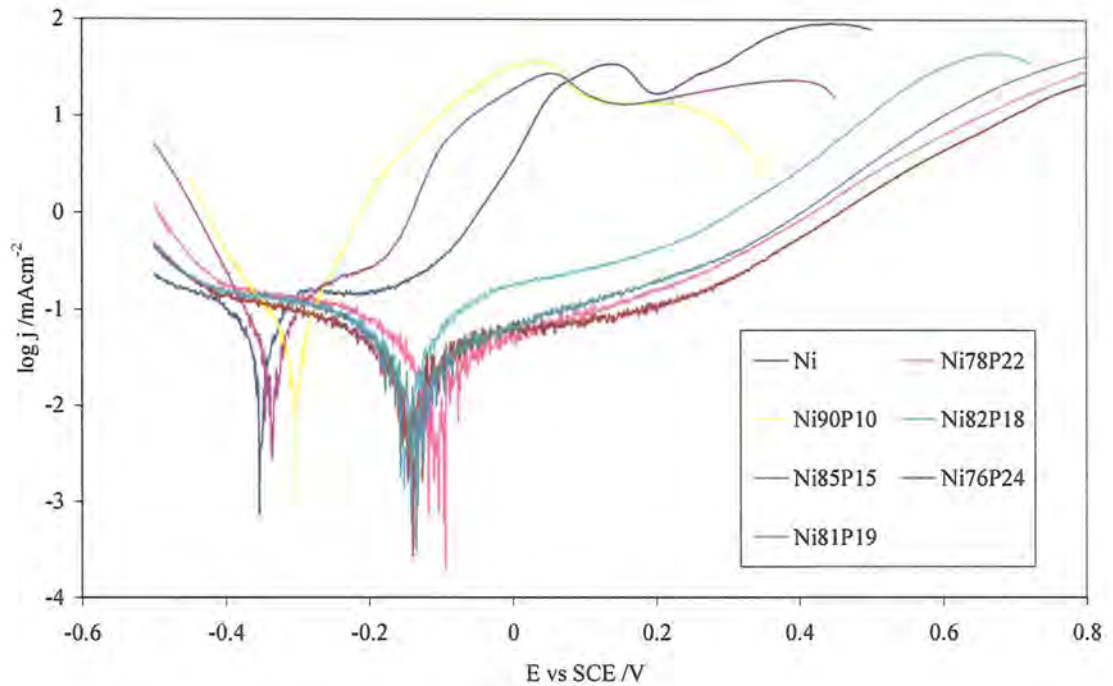
Figure 2.4.8: A Tafel plot produced from the linear sweep voltammetry (LSV) of Ni-P alloys with varied compositions (atomic % displayed in legend) in 0.1 M HCl at 1 mVs^{-1}, 25 °C. Scanned from -0.5 until complete dissolution of Ni. Solution has not been purged for oxygen. Current density is refers to geometric area of the gold electrode.

The E_{corr} of pure Ni is the lowest at –350 mV. With increasing P content the corrosion resistance increases as expected. A substantial increase in E_{corr} to –100 mV for $Ni_{0.78}P_{0.22}$ this is attributed to the crystalline-amorphous phase transition, which translates into a shift of *ca* –250 mV. Ni shows an initial active corrosion region followed by a transition to a passive region and then an increase until it reaches the kinetically controlled current density. This could be due to insulating passive regions of Ni which could exist from $Ni(OH)_2$, and NiO formation.

For the Ni-P films a much slower dissolution of Ni is observed, until the kinetic limit of current is reached as in pure Ni, that is the dissolution of Ni free from any

protective film passivation. The protecting nature of P as a passivating film has been attributed to a layer of adsorbed hypophosphite, which acts as a protective layer.[90, 91] The formation of an amorphous phase at high amounts of P is also ascribed to the corrosion resistance.[90] With only low amounts of P in the alloy there is no formation of an amorphous structure therefore the Ni is corroded more quickly as expected.[90] Another illustration to demonstrate the improved corrosion resistance is to measure an effective E_{corr} when the current reaches an arbitrary value. In Figure 2.4.9 the potential at which the corrosion current reaches 1 mAcm^{-2} is displayed.
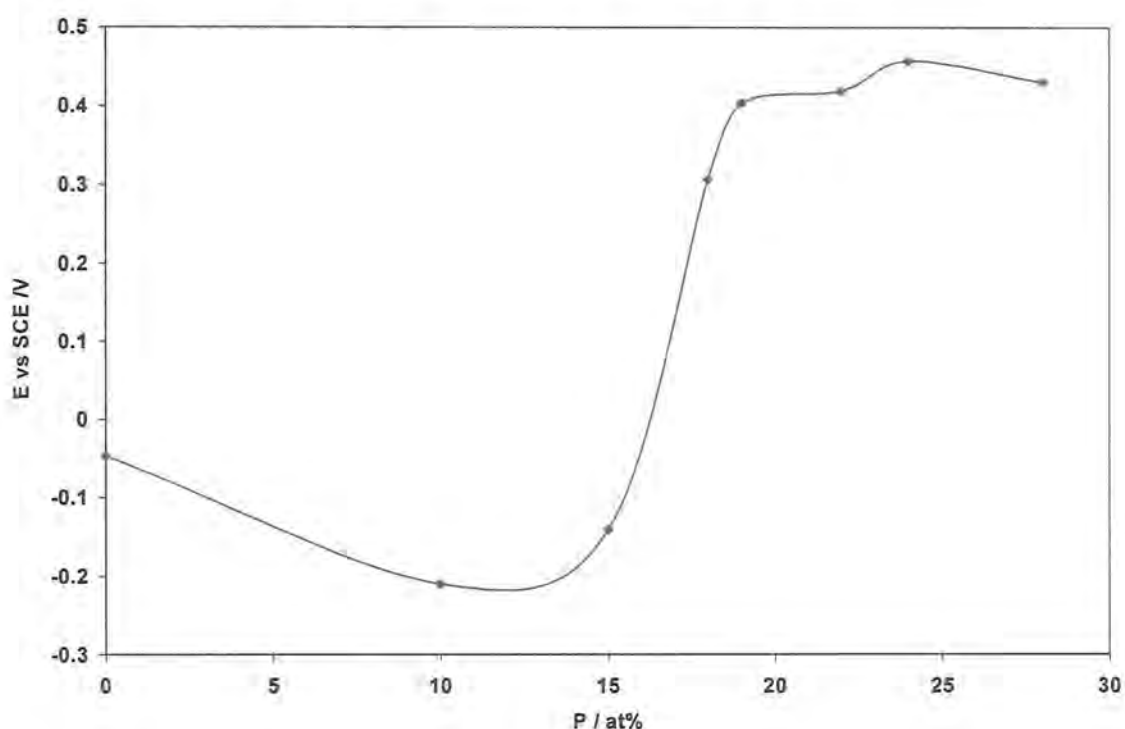
Figure 2.4.9: The potential E in V when the corrosion current reaches the value of 1 mAcm^{-2}, for various amounts of P in the alloy.

The crystalline-amorphous phase transition can be clearly identified in the region between 15-18 at % P, indicated by a significant increase in corrosion resistance.

This initial work on non-templated films has seen the identification of the nickel (II) acetate / phosphorous acid bath as one capable of producing smooth Ni-P alloy films with uniform P content. The deposition solution shows good compatibility with surfactants to produce homogeneous liquid crystalline phases. Good corrosion resistance has been identified at around 18 at. % P in HCl *via* the formation of an amorphous phase.

2.4.4   Nanostructured NiP

Initial conditions for depositing liquid crystal or mesoporous Ni-P films (MNiP) were 25 °C and using 55 % wt. Brij 56/0.2 M Ni(ac)$_2$, 0.5 M Na(ac), 0.2 M H3BO$_3$, 0.6 M H$_3$PO$_3$.   Polarising light microscopy indicated a well defined hexagonal region. Electrochemical cycling in KOH is used to determine the activity / structural quality of the nanostructure by determining the electrochemically accessible surface area (EASA) in terms of a coulombic charge. (This surface area is related to the amount of charge obtained from integrating the cathodic peak of Ni$^{2+/3+}$.)

Initially deposited mesoporous nickel-phosophrous (MNiP) films revealed only a slight enhancement in roughness factor indicative of a low surface area and a poor quality disordered nanostructure.   However, on inspection of the anodic stripping voltammetry revealed the deposition efficiency of the plating was low ~5 %; such a thin film is not expected to produce any significant enhancement in the roughness factor even if the nanostructure was well ordered and accounts for the low roughness enhancement.   A similar retardation is observed on plating efficiency when moving from aqueous to liquid crystal in the Ni only system (Table 2.4.1).

Deposition Efficiency	Non- templated (Aqueous)	Templated (Liquid Crystal)
Nickel only bath	85-90 %	45 %
Nickel, Phosphorous bath	55 %	5-10 %

Table 2.4.1: Deposition efficiency as calculated from the charge associated with the Ni → Ni^{2+} peak from anodic stripping voltammetry and the deposition charge.

There are also other factors which could account for the apparent lower activity of MNiP in alkaline solution. (i) The deposition efficiency does not account for the stripping/oxidation of P, consequently the charge obtained on stripping could be an over estimate for Ni. (ii) We would expect less activity for cycling Nickel because for example in Ni$_3$P (confirmed on EDX) means 25 % of the Ni is no longer available for

the same thickness of film. So it is still feasible to assume that MNiP is templated but in such small quantity that only a very thin film is produced.

Attempts were made to speed up the rate of reaction by increasing the temperature. With Brij56 the temperature was raised to first 30°C, then up to the maximum temperature possible; 38°C, where the hexagonal phase becomes unstable. This increased the efficiency to *ca.* 10 %, consequently the speed of plating was slightly increased. Higher temperatures were attempted using the Brij78 phase, with initial studies exhibiting a hexagonal phase stable to ~85 °C via optical microscopy. However prolonged heating necessary for high temperature plating decomposed the liquid crystal to form a bi-phasic unstable mix. In an optimised bath MNiP films (containing typically 20 at.% P) were deposited from a 55 wt. %Brij56 / 45 wt. % 0.2 M Ni(ac)$_2$, 0.5 M Na(ac), 0.2 M H$_3$BO$_3$, 0.5 M H$_3$PO$_3$, at 30 °C, –800 mV *vs.* SCE with a Pt gauze counter electrode. Due to the previously determined low efficiency of the reaction the deposition was left for 300 hrs. Figure 2.4.10 shows a typical cyclic voltammogram of both the MNiP and non templated NiP in KOH.
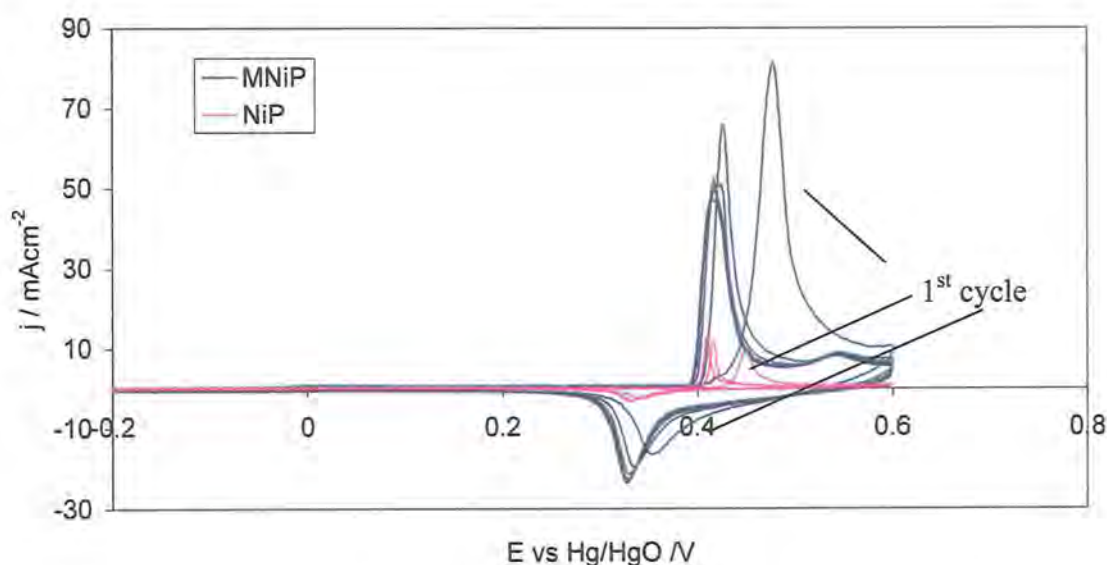
Figure 2.4.10: Cyclic Voltammetry of mesoporous NiP (MNiP) & non-templated NiP is shown in 6 M KOH at 20 mVs^{-1}, 25 °C. Deposition charge NiP 1.8 Ccm^{-2}, MNiP 2.73 Ccm^{-2}, (adjusted for efficiency i.e. 2.73 C cm^{-2} of Ni was found from stripping voltammetry). Current density refers to geometric surface area.

MNiP has much higher peak currents and capacity than the non-templated NiP. Previously MNiP had shown far less activity, only around 30 mC cm^{-2} of cathodic charge, compared with non-templated NiP at around 10 mCcm^{-2}. Non-templated NiP films show surprisingly high charge indicating the aqueous deposit itself has a rough surface with a degree of porosity. In Figure 2.4.10 MNiP shows capacity on the cathodic peak of around 100 mC cm^{-2}. Values of up to 100-150 mCcm^{-2} can be obtained repeatedly. This order of magnitude increase compared to flat NiP is attributed to increased area due to the porous nanostructure. The efficiency of deposition however, remains a problem, especially with such long timescales for plating. This is largely due to the formation of PH$_3$ gas as an intermediate, as well as hydrogen evolution.

2.4.5   Corrosion of Nanostructures

2.4.5.1   Corrosion in HCl

Figure 2.4.11: Tafel plots show Ni (blue), Ni82P18 (red) and Meso Ni-P (cyan) in 0.1 M HCl from –0.6 to +2.0V *vs.* SCE, at a rate of 1 mVs^{-1}, 25 °C. Log of current density refers to geometric surface area.

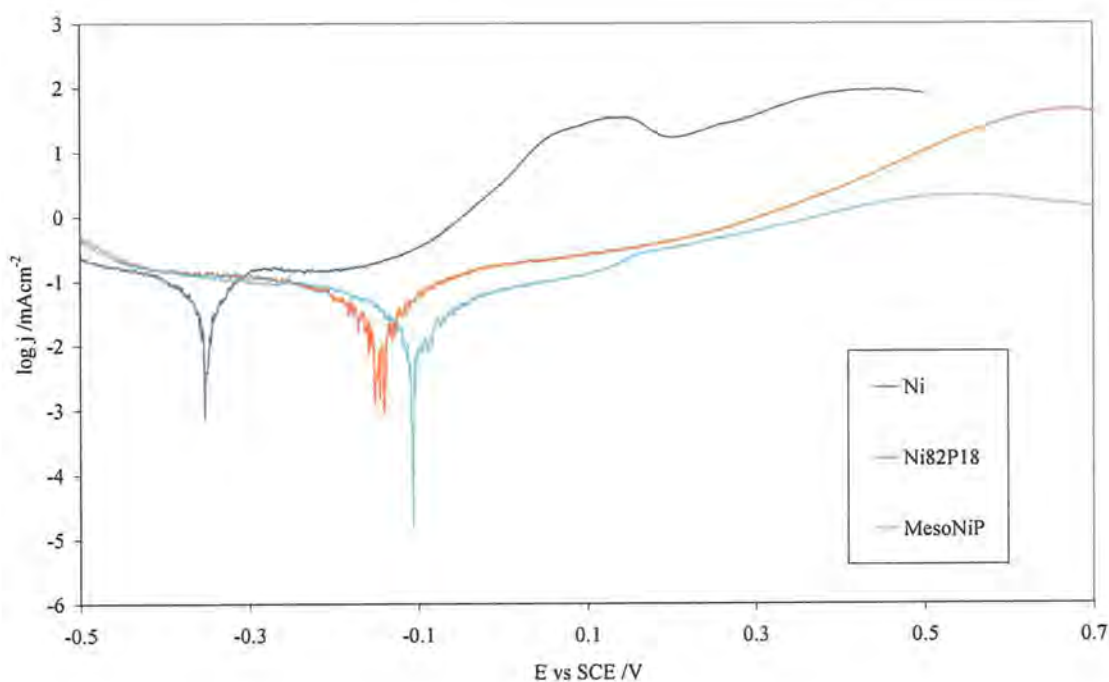Corrosion testing was extended to compare the MNiP with the corrosion behaviour of the non-templated deposits. (Figure 2.4.11) Interestingly the MNiP shows a small increase in the E_{corr}. This could be due to an increased amount of P in the deposit (as determined by EDX analysis), which indicates 25 at. % P in this sample typical for the MNiP. In planar Ni-P deposits tested the P at. % is typically 18 %. Corrosion currents were also unexpectedly low, for the MNiP again this can be ascribed to the increased passivation due to P.

2.4.5.2   Corrosion in a Lithium Battery Electrolyte

Aluminium was chosen to compare results for corrosion in a lithium battery electrolyte. Al foil is used in Li-ion technology by both manufacturers and researchers alike, as it naturally forms a passive layer to help prevent corrosion at high potentials. However, during long-term storage in the charged state, or on charge-discharge cycling, pitting corrosion has been observed in both Li and Li-ion batteries. Pitting corrosion, where the Al surface is locally corroded to form many pin like holes can greatly affect the calendar life and cycling performance of a battery. The pitting potential (E_p) can be easily defined by cyclic polarisation measurements, determined from the point at which the current starts to rise rapidly above the background current. Much work has been carried out to identify and solve the problem of Al corrosion in lithium batteries. Most previous studies focused on Al stability with respect to the electrolyte at high potentials that are reached during the charge of a lithium battery. Recent work by Zhang and Jow[92] found that although variations in the Li salt can improve the passivity of Al at high potentials, pitting corrosion occurs at ~ 3.2 V *vs.* Li, irrespective of the salt.[93, 94] Therefore Al is an excellent gauge for evaluation of the corrosion resistance of both the NiP and MNiP films.

Corrosion testing in 1 M LiPF$_6$ in PC electrolyte was conducted with the electrochemically plated MNiP, and MNi, contrasting with that of high purity Al using linear sweep voltammetry. As with the corrosion in acid systems the amount of P in the deposit yielded a significant effect in corrosion resistance in the Lithium electrolyte, with theoptimum again proving to be around 18 at. % P.
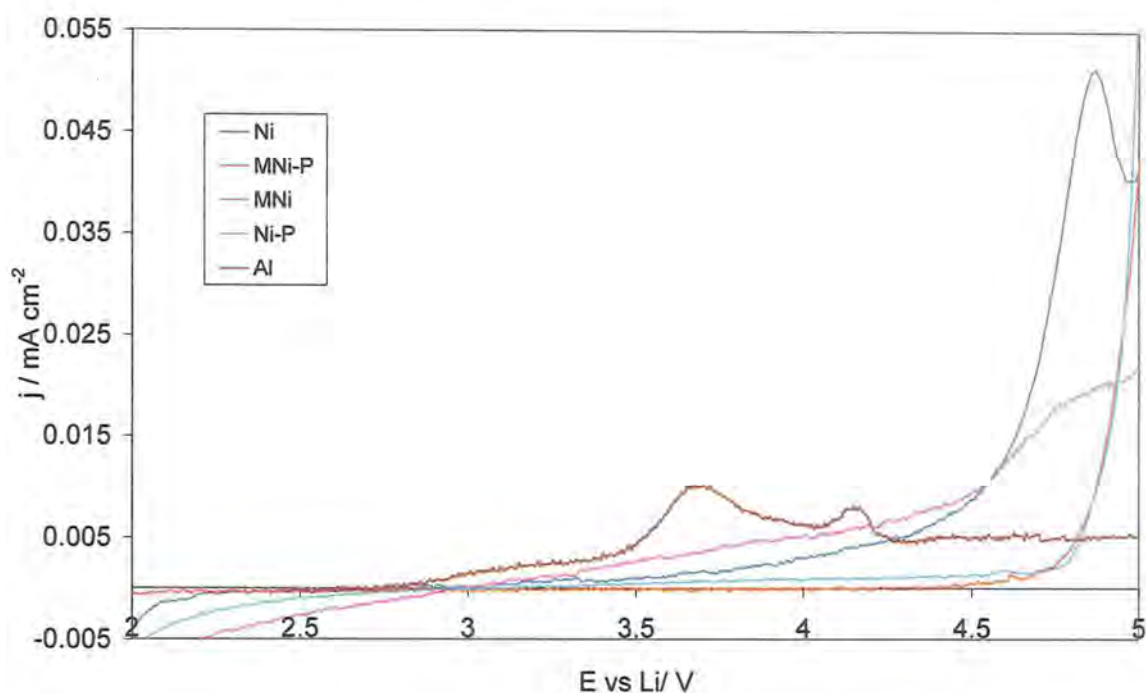
Figure 2.4.12: Plot displays linear sweep voltammetry comparing the corrosion behaviour of a variety of NiP alloys with that of Al in 1 M $LiPF_6$ in PC at 1 mVs^{-1}, 25 °C in anaerobic conditions. All Ni-P alloys deposited were from (55 wt. %. Brij 56) /0.2 M Ni(ac)$_2$, 0.5 M Na(ac), 0.2 M H_3BO_3, 0.6 M H_3PO_3. An M subscript in legend refers to Mesoporous all other films are non-templated.

The results from Figure 2.4.12 show the excellent corrosion resistance demonstrated by the Ni-P alloy film(s) when comparing to Al. The E_P of Al is slightly harder to define than for the Ni-P films however the corrosion current appears rise above the background current at ~3.2 V *vs.* Li consistent with literature values.[95] Both Ni and mesoporous Nickel (MNi) show a passive region with currents reaching around 10 $\mu A\ cm^{-2}$ at ~4.5 V. Ni corrosion current begins to rise rapidly to ~50 $\mu A\ cm^{-2}$ where another passive region is encountered. The Ni-P film and MNi-P, both show excellent corrosion resistance with the currents not more than 1 $\mu A\ cm^{-2}$ until the E_P is reached at ~ 4.75 V *vs.* Li, where the current then rises exponentially. This result is promising; however, the surprise is that the MNiP also yields low current, when compared to Ni-P. MNi-P also contains 7 at. % more P in the deposit, which might help to increase passivation.

57
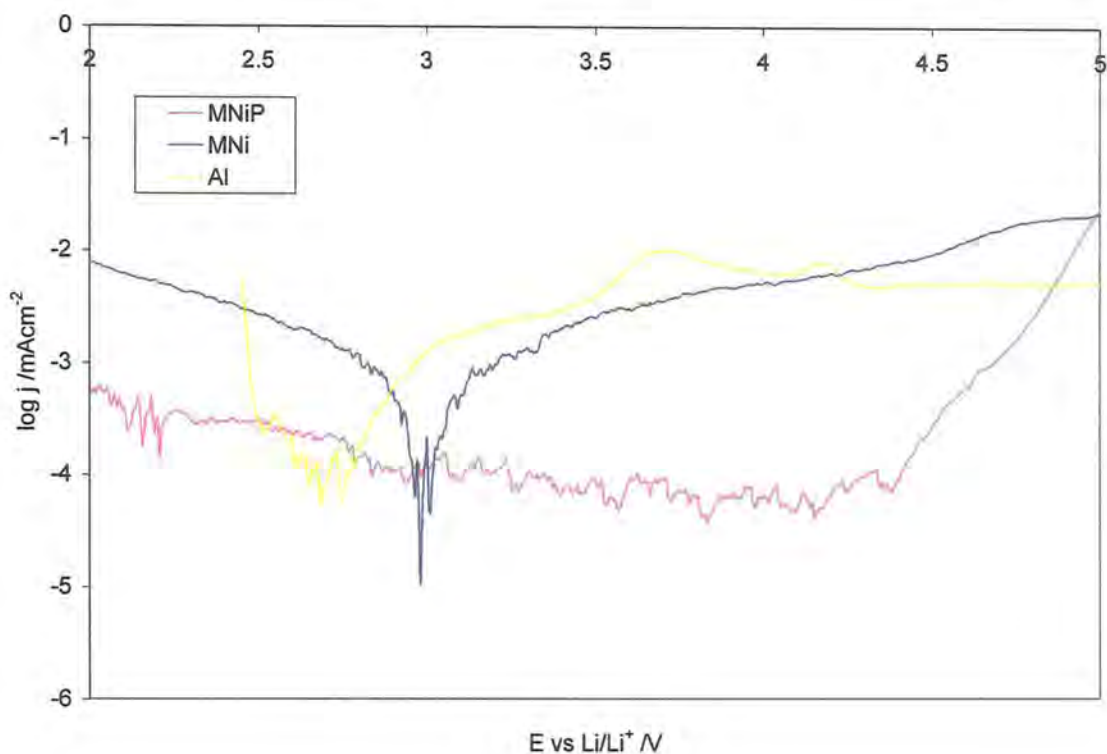
Figure 2.4.13: A Tafel plot of the corrosion of MNi, MNiP and polished Al, at 1 mVs^{-1}, 25 °C, in 1 M LiPF$_6$ in PC. Both nickel samples deposited with equal charge ~1.2 Ccm^{-2}.

Corrosion of the aluminium is consistent with literature values[*96, 97*], with the pitting potential just above 3.2 V (more clearly deciphered from Figure 2.4.12). The currents are slightly lower than observed by Zhang and co-workers, however, this may be due to a slower scan rate. Al shows very good passivity especially at potentials above 4.2 V. The MNi shows similar currents to Al, but MNiP exhibits extremely low corrosion activity <1 μA (Figure 2.4.13) until the rapid onset of corrosion at 4.5 V. This potential however is at the upper limit used within lithium batteries.

2.4.6   Lithium ion exchange and redox chemistry

2.4.6.1   Direct Ion exchange

The MNiP was oxidised to NiOOH by potential step to 0.6 V *vs.* Hg/HgO in 6 M KOH for 100 s, samples were then washed in water then dried at 50°C under vacuum for 24h. In all expressions given P is omitted for simplicity. Cells were assembled and the ion exchange carried out by immersion in the 1 M Li salt at room temperature according to the following reaction:

$$NiOOH + Li^+ \Leftrightarrow LiNiO_2 + H^+ \qquad\qquad Eq. \ 2.4.5$$

The large concentration of Li^+ ions is expected to shift the equilibrium to the right in the absence of H^+. The ion exchange product was then cycled between 2.0 and 4.5V at 50 mVs^{-1} (fast rate is used due to the mesoporous electrode). However no reversible capacity was observed in either LiPF$_6$, or LiN(SO$_3$CF$_3$)$_2$ (LiTFSI) at high voltage (Figure 2.4.14). This would indicate that the ion exchange above is not occurring to any significant degree. The phase of NiOOH may not be conducive to ion exchange, loss of black colour in the oxidised electrode characteristic of the NiOOH sturcture may indicate a loss of the NiOOH state, preventing any ion exchange from occurring.
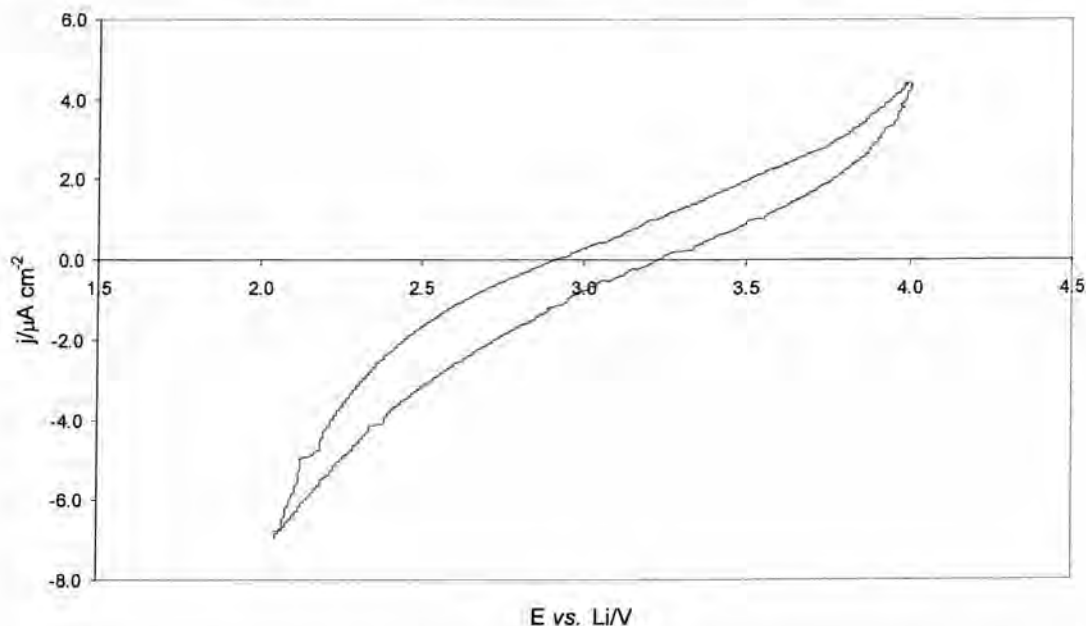
Figure 2.4.14: MNiP cycled as a positive electrode between 2.0 V and 4.5 V *vs.* Li at 50 mV s^{-1} in LiPF$_6$ / PC.

2.4.6.2   Mesoporous NiP as a Negative Electrode

Cycling the nanostructured Ni as a negative electrode at lower voltage has been initially studied by Nelson. Currents achieved were not consistent with the high activity of a meso-electrode. This was attributed to corrosion via formation of HF in equilibrium with the PF_6^- ion when using $LiPF_6$ as the ion source. It was attributed to the break down of the Ni-O bonds and the structure loss. MNiP with its corrosion resistant properties should go some way to reducing this problem. In Figure 2.4.15 the current is five times higher than observed with MNi, more consistent with the performance expected of a mesoporous electrode. This indicates that the P in the deposit is acting to reduce the corrosion. There is however still a significant capacity loss on cycling.
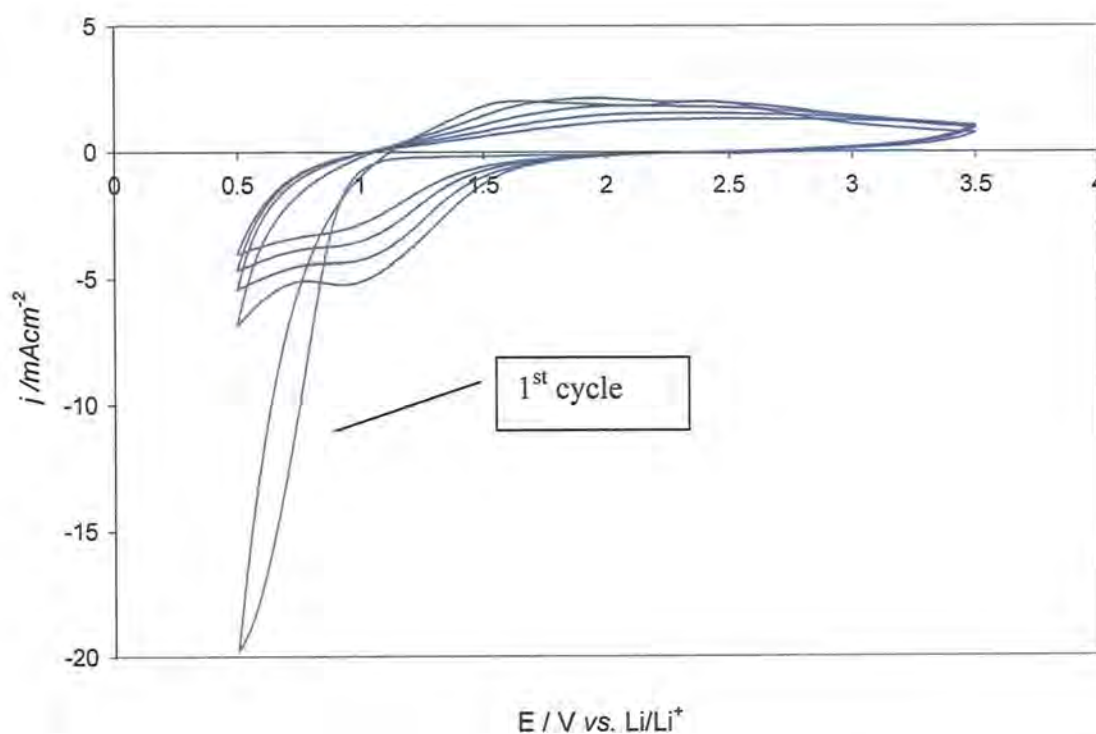
Figure 2.4.15: Cyclic Voltammetry of oxidised MNiP film transferred to 1 M $LiPF_6$ in PC for ion exchange cycled at 50 mVs^{-1}, 25 °C.

Figure 2.4.15 shows two broad peaks on oxidation at around 2 and 2.5 V *vs.* Li with corresponding reduction waves at 1 and 0.5 V *vs.* .Li. The former is not observed when MNi is cycled, and is always observed with MNiP On the first cycle there is a large

current on the first discharge (negative sweep) with different behaviour and shape to subsequent cycles. Such a nucleation loop on the first cycle would indicate support for the mechanism proposed by Poiziot and co-workers.[98] It is postulated that the formation and decomposition of Li_2O accompany the reduction and oxidation of the metal, according to reaction below. (*Eq. 2.4.6*)

$$Ni(OH)_2 + 2Li \Leftrightarrow Li_2O + Ni + H_2O \qquad\qquad Eq.\ 2.4.6$$
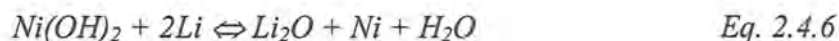
Once transferred to non-aqueous solution H_2O would be in only a few ppm so that NiO would be cycled instead of $Ni(OH)_2$. MNiP was also cycled in LiTFSI in PC, the voltammetry can be seen in Figure 2.4.16. In this case the same redox chemistry is observed as for $LiPF_6$. However, this time there was no capacity loss on cycling and even an increase in capacity in oxidation was observed. Currents were high as expected for a meso electrode, but still not in the same magnitude as for the alkaline chemistry. Again current density was higher on cycling MNiP than with MNi.
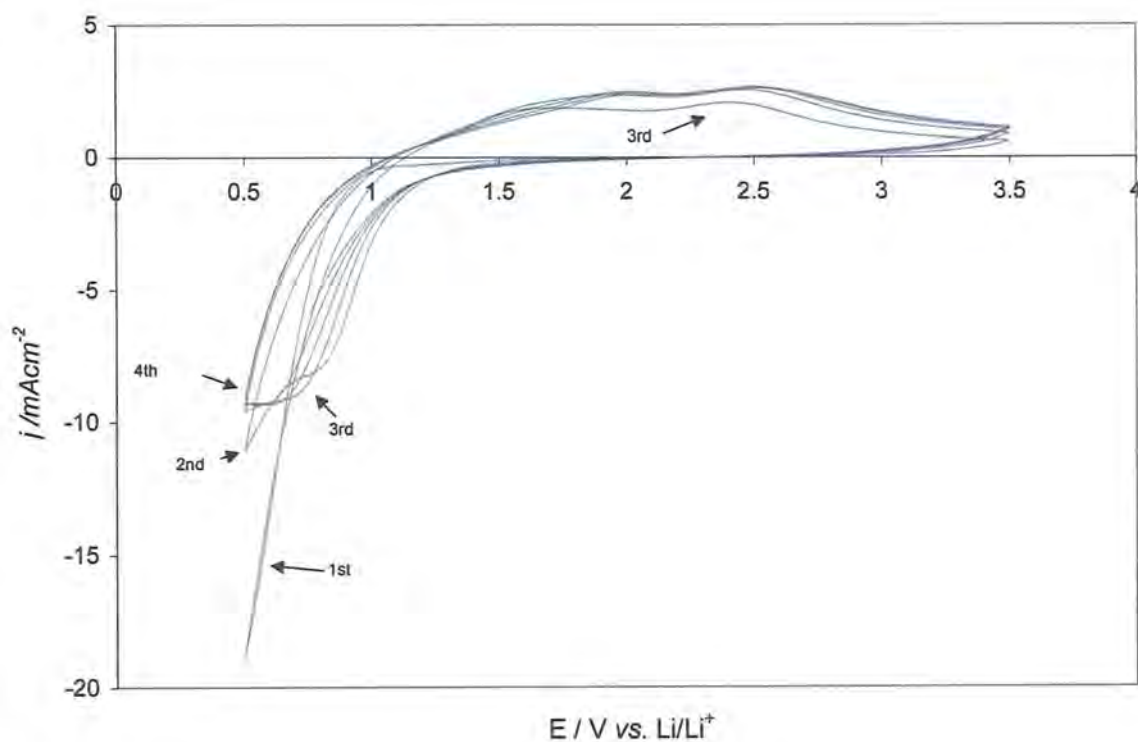
Figure 2.4.16: Cyclic Voltammetry of ion exchanged MNiP in LiTFSI at 50 mVs^{-1}, 25 °C.

Interestingly, the current densities are significantly higher than observed for Figure 2.4.14, a one electron process, whereas Figure 2.4.16 and Figure 2.4.17 describe a two electron Li^+ ion storage mechanism (Poiziot), however this can not explain the huge discrepancy in current. The difference in capacities can be derived from the effectiveness of the ion exchange process. The functioning of the mesoporous electrode as a negative electrode material (*Eq. 2.4.6*) only requires the presence of $Ni(OH)_2$, whereas capacity as a positive electrode material relies on a successful ion exchange reaction. This is clear evidence for the ineffectiveness of the direct ion exchange method but also indicates the potential for increased capacity as a positive electrode material with the use of an efficient ion exchange method.

2.4.6.3   Improving the Ion-Exchange Reaction

After the failed attempts to ion exchange for Li, it was decided to attempt ion exchange MNiP without vacuum drying, so called 'instantaneous ion exchange'. This may prevent the decomposition of the NiOOH phase (which may occur on drying over 24 hours). After cycling in 6 M KOH for four cycles over the range -1.2 V to 0.6 V *vs.* Hg/HgO the electrode was removed from the solution under potential control in the oxidised state NiOOH, 0.6 V. After rinsing with de-ionised water, and the removal of excess water using absorbent paper towel, the MNiP electrode was transferred immediately to a pre-assembled cell containing LiTFSI / PC with a Lithium counter and reference electrode. The cell was kept moisture free under a stream of Argon gas. Figure 2.4.17 shows the electrochemistry of the $Ni^{2+/3+}$ couple for MNiP immediately before transfer to the LiTFSI / PC. (It shows a cathodic charge of ~105 mC cm^{-2}.) The first cycle on subsequent transfer into the lithium electrolyte can be seen in Figure 2.4.18. On the first full discharge recorded a reduction current (tentatively attributed to insertion of Li) occurs with of 40 mC cm^{-2}, 40 % of the activity observed with intercalation of H^+.

Figure 2.4.17: Cyclic voltammetry of MNiP in 6 M KOH scan rate 20 mVs^{-1}, 25 °C pre-cycling in LiTFSI. MNiP deposited with ~6.5 C cm^{-2}.
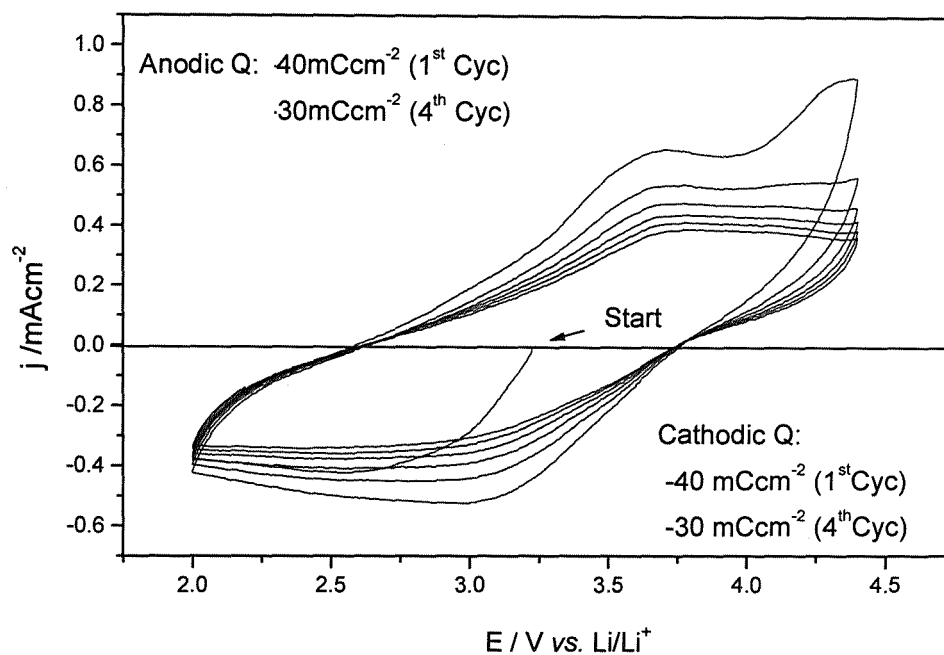
Figure 2.4.18: cyclic voltammetry at 20 mVs^{-1} for ion exchanged MNiP in 1 M LiTFSI / PC, after immediate transfer from KOH., 25 °C. MNiP deposited with ~6.5 C cm^{-2}.
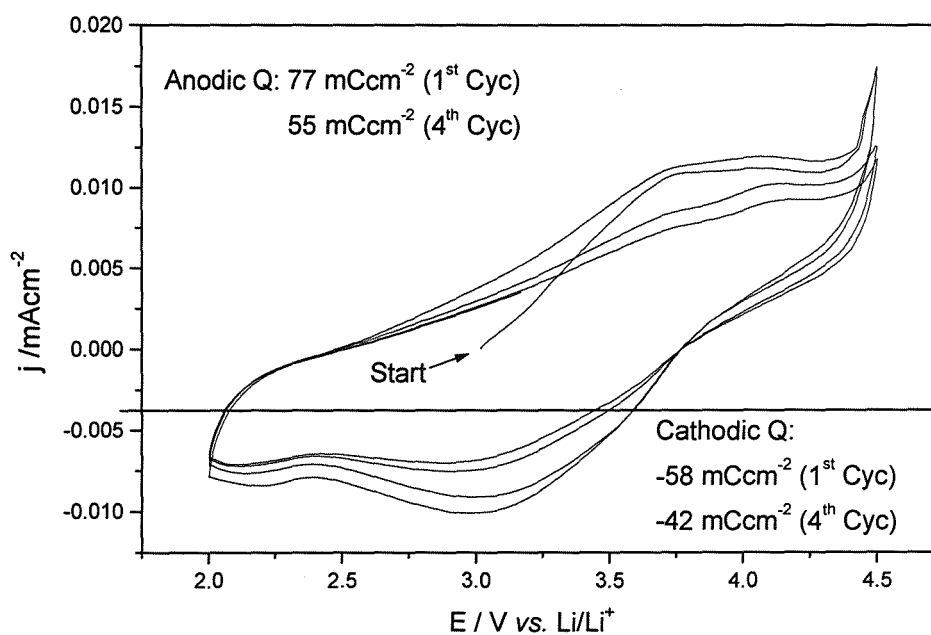
Figure 2.4.19: Cyclic voltammetry at 0.25 mV s^{-1} for ion exchanged MNiP in 1 M LiTFSI / PC, after immediate transfer from KOH. Scan rate 0.25 mVs^{-1}, 25 °C. MNiP deposited with ~6.5 Ccm^{-2}.
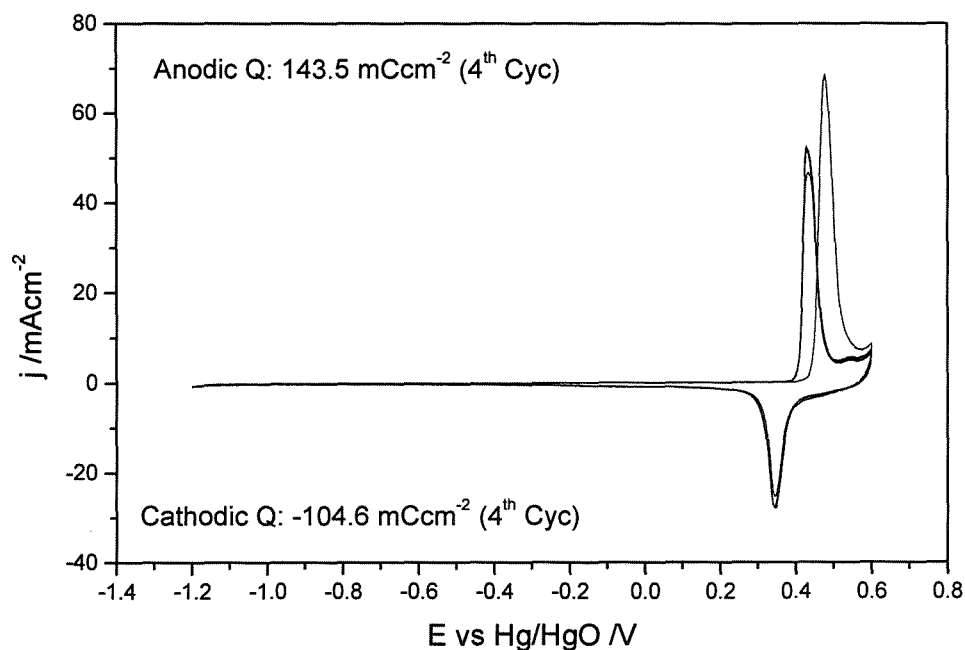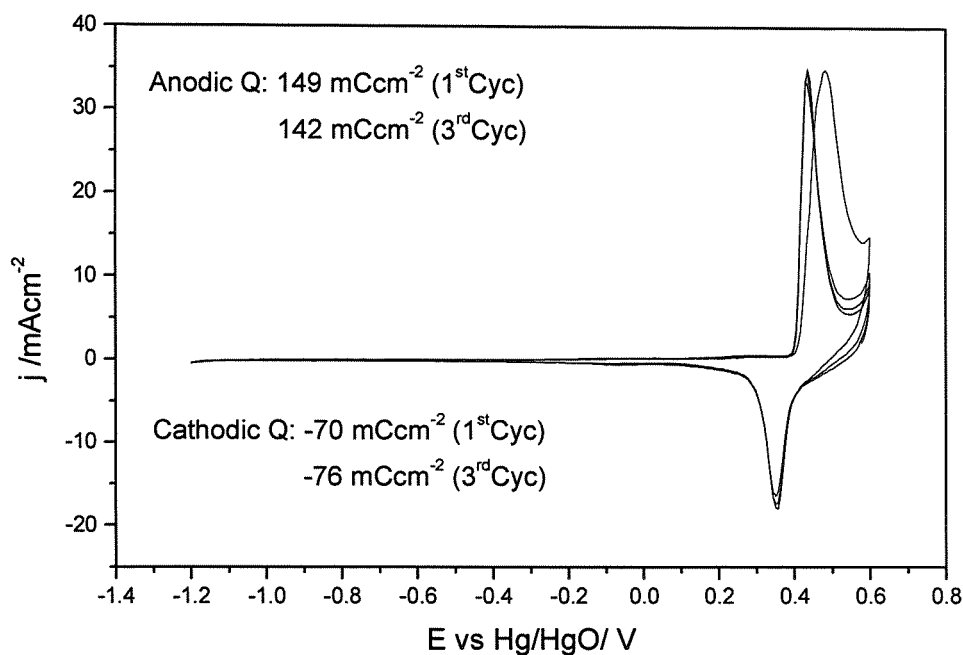
Figure 2.4.20: Cyclic voltammetry of MNiP in 6 M KOH scan rate 20 mVs^{-1}, 25 °C post-cycling in LiTFSI. (MNiP deposited with ~6.5 C cm^{-2}).

Figure 2.4.18 shows two partially superimposed anodic peaks appear at 3.7 V and 4.5 V *vs.* Li, the latter disappears on cycling. Voltammetry at 0.25 mV s^{-1} in Figure 2.4.19 failed to resolve any peaks however both voltammograms display cathodic activity (insertion) below 3.75 V *vs.* Li they are related in both magnitude and position to the anodic peaks (extraction), and can be tentatively assigned to the reversible storage of Li$^+$ ions within the structure.

The instantaneous ion exchange method has demonstrated higher activity for the storage and release process of Li ions. However this process was at a lower than expected voltage than reported for LiNiO$_2$, which is 3.5 V *vs.* Li for the cathodic peak or discharge, (insertion of Li$^+$ ions). This redox activity therefore could not confidently be assigned to this process. It has also been seen that this process diminished with every cycle, this was not due to a break down in the film structure as subsequent transfer back into KOH in Figure 2.4.20 demonstrated the electrode retained good activity. It seems likely that this process may have been due to the cycling of protons which is possible as residual KOH may be left in pores as the films had not been dried under vacuum before transfer to the non-aqueous electrolyte. To resolve whether KOH in the pores was being cycled a repeat experiment was carried out. After cycling to

prepare the oxidised NiOOH state in KOH, the three samples were briefly rinsed in water and the excess solution on the surface of the electrode soaked up into tissue paper. The electrode then transferred into the lithium electrolyte 1 M LiTFSI/PC, where ion exchange for Li ions could take place. The result is compared in Figure 2.4.21.
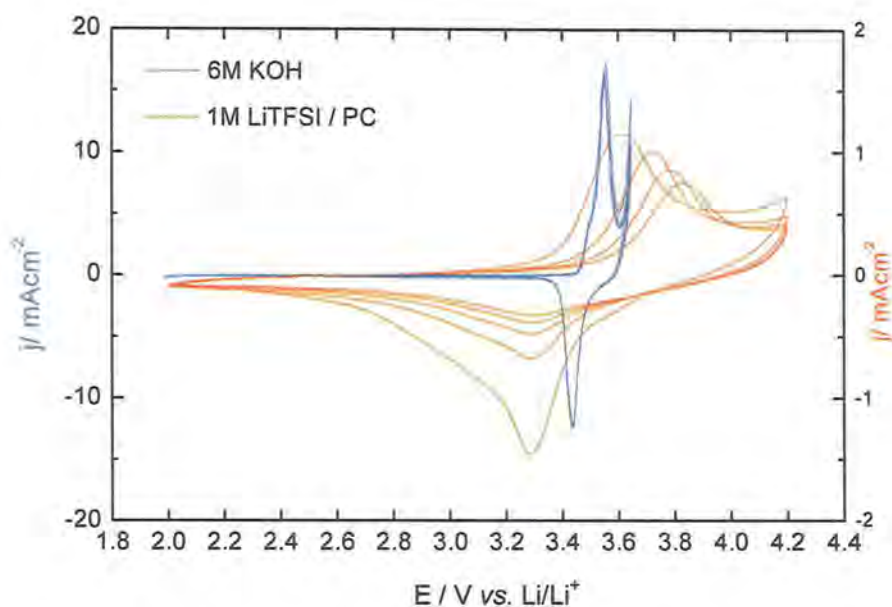
Figure 2.4.21: Overlay of H_l e -NiP in both KOH and 1 M LiTFSI in PC, scan rate is 20 mVs^{-1}, 25 °C in both cases.

Although in LiTFSI the potential has shifted more positive and the current is a lot lower (red) it seems highly likely that the redox activity is due to protons being removed from the structure and not the cycling of any ion-exchange reaction product. The current declines as once protons have been removed they can diffuse away from the electrode into the bulk where their concentration is a few ppm. The anodic peak shift to the right shows it is harder and harder to remove any protons from the structure as the diffusion distance for extracting protons increases, whilst continued cycling sees electrode activity decay to a few microamps. An ion exchange reaction has not occurred on instantaneous transfer to Li electrolyte. A third and final method, ion exchange in LiOH solution was subsequently attempted.

2.4.6.4   Ion exchange in LiOH

Results for the ion exchange reaction in 1.5 M $LiOH_{(aq)}$ at 50 °C for both cycled and non-cycled sample showed similar behaviour. Initially there was the removal of the KOH from the pores, at a low potential at ~3.3 V *vs.* Li. (Figure 2.4.21) However this behaviour appeared to mask a higher voltage process, with anodic and cathodic peaks at 4.2 V and 3.5 V *vs.* Li respectively, shown in Figure 2.4.22.
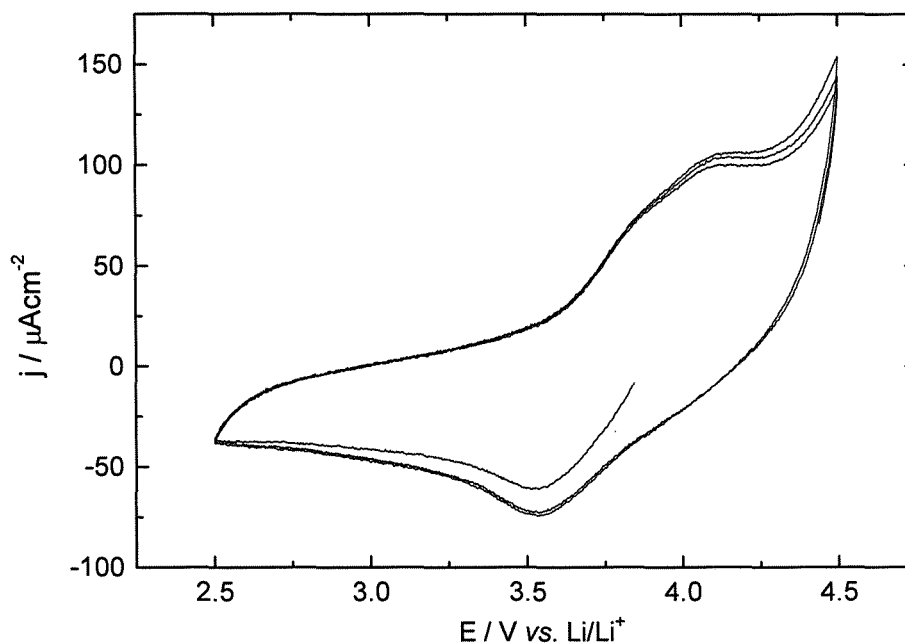
Figure 2.4.22: Cyclic Voltammetry, in 1 M LiTFSI/PC. 10 mVs^{-1} of the ion exchange product in 1.5M $LiOH_{(aq)}$ at 50°C for 24hrs.

As can be seen from Figure 2.4.22 there is a definite reversible storage process, which shows good cyclability over 3 cycles. Although the currents are only in the μA region, the significance of the result is that the voltage is equivalent to that of cycling $LiNiO_2$. The currents are also significantly higher than those reported in previous work by Nelson.

To quantify the extent of the ion exchange reaction the conversion of the active NiOOH layer to $LiNiO_2$ was calculated. The amount of active material is assumed from the last cathodic cycle of the electrode in LiOH, (115 $mCcm^{-2)}$. This relates to 13.5 mg cm^{-2} of active material, (small as it is only surface layers of the electrode). From the cathodic charge in LiTFSI, (insertion of Li ions) we can assign a degree to which the ion exchange has taken place. At slower scan rates as much as 25 $mCcm^{-2}$, has been

extracted. At the same scan rate as in KOH, (20 mVs^{-1}) around 15 mCcm^{-2} has been extracted. The slower rate of 25 mCcm^{-2} equates to ~65 mAhg^{-1} of LiNiO$_2$ being cycled. The theoretical capacity of LiNiO$_2$ is around 270 mAh g^{-1}; therefore the ion exchange is only 22% complete.
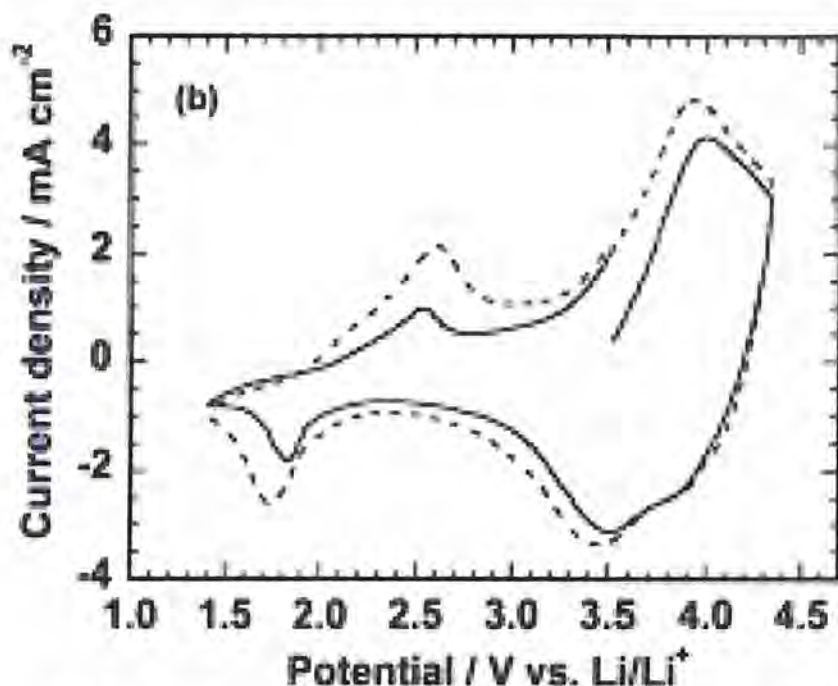
Figure 2.4.23: Cyclic voltammetry of solid-state preparation of LiNiO$_2$ at 10mVmin^{-1} in LiClO$_4$/PC (taken from[82]).

The voltage peaks can be contrasted to those in the literature an example of a solid state high temperature preparation of bulk LiNiO$_2$ in Figure 2.4.23, by Maruta *et al.*[82] Although the currents are a lot higher, the amount of active material is a lot greater and the scan rate is also different. The capacity in mAh g^{-1} obtained by Maruta is approximately 150 mAh g^{-1}, when cycling to 4.2 V, where only half of the Li is removed. In this work, the ion exchange has not been highly successful, nor is the reversibility good at high scan rates. This would imply that the diffusion of Li ions through the structure is still slow. This may be due to the problem with the disordered structure of the gamma phase of NiOOH, limiting the extent to which ion exchange can occur.

2.5 Conclusions

Deposition of the first nanostructured Ni-P alloy films have been demonstrated; however the plating of the films was extremely slow as a result of the poor deposition efficiency ~10 %. Ni-P alloy films have shown an increase in the corrosion resistance *vs.* MNi in lithium battery electrolytes. The protecting nature of P as a passivating film has been attributed to a layer of adsorbed hypophosphite. The formation of an amorphous phase at high amounts of P coincides with the shift of the E_{corr} for pure Ni – 350 mV to –100 mV *vs.* SCE for $Ni_{0.78}P_{0.22}$ in HCl. In organic electrolytes the pitting potential (E_P) was shifted from ~3.2 V to 4.75 V *vs.* Li in the optimised Ni-P alloy. The Nanostructured deposits generally do not show significantly higher currents than the non-templated equivalents in either HCl, or the $LiPF_6$; this is unexpected but could be due to increased passivation through extra P incorporated via the templating method. Further work should involve improved analysis of the corrosion in lithium electrolytes, to use more agitating salts and different solvents to determine the versatility of the corrosion resistance of the Ni-P alloy. An optimised plating bath should be investigated to try and improve the efficiency of plating.

The objective of the improved corrosion resistance was to preserve the Ni-O bond in the nanostructured material. This was to enable ion exchange of Li^+ for H^+ in the NiOOH structure and cycle $LiNiO_2$. The ion-exchanged MNiP did yield significantly higher electrochemical activity than those reported for MNi in previous work by Nelson, however despite this, the ion exchange reaction was not significant. Quantitatively, insertion of Li ions from cyclic voltammetry at 5 mV s^{-1} yielded 25 $mCcm^{-2}$ from 13.5 mg cm^{-2} ; which equates to ~65 mAh g^{-1} of $LiNiO_2$ being cycled. The theoretical capacity of $LiNiO_2$ is around 270 mAh g^{-1}; therefore the ion exchange is only 22 % complete. This implies that the diffusion of Li ions through the MNiP structure is still slow. This may be due to the problem with the disordered structure of the gamma phase of NiOOH, limiting the extent to which ion-exchange can occur.

Neither the MNi or the MNiP electrodes have achieved fast chemistry in Lithium systems, therefore an aqueous negative electrode to partner the mesoporous Ni electrode with similarly fast kinetics is the next challenge Chapter 4 investigates one possible candidate; Nanostructured TiO_2 where the possibility of electrochemical reduction by lithium ion insertion from aqueous LiOH is studied. The uniform nanostructure is expected to facilitate the reaction kinetics previously demonstrated for nanostructured NiOOH.

Chapter 3

Preparation of Nanostructured TiO₂

3.1 Background and Objectives

The purpose of this short chapter is to detail the preparation and characterisation of the nanostructured TiO_2 used for electrochemical studies in chapters four and five. Both thin films prepared from dip coating as well as particles of monolithic structures in powder form are prepared.

3.1.1 Evaporation Induced Self- Assembly method

The sol- gel method (1.2.1.1) has been extended to make nanomaterials by introducing surfactants into the reaction mixture. Nanostructured Silica has been successfully produced with a rich variety of structures using the so-called Direct Liquid Crystal Template Method.[38] Surfactant, water and reactants can be dissolved in common solvent such as ethanol, this mixture allows easy application to various substrates by dip/spin coating for thin films, or by simply pouring the sol in a Petri dish (to prepare powders). The solvent begins to evaporate preferentially and concentrate the initial diluted solution of surfactant, water and metal alkoxide.

1. **Fast decrease in film thickness, evaporation of solvent rich vapours.**

2. **Slower evaporation solvent / H_2O / HCl.**

3. **Random orientated mesostructure (micelles; defined size, average inter-distance).**

4. **Organisation and alignment.**

5. **Residual H_2O / HCl lost, further condensation, contraction.**
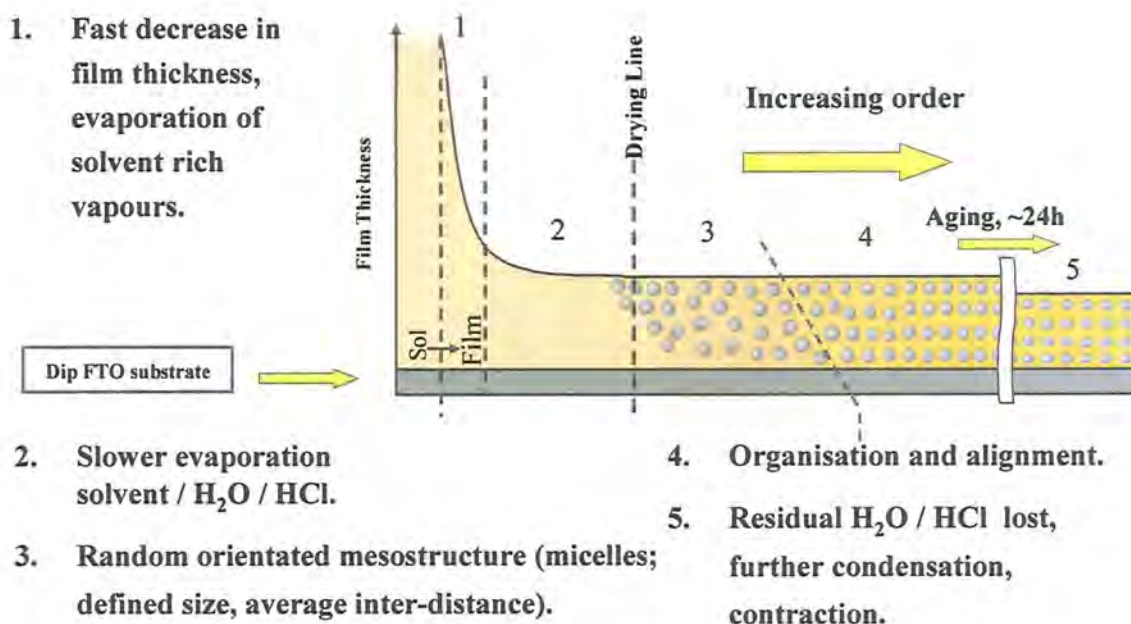
Scheme 3.1.1 The steps involved in the Evaporation Induced Self- Assembly method (EISA).

If the involved variables are finely tuned, it is possible to synchronise formation of micelles and their organisation into liquid crystal phases with the condensation of the inorganic framework. Once the framework has formed, (steps 1-5 in Scheme 3.1.1) it is possible to remove the surfactant by heating in air (calcination). This method has been used successfully to template nanostructured silica in a wide variety of phase templates with a high degree of structural order.[*43, 99, 100*] Amongst others, Titania has been produced by a number of other research groups however; such films/powders (Titania in particular) have not been produced consistently with the same degree of structural order as with silica.[*38, 49, 101-103*] This is often attributed to the hydrolysis – condensation reactions undertaken by the metal alkoxide precursor e.g. titanium ethoxide in this work:
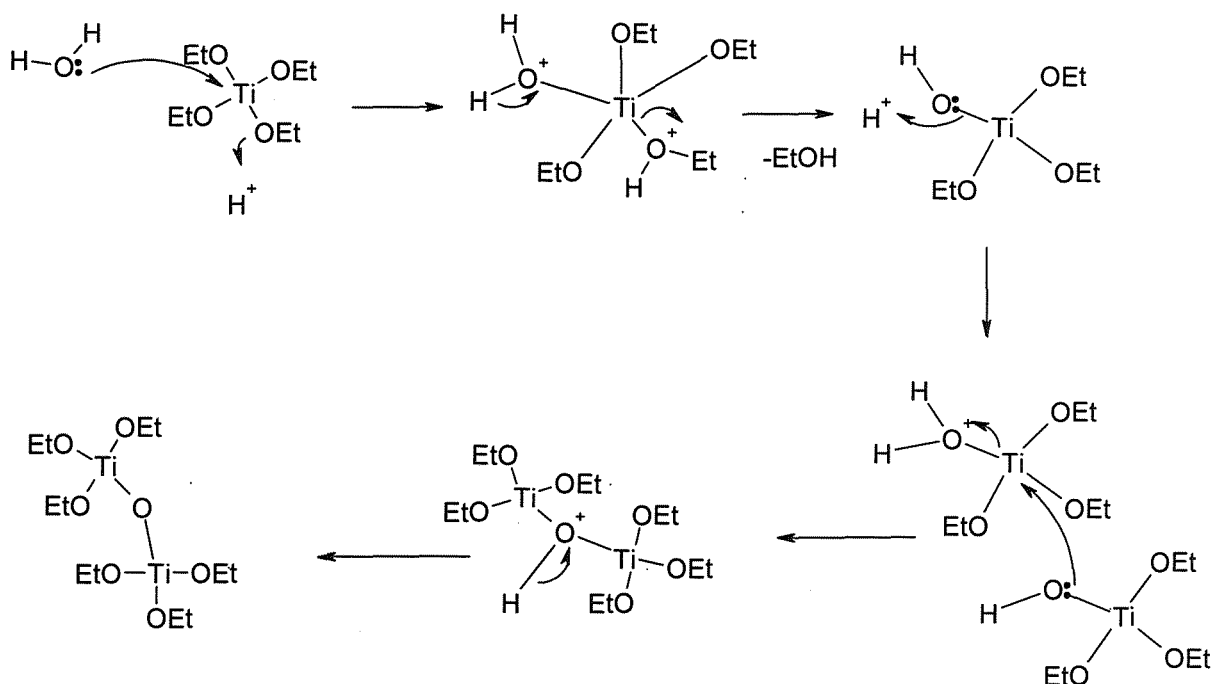
Scheme 3.1.2 Steps involved in hydrolysis and condensation of titanium ethoxide precursor.

This reaction should only take place in the aqueous phase surrounding the surfactant. The first reaction rate is controlled therefore, by using a concentrated acid e.g., HCl to prevent condensation occurring before the template has had time to form. Subsequent condensation then proceeds, which then continue from the $Ti_2O(OEt)_6$ dimer (bottom left) throughout the solution to form an extended network around the template.

3.1.2   Experimental

The hexagonal (H_I) and cubic (I_I) templates were selected by surfactant water ratios obtained from the phase diagrams of Brij78 and Pluronics F127 in this work. Both have large domain sizes which make them suitable for structural templating, and indeed work on mesoporous silica[100] has shown phase boundaries are not significantly affected by the introduction of the other reactants into the aqueous phase.
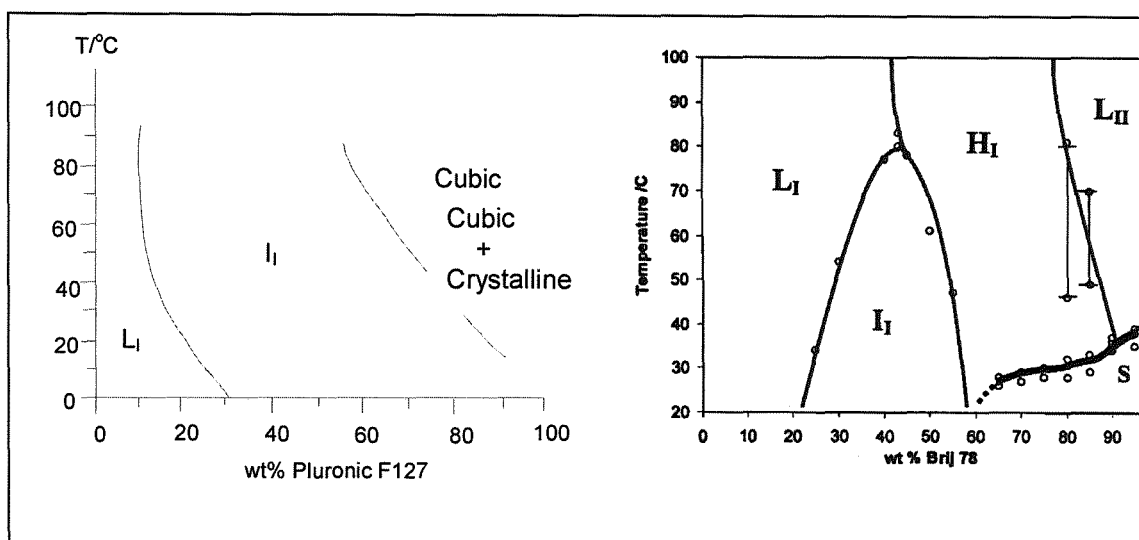
Figure 3.1: Phase diagram for Pluronic F127 + distilled water.[32] Phase diagram for Brij 78 + distilled water.[100]

A solution was prepared as follows; F127 Pluronic Surfactant (2.0 g, Sigma) was dissolved in MeOH (15.0 g, HPLC grade, Aldrich) with gentle heating. HCl (18 M, 2.2 g, Fischer) was added dropwise followed by Ti(OEt)$_4$ (3.2 g, Aldrich) then the solution was agitated until the solids were dissolved completely and then stirred overnight to form a clear solution.

3.1.2.1   Dip coating

Glass slides with a thin layer of fluorine doped tin oxide (FTO) (Asahi glass, textured F:SnO$_2$, 2.5 x 3.5 x 0.1 cm) are dipped into the coating solution and then removed at a constant rate (300 mm min^{-1} or 0.5 cm s^{-1}) using a Nima dip coater. Prior to dip coating, the glass slides were cleaned using a detergent solution (Decon90), rinsed with water, followed by acetone, and then dried at 45°C.

•Slow hydrolysis controlled by [H $^+$] sol-gel oxide formation, ageing and condensation inside template.

$$Ti(OEt)_4 + H_2O \rightarrow Ti(OH)_4 \rightarrow TiO_2$$
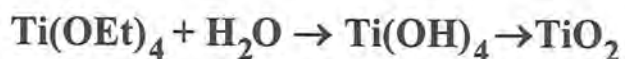
•Final calcination to Anatase at ~ 400 ºC, N_2, 2 hrs O_2

•Control film thickness by dip rate and no. of dips.

1 dip ~ 0.5 µm,

4 dip ~ 1.3 µm.

Dip on ITO Substrate

Ti (OEt)$_4$
solvent
surfactant
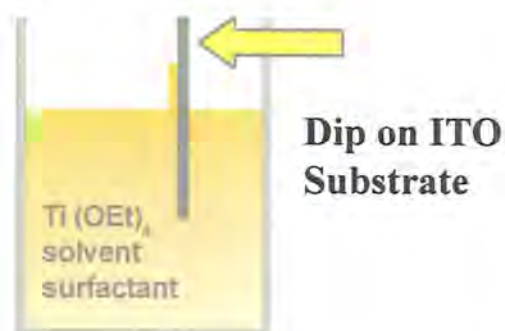
Scheme 3.1.3: Schematic of dip coating procedure.

Single-dip and 4-dip samples were then treated slightly differently. Single-dip samples were aged (to remove excess solvent, allowing the lyotropic phase to form) at 45 °C for 24 h, heated to 400 °C under N_2 and then calcined under O_2 for 2 h to remove the surfactant. 4-dip samples were prepared by repeatedly dipping the glass into the solution with 30 s between dips. These samples were then aged at 45 °C for 24 h, heated to 190 °C in air and left for 2 h. Following this, in order to prevent the films from powdering upon calcinations, the samples were dipped into a solution containing methanol (15 g), conc. hydrochloric acid (0.3 g) and titanium (IV) ethoxide (0.3 g), re-aged at 45 °C for 24 h and finally heated to 360 °C in air and left for 2 h. As a control, non-templated films were prepared in the same way as the single-dip samples with the surfactant excluded from the dipping solution.

3.1.2.2 Powders

For powders an identical precursor solution was prepared as for films, however instead of dip-coating it was decanted into three separate Petri dishes and with a wet film thickness of ~ 1 mm and then aged at 40 °C for 2-3 days as the films were much thicker than for dip-coating. The resultant translucent gel was scraped off and transferred to an alumina boat for calcinations as for the films however, oxygen time of 2-3 hours was longer due to the increased amount of material. This resultant powder consisted of agglomerates up to a few millimetres in size, which were then subsequently ground down to a fine powder using a pestle and mortar.

3.1.2.3 Structural Characterisation

Structural characterization of the films and powders was carried out in order to confirm the templating effect of the liquid crystal on the deposit morphology. Transmission electron microscopy (TEM) was performed on a JEOL 2000FX TEM working at 200 kV. Samples were prepared by scraping particles from a film into ethanol. Particles were then removed from the ethanol by pipette and dispersed on Cu TEM grids with evaporation of the ethanol.

Scanning electron microscopy (SEM), images were obtained at an accelerating voltage of 15 kV (Philips XL30ESEM). Small amounts of the powder were placed on carbon film and sputtered with gold for viewing with the scanning electron microscope (SEM). This technique was used to get an idea of the agglomerate/particle size distribution of the milled powders. Anatase nanopowder obtained from Aldrich was used as received, samples were prepared in a same way as our material. Lower resolution SEM. micrographs were recorded using a Philips XL-30 scanning electron microscope to study particle size distribution for powders, as well as and film thickness.

High-resolution tapping mode AFM image of 0.5 μm I_l F127 templated TiO_2 templated titanium dioxide film surface acquired with a single-walled carbon nanotube AFM tip (lateral resolution 5 nm)

Both small angle x-ray scattering (SAXS) and wide angle x-ray scattering (WAXS) were carried out using a Siemens D-5000 diffractometer (Cu-K$_\alpha$ radiation) with a scan rate of 5° min^{-1}. X-ray diffraction was used to confirm crystal structure and particle size (line broadening) for powders in this work as well as the Aldrich material.

Brunauer-Emmett-Teller (BET) was used to obtain surface area and pore size distribution using nitrogen adsorption isotherms at 77 K. (Gemini, Micromeritics) BET theory is a model for gas molecules adsorbing on a solid surface. It was first proposed by Stephen Brunauer, Paul Hugh Emmett and Edward Teller in an article in 1938.[104] BET theory is based on the Langmuir theory for monolayer gas molecule adsorption and then extended to include multiplayer adsorption. This means that a total surface area S_{total} and a specific surface area S is approximated using:

$$S = \frac{S_{total}}{a}$$

Eq. 3.1.1

$$S_{total} = \frac{(v_m N s)}{M}$$

Eq. 3.1.2

Where v_m is the monolayer adsorbed gas quantity, N is Avogadro's number, s is the adsorption cross section, M is the molecular weight of adsorbate and a is the mass of sample solid.

3.2 Results and Discussion

3.2.1   Films

SEM micrographs in Figure 3.2.1 show uniform film thicknesses of 0.5 µm and 1.3 µm throughout for the single-dip and 4-dip films respectively.   Adhesion to the FTO substrate is good and the films are homogeneous in cross section as well as in surface profile. (Figure 3.2.1) The layer immediately below the film is observed at 900- 1000 nm for both sample is the conducting FTO, beneath which this the insulating glass slide begins charging as electrons accumulate due to low conductivity.   The non-uniform layers observed under these two surface layers are hard to explain but are due to strange artefacts related to the charging effects and the contrast of the SEM.

Figure 3.2.1: SEM micrographs of the 1 dip (top) and 4 dip (bottom) TiO_2 films coated on FTO glass.
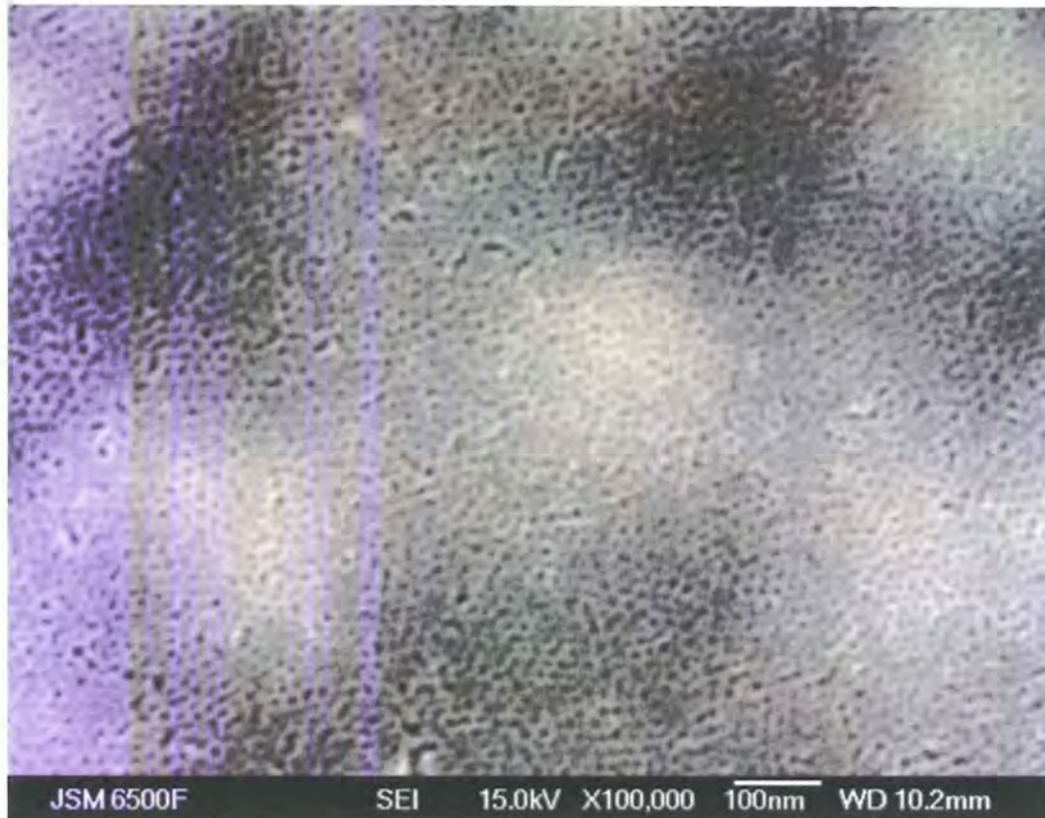
Figure 3.2.2: Scanning Electron Micrograph of a 0.5 μm (I_I F127 templated) TiO_2 film.

Films showed macroscopically smooth surfaces with few cracks, however on magnification under high resolution SEM the nanostructure becomes apparent. Figure 3.2.2 shows evidence of the I_I cubic template with a high degree of order in two dimensions. Another important feature is the pores appear to penetrate down through the cross-section of the film. This is structurally important as it permits easy penetration for the electrolyte to the back of the film and indeed this was one of the prerequisites set out for designing a high performance nanostructured electrode. It is easier to make an estimate of the pore sizes from the High-resolution AFM in Figure 3.2.3 which shows the nanostructure as an array of pores, with a repeat distance of approximately 12 - 15 nm , giving a pore volume fraction of 0.3.

750 nm (vertical label)

21 nm

750 nm
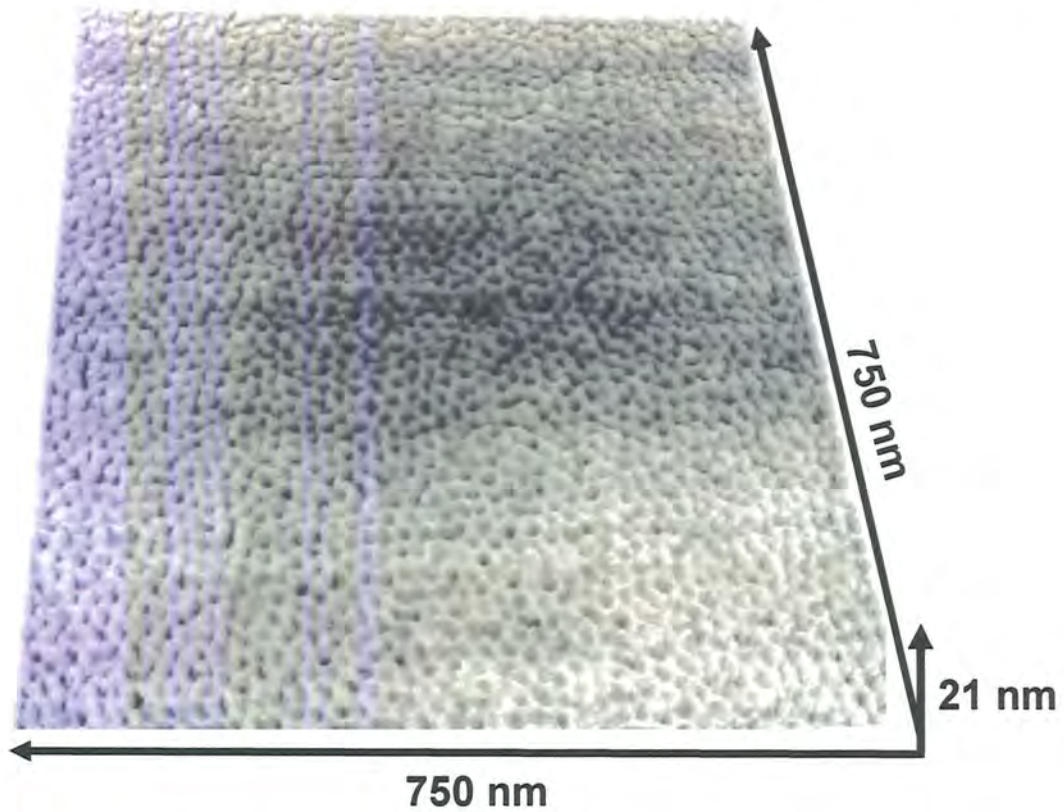
Figure 3.2.3 High-resolution tapping mode AFM image of a 0.5 μm (I_I F127 templated) titanium dioxide film. Surface acquired with a single-walled carbon nanotube AFM tip(lateral resolution 5 nm).[*105*]

3.2.2   Internally nanostructured TiO$_2$ powders

The periodicity of our internally nanostructured TiO$_2$ powders were examined using SAXD. Two different surfactants Brij ®78 and the Pluronics F127 demonstrate the ability to design different structures (Figure 3.2.4.) H$_I$ templated TiO$_2$ from Brij ®78 shows a periodicity 5-8 nm. Notice the 2θ angle has shifted to a lower number for the larger surfactant F127 in the I$_I$ cubic phase; this is characteristic for greater periodicity and indeed the 12-15 nm agrees broadly with that seen from AFM and TEM.
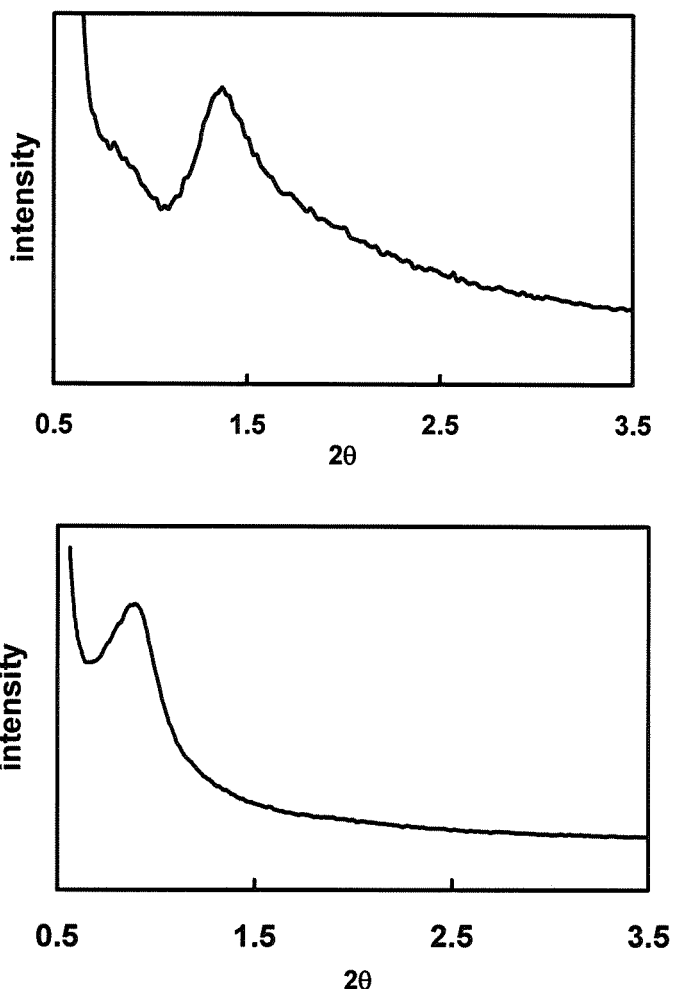
Figure 3.2.4: H_I templated TiO_2 powders from Brij ®78 (Top) and F127 in the I_I cubic

phase. (Bottom)

Figure 3.2.5 displays a typical BET nitrogen adsorption/desorption isotherm of Titania powder prepared with I_I F127. The pore size analysis based on the desorption (as is convention) was determined using a Dollimore and Heal Pore Size Distribution Function and shows an array of 7-12 nm pores which equates to a pore volume fraction of 0.3.

BET gave a surface area of 100-220 m^2 g^{-1} for our materials depending on the quality of uniformity and order of the nanostructure. It was found to be an excellent diagnostic tool for the performance of the powder in electrochemical rate studies; i.e. the higher the BET surface area the better kinetic performance of the material. (5.4.2) To allow comparison 12 nm anatase nanoparticles were obtained from Aldrich, these gave a BET surface area of ~ 180 m^2g^{-1} slightly lower than the reported value.
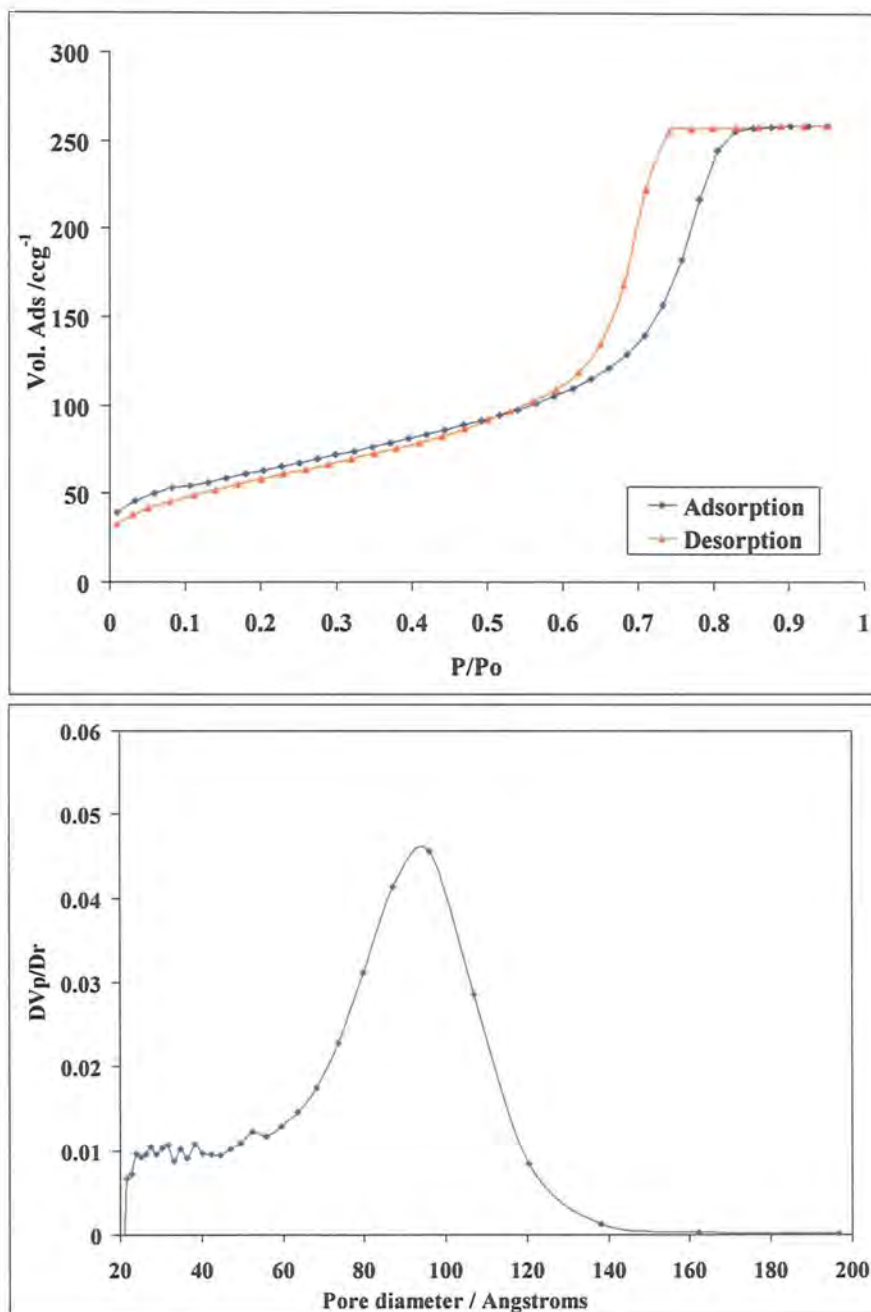
Figure 3.2.5: BET nitrogen adsorption/desorption isotherm (Top) and pore size analysis (Bottom) of Titania powder prepared with I_l F127 template.
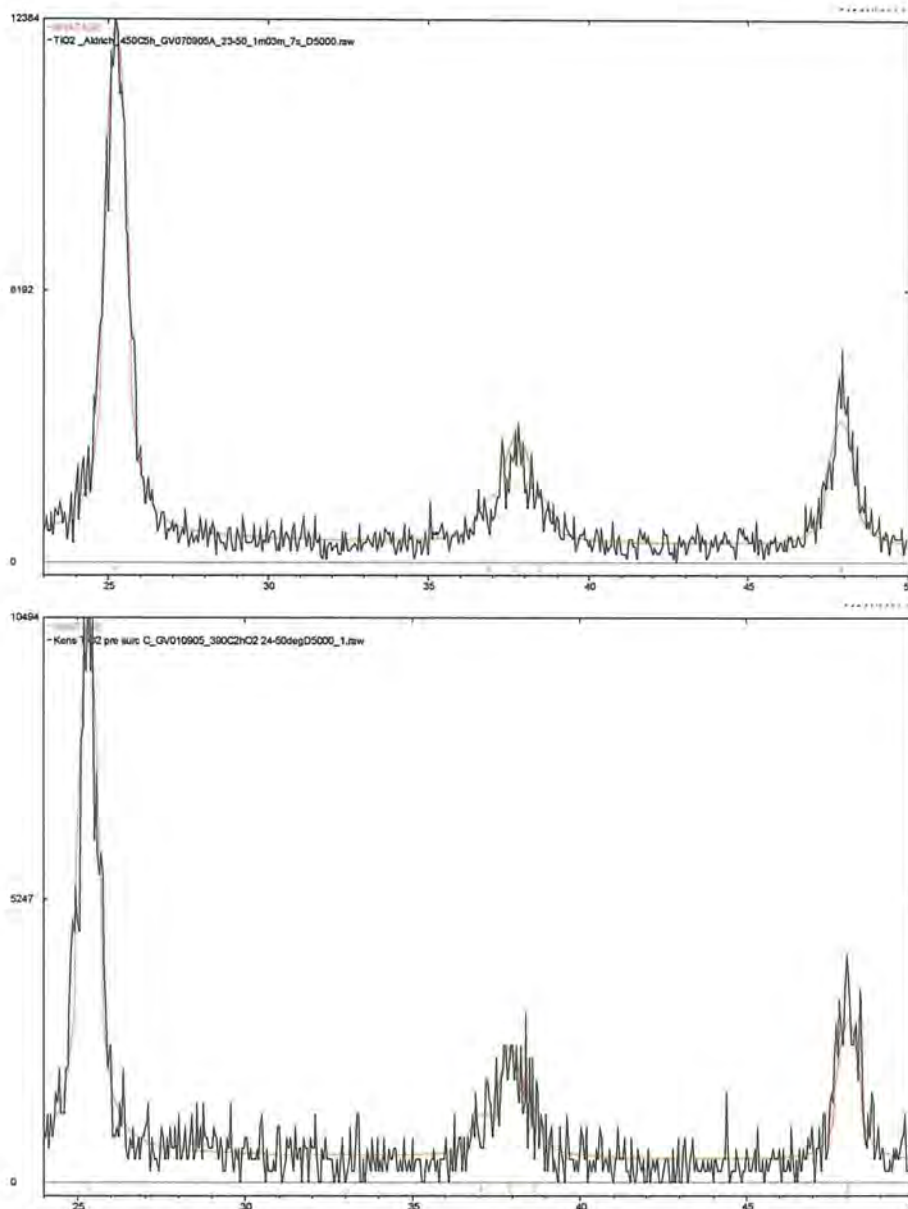
Figure 3.2.6 Wide-angle XRD data for Titania powder prepared with I_l F127 (Bottom) and commercial 12 nm anatase particles (Top). (Red trace = anatase)

Wide-angle XRD data for both Titania powder prepared with I_l F127 and commercially obtained 12 nm anatase particles (Aldrich) showed a low degree of crystallinity, predominantly anatase. SEM at low magnification shows the particles in Figure 3.2.7; The product of grinding the nanostructured material shows large distribution of particle sizes and shapes, with a characteristic length of about 10 μm from the sides to the centre of the particles, for the majority of the sample. By contrast, the agglomerates of the nanopowders were much smaller, and characterised by corresponding lengths of about 0.5 μm.

Figure 3.2.7 SEM micrograph for Titania powder prepared with I_l F127 (Top) and commercial 12 nm anatase particles (bottom).

TEM on the I_l F127 nanostructured material shows a pore-to-pore separation of 12-15 nm. SEM on the nanosize material showed agglomeration from grains under 25 nm radius and WAXD showed a grain size of about 15 nm. Therefore, the grain radius is estimated to be around 10 nm.
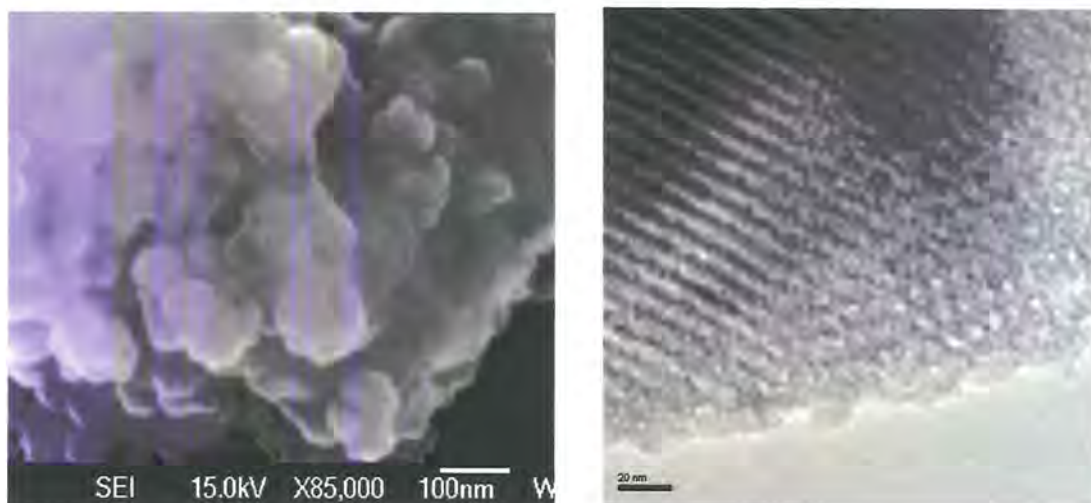
Figure 3.2.8: SEM of commercial 12 nm anatase particles (left) and TEM micrograph for Titania powder prepared with I_l F127 (Right).

3.2.3 Improvement of mesoporous titania powder

Preparations of mesoporous silica[100] show the surface area of such powders could reach in excess of 300 m^2g^{-1}. Many studies have reported different methods to improve the periodicity of TiO_2 films.[44, 46] These attempts have been characterised by controlling the rate at which the inorganic material forms around the template. These may include changing solvents, acid type or strength as well as other factors such as relative humidity, as well as careful and complicated treatments to remove the surfactant (at a lower temperature), preventing the crystallisation and grain growth and collapse of the mesostructure to give areas of dense material[106].

Many attempts were made to improve quality and uniformity of the mesoporous structure throughout the mass of the powder. However, despite changing many parameters (as detailed above) it was not possible to improve the surface area of powders reproducibly and typically BET gave a surface area of 100-220 m^2 g^{-1}. (See Appendix for experimental conditions). Despite many reports of successful preparation of mesoporous TiO_2 in the literature the reproducibility is a weak point in many cases. Indeed over thirty preparations in this work failed to yield a systematic reason for the deviation in quality of the meso structure. The mechanism for the formation is kinetically controlled and is often influenced by atmospheric conditions in which films are prepared. Other non-obvious factors such as mixing or ageing time, as well as purity of precursors can also have a significant effect.

The system of thin film formation differs from that of bulk powders in that diffusion distances in which the solvent or atmospheric moisture may travel to escape/penetrate the structure are greater in the latter; which may go some way to explaining why the preparation of the thin films is somewhat more reproducible. The highest surface area powders, (150-220 m^2 g^{-1}) obtained from the I_I cubic phase templated from Pluronics F127 were chosen for electrochemical characterisation and made into composite electrode films to be studied in chapter 5.

3.3 Conclusions

Using the complementary techniques of TEM, powder X-ray diffraction and N_2 adsorption/desorption isotherms, a series of mesoporous cubic and hexagonal Titania films and powders have been characterised.

A multi-dip method was used to produce films of 0.5 μm and 1.3 μm, which were homogeneous in cross section as well as in surface profile and show good adhesion to the FTO substrate. Films templated from the I_1 cubic template showed a high degree of order in two dimensions. Pore sizes estimated from the High-resolution AFM show the nanostructure as an array of pores, with a repeat distance of approximately 15 - 18 nm.

The periodicity of our internally nanostructured TiO_2 powders were examined using SAXD. Two different surfactants Brij ®78 and the Pluronics F127 demonstrate the ability to template different structures. H_1 templated TiO_2 from Brij ®78 shows a periodicity 5-8 nm, the larger surfactant F127 in the I_1 cubic phase has a greater periodicity and indeed the 12-15 nm agrees broadly with that seen from AFM and TEM.

BET of Titania powder prepared with I_1 F127 gave the highest surface area 220 m^2g^{-1}, the pore size analysis shows an array of 7-12 nm pores which equates to a pore volume fraction of 0.3. Many attempts were made to improve quality and uniformity of the mesoporous structure throughout the mass of the powder. However, despite changing many parameters it was not possible to improve the surface area of powders reproducibly and typically BET gave a surface area of 100-220 m^2g^{-1}. To allow comparison 12 nm anatase nanoparticles were obtained from Aldrich, these gave a BET surface area of~ 180 m^2g^{-1} slightly lower than the reported value.

Wide-angle XRD data for both Titania powder prepared with I_1 F127 and commercially obtained 12 nm anatase particles showed a low degree of crystallinity, predominantly anatase. For the nanostructured material a large distribution of particle sizes and shapes were observed; with a characteristic length of about 10 μm from the sides to the centre of the particles for the majority of the sample. By contrast, the agglomerates of the nanopowders were much smaller, and characterised by corresponding lengths of about 0.5 μm.

Chapter 4

Lithium Insertion into TiO$_2$ from Aqueous

Solution — Facilitated by Nanostructure

4.1 Background and Objectives

Chapter two demonstrated that attempts to reproduce the impressive rate performance of the aqueous $Ni(OH_2)/NiOOH$ electrode as a high rate lithium storage electrode in aprotic media were ultimately unsuccessful. Therefore, in this chapter the focus is turned to finding a suitable nanostructured negative electrode that can be used in an aqueous system. To maximise power density the voltage window should be as wide as possible; the best electrode pair maximises cell potential without causing gas evolution. With a Ni positive electrode, a M-Hydride negative limits cell voltage to 1 V, a Ni-Cd cell extends cell voltage to 1.5 V but is toxic. (Figure 4.1.1) This chapter investigates the environmentally benign TiO_2 as a negative candidate.
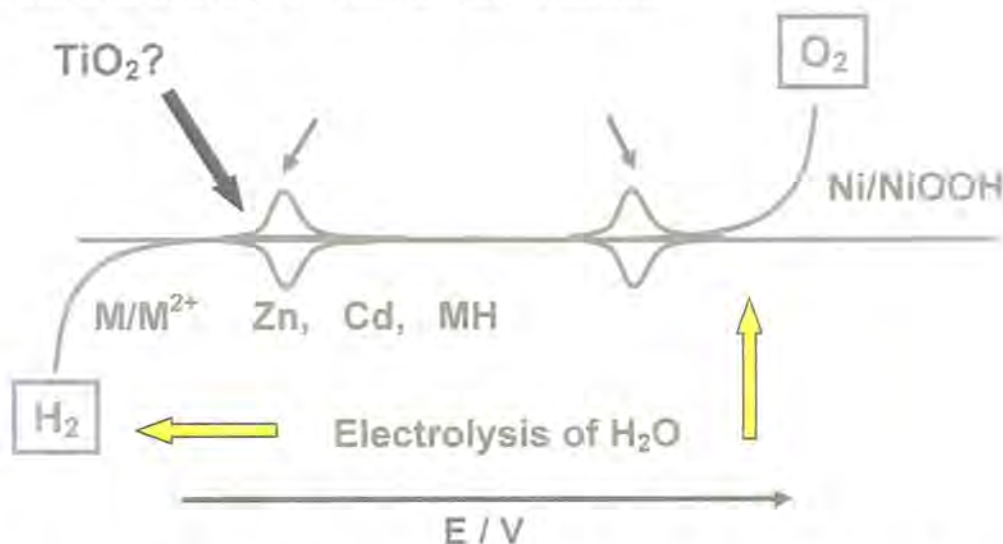
Figure 4.1.1. TiO_2 has a number of advantages over existing negative electrode technologies for aqueous batteries. It is cheap, non-toxic and would increase cell voltage to ~1.7 V, however insertion of Li ions is predicted to be negative of H_2 evolution.

This chapter seeks to examine the possibility of electrochemical reduction of TiO_2 by lithium ion insertion from aqueous LiOH, using nanostructure to facilitate the solid state reaction kinetics as previously demonstrated for nanostructured NiOOH.[75] Nanostructured TiO_2 is investigated as an alternative to hydrogen storage electrodes in alkaline cells for battery and supercapacitor applications. The advantage would be a much higher current density given by a nanostructured electrode filled with a highly

conducting electrolyte, as compared with a normal microparticulate electrode in which the discharge rate is limited by solid state diffusion.[74]

By contrast with some other transition metal oxides, such as WO_3, there are very few reports of the reduction of TiO_2 in an aqueous solution. The reduction potential for proton insertion into TiO_2 is below that of the hydrogen evolution reaction (HER), so that the latter is generally favoured. For example, in early work on electrochemical charging and discharging of rutile with hydrogen at pH 10, a doping level of only 7 x 10^{-19} cm^{-3}, (equivalent to a stoichiometry of $H_{0.002}TiO_2$) was reported on charging at –2 V *vs.* SCE.[107] In aprotic lithium ion electrolytes however, rutile and many other forms of TiO_2 have exhibited reversible insertion and extraction of lithium up to a stoichiometry of about $Li_{0.5}TiO_2$, which is sufficient for applications in lithium batteries. Mesoporous forms have also been used for lithium storage, and an additional pseudocapacitance has been found as a result of the high internal surface area. This is discussed extensivly in chapter 5.

The anatase form of TiO_2 undergoes lithium ion insertion at an average potential of 1.85 V *vs.* Li[108], which roughly corresponds to –1.2V *vs.* the standard hydrogen electrode (SHE) at pH 0. The very negative value suggests that lithium ion insertion from an acid solution would be overwhelmed by the evolution of hydrogen gas formed by electrolysis of water. In an alkaline solution however, e.g. 1 M LiOH, the Nernst equation predicts the onset of hydrogen evolution to be –0.83 V *vs.* SHE, with a much lower overpotential for the HER. The situation can be better understood with the aid of Dahn's calculation of the HER potential versus lithium[109], used to relate the lithium and reversible hydrogen electrode (RHE) reference scales in (*Eq. 4.1.1-5*):

$$H_2O(l) + e^- \rightleftharpoons OH^- (aq, 1 \text{ M LiOH}) + \tfrac{1}{2} H_2 (g, STP) \qquad E^\theta (RHE) \qquad \qquad Eq. \ 4.1.1$$

$$Li^+ (1 \text{ M LiOH}) + e^- \rightleftharpoons Li (s) \qquad E^\theta(Li/LiOH) \qquad \qquad Eq. \ 4.1.2$$

$$Li (s) + H_2O (l) \rightleftharpoons LiOH (aq, 1 \text{ M}) + \tfrac{1}{2} H_2(g, STP) \qquad \Delta G_1 = -214.5 \text{ kJ mol}^{-1} \qquad Eq. \ 4.1.3$$

$$\text{Hence } E^\theta (RHE) - E^\theta (Li/LiOH) \qquad = -\Delta G_1 / F = 2.23 \text{ V} \qquad \qquad Eq. \ 4.1.4$$

$$TiO_2 + x \, Li^+ + xe^- \rightleftharpoons Li_x TiO_2 \qquad \begin{array}{l} E \sim -0.38 \ V \ vs. \ RHE \ at \\ pH \ 14 \end{array} \qquad Eq. \ 4.1.5$$
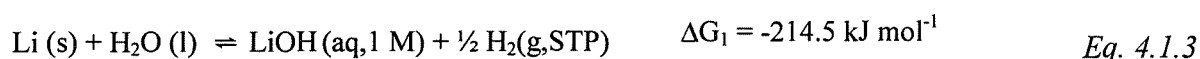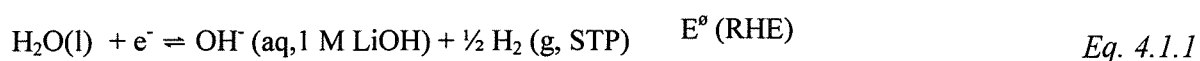
Relating the insertion potential of lithium in anatase (1.85 V *vs.* Li) to the calculated value of the RHE electrode (2.23 V *vs.* Li) predicts an insertion overpotential of E ~ - 0.38 V *vs.* RHE at pH 14; a much lower overpotential for hydrogen evolution than in water.

$$NiOOH + H^+ + e^- \rightleftharpoons Ni(OH)_2 \qquad E \sim + 1.32\ V\ vs.\ RHE\ at\ pH\ 14 \qquad\qquad Eq.\ 4.1.6$$
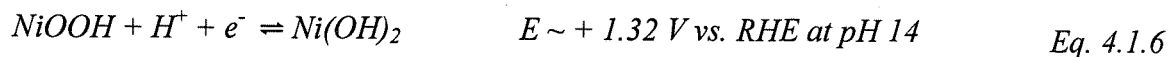
An all-nanostructured supercapacitor with a TiO_2 negative electrode, coupled with a $Ni(OH)_2/NiOOH$ positive electrode , reaction displayed in *Eq. 4.1.6* [*110*], should have a very high power output and one of the highest cell potentials possible in an aqueous system. In fact, the $Li_xTiO_2/NiOOH_{2-x}$ cell is amongst the highest possible voltage for an alkaline system with a value potentially, close to 1.7 V (the sum of -0.38 and 1.32 V *vs.* RHE).

4.2 Experimental

4.2.1 Sample preparation

Nanostructured TiO_2 films were prepared by evaporation induced self assembly (EISA) as discussed in Chapter 3.[*43, 48, 111*] For electrochemical studies with single-dip, 4-dip and control (non-templated) films prepared on a fluorine-doped SnO_2 (FTO) conducting glass substrate. Electrical contact was made to some exposed FTO at the edge of the TiO_2-coated slide and polyimide tape used to mask an area of the TiO_2 film approximately 1 cm^2. A modification of this masking method was developed to electrochemically isolate the active TiO_2 area from the rest of the substrate. This enabled crack free areas of the deposited film to be selected after inspection with optical microscopy. After surface scoring of TiO_2 surface film with a needle, any exposed FTO was covered by quick setting epoxy resin, to leave an electronically connected TiO_2 isolated from the rest of the film (the method is displayed in Figure 4.2.1). This was particularly important for charge storage testing, in order to prevent parasitic reactions on any exposed FTO substrate.
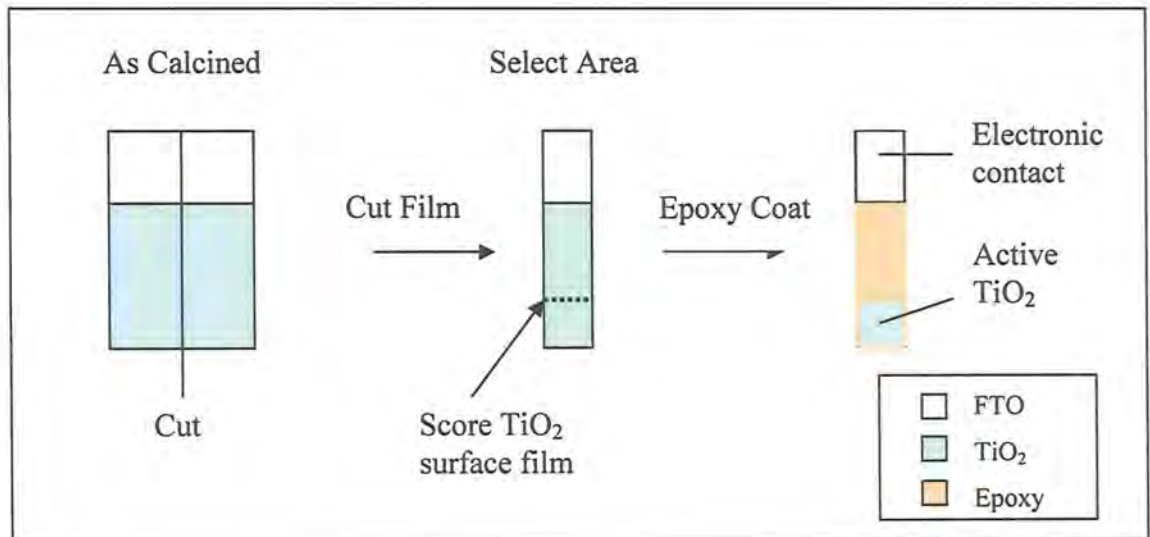
Figure 4.2.1: Electrode preparation technique for films coated on FTO. Scoring of TiO_2 film to isolate active material but maintaining connection with electronically conducting FTO under layer. Epoxy resin covers any exposed areas of FTO.

4.2.2   Electrochemical Cell.

A large scale electrochemical cell was designed, such that it could accommodate the size of the dip-coated TiO_2 films. The function of the cell was to keep the working electrode in an anaerobic environment. This was important when considering the operating potentials of the working electrode with a high overpotential for oxygen reduction. The counter electrode, a high surface area Ni mesh, was isolated in a separate chamber separated by a glass frit in order that any evolved gases were kept out of the main chamber.

The electrolyte, 1 M aqueous LiOH, except where stated, was purged with Argon gas for 1 hour prior to electrochemical investigations. A blanket of Argon gas over the surface of the electrolyte reduced any oxygen contamination from the air. An Hg/HgO reference electrode containing (1 M LiOH) was used with a custom made luggin capillary. An exact conversion into the reversible hydrogen electrode (RHE) scale was made according to equations *Eq. 4.2.1*, *Eq. 4.2.2* and *Eq. 4.2.3*(8) and (9) by adding 0.925 V ($\Delta G/2F$ for the reaction $Hg + H_2O = HgO + H_2$).

$$HgO + 2H^+ + 2\ e^- \rightleftharpoons Hg + H_2O \qquad\qquad E^0\ (Hg/HgO) \qquad\qquad \textit{Eq. 4.2.1}$$

$$2H^+ + 2\ e^- \rightleftharpoons H_2 \qquad\qquad E^0\ (RHE) \qquad\qquad \textit{Eq. 4.2.2}$$
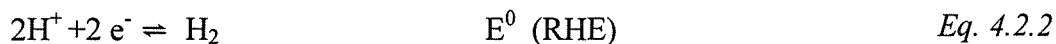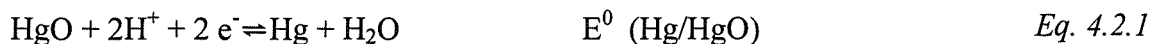
Subtracting (Eq. 4.2.2fromEq. 4.2.1)

$$HgO(s) + H_2(g) \xrightarrow{\ 2e^-\ } Hg(l) + H_2O(l) \quad \Delta G^o = -178.6\ kJmol^{-1}$$

$$\therefore E^o_{Hg/HgO} - E^o_{RHE} = \frac{-\Delta G^o}{2F} = +0.925\ V$$

<div align="right">Eq. 4.2.3</div>
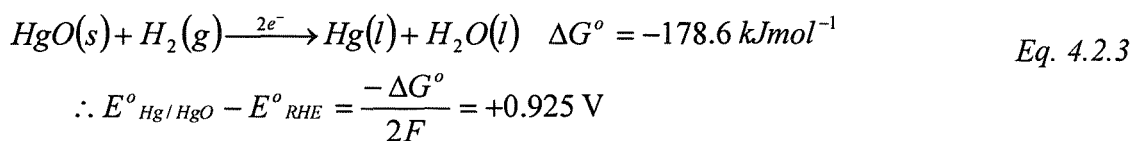
This conversion is applied where all voltages are reported verses RHE. Electrochemical studies in non –aqueous electrolytes were carried out in a large scale flooded cells in a three-electrode configuration, and were assembled in an argon-filled glove box (H_2O, O_2 <1 ppm; Unilab from MBraun). Metallic lithium was used both as the counter and reference electrode, with 1 M $LiN(CF_3SO_2)_2$ (Fluka) in propylene carbonate (PC, Aldrich 99.8 %) as the electrolyte.

4.2.3   Electrochemical studies

For potential step experiments the films were charged for 6 s at −0.85 V *vs.* RHE and discharged for 6 s at +0.45 V *vs.* RHE.   In polarisation analysis the steady state current was measured 60 s after stepping the potential, well after the decay of the transient due to ion insertion. To demonstrate the supercapacitor concept, a cell was constructed with an excess of a nanostructured $Ni/Ni(OH)_2$ film[80] as the positive electrode, and coupled with a 4-dip nanostructured TiO_2 as the negative.   The $Ni(OH)_2/NiOOH$ electrode was first charged to + 1.525 *vs.* RHE for 60 s. The TiO_2 electrode was then separately charged to −0.7 *vs.* RHE also for 60 s. The cell was then discharged over a load of 500 Ω. Electrochemical studies were performed using a 16-channel potentiostat (VMP2 Princeton, Applied Research; Biologic-Science Instruments).

4.3 Results and Discussion

4.3.1.1 Nanostructured TiO$_2$ *vs.* Non Templated

The open circuit potential of all the films inserted into water was around 0.5 V *vs.* RHE. From Figure 4.3.1 it can be seen that the non-templated TiO$_2$ shows little reversible electrochemistry with less than 1 mC cm^{-2} anodic charge, conversely 52.0 mC cm^{-2}, was extracted from the templated film of 0.5 µm thickness. An important feature to note at the cathodic peak is that despite the high overpotential for hydrogen generation for this sample there is no exponential increase in current and indeed if anything there seems to be a retardation in the peak current at voltage limit of -0.85 V *vs.* RHE.
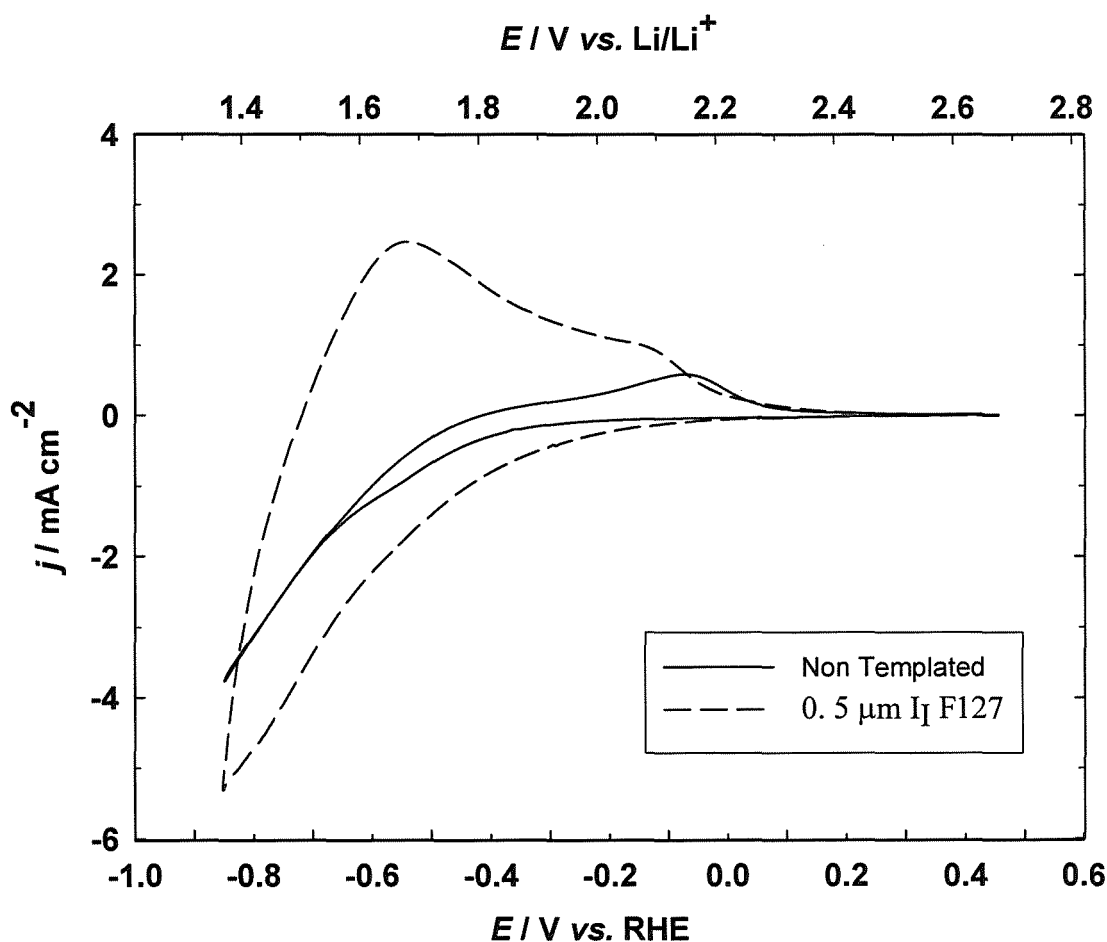
Figure 4.3.1: Cyclic voltammograms of a 0.5 µm I$_I$ film templated from F127 surfactant and a film from the same mixture in absence of surfactant. The potential on the lithium scale, given for comparison, is estimated by adding 2.23 V (Equation 4). (+0.45 V and -0.85 V *vs.* RHE at 20 mV s^{-1} in de-oxygenated 1 M aqueous LiOH at 25 °C).
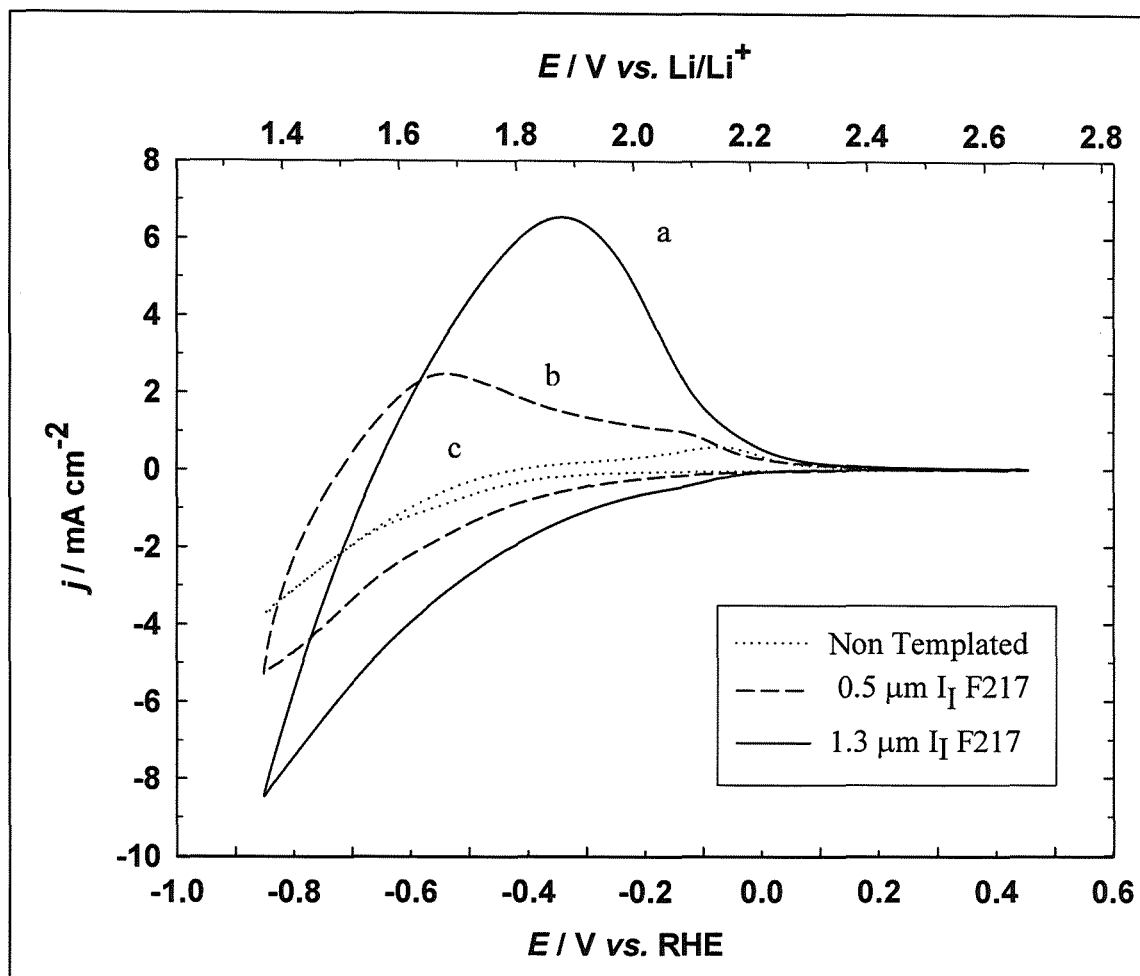
Figure 4.3.2 Cyclic voltammograms of (a) 1.3 μm I_I TiO_2 film, (b) 0.5 μm I_I TiO_2 film TiO_2 film and (c) a non-templated TiO_2 film between +0.45 V and -0.85 V *vs.* RHE at 20 mV s^{-1} in de-oxygenated 1 M aqueous LiOH at 25 C. The potential on the lithium scale, given for comparison, is estimated by adding 2.23 V (equation 4).

The cyclic voltammograms of the 0.5 μm (single-dip), 1.3 μm (4-dip) nanostructured, and non-templated samples in Figure 4.3.2 all show an increase in cathodic current at negative potentials *vs.* RHE. However, only the nanostructured films both showed large anodic peaks on the reverse scan, and a deep blue colouration indicating reduction by insertion of lithium ions and an accompanying electron. Such electrochromism, is observed with tungsten oxide[64, 65] and is well known for TiO_2 in non-aqueous systems thought to be due to the insertion of cations (namely Li^+) into the bulk structure. It is believed that this is the first evidence of electrochromism of TiO_2 in aqueous electrolyte. Referring to the lithium reference scale in Figure 4.3.2, we find

that the cathodic current increases monotonically from approximately 2.2 V. The anodic sweep peaks at about 1.9 V then returns to zero at 2.2 V. These results are consistent with previous work on lithium insertion into mesoporous anatase from a non-aqueous solvent showing a number of peaks between 2.2 and 1.4 V due to a combination of bulk and surface processes.[72] In Figure 4.3.2, any individual peaks are presumed to have merged due to the rather high scan rate and the effects of solid state diffusion. The anodic charges were 52.0 mC cm^{-2} (referring to the external surface only) and 127 mC cm^{-2} respectively for the 1-dip and 4-dip samples compared to less than 1 mC cm^{-2} for the non-templated sample. These data indicate charge storage values of about 1000 C cm^{-3} or 315 C g^{-1} and an average composition of $Li_{0.27}TiO_2$, assuming a bulk density of ~4 g cm^{-3} and a pore volume fraction of 0.3. The cathodic charges, -81.2 and -157 mC cm^{-2} respectively, include the parasitic reaction of hydrogen evolution. Charge efficiencies of 64% and 81% respectively show how the increased charge capacity of the thicker film reduces the significance of the parasitic reaction. Wagemaker[112], observed increase in solid solution behaviour for anatase, which permits lithium up to 0.23 for 7 nm particles; also observed for nanocrystalline anatase by Maier *et al.* in non-aqueous solution.[113] This could explain the fact that such fast insertion into the nanostructure is possible. The mechanism for Lithium insertion in TiO_2 is discussed in detail in chapter 5.

4.3.1.2   Lithium Insertion versus Proton Insertion

The low thermodynamic activity of protons in the alkaline solution strongly favours lithium ion, rather than proton insertion, and it is difficult to conceive of any reaction other than lithium ion insertion to account for such a high reversible charge in this experiment. For confirmation of lithium ion insertion over that of protons, reduction for a film was performed with KOH instead of LiOH as the electrolyte. The ionic radii of Li^+ and K^+ in crystals are 0.69 and 1.38 Å respectively[114], it is unlikely therefore, that the latter would be inserted leaving protons as the only remaining intercalation candidate.
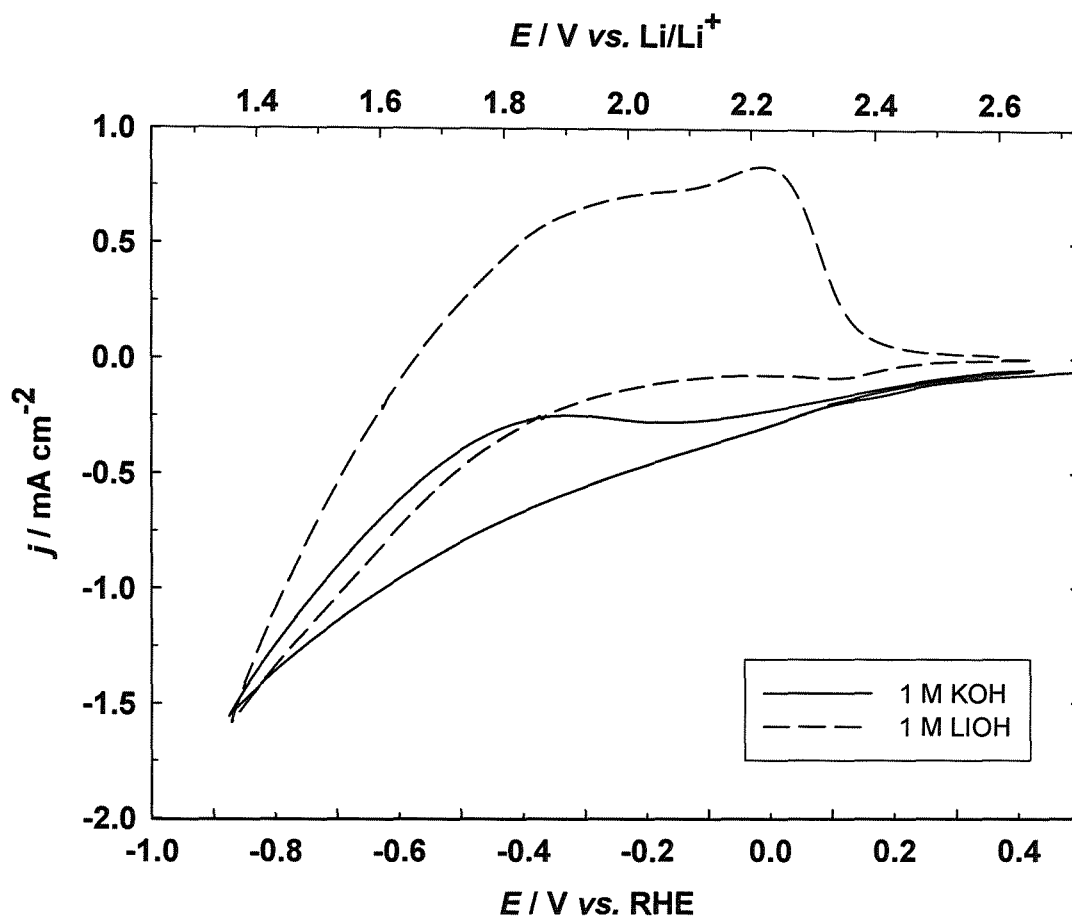
Figure 4.3.3: Cyclic voltammograms of 0.5 μm H_I TiO$_2$ film in either de-oxygenated 1 M aqueous LiOH or 1 M aqueous KOH between +0.425 V and -0.875 V *vs.* RHE at 20 mV s^{-1}, 25 °C.

In Figure 4.3.3 the voltammogram displays a slightly different shape, in this case, during reduction of the film the charge at the more negative level seems to have decreased. In the KOH electrolyte, gas bubbles were evolved and the film remained colourless throughout, on the reverse sweep no anodic current was measured. When compared to the same film in LiOH solution, these data show that it is the Li$^+$, rather than H$^+$ or K$^+$, that inserts into the nanostructured TiO$_2$ during reduction. This phenomenon is supported by Yuan *et al.* [115] who recently demonstrated reversible Li$^+$ storage from lithium hydroxide in nanoparticulate MnO$_2$. Whilst in KOH a reduced amount of charge was observed.
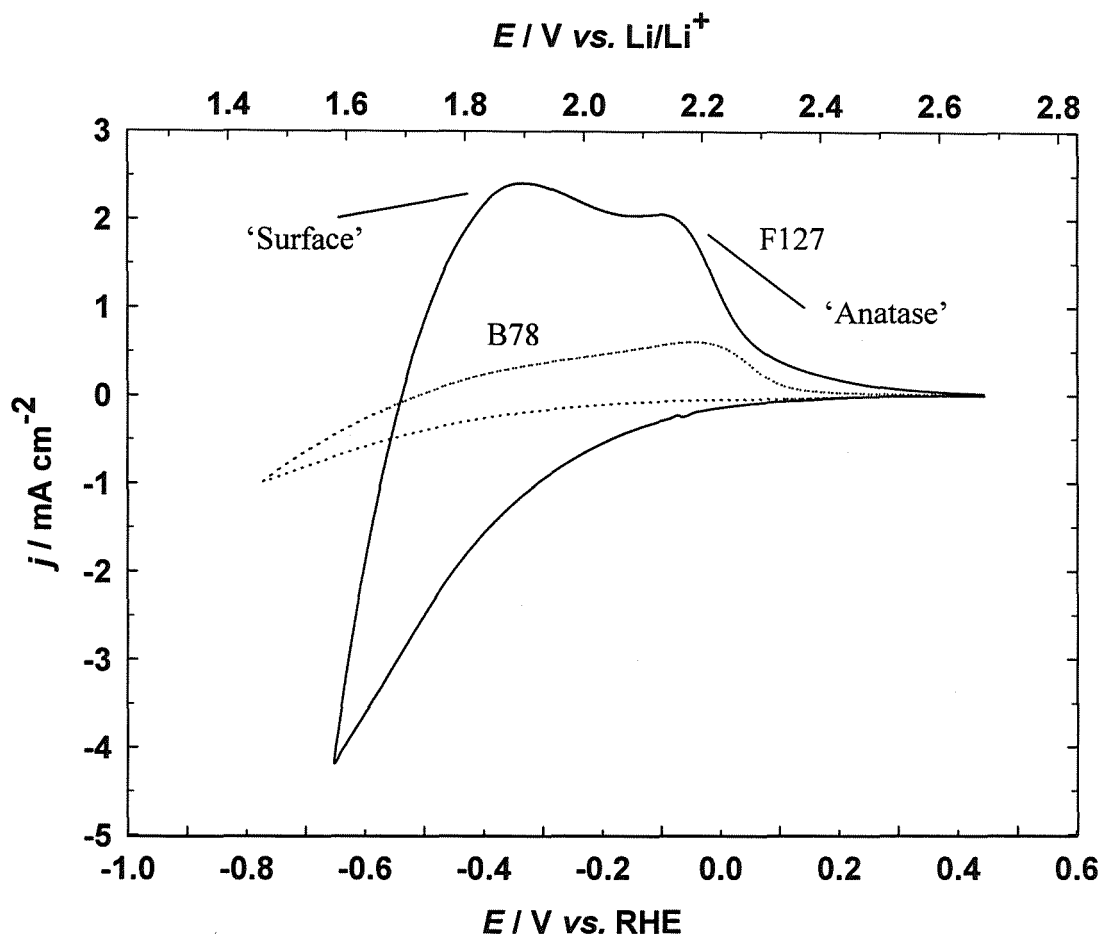
Figure 4.3.4: Cyclic voltammograms to compare a 0.5 μm film templated from either B78 or F127 at 20 mV s^{-1} in de-oxygenated 1 M aqueous LiOH at 25 °C. The potential on the lithium scale, given for comparison, is estimated by adding 2.23 V (equation 4).

In Figure 4.3.4 and Figure 4.3.3 the films are prepared with a hexagonal template B78; a preparation which should lead to thicker walls and a lower surface to bulk ratio. This decreased ratio is characterised by an increased ratio of the cycled charge corresponding to the higher voltage 'anatase' plateau when comparing with the cubic TiO_2 where the lower voltage 'surface' peaks engulf the high voltage 'anatase' peak. The effect of nano size particles on the insertion chemistry of lithium into TiO_2 is discussed in detail in 5.4.2.

E / V *vs.* Li/Li$^+$
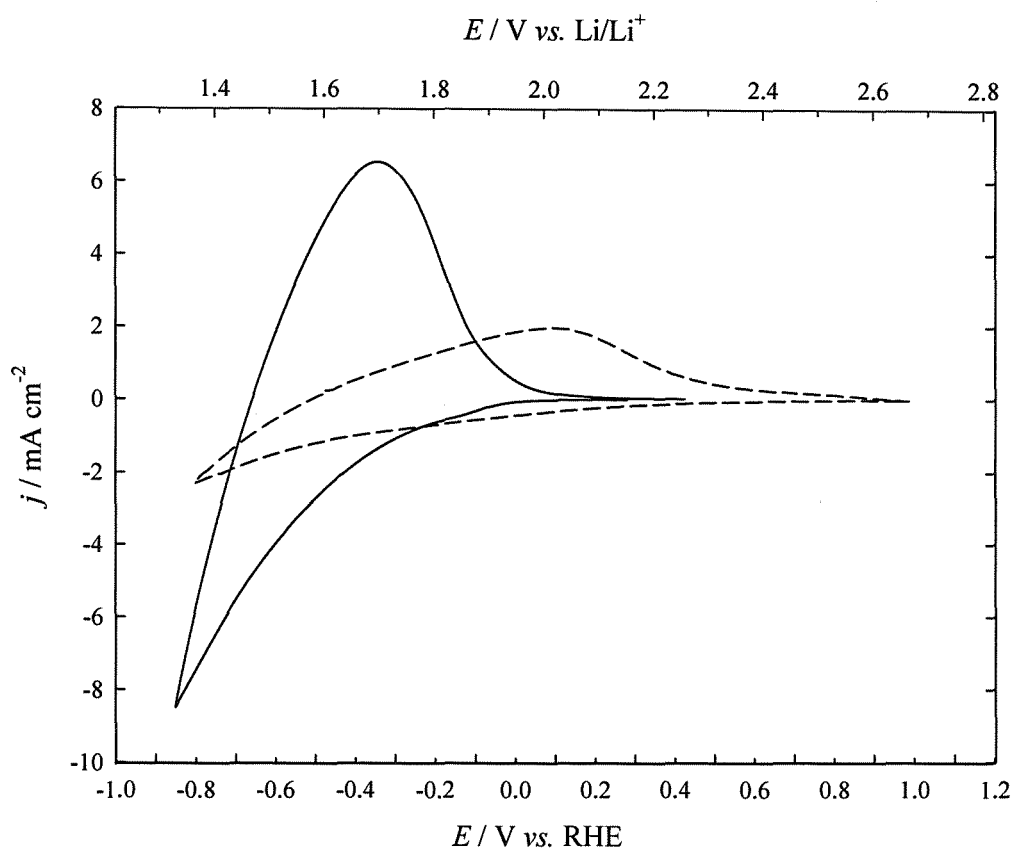
Figure 4.3.5: Cyclic voltammograms of 1.3 μm (4-dip) nanostructured TiO$_2$ films at 20 mV s^{-1}, 25 °C; Full line: de-oxygenated 1 M aqueous LiOH at +0.45 V and -0.85 V *vs.* RHE; Dashed line: 1 M LiN(CF$_3$SO$_2$)$_2$ in PC, +1.0 V and -0.85 V *vs.* RHE

Figure 4.3.5 compares aqueous and non-aqueous electrolytes, again under the relatively fast scan rate of 20 mV s^{-1}. In both cases, cathodic currents continue to increase towards the scan limit and approach zero around 1.5 and 1.6 V respectively. The higher gradient observed for the aqueous electrolyte indicates a lower resistance and corresponding ir drop. At this scan rate the potential at zero current is more negative in the case of the aqueous electrolyte, indicative of a higher degree of reduction of the TiO$_2$. The larger charge under the anodic peak, 127 compared with 48.9 mC cm^{-2} in the non aqueous case confirms this. Although a non aqueous electrolyte will ultimately allow a higher degree of reduction in the absence of the competing HER reaction, the result of this experiment shows that reduction is faster in water.

Scan rate / mV s^{-1}	Cathodic charge / mC cm^{-2}	Anodic charge / mC cm^{-2}
5	-55.0	33.9
20	-38.5	32.8
50	-27.5	25.7
100	-20.8	19.5

Table 4.3.1: Charge stored in a film cycled in Figure 4.3.6 cyclic voltammograms of single-dip nanostructured titanium dioxide at different scan rates. Cycling between +0.45 V and -0.70 V *vs.* RHE at 20 mV s^{-1} in de-oxygenated 1 M aqueous LiOH at 25 °C.

Variable scan rate cyclic voltammetry was used to deconvolute the charge/potential relation from mass transport effects. Although the voltammograms, shown in Figure 4.3.6, become increasingly symmetrical about the x-axis down to 20 mV s^{-1}, a further reduction in scan rate introduced complications due to the parasitic reaction. Table 4.3.1 shows the anodic charge reaching a limiting value at a scan rate sufficiently low for the concentration profile to penetrate to the back of the film. However, the cathodic charge increases rapidly at low scan rates when the electrode is exposed to a high overpotential for the HER.
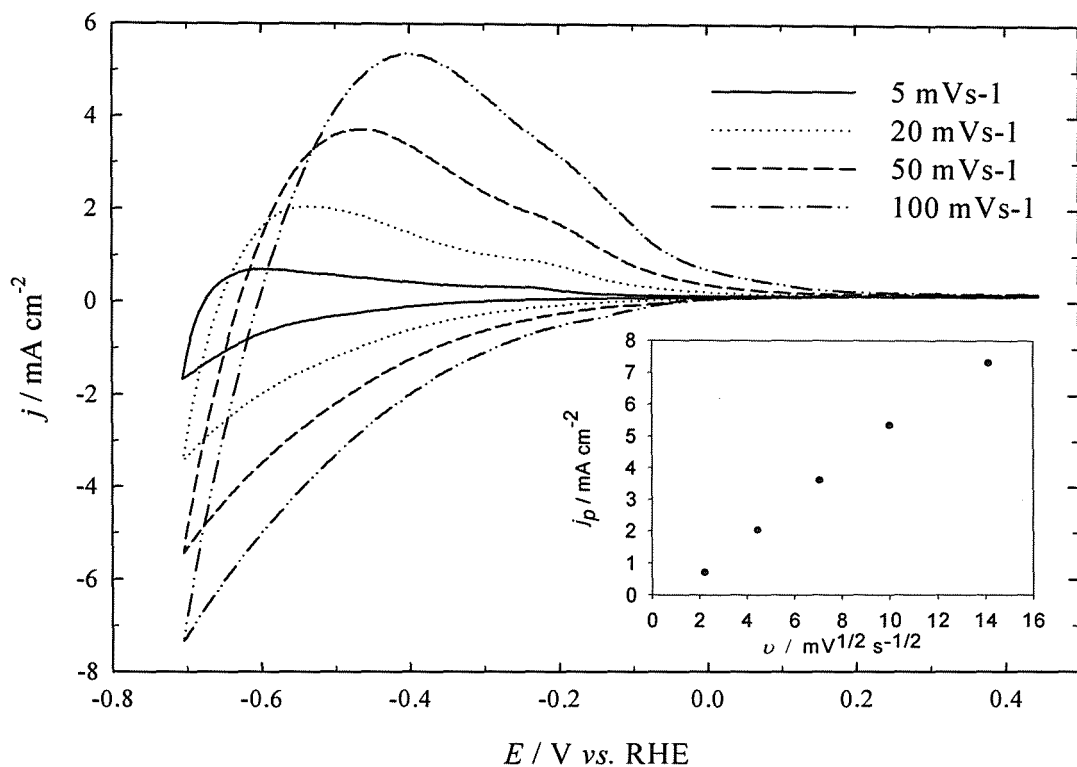
Figure 4.3.6: Cyclic voltammograms of single-dip nanostructured TiO_2 at different scan rates. Cycling between +0.45 V and -0.70 V vs. RHE in de-oxygenated 1 M aqueous LiOH at 25 °C. The inset is a plot of the anodic peak current density (j_p) vs. scan rate$^{1/2}$.

4.3.2 Charge Storage properties.

Of obvious importance to any charge storage electrode is the resistance to self-discharge. At such negative potential limits in water parasitic reactions are inevitable and these have been observed in the slow sweep voltammetry. It is important to identify and quantify the effects of such reactions in order that they can be controlled or eliminated. For a quantitative study of the HER, a series of polarisation measurements was performed and results are displayed as a Tafel plot in Figure 4.3.7.
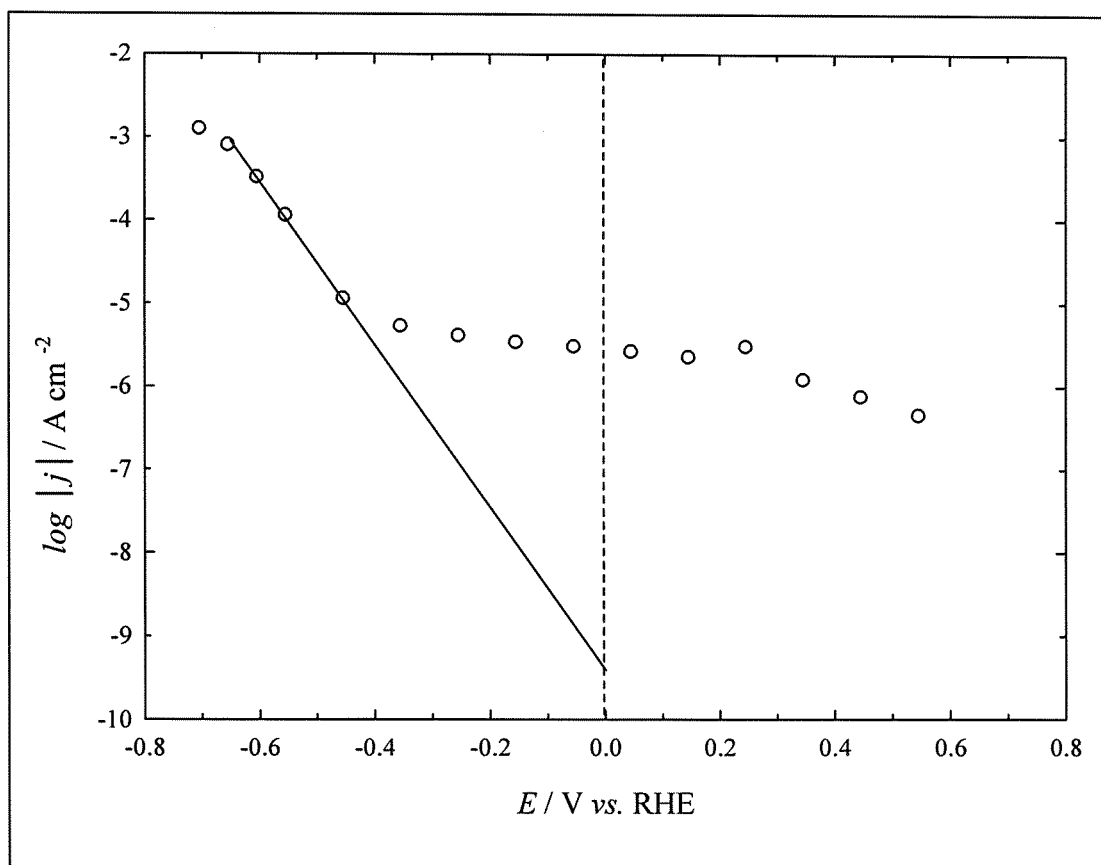
Figure 4.3.7: Tafel plot of polarisation current(for geometric electrode area) *vs.* potential for 0.5 μm I_l F127 TiO_2 film in de-oxygenated 1 M aqueous LiOH at 25 °C.

At potentials above 0.3 V *vs.* RHE we observe a potential dependent current, assumed to be kinetically controlled oxygen reduction. Between 0.3 and -0.4 V, the current is approximately constant, suggesting diffusion limitation of oxygen or some other diluted species. Below -0.4 V we observe a rapidly rising current, probably due to the hydrogen evolution reaction (HER), rising with a Tafel slope of about 100 mV per decade. At about -0.65 V some restriction, e.g. ohmic loss, causes a deviation from linearity. Extrapolating the Tafel region current to zero overpotential we calculate an exchange current between 10^{-9} and 10^{-10} A cm^{-2} based on the external area, or between 10^{-11} and 10^{-12} A cm^{-2} based on the pore surface. Small gas bubbles observed at the most negative potentials were at fixed points on the electrode, suggesting that the observed currents were exaggerated by defects in the film from the underlying substrate. Such defects were observed using high resolution SEM and are displayed in Figure 4.3.8
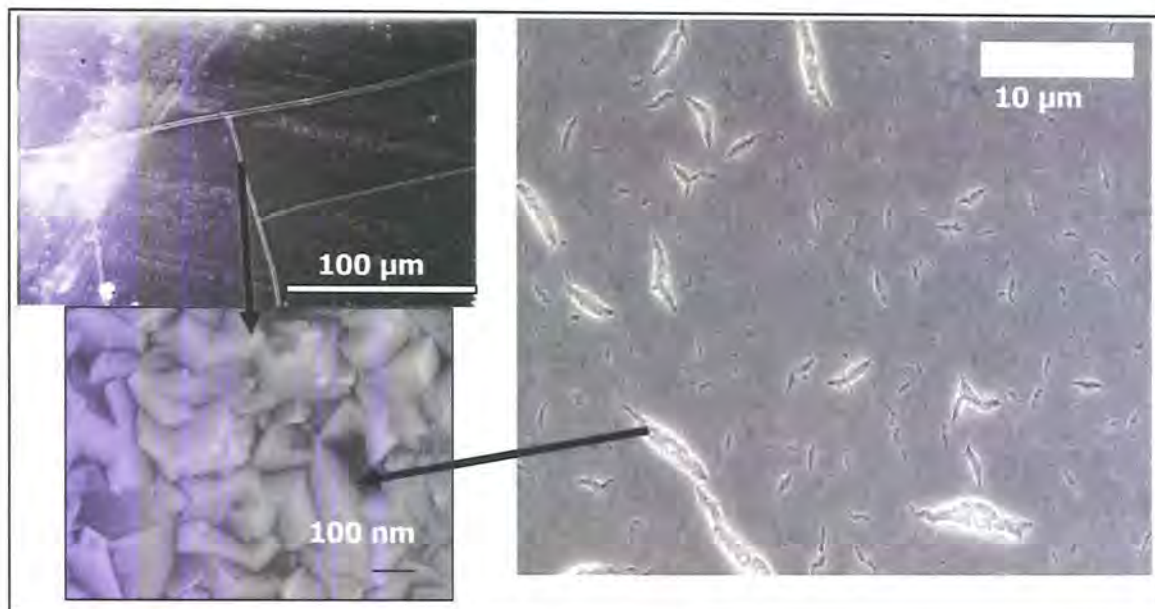
Figure 4.3.8: HER current may be due to exposed FTO substrate. SEM of 0.5 µm I_l F127 TiO_2 film.

4.3.2.1   Self –Discharge profiles

For the successful application of nanostructured TiO_2 as a charge storage electrode in aqueous electrolyte self-discharge time must be as low as possible. This may be estimated roughly by ratio of charge density to self-discharge current density. However, the self-discharge current is potential dependent so that the self-discharge rate decreases sharply with increasing potential. For example, a 0.5 µm film charged at -0.85 V *vs.* RHE (-1.65 *vs.* Hg/HgO) to an initial charge level of 56 mC cm^{-2} retained 23 mC cm^{-2} after standing at open circuit for 5 minutes despite the fact that the self discharge current is more than 1 mA cm^{-2} at the starting potential.

Given that the time constant is a ratio between charge and current, it may be argued that thicker films may give longer storage times – e.g. extrapolating to a 130 µm film we would have half-lives of about 1000 minutes, which would certainly be acceptable in an ultra-high energy supercapcitor. The extrapolation does, however, depend on the relation between the HER kinetics and film thickness, which is presently not known for these nanostructured materials; we do not know whether a sustained HER can occur in such small pores. Another unknown factor is the effect of the substrate material or current collector. In this case we used fluorine-doped SnO_2; this may not be an ideal choice; further work should identify a more suitable current collector.

Figure 4.3.9 displays the result of three open circuit discharge profiles under different aerobic systems. The first where the system is purged with argon for an hour to remove oxygen gas dissolved in the electrolyte. The second is when air was introduced into the cell for two minutes. Immediately it becomes obvious that a higher concentration of dissolved oxygen will increase the rate of self-discharge; further confirmed by the final introduction of pure oxygen into the cell. To examine the charge-voltage relationship a series of discharges at different points (times) along the voltage profile were carried out (Figure 4.3.10) the charge extracted is plotted *vs.* the OCV from which the discharge began. (Figure 4.3.11)
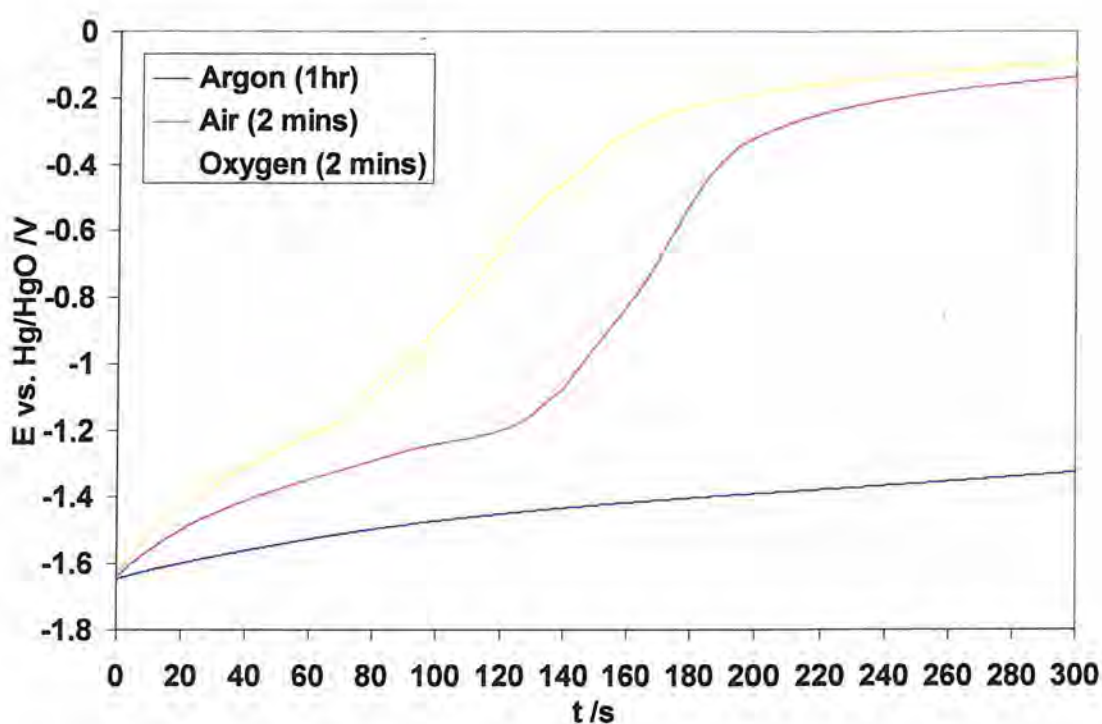
Figure 4.3.9: The open circuit discharge profile of a 0.5 μm B78 film charged at -0.85 V *vs.* RHE (-1.65 V *vs.* Hg/HgO) under different aerobic conditions.
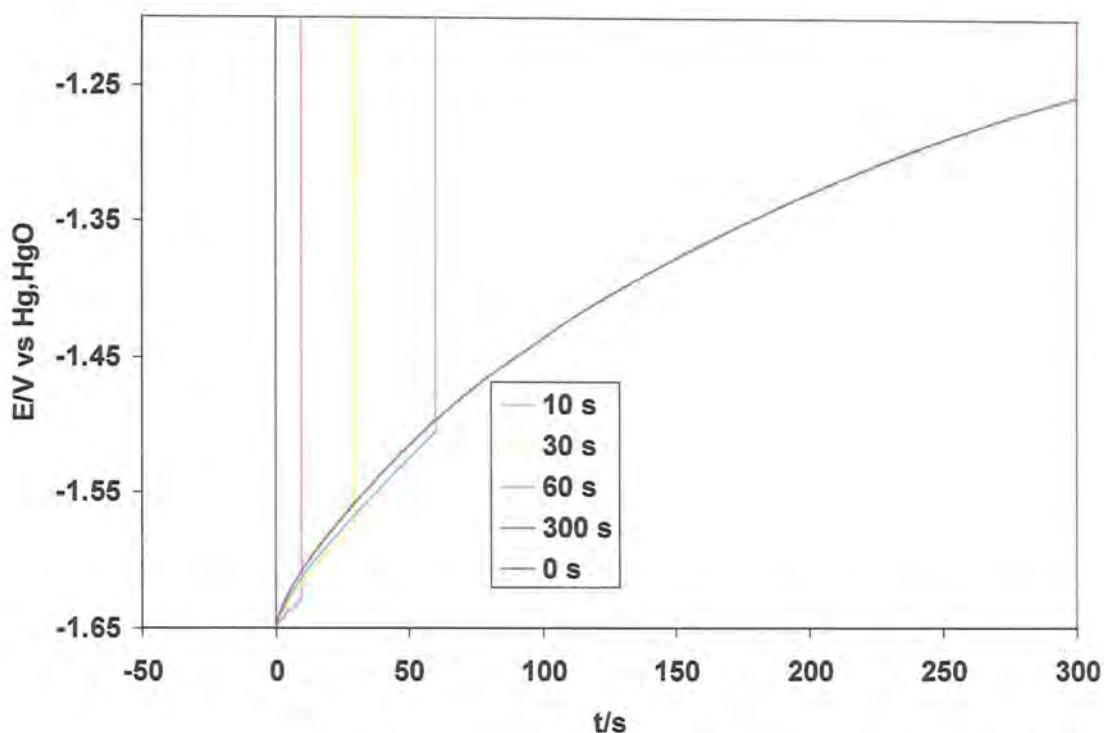
Figure 4.3.10 The open circuit discharge profiles of a 0.5 μm B78 film charged at -0.85 V *vs.* RHE (-1.65 V *vs.* Hg/HgO) then discharged under potential step at different time intervals.
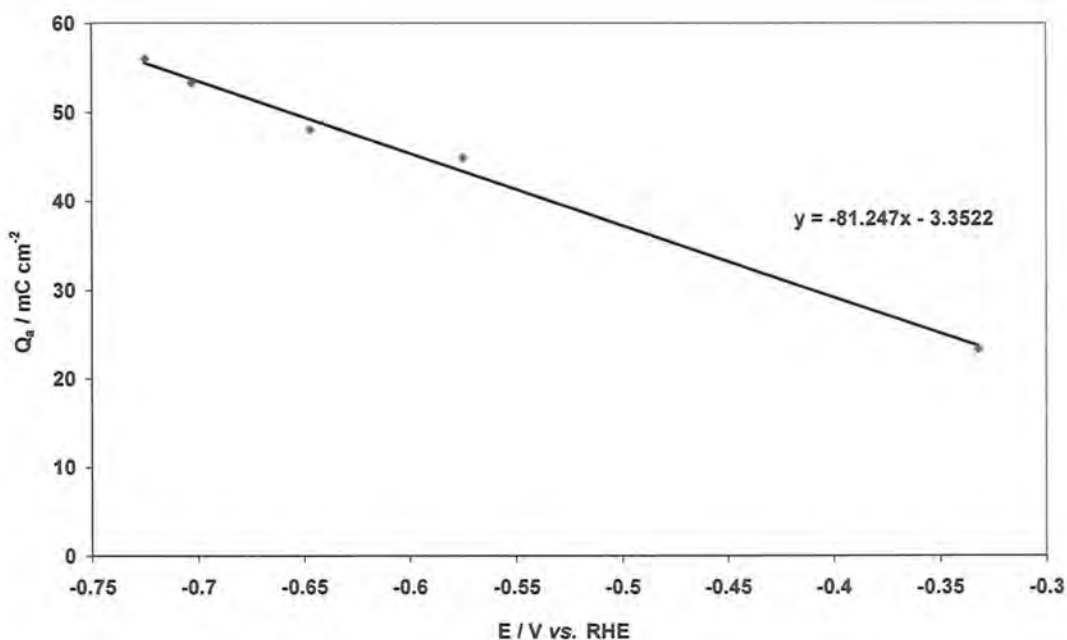
Figure 4.3.11 Charge obtained from the extraction of lithium at different times/OCPs on the self-discharge curve after a potential step to +0.45 V *vs.* RHE for a 0.5 μm B78 film.

Figure 4.3.11 shows that the OCP is proportional to the charge stored within the film. This relationship can be used to investigate the self-discharge using the Cottrell equation: $j = t^{-1/2}$ where j = current density and t = discharge time.

This can be integrated to $Q = t^{1/2}$ where Q is charge in coulombs.

Because charge is broadly proportional to voltage we plot the integrated form of the Cottrell equation $V = t^{1/2}$ in Figure 4.3.12 for a complete open circuit discharge. The profile of the discharge is linear which fits a diffusion-controlled process of some dissolved gas (possibly residual oxygen), deviation from the linearity only occurs at the start of self-discharge. This can be explained as there is a low concentration of oxygen; the cell has just been subject to high overpotentials and the oxygen has been consumed close to the electrode.
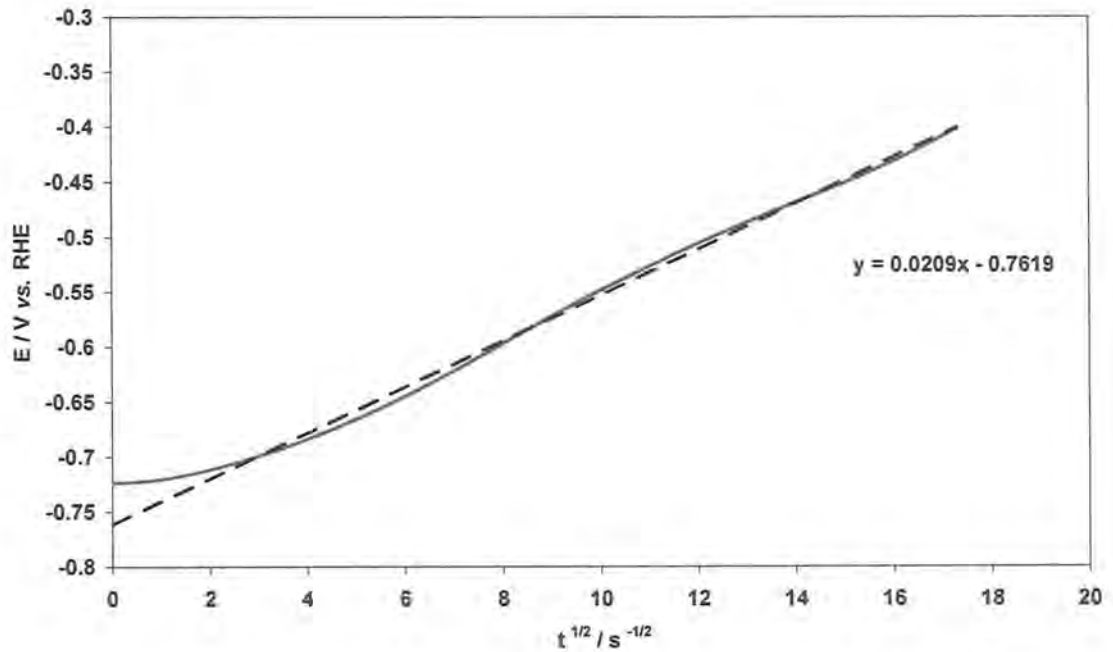
Figure 4.3.12: Plot of the open circuit discharge profiles of a 0.5 μm film charged at -0.85 V *vs.* RHE (-1.65 V*vs.* Hg/HgO).

4.3.2.2   Rate performance.
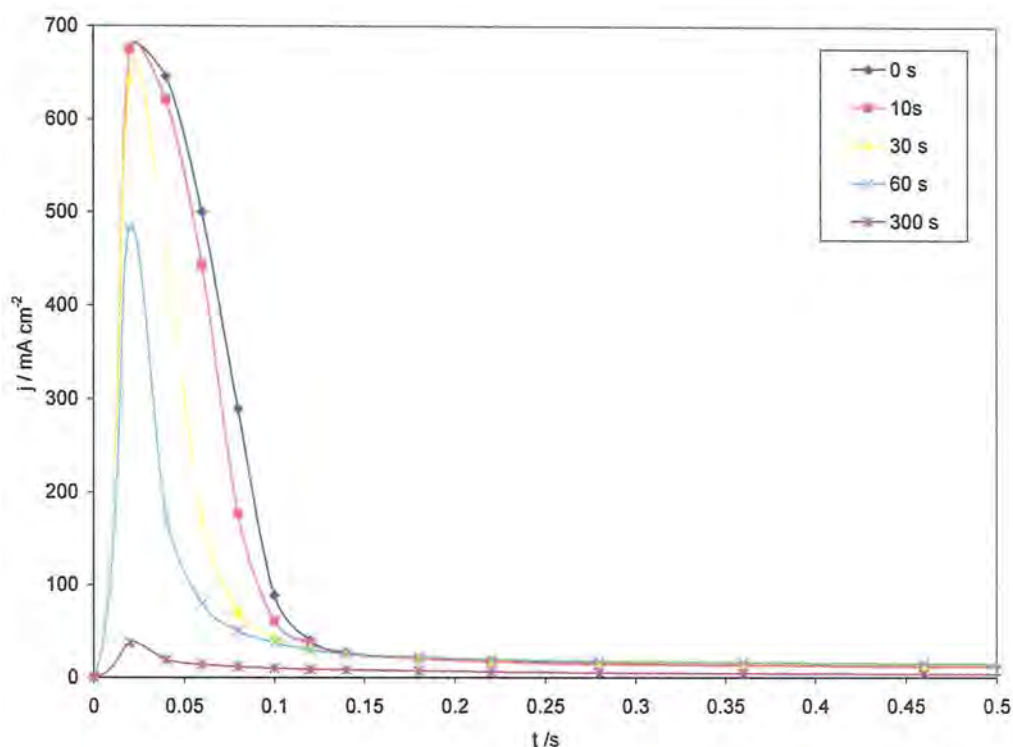
Figure 4.3.13: Potential step discharge of a 0.5 B78 μm film at various time intervals during open circuit discharge. The film was each time pre charged at - 0.85 V *vs.* RHE for 30 s (-1.65 V *vs.* Hg/HgO) then discharged at + 0.4 V *vs.* RHE.

After the potential step discharge 56, 52, 49, 47, and 23 mC cm^{-2} were extracted after 0, 10, 30, 60 and 300 s respectively. The impressive current pulse obtained of around 0.7 A cm^{-2} for the 0.5 μm film demonstrates the fast kinetics for extracting lithium from the TiO$_2$. This discharge however seems to split into two different processes. The first is extremely fast with around half of the charge ~30 mC extracted inside the first 0.1 s. It seems likely that this can be attributed to extracting lithium from the surface sites[72] where solid state diffusion has no time to affect the discharge. After the initial current spikes there is a still another 25 mC of charge which is extracted at current densities < 10 mA cm^{-2}. This is likely to be limited by the solid sate diffusion of lithium ions from within the wall of the TiO$_2$. The electrochemistry of these processes for nano size TiO$_2$ is discussed in 5.4.2.
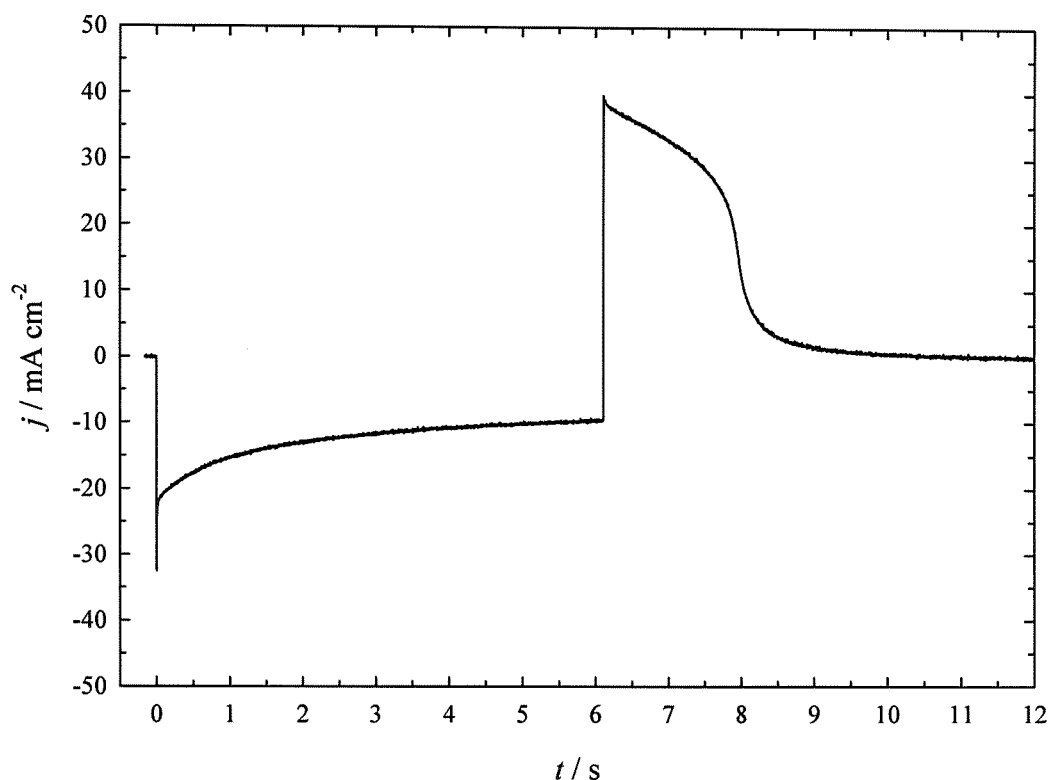
Figure 4.3.14: Potential step charge/discharge cycle of a 1.3 μm I$_l$ TiO$_2$ film charged for 6 s at –0.85 V *vs.* RHE and discharged for 6 s at +0.45 V *vs.* RHE in de-oxygenated 1 M aqueous LiOH at 25 °C.

Figure 4.3.14 shows the result of a potential step charge/discharge experiment performed on the 4-dip (1.3 μm) nanostructured film, in which the current was 40 mA cm^{-2} and 65 mC cm^{-2} was released within 3 s. Although the total charge released is more than the 0.5 μm film the current peak is not as impressive, however this may be because of the resolution of the potentiostat, which was recorded on the Solatron and not VMP2. The charge extracted is < 100 mC cm^{-2}, however, this result is most significant when we realise that it is for a macroscopically planar electrode surface, so that much larger current densities can be expected for electrodes in which the same film thickness is distributed over a microscopically roughened current collector as in modern battery electrodes. Accordingly, since the actual TiO$_2$ film thickness here was only 1.3 μm, we can predict (conservatively) an external current density of 5 A cm^{-2} should be possible for a typical battery electrode thickness of 130 μm. However a projection using the results from the 0.5 μm film provides an estimate of the current density >100 Acm^{-2}.
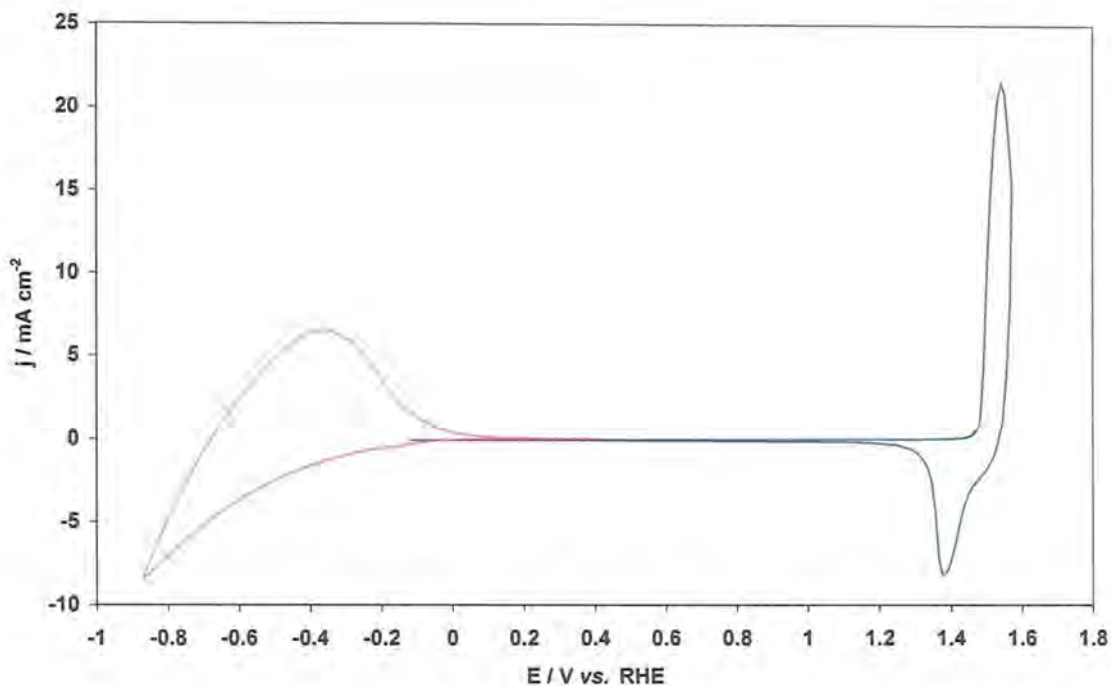
Figure 4.3.15: Cyclic voltammetry of both nanostructured TiO_2 (pink) and $Ni(OH)_2/NiOOH$[77] (blue) at 20 mV s^{-1} in de-oxygenated 1 M aqueous LiOH, 25 °C.

Cyclic voltammetry of both nanostructured TiO_2 and $Ni(OH)_2/NiOOH$ are superimposed in Figure 4.3.15and show the nanostructured NiOOH electrode in LiOH displays very high current densities as previously reported in KOH, allowing a coupling of this electrode with TiO_2 as in Eq. 4.3.1:

$$TiO_2 + Ni(OH)_2 + xLiOH \rightleftharpoons Li_xTiO_2 + NiOOH_{(2-x)} + xH_2O \qquad \text{Eq. 4.3.1}$$
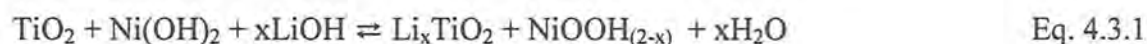
The potential profile of the cell during discharge at constant load appears in Figure 4.3.16. An open circuit potential of 1.75 V is observed, with an average cell potential of 1.6 V for most of the 51 mC cm^{-2} discharge. (These potentials are well in excess of Ni/MH and Ni/Cd systems which discharge between 1.0 and 1.3 V)[116]. A specific energy of 90 Wh kg^{-1} can be calculated, based on the mass of the charged electrodes. Albeit a modest energy for a battery, this would be an outstanding value for a supercapacitor, especially if accompanied by the high power densities indicated in these preliminary results. However, further work is required to establish whether the storage times can be increased to acceptable values.

4.4 Conclusions

Lithium ion insertion in TiO_2 from aqueous LiOH has been facilitated by a nanostructured electrode; in spite of the parasitic HER. It also demonstrates fast kinetics required of a supercapacitor electrode. A limiting composition of $Li_{0.27}TiO_2$ was obtained at a potential of -0.85 V *vs.* RHE beyond which the HER caused a rapid self-discharge. An exchange current for the HER was extrapolated to between 10^{-9} and 10^{-10} A cm^{-2} based on the external area, or between 10^{-11} and 10^{-12} A cm^{-2} based on the nanostructured area.

The concept of an all-nanostructured supercapacitor, with nanostructured NiOOH as the positive electrode and LiOH as the electrolyte, was shown to have an average potential of 1.6 V and a specific energy density of 90 Wh kg^{-1}. Thicker films produced in this work however were prone to cracking limitations of the preparation method were detailed in 3.2.3 and could not be cycled successfully. Therefore, as scale up of the thin films was not possible the only was to cycle more material was to use the nanostructured powders prepared by the same method. Sintered powders however, failed to produces significant insertion currents. Consequently, attention turned toward cycling the powders in a composite electrode structure as a high rate non-aqueous negative.

Chapter 5

Nanostructured TiO₂

Investigation as high rate lithium battery electrode

5.1 Introduction

Nanostructured materials meet the demand for electricity storage devices capable of delivering a high power density as well as a high energy[74]. Several nanostructured forms of TiO_2 have been investigated as the negative electrode in lithium ion batteries[113, 116], and it was recently noted that nanotubes[117] and nanowires[69] allow unusually high discharge rates. This chapter investigates the high rate performance of liquid crystal templated TiO_2 powders and compares the results with other TiO_2-based nanomaterials, as they should also yield impressive rate performance. This brief introduction will set the context for subsequent discussion.

Some capacity values of Lithium Titanates:

Anatase -165 mAh g^{-1}

$Li_4Ti_5O_{12}$ 175 mAh g^{-1}

TiO_2-(B) nanotubes/wires 250-300 mAh g^{-1}

5.1.1 The insertion mechanism of lithium in Anatase

When intercalated with lithium, as required for battery applications, TiO_2 anatase undergoes spontaneous phase separation into lithium-poor ($Li_{0.01}TiO_2$) and lithium-rich ($Li_{0.6}TiO_2$) domains on a scale of several tens of nanometres.[118] During discharge, batteries need to maintain a constant electrical potential between their electrodes over a range of lithium concentrations. The two-phase equilibrium system in the electrodes provides such a plateau in potential, as only the relative phase fractions vary on charging (or discharging) of the lithium. Just as the equilibrium between a liquid and a vapour is maintained by a continuous exchange of particles between the two phases, a similar exchange is required to maintain equilibrium in the solid state.[119]

5.1.2 How nanomaterials can change bulk properties.

Nanostructuring of electrode materials, is historically carried out to shorten diffusion lengths and hence improve rate performance. Nanoparticles have also shown dramatic changes to their intrinsic properties[2, 4], influencing both ionic and electronic charge transport relevant in electrochemical processes.[1, 120]

Bruce, recently reported extra capacity in TiO2-B nanotubes / wires where, after insertion into the bulk, a further pseudocapacitive charging process was observed at voltages lower than that of anatase-titanate plateau.[69] This pseudocapacitive process was also observed by Kavan for mesoporous P123 templated thin films (200-500 nm) in slow scan rate voltammetry (0.1 mVs^{-1}) and characterised by two so-called S-peaks with formal potentials of 1.5 and 1.6 V *vs.* Li.[103] Another characteristic feature was an A-peak, (anatase) formal potential 1.8 V *vs.* Li, which scaled with the square root of scan rate; characteristic of an irreversible diffusion controlled process.

These S- features were seen to scale with scan rate; indicative of a capacitive process and are attributed to surface sites on the 'mesoporous skeleton'. These features were however poorly reproducible and disappeared on heating (Sintering reduces the surface area).[72, 103] Anatase TiO_2 has shown strong particle size dependent electrochemistry and insertion capacity. The above phenomena can be explained by carefully considering how the crystal structure and insertion behaviour will change as particle is changed from micro to the nano scale[121] this forms a large part of the discussion in 5.4.4.

5.2 Background and Objectives

Nanomaterials have been studied as potential candidates for improving the rate performance and consequently the power densities of lithium batteries, (as discussed in 1.6.2.), but have been largely investigated in the form of thin films[72, 122]. Chapter four in this thesis demonstrated exceptional rate performance of thin films (≤ 1.3 µm) of nanostructured TiO_2 in both aqueous and aprotic media. Synthesising films of a thickness great enough to be utilised in a battery or ultra capacitor device was however, ultimately unsuccessful.

This chapter seeks to extend the investigation of this high rate performance; by examining the nanostructured TiO_2 in a 'thick' composite electrode such as that used in conventional battery. The nanostructured TiO_2 is prepared in 'bulk' using a modified preparation described in chapter three.

The rate-determining step concerning diffusion through such an electrode is considered diffusion in the solid-state of the active material ($D \sim 10^{-14-17}$ cm^2 s^{-1}). The driving force behind nanostructuring electrode materials is therefore to reduce the particle size of the active material and hence the diffusion distance within the solid state; resulting in improved rate performance. Composite electrodes approaching commercial thickness (~ 100 µm) containing a conducting additive, (carbon) binder, as well as micron sized particles of active material produce a complicated diffusion picture which needs to be considered. The performance is a reflection of not only the active material but also the electrode properties such as thickness; the effect of diffusion through the cross section of the composite electrode or solid-state diffusion within the active material may be the rate-determining step. It is important to note the complication of using relatively 'thick' (10-150 µm) composite electrodes in high rate testing. In such cases large geometric specific current densities are inevitable, this can cause experimental complications, particularly the ohmic drop across the cell. This chapter will also demonstrate the importance of experimental technique in examining high rate performance of nanomaterials. The aims of this chapter may be summarised in three broad parts:

- Examine the rate performance of nanostructured TiO_2 in a composite electrode.
- Optimisation of experimental technique for high rate testing.
- Evaluation of rate determining step for diffusion within a composite electrode.

5.3 Experimental

5.3.1   Mesoporous powders

The term nanostructured is widely used in the literature and has become somewhat ambiguous when referring to different forms. In this chapter, reference is made to both 'nanostructured' and 'nanoparticulate' powders.   Our nanostructured powders are typically micron sized (2-30 μm) particles with an internal porous nanostructure; where nanoparticulate is in the conventional sense; nano sized particles.

This chapter is primarily concerned with testing the rate performance of our nanostructured TiO_2.   However, for comparison, other Titanates were studied, a summary of which appear in Table 5.3.1. All samples except nanostructured TiO_2 were obtained commercially

Material	Origin	Part. size	BET
			m^2g^{-1}
TiO_2 micro particles	Degussa P25	0.3-1.5 μm	50
TiO_2 nano particles	Aldrich, Anatase	12 nm	180
TiO_2 nanostructured	EISA, F127 P123 B78	2-30 μm	40-180

Table 5.3.1A Summary of the physical properties of Titanates used in this chapter.

Nanostructured TiO_2 powders were prepared by evaporation induced self assembly (EISA)(as discussed in detail Chapter 3)[43, 48, 111].   For this chapter primarily nanostructured TiO_2 powders templated from a I_1 F127 were made into composite electrodes. (That is powders templated with F127 surfactants to yield a cubic (I_1) porous morphology.) BET was used to calculate the surface area and other structural methods were used as set in Chapter 3.   This chapter focuses on the electrochemical characterisation.

5.3.2   Composite Electrode Preparation

In commercial battery electrodes, a composite electrode will also contain (in addition to the active material, AM) a conductive additive such as carbon and some form of binder to hold the components together. Nanostructured TiO_2 was in the form of a finely ground powder, (section 3.2.2) other active materials were used as received. Two methods were used to prepare composite electrodes. Pressed or Doctor Bladed films were prepared depending on the use of either a solid PTFE or soluble PVDF binder respectively. Acetylene carbon black (ACB Shawinigen, 100% compressed) as the conductive additive was used in both. From the resultant thin film(s) it was then possible to cut a number of electrodes.

5.3.2.1   Pressed Films by Roll Milling

Pressed films prepared from dry mixing of the individual components enable a high degree of repeatability enabling a homogeneous composition of the three electrode components. This facilitates both good electrical conductivity and mechanical properties, thus, it was used predominantly in all the electrochemical testing. A solid powder binder Polytetrafluoroethylene PTFE (Teflon®, C6-N, DuPont) and Acetylene carbon black (ACB Shawinigen, 100% compressed) were mixed with the active material (AM). The exact method of mixing and pressing or milling the composite films is important to achieve a homogenous distribution of all three components of the electrode material. All mixing used a pestle and mortar.

1. Mix up fine powders of Active Material with ACB using micro-spatula until evenly distributed.
2. Add downward pressure using pestle for ~3 minutes until an extremely fine powder is achieved.
3. Add the binder to the powder until it is evenly distributed throughout the mixture.
4. Mix in the binder slowly in a circular motion before applying strong downward pressure to bring the film together
5. Fold the mixture together using pestle and spatula and crush the components together, until a constant texture was produced (*i.e.* no cracks) with a rectangular lump ready for milling.

Films were then formed of regular thickness from the rectangular lumps of material by roll milling. A Durston Minimill (sheet area of 80 mm) was used to compress the composite into a thin film from which electrode can be cut, Figure 8. This technique allowed accurate preparation of films to a uniform thickness (150 μm-45 μm $^+/.$ 2 μm.) and ensures that a uniform compaction of the composite is obtained. (A micrometer was used for all thickness measurements.) From each of the films a number of pellets were cut using a standard size cork borer of 1.1 cm diameter; for each pellet; both the thickness and weight then recorded. Pellets were individually wrapped in foil, labelled and transferred into a Buchi TO-50 (vacuum oven) for at least 10 hours, at 130°C. After cooling samples were transferred to an argon-filled glove box for cell assembly and storage.

Figure 5.3.1: A Durston Minimill, as used for milling composite electrode films.[*123*]

5.3.2.2   Doctor Bladed films

Doctor Bladed films mean it is possible to produce films of a thickness below 40 μm, less than the thinnest achieved via role milling. The method involves dissolving the three components of the composite electrode in an organic solvent, spreading a thin film and allowing it to evaporate. In the absence of mechanical mixing, the binder must be both soluble and stable in the organic solvents. Polyvinylidene Difluoride, or PVDF-is a highly non-reactive and pure thermoplastic. A high purity battery specification PVDF-(Homopolymer) was dissolved in Dimethylformamide DMF, at 50 °C. The composite mixture was dissolved in (1:3 wt. %) solvent, with typically 0.5-8 g of active material. Two different compositions were used for nanostructured and nanoparticulate powders:

- Nanostructured comprised: AM 65%; ACB 25%; and PVDF 10%;
- Nanoparticulate comprised AM 60%; ACB 25%; and PVDF 15%.

Nanoparticulate composites needed more binder due to the difficulties in packing the low density nanoparticles together. After mixing for two hours at 50 °C the mixture was finally homogenised using a mechanical shaker. The mixture was then coated on 13 µm Al foils using a range of K-bars to produce a series of films from 60- 30 µm for the nanostructured and 20-5 µm for the nanoparticulate. The thickness of the former is limited by the particle or agglomorate size obtained from milling in a pestle and mortar. Consequently, the films cross sections will be non-uniform on microscopic level containing 'islands' which are detected by the micrometer. However, for the nanoparticulate the agglomerates are much smaller and smooth films can be obtained.

Films were checked for electronic conductivity by depositing an identical sample on a glass microscope slide, and calculated using sheet resistance measured with a four-point probe method (FPP). An acceptable electric conductivity of ~0.2 S cm^{-1} was achieved by having higher amounts of ACB (25 wt. %) to compensate for such a high amount of binder, (15 wt. %). Electrode pellets were cut and dried as the pressed pellets. The weight and thickness are quoted minus the contribution of the Al substrate. Details of all films used in this work can be found in the Appendix.

5.3.3 Electrode Thickness

Pressed pellets were produced over a range of 120-50 µm, the packing density is assumed constant throughout the film, when a constant pressure is applied. Pellets were cut using a controlled diameter, meaning any weight scatter is due to deviation in film thickness from the rolling method, such that, any deviation in the weight of pellet within a film is due to a small deviation in thickness. The density of each film at different thicknesses can be calculated from the average film weight and thickness. It can then be used to normalize the electrode thickness (µm$_{corr}$) with respect to the weight. These corrected values are listed in the appendix and are used for all thickness calculations and given thickness unless stated otherwise. The theoretical density (ρ_{Thero}) is calculated from the individual densities and proportions of the components of the composite electrode matrix. The volume fraction is the measured density divided by the theoretical density. The results appear in the appendix.

The density is inversely proportional to electrode thickness as expected; this is natural as the films become more compressed. The Aldrich nano-powder has a lower density, this is because the 12 nm nanoparticles do not compress as well, and they have

a much higher volume fraction ~ 40 % as compared to the nanostructured ~ 30 %. Pellet thickness can vary significantly from the observed film thickness. It is important to consider small differences in electrode thickness, e.g. a 5 μm deviation can, during high rate testing be expected to show a significant change to the electrode kinetics.

5.3.4   Electrochemical Cells

Electrochemical cells were prepared in an argon-filled glove box. (H_2O, O_2 < 1 ppm; Unilab from MBraun). Preparation of cells with a two and three electrode configuration is described below. A three-electrode configuration was developed to reduce the ir drop in high rate cycling.

5.3.4.1   Two-electrode cell.

This particular type of cell can be made of either brass or stainless steel, the former being employed in this work as it is known to be electrochemically inert at the voltages used. Advantages of these types of cell are that they are re-usable and that an even pressure is applied by adjusting the individual screws. The basic design of the cell is a base and a lid held together by three bolts. Into the base of the cell fits a spring onto which the current collector (a stainless steel disc) sits, the spring ensures a good contact between the electrodes and current collectors. The lid is the positive current collector and an O-ring provides an airtight seal. The components of the cell fit between these current collectors.

For cell assembly the lithium metal negative electrode was placed on the lower current collector. Lithium electrodes were pressed (again using a cork borer) from sheet lithium metal. Scraping off oxidised material from the surface with a spatula means a fresh electrode surface before rolling (to ~0.2 cm thick) with a glass vial to ensure a smooth shiny surface. The lithium electrode was cut (diameter 1.1 cm^2) and flattened before being introduced into the cell. To create a barrier between the two electrodes and prevent short circuits, two glass-fibre separators (cut from Whatman, GF-F glass micro-fibre filters, thickness 0.42 mm) were imbibed with the chosen electrolyte, *ca.* ~10 drops of 1 M $LiPF_6$ in EC:DMC 1:1 wt./wt. (provided by Merck). Where Ethylene carbonate (EC) and dimethyl carbonate (DMC).

The positive electrode was positioned centrally on top of the separators and negative electrode before the positive current collector or lid was then fastened, taking

care not to disrupt the alignment of the cell components. During the process of sealing the cell it is essential that an even pressure be maintained and that no contact made between the base and lid of the cells to prevent short circuits. On completing the assembly of the cell the open circuit potential was recorded. (~ +3.0 V *vs.* Lithium if no short has occurred) The cell was lastly wrapped with parafilm to provide extra integrity to the seal.
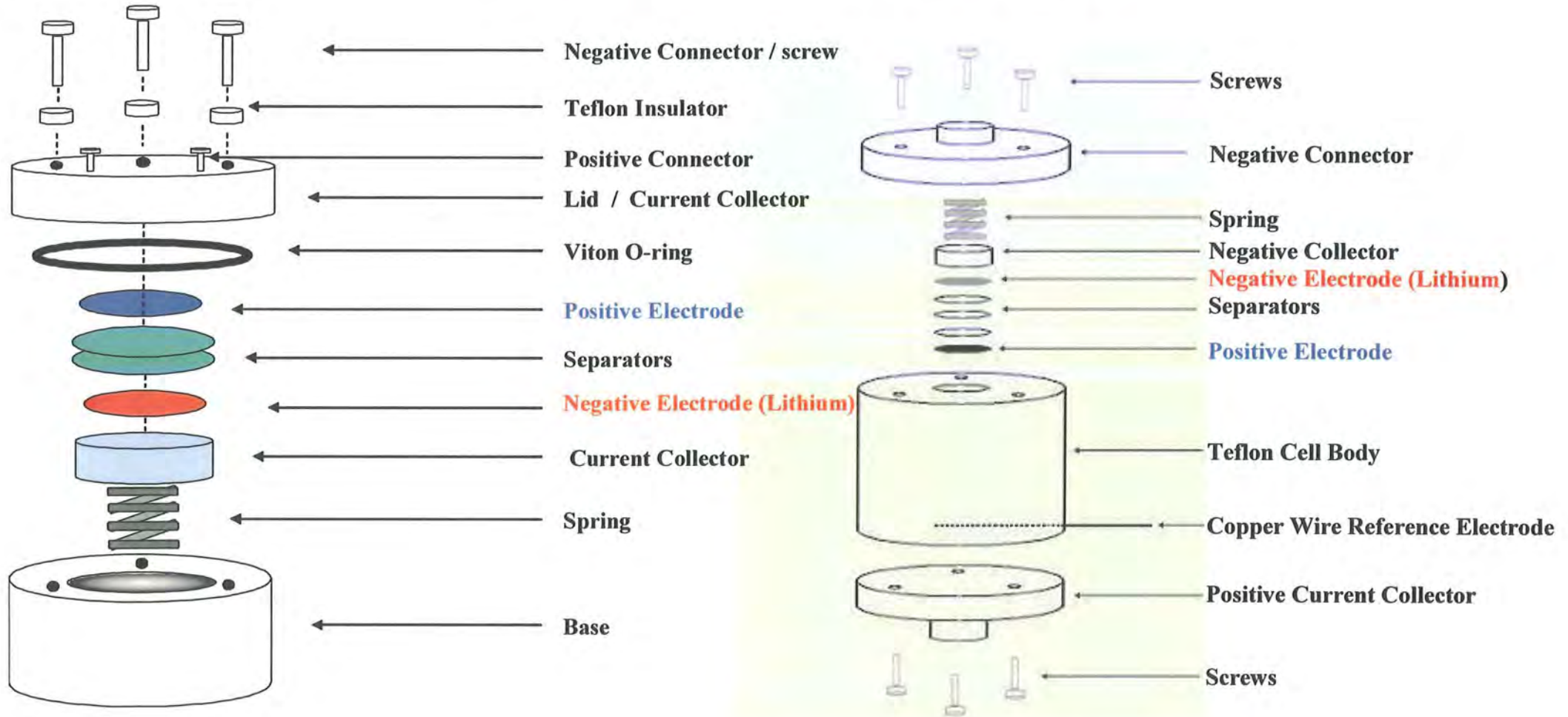
Figure 5.3.2: Schematic of both Two-electrode (2 electrode.) and Three electrode (3 electrode.) cell configuration .

5.3.4.2   Three-electrode cell.

A three-electrode cell was prepared using a Teflon® housing, a stainless steel base and an Aluminium lid. The major difference is the Teflon® allows a small hole ~100 μm diammeter to be drilled; through which a Cu wire with a 50 μm diameter was inserted; on which Li was plated prior to cycling and used as a reference electrode. The cell was assembled as with the stainless steel cell but an extra separator was used to sandwich the reference electrode one separator away from the positive electrode and two away from the lithium negative. It was critical to both isolate and to place the R.E. at the correct height to prevent short circuits. The Cu wire was plated with Lithium at -0.150 mA for 50 minutes for around a 20 μm coating which proved a stable electrode for a period of ~2 weeks. It is also possible to re-plate if necessary.

5.3.5   SEM of composite electrodes and powders

Samples for SEM were taken from both powders and made using the standard preparation techniques set out in the previous chapters. Low-resolution work was carried out on the Philips XL-30 SEM. High-resolution images were taken using the FEG-SEM after sputtering the poorly conductive TiO_2 samples with a few nm of carbon to prevent accumulation of charge on the surface.

5.3.6   Electrochemical Testing Regime

All electrochemical studies were performed using a 16-channel potentiostat (VMP2 Princeton, Applied Research; Biologic-Science Instruments). Cells were connected as specified above, and subject to a standard testing regime (Figure 5.3.3). The major part of the high rate testing is at constant current. Two variations of this method are set out below:

1. *Continuous Cycling,* denoted CC where the charge and discharge follow immediately with no rest period in between cycles. (some cycling is interrupted for AC impedance) Cycling at different current densities resulted in the electrode being under different starting conditions for charge or discharge, e.g. at high rates the electrode would not be fully charged or discharged, or indeed that concentration profile within the electrode would not be uniform. For careful study of electrode properties, a new testing procedure with time for equilibration is outlined below.

2.*Continuous Cycling with Equilibration,* denoted, CCE.

In this method, the end of each charge/discharge was followed with a period held at the charge or discharge potential limits (2.5-3.0 or 1.0-1.2 V *vs.* Li/Li$^+$). This enabled equilibration of the concentration profile within the electrode, and secondly ensured that the electrode was fully charged or discharged before subsequent cycles.

3- Electrode   2- Electrode

1. AC Impedance in 2-electrode. Configuration at OCV. (Blocking)

2. Lithium Plating of Cu reference electrode -0.150 mA cm^{-2} for 50 mins.

3. AC Impedance in 3-electrode. configuration

4.Constant Current cycling: CC or CCE
The cell was subjected to a series of mass specific currents for 5 cycles at voltage limits of 1.0 to 3.0 V *vs.* Li/Li$^+$. From high to low current density: 3000; 2000; 1000 500; 200; 100; 50 mA g^{-1}.*

Figure 5.3.3 Standard Electrochemical testing Regime. *In some experiments cycling was interrupted for AC impedance measurements.

5.4 Results and Discussion

5.4.1 Lithium Insertion in Nanostructured TiO_2 in a composite electrode

Prior to high rate testing, cycling at low rates was employed to obtain a thermodynamic capacity and examine the electrochemical profile of our nanostructured material. At a specific current 10 mA g^{-1} an impressive 300 mAh g^{-1} is obtained on the first discharge corresponding to a stoichiometry of $Li_{0.9}TiO_2$. 240 mAh g^{-1} is extracted on the first charge $Li_{0.7}TiO_2$.(Figure 5.4.1) this case confirms some additional reduction beyond the $Li_{0.5}TiO_2$ reported for anatase.
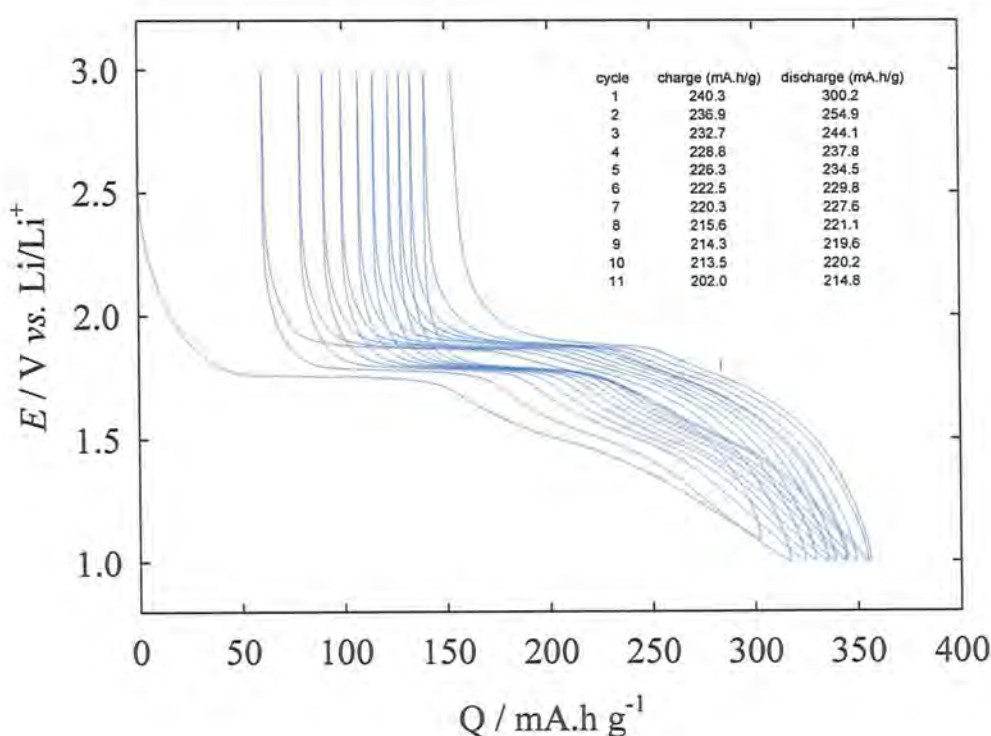
Figure 5.4.1: F127 TiO_2 cycled at 10 mAg^{-1} in 1 M LiPF6 in 1:1 EC:DMC. 100 um 80 % AM 20 % (two- electrode cell KS2) Note that the 1st discharge is prematurely ended ~150 mV before the other cycles.

In bulk anatase materials the charge is mainly obtained from a plateau at 1.78 V *vs.* Li/Li$^+$ which is attributed to the two-phase insertion of lithium, forming lithium poor Li$_{0.01}$TiO$_2$ anatase and lithium rich Li$_{0.5}$TiO$_2$. In Figure 5.4.1 the insertion shows a long monotonous potential decrease on the first discharge, and not on subsequent cycles. This would indicate a stoichiometry greater than Li$_{0.5}$TiO$_2$. Extra capacity on the first discharge is often rationalised by the reduction of surface groups, *e.g.* –OH, however, Tarascon *et al[116]* recently described this region as a characteristic feature of high surface area titanium oxides.

Decreasing the particle size can affect the insertion properties. The extended capacity in this region is rationalised by the formation of an extended solid solution domain, allowing 0.014 Li for bulk to 0.15 Li per TiO$_2$ for ~200 nm particles. This particle size effect can be explained by the stabilisation of nanoparticles due to increased surface energy and indeed the presence of this solid solution has been confirmed by both X-ray and neutron diffraction.[*121*] One might expect our nanostructured TiO$_2$ to extend this region further on account of even smaller particles of 10-15 nm, and indeed, we see 60 mAh g^{-1} corresponding to a stoichiometry of Li$_{0.18}$TiO$_2$. This feature is not completely reversible and accounts for some of the capacity loss on the first charge discharge indicating that Li$^+$ may be trapped in these sites. On the second and subsequent cycles, the solid solution region corresponds to a reversible charge of 25 mAh g^{-1} equivalent to 0.075 Li per TiO$_2$. The anatase plateau seems to account for less than Li$_{0.5}$TiO$_2$, which can be explained due to the increased surface area (163 m^{2}g^{-1}), which means that the interstitial octahedral sites in the 'bulk' crystal lattice have been reduced at the expense of surface sites.

Generally increasing the surface area of a material can induce a substantial capacitive component to the overall capacity. The main effect of decreasing the crystallite size is to broaden the type of site and energy levels accessible in the materials, thus yielding a broad voltage distribution for the electrochemical reaction to take place. These surface sites can be observed in a long sloped region below 1.78 V *vs.* Li/Li$^+$ which extends to the end point of discharge selected at 1 V *vs.* Li/Li$^+$. This sloped region is discussed in detail below (Section 5.4.2)
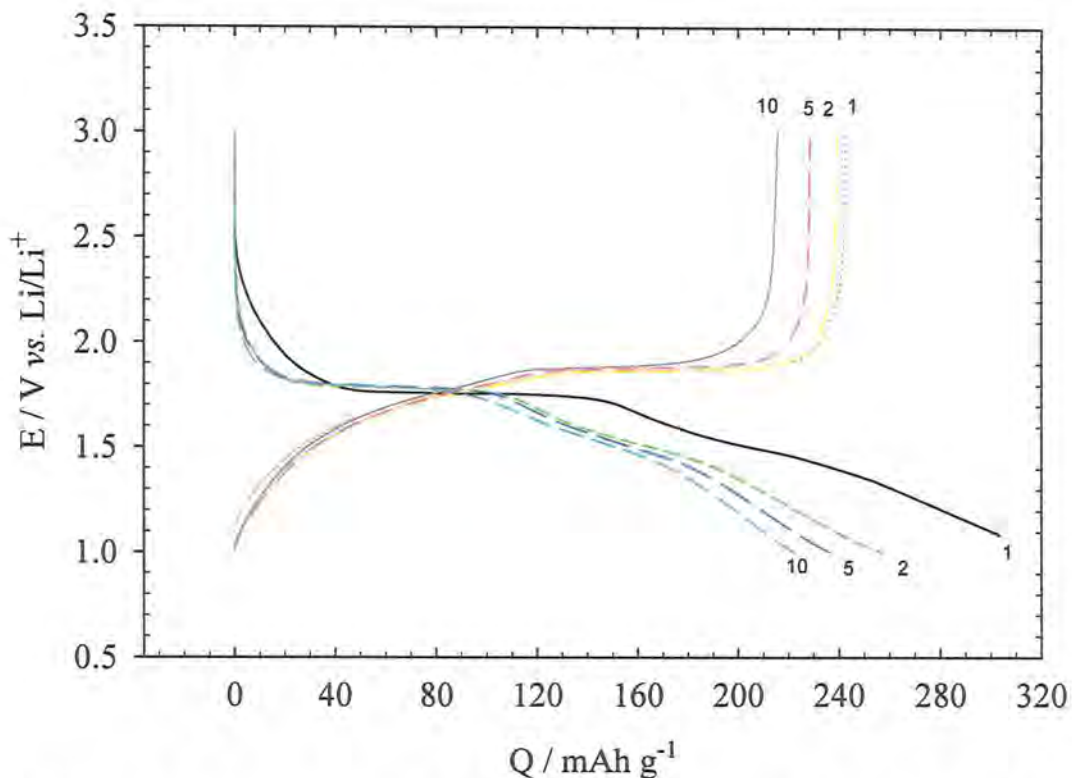
Figure 5.4.2: F127 TiO_2 cycled at 10 mAg^{-1} in 1 M $LiPF_6$ in 1:1 EC:DMC. 1.0.- 2.5 V *vs.* Li , cycle number displayed. (110 μm thick composite; 80 % AM, 15 % ACB, 5 % PTFE in a 2 electrode cell)

Using highly divided materials is clearly beneficial for cyclability and our nanostructured TiO_2 has well in excess of 200 mAh g^{-1} after 10 cycles, at 10 mA g^{-1} After high rate testing, an electrode was cycled at 50 mA g^{-1}, displayed in Figure 5.4.3 ~ 200 mAh g^{-1} is observed for ~50 cycles, after 21 days the electrolyte dried, which was observed by a huge increase in the ir drop, therefore the rapid capacity decline is not due to dislocation or performance of the active material. The cell is also likely to be subject to the formation of lithium dendrites, which are more readily formed from high rate plating and stripping of lithium on the lithium negative electrode.
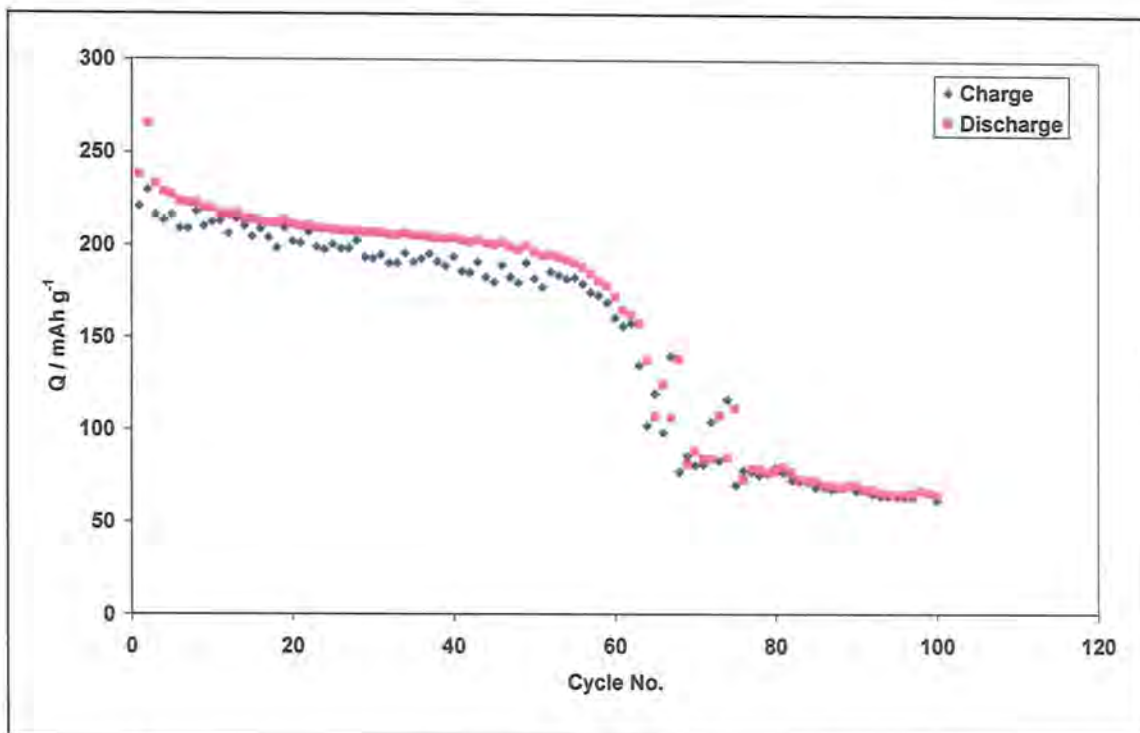
Figure 5.4.3: F127 TiO$_2$ cycled at 50 mA g^{-1} in 1 M LiPF$_6$ in 1:1 EC:DMC. (110 μm thick composite; 80 % AM, 15 % ACB, 5 % PTFE in a 2 electrode cell n.b. cell has been subject to high rate testing.)

5.4.2   The effect of particle size on the insertion into anatase TiO$_2$

The extra pseudocapacity, in tandem with exceptional rate capability reported above is observed in many other forms of nano TiO$_2$; including anatase as well as other titanium oxide phases, such as spinel, rutile and recently in TiO$_2$-B nanotubes/wires.[99, 124, 125] It not easy to identify any features which may occur in this voltage region using galvanostatic cycling, therefore slow scan rate cyclic voltammetry of the nanostructured material was carried out.

Figure: 5.4.4, yields a result analogous to Zukalova *et al.* (for mesoporous P123 templated thin films, 200-500 nm in thickness).[126] For such thin films it was possible to resolve two so-called surface peaks, (S-peaks) with formal potentials of 1.5 and 1.6 V *vs.* Li/Li$^+$. Also observed was an A-peak (anatase) formal potential 1.78 V *vs.* Li, which scaled with the square root of scan rate; characteristic of an irreversible diffusion controlled process.

128
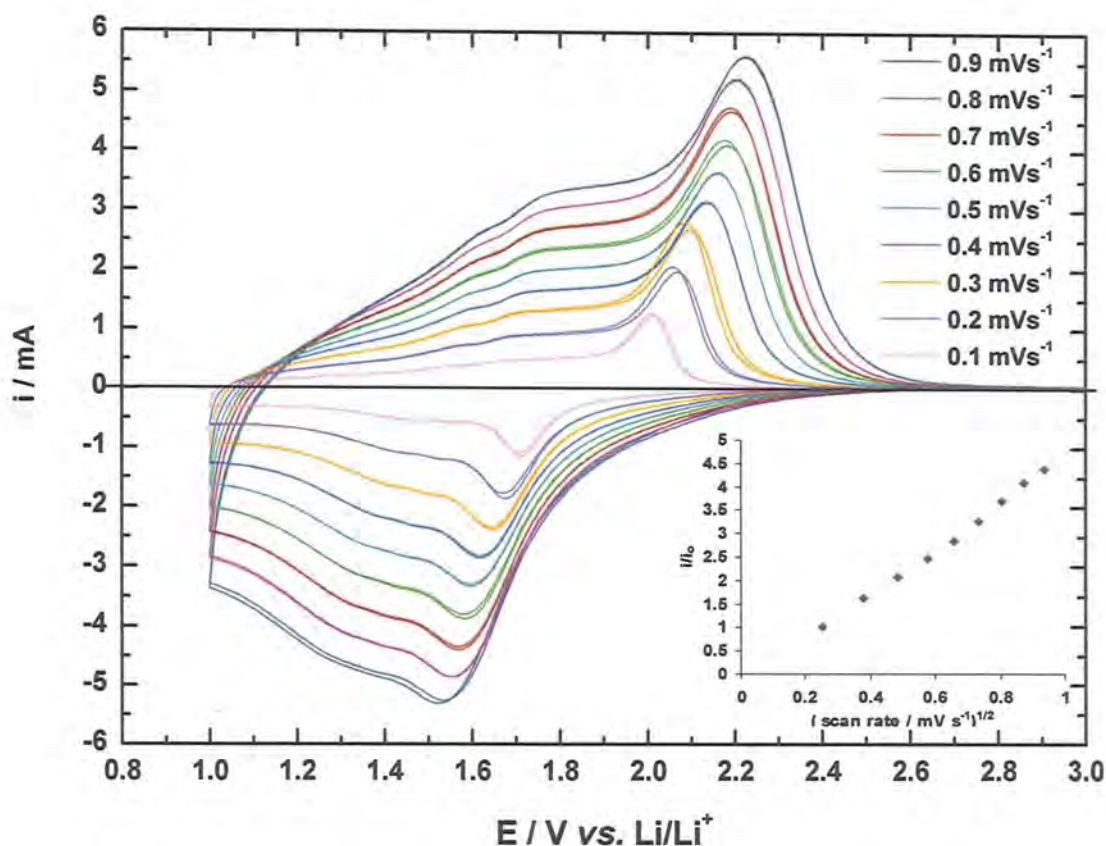
Figure: 5.4.4 Cyclic voltammetry of F127 TiO_2 from 1.0-3.0 V *vs.* Li at 0.9-0.1 mVs^{-1} (2 cycles at each scan rate) in 1 M $LiPF_6$ / 1:1 EC:DMC, 57 µm. The insert plots the peak anodic current normalised by the slowest scan rate (0.1 mV s^{-1}) against the square root of scan rate.

These S- features scaled with scan rate; indicative of a capacitive process and are attributed to surface sites on the 'mesoporous skeleton'. These features were however poorly reproducible and disappeared on heating. Our bulk 45-100 µm nanostructured composite electrode material also exhibits extra capacity at lower voltages as can be seen in

Figure: 5.4.4. However S-peaks or inflections are obscured by long tails after the peaks because our sample in this case was a thick composite electrode rather than a thin film. The A-peak corresponds to only to the two-phase insertion of Li into anatase.

At low scan rates anodic peak current *vs.* square root of scan rate scales linearly (insert.from Figure: 5.4.4) This corresponds to a reversible diffusion controlled process here the diffusion of lithium ions in the solid walls of the nanostructure. Note, at higher scan rates a capacitive contribution may slightly affect the gradient as we are using a high volume of material as opposed to thin films. The gradient allows determination of diffusion coefficient using Eq. 5.4.1, a form of the Randles-Sevcik equation[103, 127]:

$$i_p = 0.4958 \; nFAC \; (D\alpha nF\upsilon / RT)^{1/2}$$

Eq. 5.4.1

A is the interfacial area, cm^2, C the bulk concentration is 0.024 mol cm^{-3} for x = 0.5 for anatase (since we only consider the anatase region), and α is charge transfer coefficient of Li ($\alpha \sim 0.5$).

The effective interfacial area can be obtained from BET surface area and the weight of active material.

A = 145 m^2g^{-1} x 6.50 mg = 9425 cm^2

Gradient $= \sim 4.0$ $AV^{-1/2}s^{1/2}$

$$\underline{D = \sim 5 \; x \; 10^{-16}cm^2s^{-1}}$$

This value is similar to that reported for extraction of Li^+ from a thin film of mesoporous anatase $\sim 10^{-16}cm^2s^{-1}$.[103]
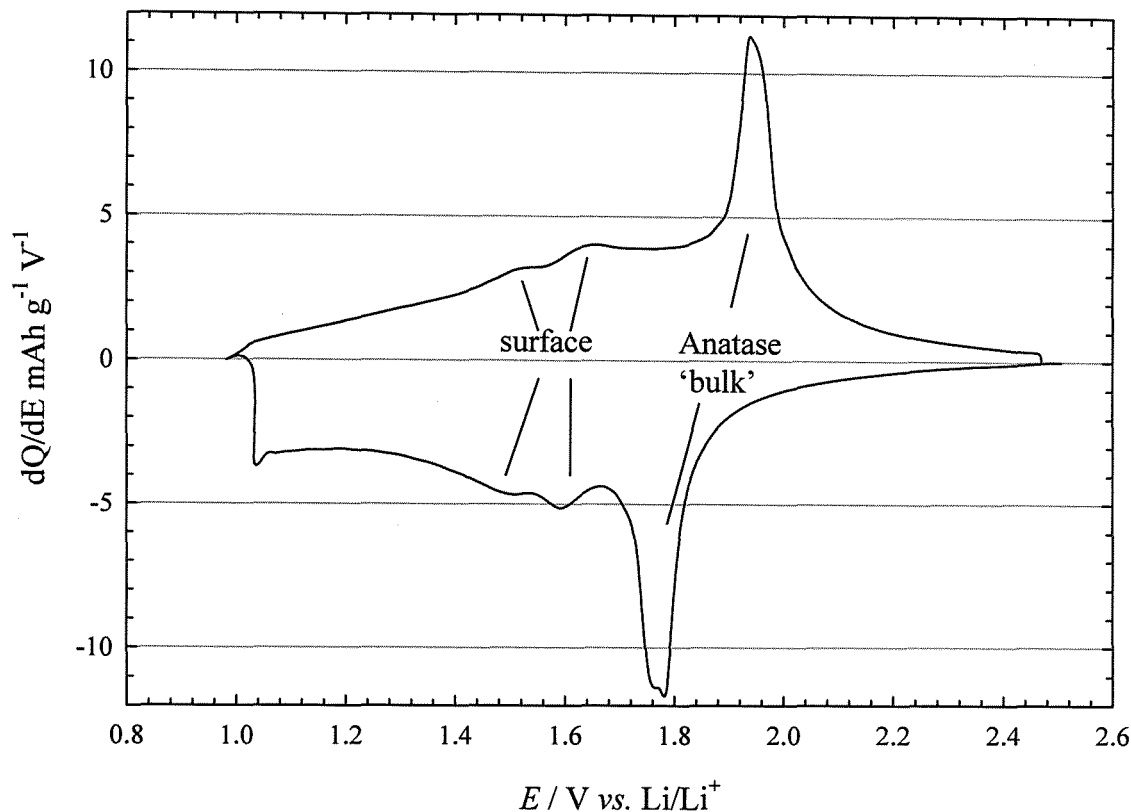
Figure 5.4.5: Galvanostatic cycling at 0.2 A g^{-1} for nanostructured TiO_2 50 μm. F127-TiO_2, 170 m^2g^{-1}, Teflon cell TiO_2/ Li in 1 M $LiPF_6$ in EC:DMC. (The voltage has been plotted after correcting for measured ir drops to allow better comparison of peak splitting)

A differential plot of the galvanostatic cycling resolves the presence of the surface (S) peaks in our nanostructured form of TiO_2, with formal potentials of ~1.5 and ~1.6 V *vs.* Li/Li$^+$. The above graph has been corrected for ir drop so you would expect this so called surface process to have almost no peak separation and indeed there is only ~ 40 mV between insertion and extraction. This is in contrast to the A peaks, (200 mV separation). Many authors have speculated on the nature and origin of these surface peaks, Kavan proposed they may be linked to TiO_2-B (with an open crystal structure), however they could not link the S peaks to the presence of any specific crystal phase.[99]

Wagemaker *et al.[121]* recently reported the idea of forming new phases for high surface-area lithium insertion in high surface area anatase, including a number of excellent studies relating the phase behaviour and mobility of lithium ions in various forms of titanium oxides. Neutron Scattering and ^{7}Li NMR amongst other methods

131

have been used to investigate the $Li_4Ti_5O_{12}$ spinel,[*128*] as well as comprehensive studies on anatase.[*118, 129, 130*] In particular a recent paper[*121*] regarding the impact of particle size on Lithium insertion into anatase was particularly useful in interpreting electrochemical data.

A phase diagram of Lithium in TiO_2 *vs.* particle size displays anatase chemically reduced with butyl lithium and then probed with Neutrons to identify the crystal structure is presented below:
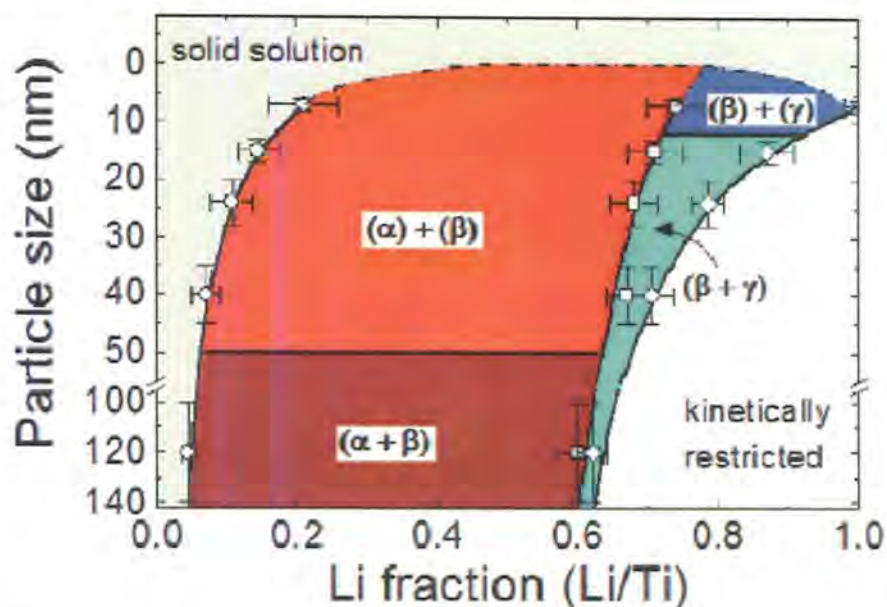
Figure 5.4.6 Phase diagram of the Li composition in anatase TiO_2 versus crystal particle size based on the neutron diffraction results.(Reproduced from [*121*])

In α indicates the anatase phase, β the Li-titanate phase and γ the Li_1TiO_2 phase. The different notations of the phase coexistence, for instance $(\alpha+\beta)$ or $(\alpha)+(\beta)$, reflect respectively, the coexistence or non-coexistence of the two phases within one crystalline particle. The kinetically restricted domain reflects the poor ionic conductivity of the Li_1TiO_2 phase, (which may be expected due to the filling of interstitial lithium sites) which implies that particles larger than 7 nm cannot be fully transformed to this phase on the time scale of the reaction. Therefore effectively, a small 'nano shell' of Li_1TiO_2 phase around each particle can be imagined, penetrating around 3-4 nm. For large micro sized particles this is a relatively small proportion and cannot be detected electrochemically. As the particles become smaller, <120 nm the ratio of surface to bulk will increase significantly, meaning the Li_1TiO_2 penetrates an increasing amount of material. The effect of particle size should be manifest in the electrochemical study, by comparing different particle size powders; it can be determined whether our

nanostructured macroscopic powders do indeed perform as similar dimension nanoparticles.
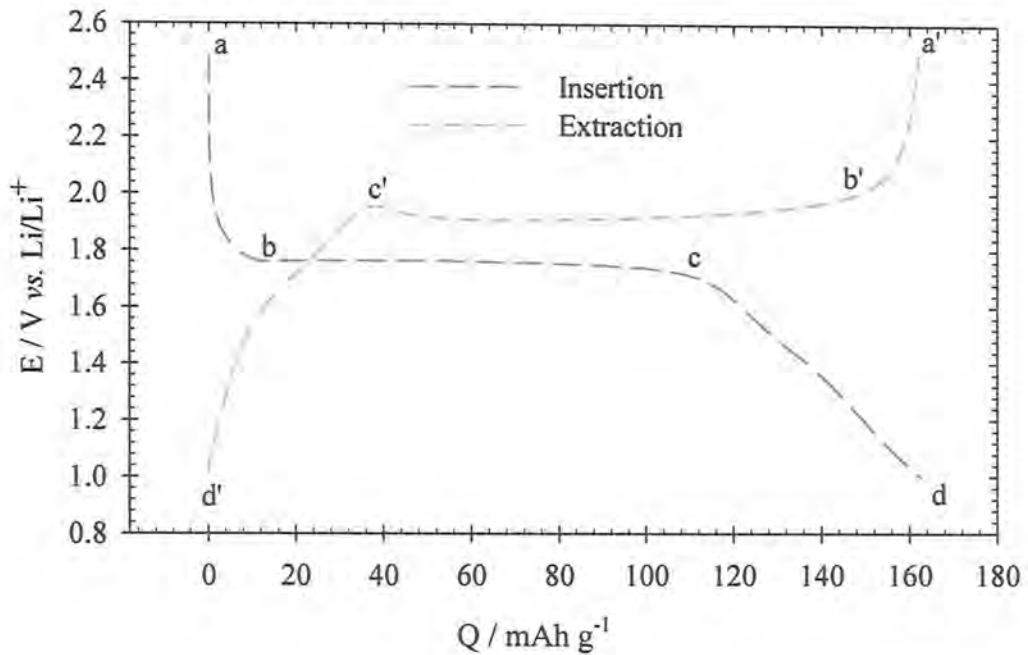
Figure 5.4.7: Galvanostatic cycling (20th cycle) at 0.05 A g^{-1} for Degussa P25 , 0.3-1.5 μm 50 m^2 g^{-1} material, TiO_2/ Li in SS 2-electrode cell, 1 M LiPF6 in EC:DMC.

For larger particles (Degussa P25 , contains anatase and rutile phases in a ratio of about 3 : 1, particle size 0.3-1.5 μm, 50 m^2 g^{-1} surface area), extended solid solution behaviour can be observed in regions before and after the 2-phase insertion in bulk anatase. However, not to the extent of the nanostructured materials, this is predicted by the particle size effect discussed above. From Figure 5.4.7 the solid solution region at the beginning of the insertion (denoted a-b) is ~10 mAh g^{-1} corresponding to a stoichiometry of $Li_{0.023}TiO_2$ in anatase, before the main plateau (b-c) which accounts for $Li_{0.33}TiO_2$ for the two-phase reaction for the formation of Li-titanate. The last region (c-d) accounting for the formation of the Li_1TiO_2 phase accounts for 53 mAh g^{-1}, $Li_{0.15}TiO_2$. It should be noted that this is the 20th cycle of the material and it would appear most of the capacity loss has come from the anatase-titanate- plateau, with the surface capacity still yielding the predicted amount for such a particle size amount of charge.
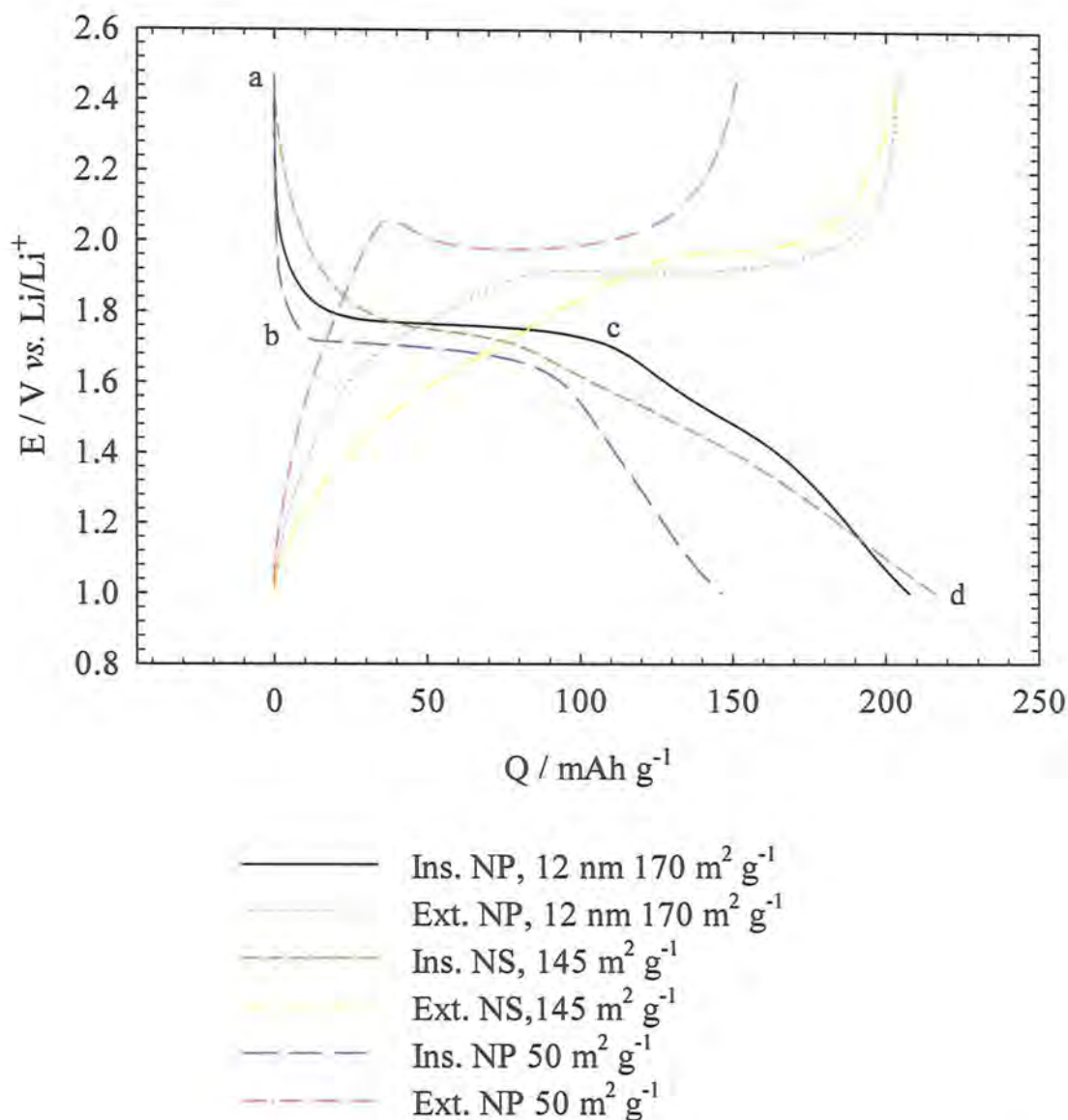
Figure 5.4.8 A comparison of different materials: Galvanostatic cycling at 0.2 A g^{-1} for nanostructured (NS) and nanoparticulate (NP) material for different particle sizes, 3 electrodeTeflon cell TiO_2/ Li in 1 M $LiPF_6$ in EC:DMC (n.b. NP,50 m^2g^{-1} is 2-electrode)

The electrochemistry of smaller particles was examined, (10-12 nm) thought to be in the same region as the wall thickness for our nNS TiO_2. (10 nm). Figure 5.4.8 shows that after 20 cycles both the NP and NS showed very similar capacities in terms of cycling; extracting around 210 mAh g^{-1}at 0.2 A g-1 ,~1 C. This is significantly more than the larger particles ~150 mAh g^{-1}. It also confirms that our internally nanostructured micron size particles display the same electrochemical properties as the 10 nm nanoparticles.

The high surface area means they both share the ability to form the Li_1TiO_2 surface phase. However there are clearly differences in the electrochemical profiles which need to be explained. For low lithium loading in anatase, up to a stoichiometry of $Li_{0.2}TiO_2$, the extended formation of a solid solution increases as particle size decreases. This is due to the increasing ratio of surface area to bulk, stabilising smaller anatase particles, therefore it is energetically possible to host more lithium ions before a phase change occurs.[121] This is in agreement with the galvanic cycling from thermodynamic cycling at slow rate for our nanostructured (NS) TiO_2, which sees an extension of this domain. So essentially micron sized particles and nanostructured particles will behave differently, the insertion of Lithium can be summarised in the scheme displayed in Figure 5.4.9.
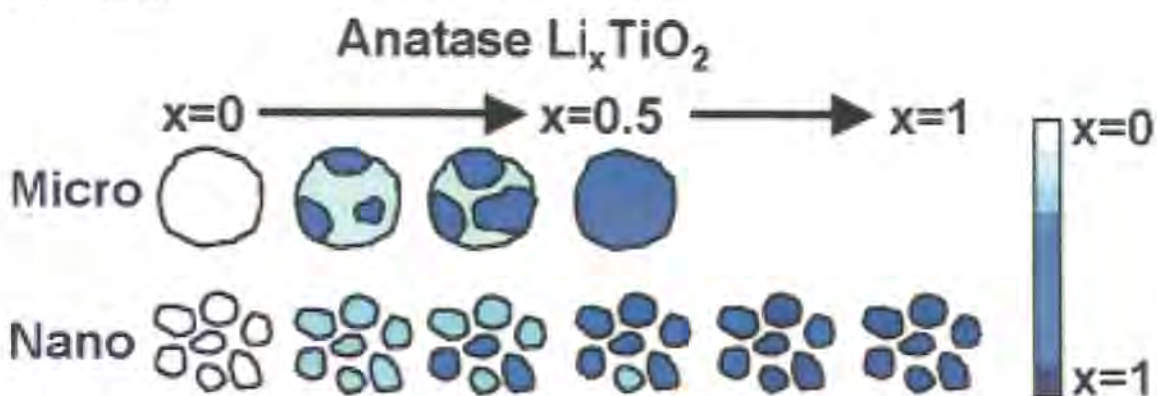
Figure 5.4.9: The different behaviours of our nano and micro size particles, and the extent and type of Lithium insertion.

In contrast to pure nanoparticles our nanostructured micron sized particles are not completely uniform and indeed a fraction of the material may simply be a non-nanostructured amorphous Titania. Electrochemically this mixture of micro-nano particles means that some will perform simply as bulk powder, with slower kinetics and will display less potential for lithium insertion at surface sites. This amorphous state explains the sloped region (c-d) which forms at the expense of the classic anatase-titanate plateau (b-c). The micro/nano mixture also explains why capacity is limited to 0.7 Li per TiO_2, even during slow cycling, as the material must be within 4 nm of the surface of the particle to be subject to the nano size effect. Much of the material is simply not able to form the Li_1TiO_2. This will complicate the diffusion picture further when the material is subject to high rate testing.

5.4.3   High Rate Cycling of Nanostructured TiO_2 in Composite Electrode

As described above the extra capacity extracted from TiO_2 due to the 'nano-effect' is clearly beneficial in improving the energy density battery material. However the primary motivation for nanostructuring materials is to reduce the solid-state diffusion distance within the active material, generally considered the rate-determining step in determining electrode performance. (section 1.6.2) This would yield faster flux within the electrode and higher power densities as a result. Therefore, this part of the thesis seeks to examine how the electrode material(s) would perform operating at high rates and what factor is limiting electrode performance. Materials were tested at high rates in composite electrodes initially under Constant Current Cycling. (CC)

5.4.3.1   Constant Current Cycling Regime

The galvanostatic cycling was started at high rates 3000 mA g^{-1} and stepped sequentially to 50 mA g^{-1}, with typically four cycles at each current density, an exemplar is displayed in Figure 5.4.10. The charge voltage cycle 'bunches' into areas where the current density (rate) is the same, with large jumps observed as the rate changes. There is a large irreversible capacity on the first cycle as discussed in Figure 5.4.1. The observed capacity in mAh g^{-1} was calculated by integrating under the curves between 1.0-.2.5 V *vs.* Li/Li^+. It is important to consider how the charge and discharge profiles change at different rates; this is not easy to determine from a continuous Charge–voltage plot.(Figure 5.4.10) For a simple representation of electrode performance versus rate it is convenient to display the values of charge for insertion (charge) and extraction (discharge) of lithium ions versus cycle no. seen in Figure 5.4.11.
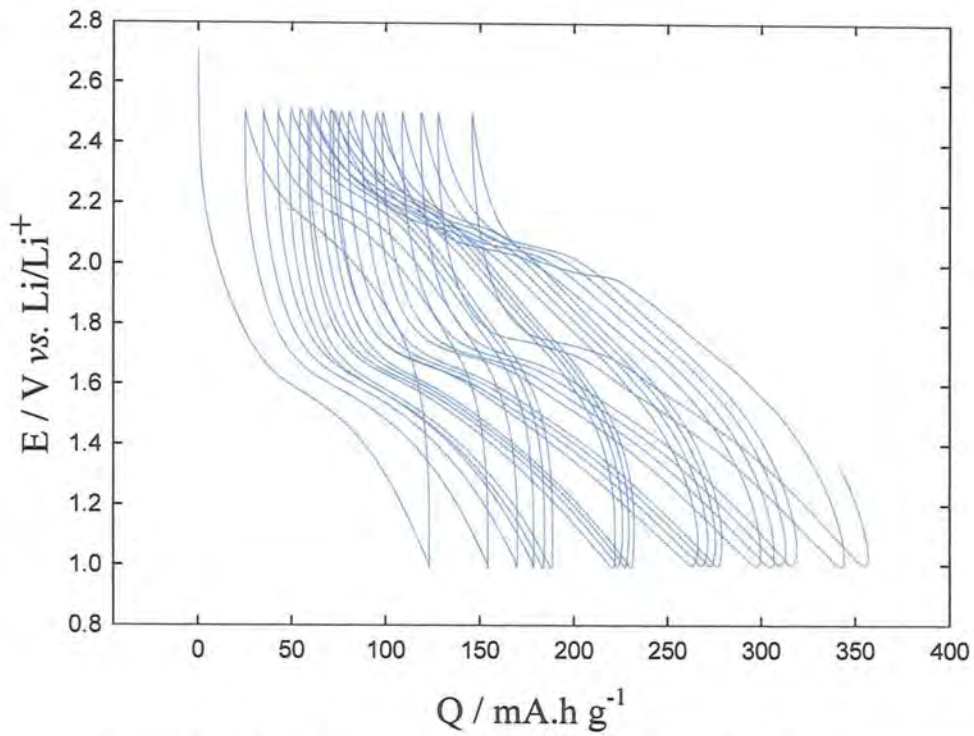
Figure 5.4.10 Galvanostatic cycling of 45.0 μm, NS TiO$_2$ Composite electrode (Pellet KS4 _3B), 3-electrode cell 1.0-2.5 V *vs* Li.
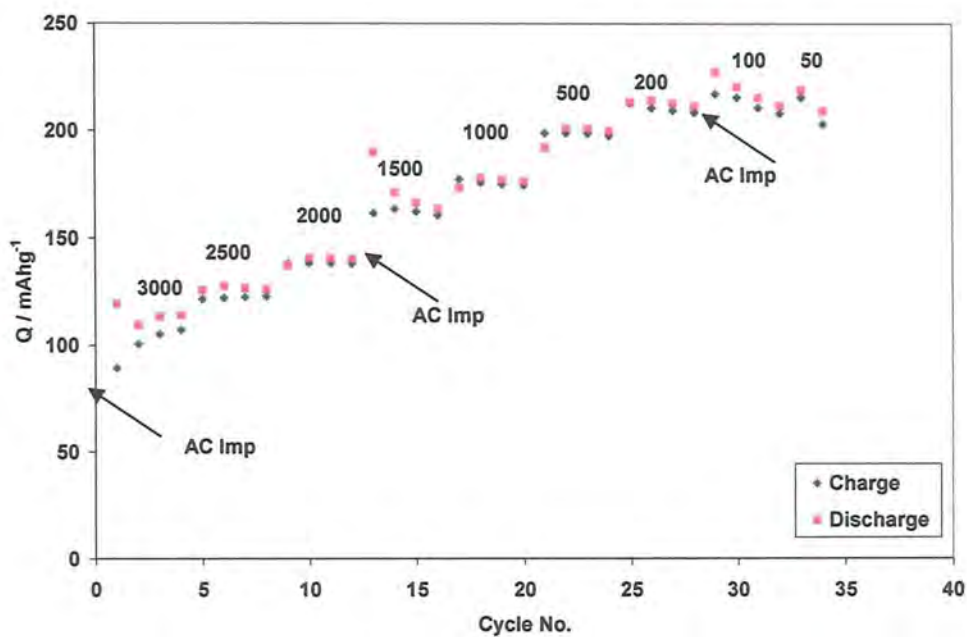
Figure 5.4.11: Typical charge *vs.* cycle no. for CC galvanostatic cycling of pellet K19D_10, 96 μm, in a 3-electrode cell, cycled from 1.0-2.5 V *vs.* Li. Numbers indicate specific currents in mA g^{-1}. Also indicated are regions where AC impedance measurements have been taken.

Electrochemical characterisation of nanostructured TiO_2 composite was primarily studied using Galvanic cycling between potential limits. The advantage of galvanostatic cycling is that the cell has a constant ir drop (where I = current in Amps, R = resistance in Ohms) this is important since at current densities in the region of 3000 mA g^{-1} ir drop will be significant. The cell configuration had a large influence on reliability and repeatability on cycling data. The cell had to be standardised before high rate data could be analysed usefully.

5.4.3.2   Evolution of Cell Configuration

Conventional testing with composite electrodes is done at relatively slow rates, therefore cell configuration or limitations such as electrolyte resistance will not affect results. This work is primarily concerned with the NS-TiO_2 as a high rate negative electrode, prepared as 'thick' composite electrode films. A complication is that high material loading means high geometric current densities, and a substantial contribution of ir drop. This means that even a well-prepared cell with a series resistance of 10 Ω would manifest a significant ir drop. The voltage range measured is substantially reduced at high rate, meaning true performance of the material cannot be determined. The cell can be configured as either a two-electrode or three-electrode (see experimental section). How this affects the capacities extracted from the TiO_2 on discharge (extraction of Lithium) can be observed in Figure 5.4.12. Clearly the ir drop affecting the 2-electrode cell decreases the voltage range and subsequently reduces the ascertained capacity. The effect at low current density decreases as expected.
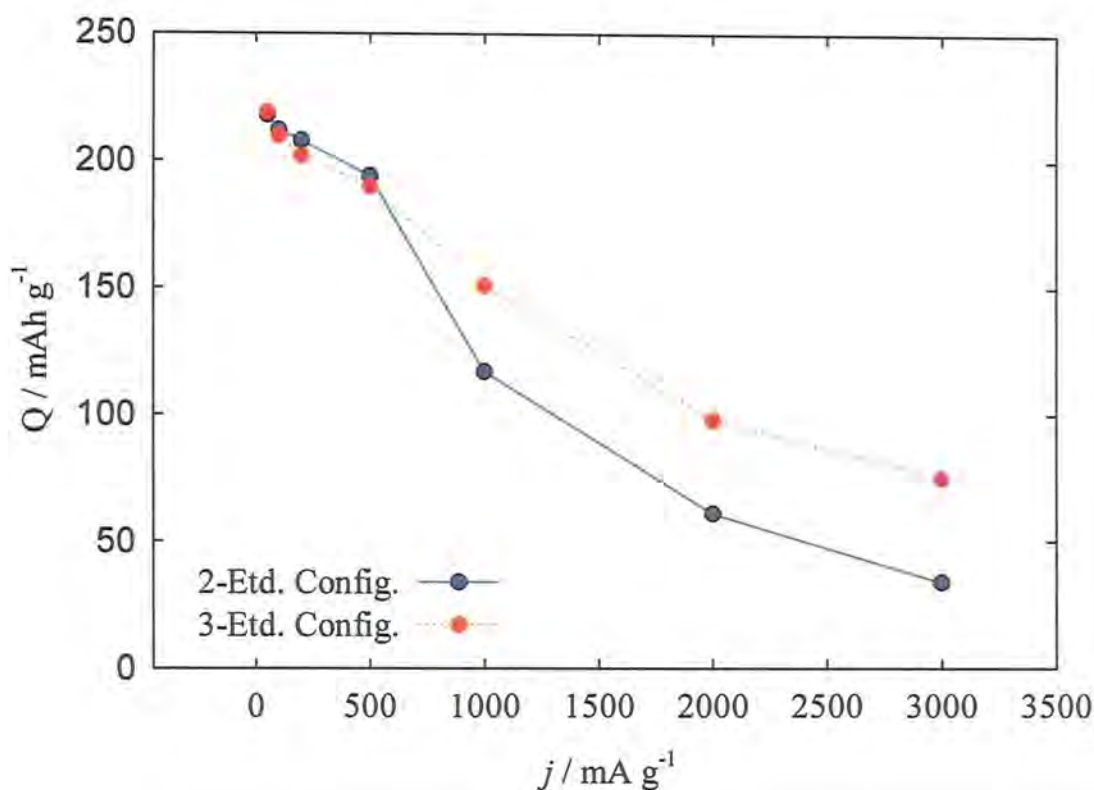
Figure 5.4.12: Graph to show differences between 2 and 3 electrode configurations in a 3-electrode Teflon cell TiO_2/ Li cell in 1 M LiPF6 in 1:1 EC:DMC. (93 μm electrode thickness.)

The major problem for a 2-electrode cell is the thick passivation layer which forms on the lithium negative electrode, contributing to the cell resistance. (~17 Ω). In Figure 5.4.13 AC impedance of a newly prepared cell shows that in the 3-electrode configuration the electrolyte resistance is reduced from 6 to 2 Ω and lithium interfacial resistance is largely eliminated; which results in a much reduced ir drop at high rates. This effect can be seen in Figure 5.4.14 which compares the experimentally measured series ir drop from high rate testing.
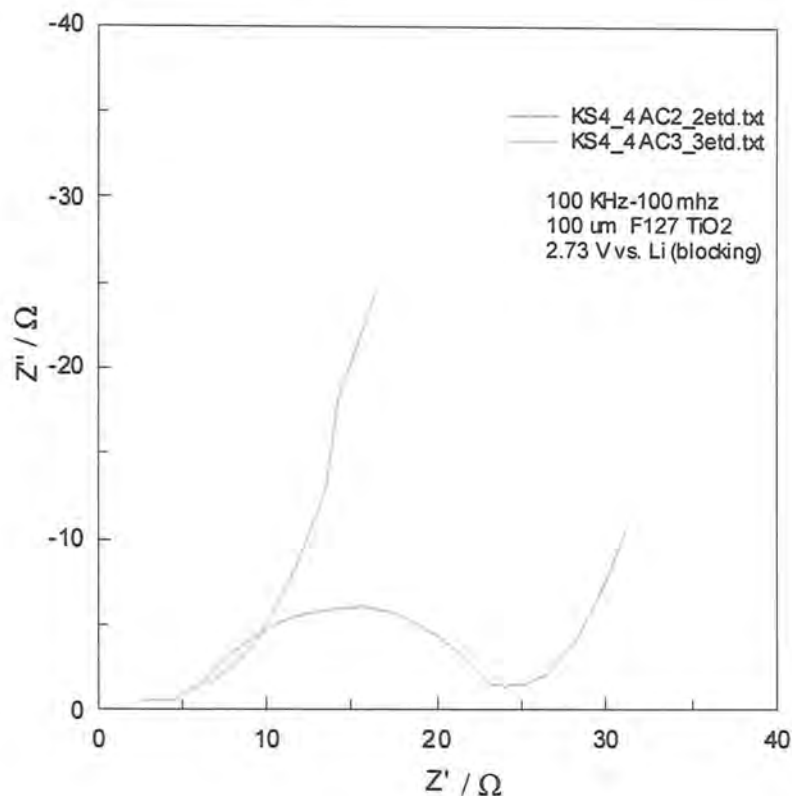
Figure 5.4.13 Nyquist plot for 93 μm thick composite TiO_2/ Li in 1 M $LiPF_6$ in 1:1 EC:DMC. 3-electrode Teflon cell in both 2 (blue) and 3(red) electrode configurations.
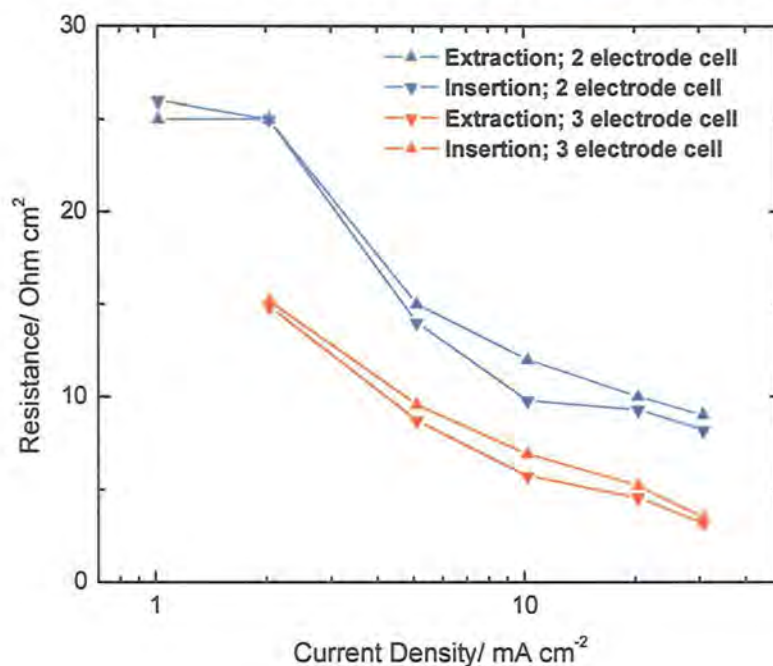
Figure 5.4.14: Series resistance measured experimentally from 3-electrode Teflon cell TiO_2/ Li in 1 M $LiPF_6$ in 1:1 EC:DMC, 45 μm thick film(Red). And 2-electrode Stainless-steel cell TiO_2/ Li in 1 M $LiPF_6$ in 1:1 EC:DMC. 96 μm thick film (Blue).

5.4.3.3   Cell Resistance *vs*. Cycle Number

As observed in Figure 5.4.11 there is a deviation in capacity for different cycles despite being cycled at the same current density or rate. This could be due to not only cyclability problems in the electrode material itself but also due to increased cell impedance, either way it is important to understand what is happening in the cell during cycling, consequently AC impedance measurements were recorded at various intervals during cycling.   In Figure 5.4.15 the high frequency part of the Nyquist plot is displayed.

Cell impedance is measured for a freshly assembled cell (AC1) after high rate cycling impedance is reduced (AC2 compared to AC1), but then gradually increases upon cycling as can bee seen AC3. This correlates well with the galvanostatic performance of cell from Figure 5.4.11 as initially the cell has higher impedance so capacity values for extraction are lower but then gradually increase as impedance reduces.   This process however, is not always observed for longer term cycling. Generally, impedance can be observed to increase on cycling as manifest in the ir drop, which can be measured manually from the galvanostatic cycling data. Recorded ir drop can be used to estimate cell resistance from the point at which the current is reversed on a charge/discharge cycle. Series or cell resistance versus cycle number is displayed in Figure 5.4.16, it must be noted that every four or five cycles the current density is stepped to a lower value, which makes the measured ir. drop harder to record precisely simply because the voltage drop is smaller.
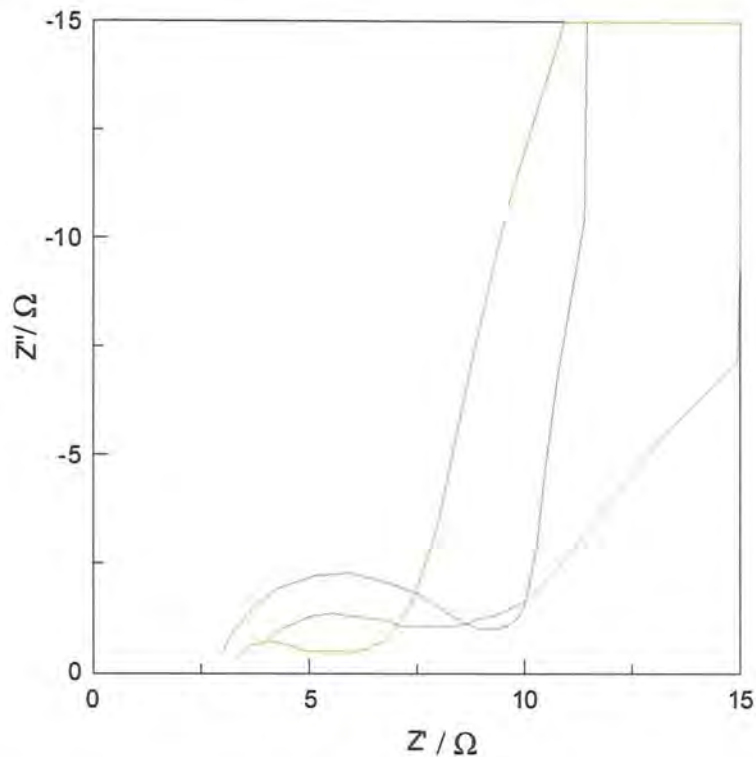
Figure 5.4.15: Nyquist plot for Cell KS4_D_2 (96.0 μm). From 100 kHz - 1 mHz the cell was equilibrated at 2.5 V *vs*. Li for 15 minutes prior to measurements being taken. Green; AC1 (pre cycling) Red; AC2, Green; AC3 Blue.
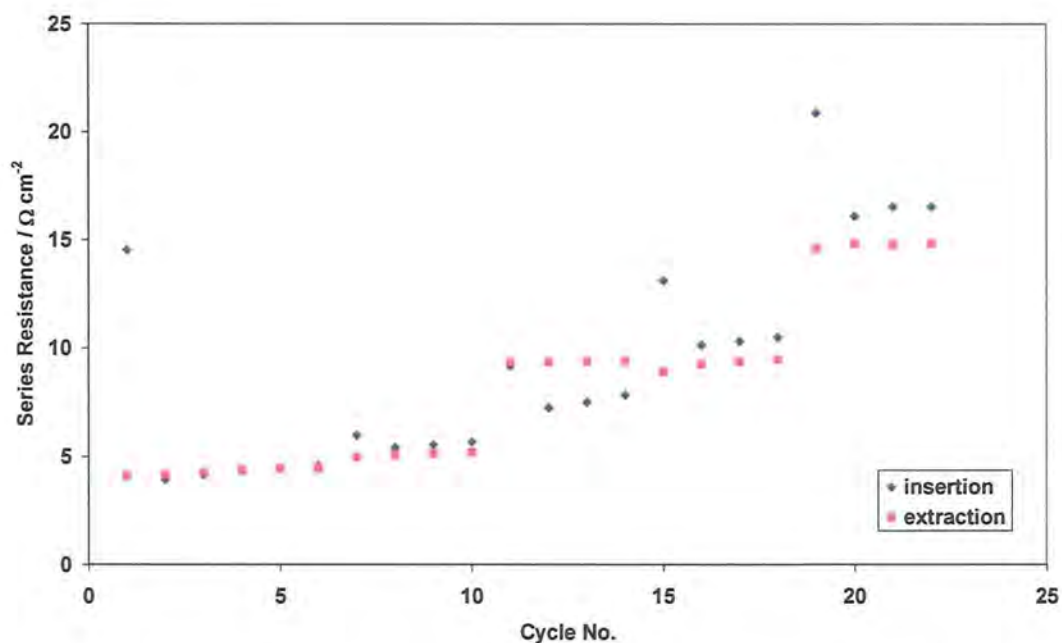
Figure 5.4.16 Series Resistance *vs*. Cycle No. for Galvanostatic cycling of a 96 μm NS TiO$_2$ in a 3 electrode cell 1.0-2.5 V *vs*. Li, (Pellet KS4D_2) ir drop is calculated from Figure 5.4.11.

There are many contributing factors to the increasing cell impedance. Generally, the parasitic current from decomposition of electrotype will deposit increasingly thick SEI's (Solid Electrolyte Interface) on the surface of both the positive and negative electrode and reference electrode. This is manifest in the increase of the size of the semi circle from the Nyquist plot. It seems that on the time scale of this experiment the electrolyte conductivity remains high and even decreases in resistance on cycling, this may be due to increased wetting of the composite electrode. The importance of using a three-electrode cell for high rate testing is highlighted; in light of increasing cell resistance with cycling it seems prudent to start with high current densities before a reduction on cycling in order that the impact of cell resistance be minimised.

5.4.4   The effect of particle size on high rate performance.

To examine the high rate performance of nano materials the composite electrode films were subject to continuous cycling at stepped current densities as set out in Figure 5.3.3. To examine the rate performance it is helpful to view the charge – discharge profile at each current density.
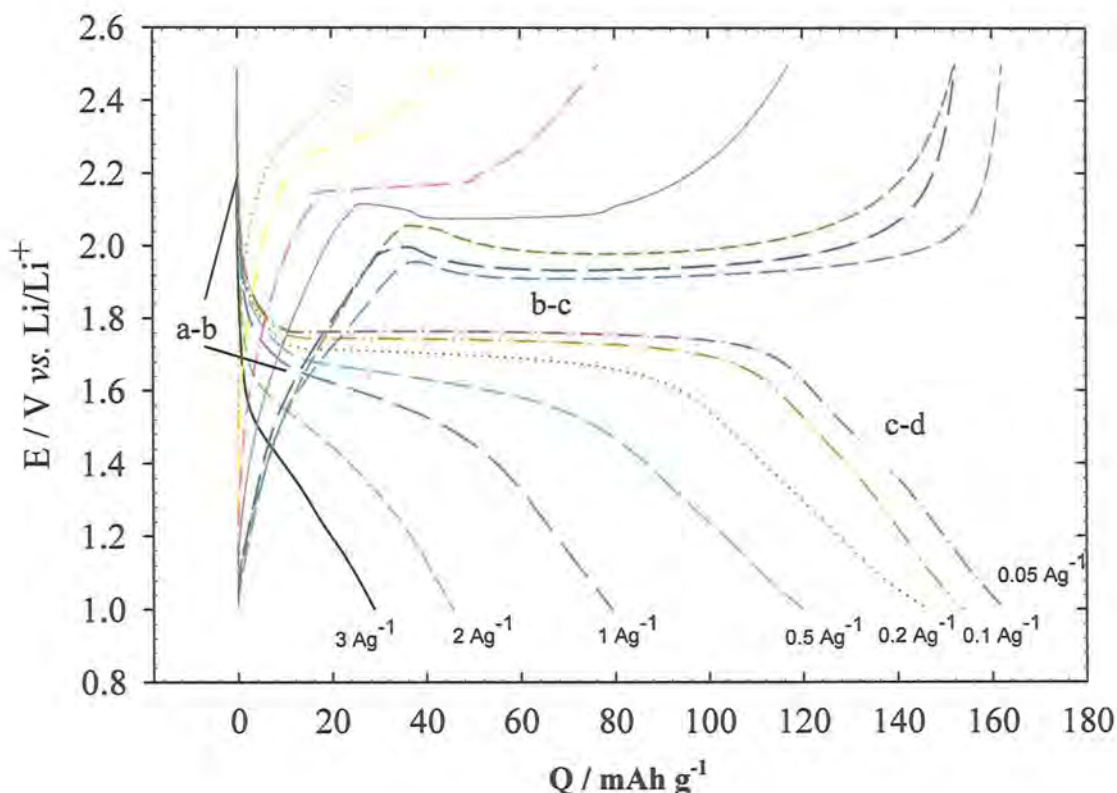
Figure 5.4.17: Galvanostatic cycling with stepped current densities starting for high to low rate (3 Ag^{-1}-0.05 A g^{-1}) for Degassa particles BET 50 m^2 g^{-1}, 65 μm composite electrode, AM loading 6.74 mg cm^{-2}. 3 electrode Teflon cell TiO$_2$/ Li in 1 M LiPF$_6$ in 1:1 EC:DMC.

From Figure 5.4.17 the TiO$_2$ powder 0.3-1.5 μm sized particles shows a clear correlation with increased current density. At a C-rate ~C/3 (where C -rate is a measure of cycling rate in battery terminology; in this case the theoretical capacity ~165 mAh g^{-1} would be discharged in 1 hour e.g. 1 C in half the time 2 C in two hours C/2 etc) the thermodynamic capacity for Anatase is realised, the sloped region c-d can be ascribed

to rutile or other amorphous phases. On discharge, higher current densities 3 A g^{-1}(up to 18 C) show a decrease in the anatase plateau (~1.8 V the region described as b-c above) with most of the insertion coming in a sloped region until the voltage limit. At the highest current density only 30 mAh g^{-1} is part inserted. The extraction of lithium firstly comes from the sloped region, before the anatase plateau it has to overcome some phase nucleation energy before the two-phase extraction of lithium from anatase can occur.

The anatase plateau is also typically more resolved for extraction of lithium, which can be explained as the particle has had time to equilibrate. It is expected that for a particle of this size the rate limiting step would be the diffusion of lithium ions within the solid state of the bulk material. Nanomaterials should however remove the limitation of solid-state diffusion and all of the material be accessed. This can be observed for 12 nm anatase particles in Figure 5.4.18:
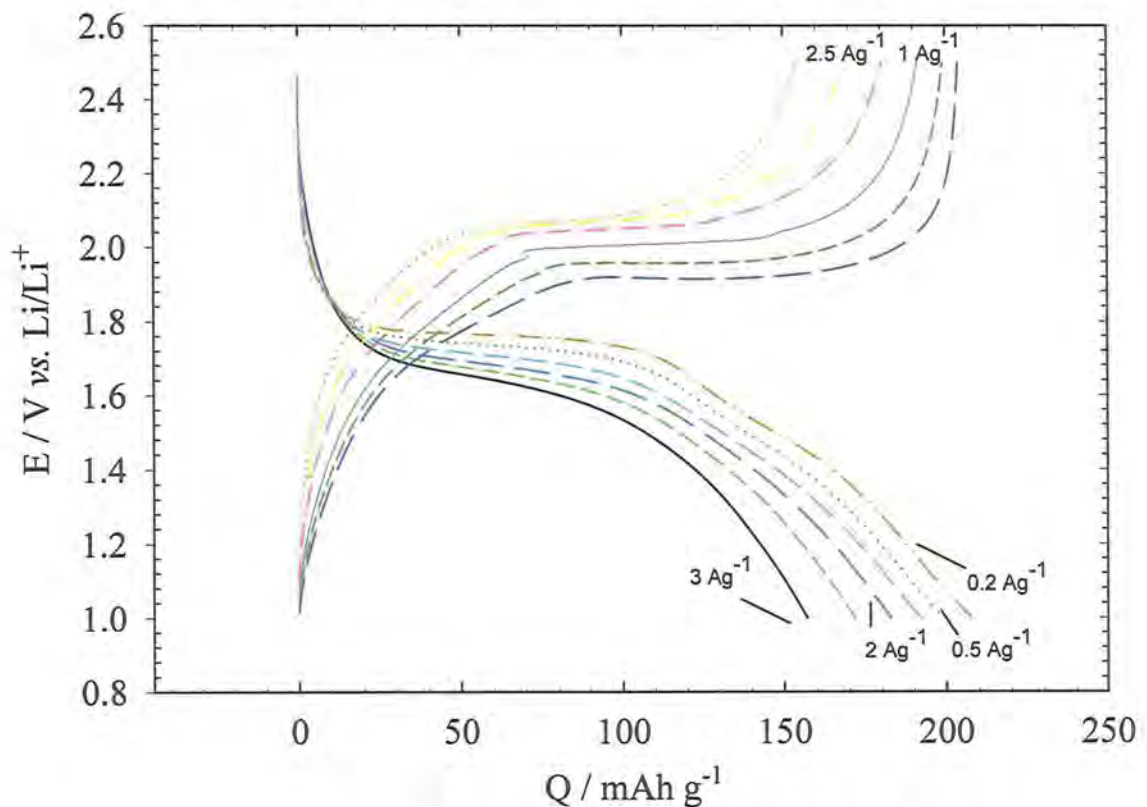
Figure 5.4.18: Galvanostatic cycling for 12 nm anatase nanoparticles with stepped current densities starting for high to low rate.(3 A g^{-1}-0.2 A g^{-1}). BET 180 m^2 g^{-1}, 50 μm composite electrode, AM loading 4.61 mg cm^{-2} (TiO$_2$/ Li cell in 1 M LiPF$_6$ in 1:1 EC:DMC.)

The nano features as described above (section 5.4.1) are still visible, the particles have had time to equilibrate, as the anatase plateau is generally well resolved for charge and discharge even at 2.5 A g^{-1}~15 C. The centre of the particle is now able to be accessed with around 160 mAh g^{-1} cycled. For all the materials discussed the extraction of lithium exhibits faster kinetics than the insertion, therefore the extraction capacity is always the same value as the insertion ± 2 mAh g^{-1}.
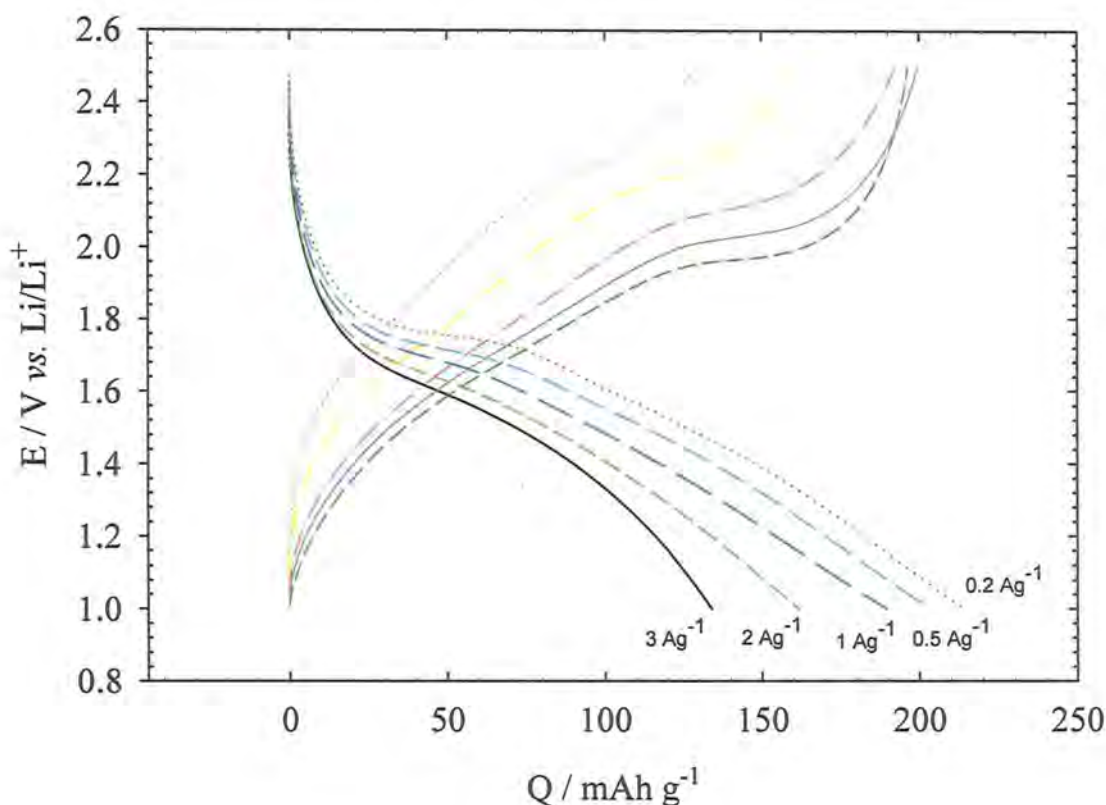
Figure 5.4.19: Galvanostatic cycling at high rate for nanostructured TiO$_2$, F127-TiO$_2$ 145 m^2 g^{-1}, 50 μm composite electrode., Teflon cell TiO$_2$/ Li in 1 M LiPF6 in 1:1 EC:DMC (Pellet KS4 3b) AM loading 5.7 mg cm^{-2}.

Our material in Figure 5.4.19 displays behaviour more analogous to that of the nanoparticles than the micron-sized particles, confirming that our micron size particles must be internally nanostructured, as they display high rate performance. Classically our material has a non-optimised structure and displays the extended sloped region on both charge and discharge. At 2.5 A g^{-1} (15 C) ~130 mAh g^{-1} is cycled, this is 30 mAh g^{-1} less than the nanoparticles, meaning not as much of our material is accessed. One

reason may be due to some regions of bulk non-nanostructured material which cannot be accessed at 2.5 A g^{-1} (15 C) where the cycle would have to be complete in a few minutes. To analyse the charge-voltage curve further and compare high and low current densities a differentiated charge-voltage plot is displayed in Figure 5.4.20.
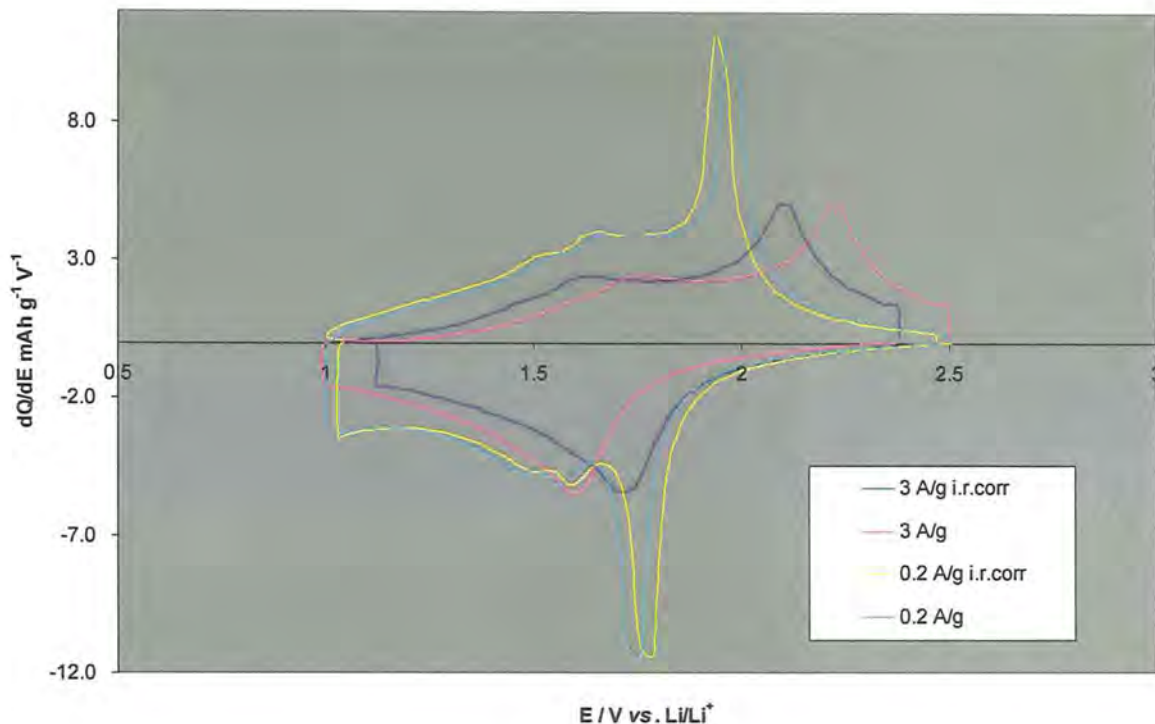
Figure 5.4.20: Galvanostatic cycling at for 50 µm nanostructured TiO$_2$ film in 1:1 EC:DMC, F127-TiO$_2$ 145 m^{2}g^{-1} , Teflon cell TiO$_2$/ Li in 1 M LiPF6 in 1(KS4 3b) ir corr means the experimental ir drops have been adjusted..

In Figure 5.4.20 the raw data and a correction for ir drop are displayed, which allows comparison of how the voltage profiles change at different rates.. At 0.2 A g^{-1} the charge inserted in 215 mAh g^{-1} with 199 mAh g^{-1} extracted. A high proportion of this charge is from the anatase-titanate plateau 1.8 V *vs.* Li/Li$^+$. Large amounts of charge are obtained at higher overpotentials characteristic of high surface area titanium oxide, the lesser peak separation indicating that this concerns a surface type process[72] or indeed insertion into the lithiated titanate or the formation of new crystal phases.[121] This mechanism was discussed in detail in 5.4.2. At 3 Ag^{-1} the charge is much less than expected at high rate; 129 mAh g^{-1} of charge extracted from 134 mAh g^{-1} of inserted charge. Most of the charge loss seems to have come at the expense of the anatase-titanate-plateau. (region b-c) This is due primarily to the fact there is less time for

lithium to diffuse into the bulk particle. Less charge is lost from the surface sites before and after plateau (a-b and c-d), this is explained by the fact that not only is this charge attributed to a surface process, but also that this is solid solution type behaviour with improved interstitial dynamics. Some charge is lost in region c-d, this is because the surface of the particle may form a Li_1TiO_2 phase with full octahedral lithium sites[_121_], normally through which the lithium ions usually pass resulting in to slower kinetics.

The rate limitation in battery electrodes is, historically, the diffusion distance within the particle of the active material, hence the drive to form small particles and reduce diffusion distances and times. However it was established during cycling that cell performance was not completely determined by the active material, but the thickness of the composite electrode, posing a question about what now limits the performance of a nanostructured composite electrode.

5.4.5   Rate Limitation in Composite Electrodes.

In determining the rate limiting step in a nanostructured composite electrode the lithium insertion may be limited by three cases;

<u>1. Diffusion of ions or electrons along the thickness of the electrode.(electrode)</u>
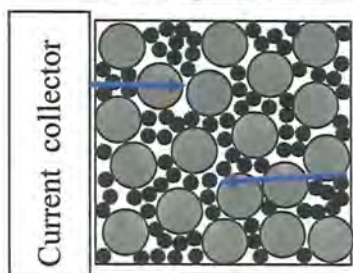
<u>2. Diffusion of ions within the pores.(particle)</u>
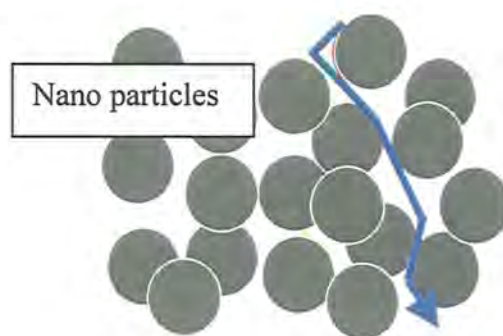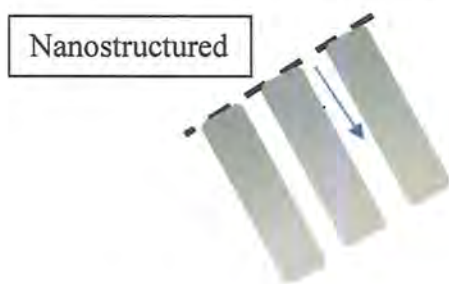
<u>3. Diffusion into the bulk solid TiO$_2$.(solid state)</u>
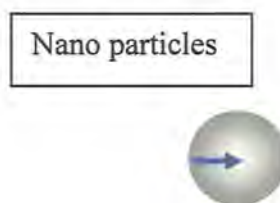
This part of the discussion seeks to establish the rate-limiting step from the above possibilities for a range of electrode structures as a function of the nano- dimensions and thus optimise the electrode fabrication route and measure the best performance.

5.4.5.1   Discussion on rate limitations in Composite electrodes.

The term "nanostructured" is used here to denote mesoporosity, rather than "nanosize" materials (which consist of aggregates of small grains or small crystals). Both types of material have the advantages of a high surface area and a small diffusion path from the surface to the interior of the solid. The latter results in a short time constant, τ_1, for equilibration of the bulk with the surface according to ambipolar diffusion of electrons and ions through the solid:

$$\tau_{solid} \sim r_3{}^2/D_{solid} \, , \qquad\qquad (1)$$

where r_3 is the diffusion distance through the solid,

D_{solid} is the ambipolar diffusion coefficient for the coupled diffusion of lithium ions and electrons through the solid. One advantageous feature of the nanostructured materials is a porosity that is structurally defined; we have a stable labyrinth of uniformly sized interconnecting pores filled with an electrolyte which acts as conduit for ions within the grain. Aggregates of nanopowders, on the other hand, are less amenable to control of the dimensions of the electrolyte channels between their grains. Therefore nanostructured materials should provide a better effective conductivity of the electrolyte within *particles* of similar dimensions, i.e. nanostructured material or aggregates of nanopowders as viewed in Figure 3.2.8.

A possible disadvantage of the nanostructured material is that the effective electronic conductivity cannot be enhanced within the particle (by addition of carbon black according to the common practice of composite electrode fabrication). Considering the diffusion time for equilibration of an electrode particle, we find that the analogous equation to (1) becomes:

$$\tau_{particle} \sim r_2{}^2/D_{particle} \qquad\qquad (2)$$

Here r_2 should correspond to the particle radius and $D_{particle}$ is an ambipolar diffusion coefficient involving the effective ionic and electronic conductivities of the composite matrix as shown in equation (3)[*131*]:

$$D_{particle} = ((\rho_{ion} + \rho_{electron})C_v)^{-1} \qquad (3)$$

where ρ are the effective resistivities and C_v is the pseudocapacitance per unit volume.

Equation (3) effectively determines the state of the art in composite electrode performance for a lithium battery. With a limiting electrolyte conductivity of about 10^{-2} S/cm and an effective pseudocapacitance of 10^4 F/cm^3 we obtain a maximum diffusion coefficient of around 10^{-6} cm^2/s provided the carbon black is effective. However, it also indicates that if the electronic conductivity of the matrix is less than the electrolyte conductivity we can expect an electronic limitation on the high rate performance of large particles according to (2). Film conductivity was measured at $>10^{-1}$ S/cm, so this would not be a rate limitation.

A final difference between nanostructured and nanosized materials may be found in the macrostructure of composite electrodes and the methods available for their fabrication. Under the conditions of electrode fabrication, e.g. by the doctor blade technique, nanopowders can agglomerate around the binders and conductivity additives to form a macroscopically uniform film. However, in the case of nanostructures, electrode fabrication is in its infancy, where thick monoliths are difficult to fabricate, and therefore in this work we fabricate composites in which grains of nanostructured material are assembled to form composite electrodes in a similar way to powders. However, composite electrodes made from granular nanostructured materials are necessarily inhomogeneous, or hierarchical, structures. The following experiments will investigate the high rate performance of both types of electrode, particularly with reference to the equations that relate the performance to the solid state diffusion coefficients, the effective diffusion coefficients in the composites, and the diffusion lengths in the solid and composite media.

5.4.5.2 The Sand equation

The sand equation (Eq. 5.4.2) is normally used to determine C (electroanalysis) or D (physical constant determination) of a solution species by plotting the square root of the discharge time against the inverse current density.[132] Here we are applying the

technique to the determination of D in a thin solid electrode in which the concentration of the electroactive species (Li) is known[*133*].

$$(I/A)\tau^{1/2} = kD^{1/2} \quad \text{where} \quad k = \frac{nFC\pi^{1/2}}{2}$$

Eq. 5.4.2

C = initial concentration of the electroactive species.
D = diffusion coefficient of the electroactive species.

This gives the relation between the discharge end point time, τ, and the current density, (I/A), assuming a semi-infinite sample to define the boundary condition for solution of Fick's Law. The effect of a finite sample is to restrict the value of the end-point time such that its product with the current density cannot exceed the total charge available. Eq. 5.4.2 requires knowledge of the cross-sectional area perpendicular to the diffusion front. Here there are three possibilities, depending on the rate determining step for discharge.

Case 1 Area. For a macroscopically thick electrode, we can expect the diffusion front to propagate into the electrode thickness, such that the geometric surface area (e.g. πr^2 for a disc electrode) should apply. Given the finite electrode thickness, the semi-infinite boundary condition becomes invalid when the diffusion front reaches the back of the electrode. This event should be visible as a deviation at the right hand part of the $\tau^{1/2}$ *vs* $(I/A)^{-1}$ plot for small currents.
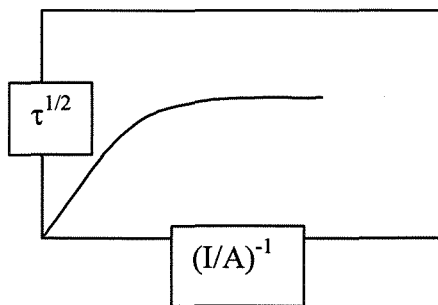
Figure 5.4.21 Predicted plot of $\tau^{1/2}$ *vs* $(I/A)^{-1}$ displaying the semi-infinite to finite diffusion transition.

Case 2: Particle: The same equation could be applied to a case where the rate-determining step is diffusion from the outside to the centre of an approximately spherical particle of an active material. This time the appropriate current density would be that at the particle surface, or the total current divided by the total external surface area of the particles within the composite.

Case 3 BET surface area. Another case is that of a mesoporous particle in which the diffusion into the walls is accessed via the internal nanostructure i.e. the surface area of the walls.

Whereas in case 1, the area is simply given by the electrode dimensions, cases 2 and 3 require an estimation of the area according to the mass-specific area (A/m), which can be measured for example by SEM or BET analysis. The (I/A) term above Eq. 5.4.2 can be replaced by the mass specific current $i_m = (I/m)$ to give

$$i_m \tau^{1/2} = k_m D^{1/2} \text{ where } k_m = \left(\frac{A}{m}\right) \times \frac{nFC\pi^{1/2}}{2}$$

Eq. 5.4.3

To express the result as a plot of charge/mass, q as a function of current/mass i rather than in terms of a relation between current and time. Therefore we shall transform the equations using

$$\tau = \frac{k_m^2 D}{i_m^2} \text{ to give } q_m = i_m \tau = \frac{k_m^2 D}{i_m}$$

This equation indicates that a plot of q *vs.* 1/i should be a straight line through the origin whose gradient, qi, indicates the value of the diffusion coefficient according to equation:

$$D = \frac{q_m i_m}{k_m^2}$$

Eq. 5.4.4

The finite sample limitation should then appear as a deviation of the line towards the horizontal at high values of $1/i_m$, (low current density) consistent with the maximum charge capacity of the sample. An example of a thick film plot of Q *vs.* $1/i_m$ appears in Figure 5.4.22.

5.4.5.3   Calculation of diffusion coefficient

We can calculate the different effective diffusion coefficients by changing the A/m factor for each possible diffusion limitation. For Case 3 (Solid State limited) the diffusion constant is calculated by assuming that the current density is based on the surface area as measured in a BET experiment. i.e. the A/m factor in Eq. 5.4.3, is the BET specific surface area (m^2g^{-1}).
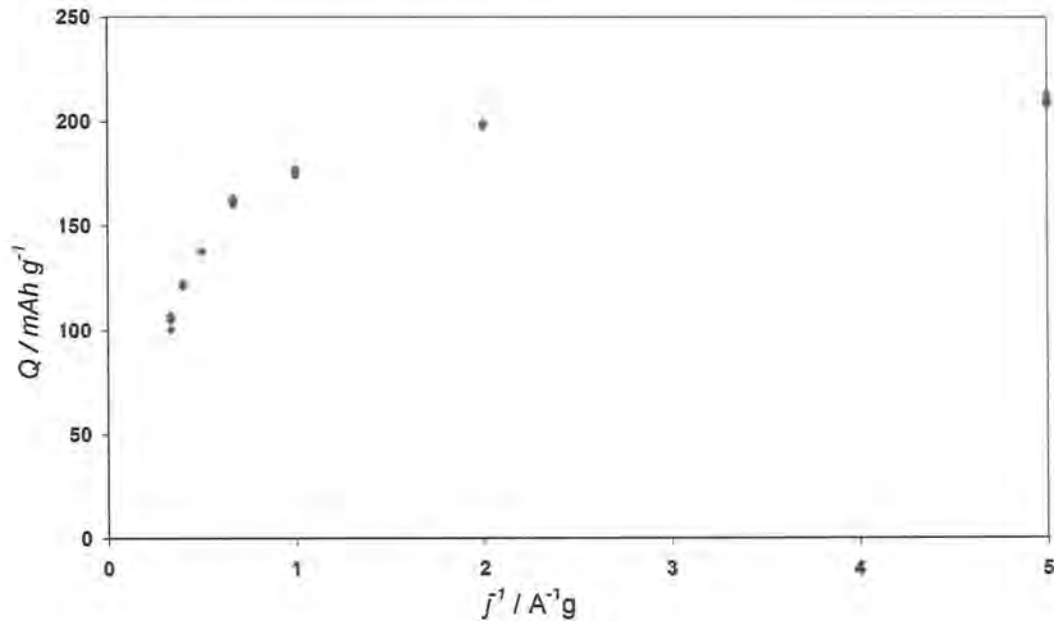
Figure 5.4.22: Q vs. j^{-1} for Galvanostatic cycling of 96. μm pellet KS4D_2, in a 3-electrode cell, where j is mass specific current density and Q is mass specific extracted charge.

The value of q.i = 410 C^2 g^{-2} s^{-1} for the 96 μm thick film above, the quantities for k_m must now be established:

$$k_m = \left(\frac{A}{m}\right) \times \frac{nFC\pi^{1/2}}{2}$$

The molar volume V_m is calculated for the molar mass of TiO_2: 79.87 g mol^{-1} and dividing by the density of ~4 g cm^{-3} (pure anatase would be slightly lower 3.9 g cm^{-3})

$$V_m = \frac{79.87\, g\, mol^{-1}}{4\, g\, cm^{-3}} = 19.96\, cm^3 mol^{-1}$$

Concentration is the inverse molar volume therefore; C_{TiO2} =0.05 mol cm^{-3}. For Li_xTiO_2 x = 0.45-0.65 depending on the starting point of discharge, which itself depends on the

C-rate. For the purpose of this calculation we will assume $x = 0.5$ the normal maximum capacity for anatase.[103] Therefore C_{Li} the bulk concentration is 0.024 mol cm^{-3} or 2.4 $\times 10^4$ mol m^{-3}, here the unit of meters is preferred as this is how the BET surface is measured. We calculate the effective interfacial area from BET surface area and the weight of active material: $(A/m) = 170$ m^2 g^{-1}

$$k_m = \left(\frac{A}{m}\right) \times \frac{nFC\pi^{1/2}}{2}$$

$$k_m = 170\,m^2 g^{-1} \times \frac{96500\,Cmol^{-1} \times 2.4 \times 10^4\,mol\,m^{-3}\pi^{1/2}}{2} = 1.2 \times 10^{11}$$

$$D = \frac{q_m i_m}{k_m^{\,2}}$$

$$D_{solid\ state}\quad \frac{410\,C^2\,g^{-2}\,s^{-1}}{3.88\,x\,10^{22}}$$

Convert m^2 to cm^2 (x by 10000)

$\underline{D}_{solid\text{-}state} = 1.06 \times 10^{-16}$ cm^2 s^{-1}

This value is within the range of values normally reported for solid state.[99] However, this value is for a thick composite electrode is probably an underestimate because of the thickness limitation mentioned above.

Case 2, particle:

The value of (A/m) indicated by SEM gives a spherical particle diameter of, say, 1 μm, for the internally nanostructured particles. To work out the surface of a sphere, divide area by volume:

$$\frac{A}{V} = \frac{4\pi r^2}{\frac{4}{3}\pi r^3} = \frac{3}{r}$$

A/m =A/V x V/m therefore = 3/ρr where ρ = density = 4 x 10^6 g m^{-3}.

A/m = 0.75 m^{2}g^{-1} therefore we can calculate a new K$_m$

$$k_m = \left(\frac{A}{m}\right) \times \frac{nFC\pi^{1/2}}{2}$$

$$k_m = 0.75m^2g^{-1} \times \frac{96500Cmol^{-1} \times 2.4 \times 10^4 molm^{-3}\pi^{1/2}}{2} = 8.69 \times 10^8$$

$$D = \frac{q_m i_m}{k_m^2}$$

$$D_{particle} = \frac{410\,C^2\,g^{-2}\,s^{-1}}{7.54\,x\,10^{17}}$$

Convert m^2 to cm^2 (x by 10000)

D$_{particle}$ = 5.44 x 10^{-12} cm^{2}s^{-1}

This value of D particle seems unacceptably high for considering the diffusion down the channel of a mesoporous particle. The relative merits of this value are discussed below after the last limitation the composite electrode matrix is discussed.

Case 1 Electrode

As discussed above an electrode thickness dependence was observed. (case 1). Here we shall take the geometric surface area, i.e. diffusion through the electrode. Now the (A/m) factor depends on the sample thickness, d, according to:

$$\frac{A}{m} = \frac{V}{md} = \frac{1}{\rho d}; \text{where d is in metres.}$$

For example, with a 100 μm thick electrode we would obtain

$$\frac{A}{m} = \frac{1}{4.6x10^6\, g\, m^{-3}x\ 1x10^{-4}\, m} = 2.5x10^{-3}\, m^2 g^{-1}$$

again for the D value a new K_m must be calculated.

$$k_m = \left(\frac{A}{m}\right) \times \frac{nFC\pi^{1/2}}{2}$$

$$k_m = 2.5x10^{-3}\, m^2 g^{-1} \times \frac{96500Cmol^{-1} \times 2.4 \times 10^4\, molm^{-3}\pi^{1/2}}{2} = 2.90 \times 10^6$$

$$D = \frac{q_m i_m}{k_m^{\ 2}}$$

$$D_{electrode} = \frac{410\, C^2\, g^{-2}\, s^{-1}}{8.38\, x\, 10^{12}}$$

Convert m^2 to cm^2 (x by 10000)

$$\underline{D_{electrode} = 4.89\, x10^{-7}\, cm^2 s^{-1}}$$

Note that in this case, we would observe an inverse square relation between D and the electrode thickness from Eq. 5.4.3 whereas in cases 2 and 3 the value should be independent of thickness, as $\tau = r^2/D$.

If we now plot the values the gradient (qi) versus d^{-2}, we should get the result:
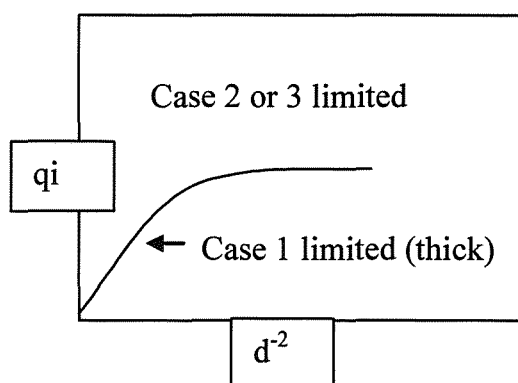
Figure 5.4.23: The gradient, qi, *vs.* the inverse square root of electrode thickness. (q.i. indicates the value of the effective diffusion coefficient).

It is important to note that the same variation as the above can be caused by a change in particle size (case 2), i.e qi would vary with (particle size)$^{-2}$ as above until the Case 3

(Solid State limited) limit was reached. The curvature of the q-i^{-1} in plot Figure 5.4.22 suggests that more than one diffusion limitation is significant in the discharge data. The possible ranges of limitations are discussed below.

Case 2 can be considered increasingly important as particle size increases. In our prepared nanostructured particles it is possible that we have some areas of poorly ordered material, this is an important consideration especially as the particle size distribution can range from sub micron to >30 μm, (as previously discussed in 3.2.3 the preparation of highly ordered mesoporous TiO_2 powder has not been optimised in this work). This is important to note especially for lower mass loading samples however, high BET surface shows this is not a major contributing factor in most preparations, and case 2 diffusion, (particle) can probably be eliminated in the case of a well-structured mesoporous material. This is argued on the grounds that the effective diffusion coefficient in the pore should be given by the De Levie transmission line analysis[134, 135], leading to $D \sim \sigma/c_v$ where σ and c_v are the effective conductivity and pseudocapcitance respectively.

$$D_{particle} \approx \frac{\sigma}{C_V} \quad \text{where} \quad C_v \approx \frac{F\Delta c}{\Delta E}$$

Eq. 5.4.5

An ionic conductivity less than 10^{-3} S cm^{-1} should be unlikely unless the pores are too narrow to allow solvent mobility.[131] The pseudocapacitance is estimated as follows:

$C_v \sim F\Delta c/\Delta E = 10^5$ C mol^{-1} x 10^{-2} mol cm^{-3} /0.5 V = 2 x 10^3 F cm^{-3}

This gives $\underline{D \sim 5 \times 10^{-7}$ cm^{2}s$^{-1}}$ and therefore the possibility that $D_{particle} = 10^{-11}$ can be eliminated.

The values of $D_{electrode}$ can be estimated by a similar analysis, but now the experimental values of 10^{-7} cm^2 s^{-1} are easier to explain, e.g. by a tortuous current path. In the early part of a galvanostatic experiment, (e.g. $t < r^2/D_{particle}$ for less than 1 second) both $D_{electrode}$ and $D_{particle}$ should be active; however, after that only $D_{electrode}$ should apply. The value of $D_{solid\ state}$ is, however, feasible due to the close packing of the anatase structure. The rate determining step is therefore expected to switch from $D_{electrode}$ to $D_{solid\ state}$ as the electrode thickness reduces beyond a critical value when $d^2/D_{electrode} \sim r_{wall}^2/D_{solid\ state}$.

158

Estimation of the value of $r_{wall}^2/D_{solid\ state}$ from the experimental data would involve a circular argument by assuming that the value obtained from qi was indeed associated with $D_{solid\ state}$. This problem is solved by reducing the electrode thickness in the hope that eventually a transition of the kind expressed in Figure 5.4.23 can be obtained.

For thick electrodes tested electrode limitation is observed and it is likely that Case 3 (Solid State limited) has never been measured, meaning the calculation of solid-state diffusion coefficient above is likely to be an underestimate. To test this hypothesis the effect of electrode thickness is investigated.

5.4.6   Evidence for electrode thickness diffusion limitation

A series of electrodes were prepared at different thickness as described in the experimental section.
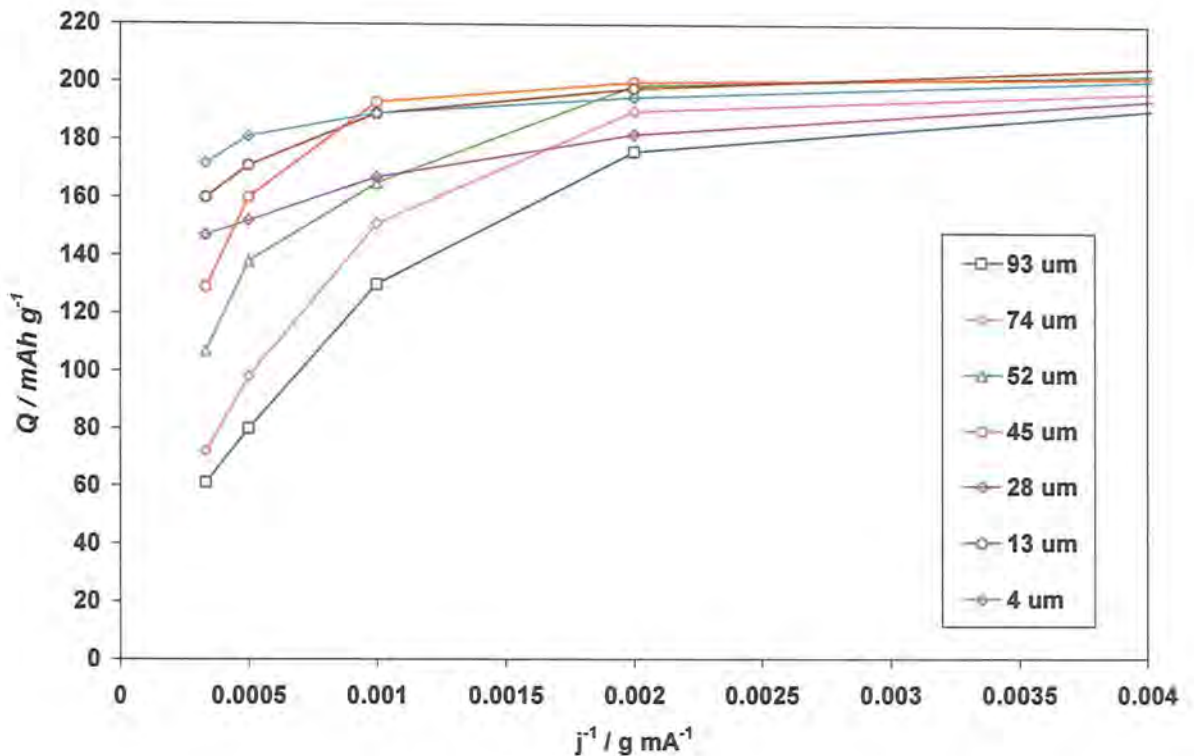
Figure 5.4.24: Plot of lithium extraction capacity (anodic, mass specific) $_s$ versus inverse of current density. Thick Films >30 μm: (Nanostructured TiO_2 75 %,PTFE 5 % ACB 20 %); Thin Films: Nanoparticles; (Anatase 12 nm TiO_2 65 %,PVdF 10 %ACB 25 %). Li cells in 1 M $LiPF_6$ in 1:1 EC:DMC, CC method.

Figure 5.4.24 depicts that for thick electrodes >30 μm, for the nanostructured material there is an electrode thickness limitation. If we now plot the values the gradient (qi) versus d^{-2}, we should get the form we predicted. We can obtain (q.i) from the gradient of the line from the Q *vs* i^{-1} plot assuming the line will tend to the origin. In

Figure 5.4.25 the behaviour of thick electrodes (>20 um) show a limitation behaving in semi-infinite condition where q.i. increases as the electrodes get thinner. Only when we get to thin electrodes with a low density and low mass loading that q.i begins to plateau as the finite boundary condition is realised. (the back of the electrode is reached and all of the expected capacity of the active material can be collected).
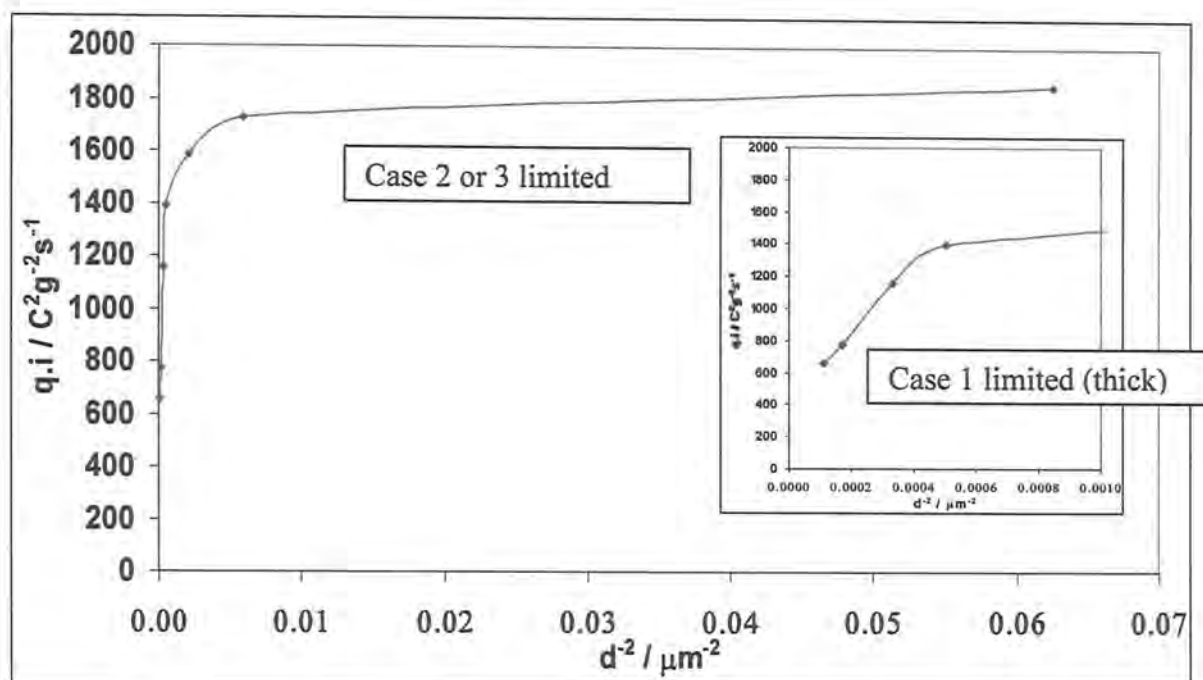
Figure 5.4.25: A plot of q.i *vs.* electrode thickness^{-2}, (d $^{-2}$) mass specific current and charge for extraction. Thick Films >30 μm: (Nanostructured TiO$_2$ 75 %,PTFE 5 % ACB 20 %); Thin Films: Nanoparticles; (Anatase 12 nm TiO$_2$ 65 %,PVdF 10 % ACB 25 %). Li cells in 1 M LiPF6 in 1:1 EC:DMC, CC method.

At high rates for a thin electrode e.g. 20μm there is time for the diffusion of lithium ions to the back of the electrode. For a thick electrode e.g. 100 μm the ions pass the same distance into the electrode, however when the [Li+] →0 a sharp discharge occurs. As the current densities get lower, the diffusion front has an increasing amount of time to reach the back of the electrode, therefore charge increasingly close to the thermodynamic capacity is reached.

Semi-infinite behaviour at high currents indicates that only the front portion of the thicker electrode is accessed. The case 1 electrode diffusion effect is clearly demonstrated by plotting the geometric current (I$_{area}$) versus the charge extracted per geometric surface area (Q$_{area}$). From Figure 5.4.26, it is clear that at high rates (small values of I$_{area}^{-1}$) that the amount of charge is independent of film thickness (all electrodes produce the same total charge). This gives a clear indication that diffusion through the electrode profile is the rate-limiting step; the diffusion profile within the electrode is so steep that only the front of the electrode is accessed for thicker films.
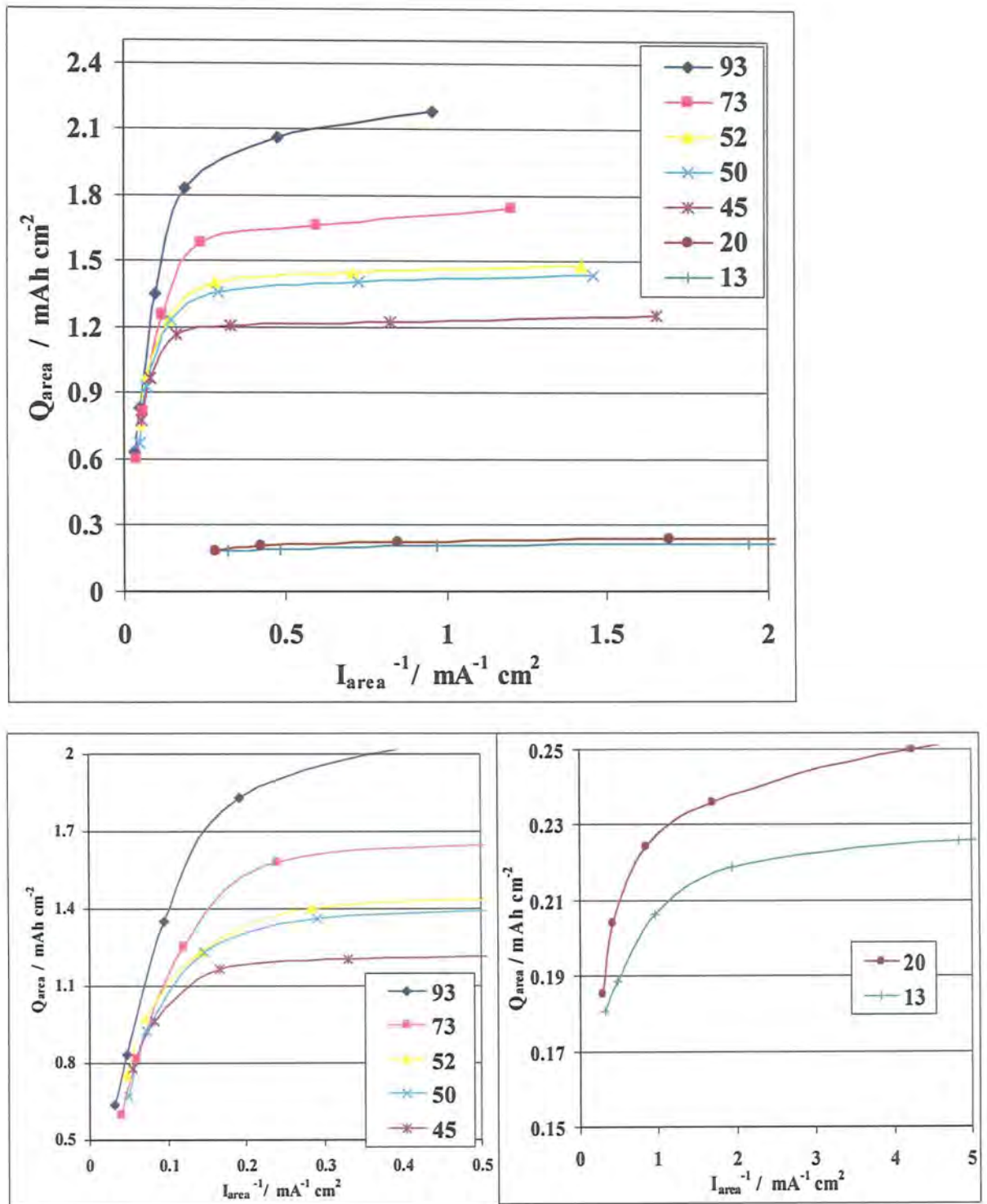
Figure 5.4.26: Plot of Q_{area} in mAh cm^{-2} (total film charge) versus inverse geometric current density. Shows effect of electrode film thickness (numbers in μm) Thick Films > 25 μm: (Nanostructured TiO$_2$ 75 %,PTFE 5 % ACB 20 %); Thin Films: (Inset) Nanoparticles; (Anatase 12 nm TiO$_2$ 65 %,PVdF 10 % ACB 25 %). Li cells in 1 M LiPF$_6$ in 1:1 EC:DMC, CC method.

This effect can be used to rationalise the charge (Q_{area})- voltage plots, at different current rates. In Figure 5.4.27 the profiles come from electrodes cycled at 3 Ag^{-1}, ~15 C. The charge-discharge profiles fall on top of each other despite having a different thickness, this means they all fall under the semi-infinite boundary condition. Notice that the thinner films have a slightly higher amount of total charge, this is because the electrodes are cycled with a lower geometric current density as they have an inherently lower effective mass loading, which, in effect reduces the I/A ratio.
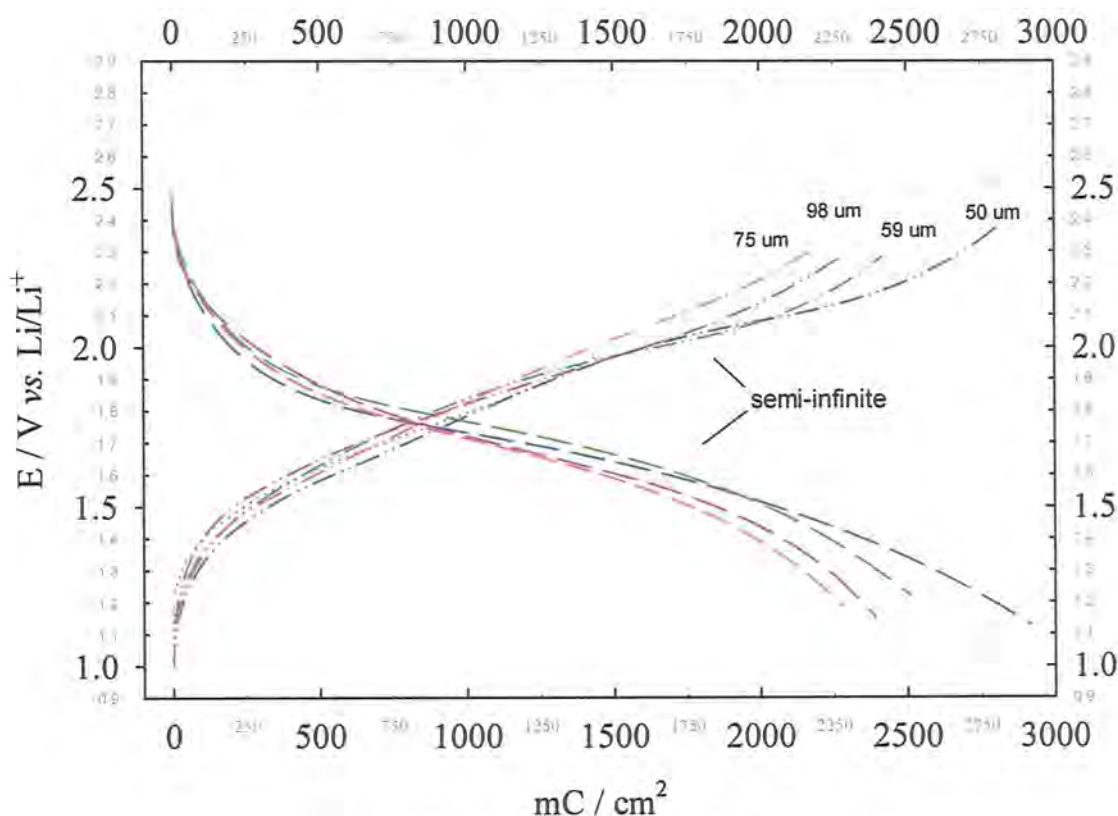
Figure 5.4.27: Thick, PTFE Nanostuctured films CC at 3 Ag^{-1}

By contrast in Figure 5.4.28 charge-voltage profiles at slow rates (0.2 mAg^{-1}), the total charge of the electrode now is approximately proportional to its thickness meaning that the diffusion front in the electrode has time to reach the back of the electrode (finite case). The finite case is also observed for the very thin films < 20 μm films of 12 nm nanoparticles prepared by the PVDF method (Figure 5.4.29). As a result, close to the expected thermodynamic capacity is obtained even at high rates, (3 Ag^{-1}.) as the electrodes are so thin they are now no longer limited by the case 3, electrode diffusion.
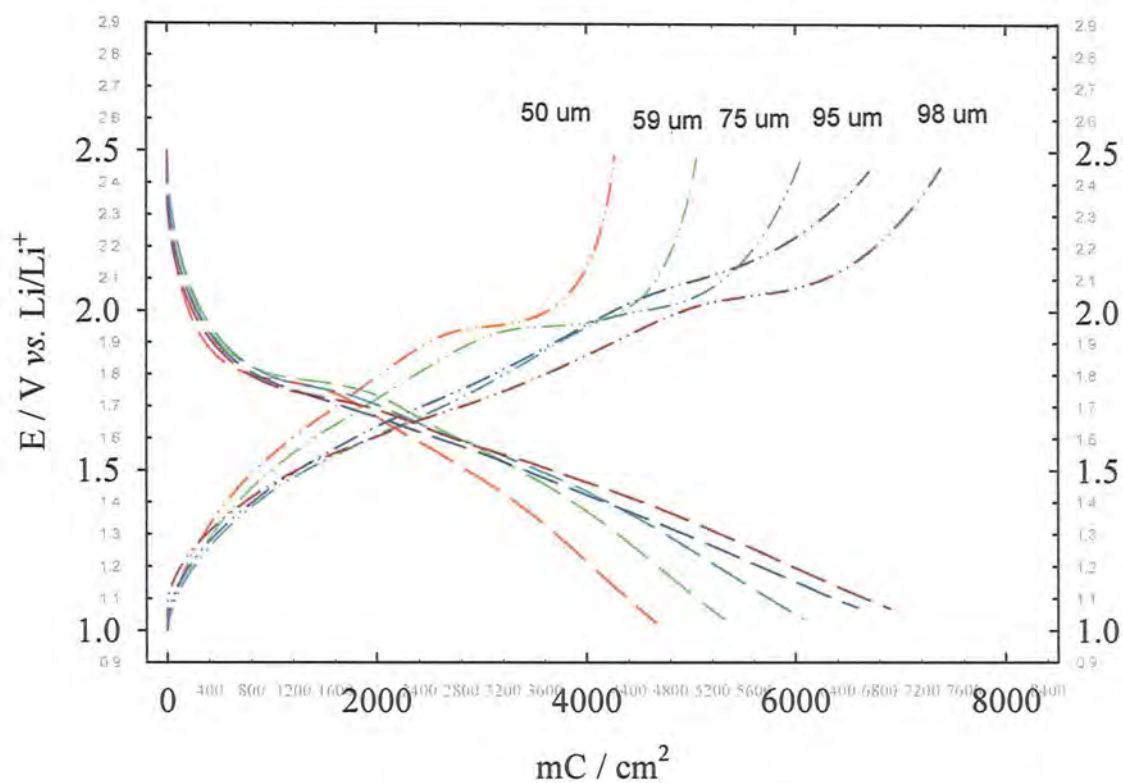
Figure 5.4.28 Thick PTFE Nanostructured films (CC) at 0.2 Ag^{-1}.
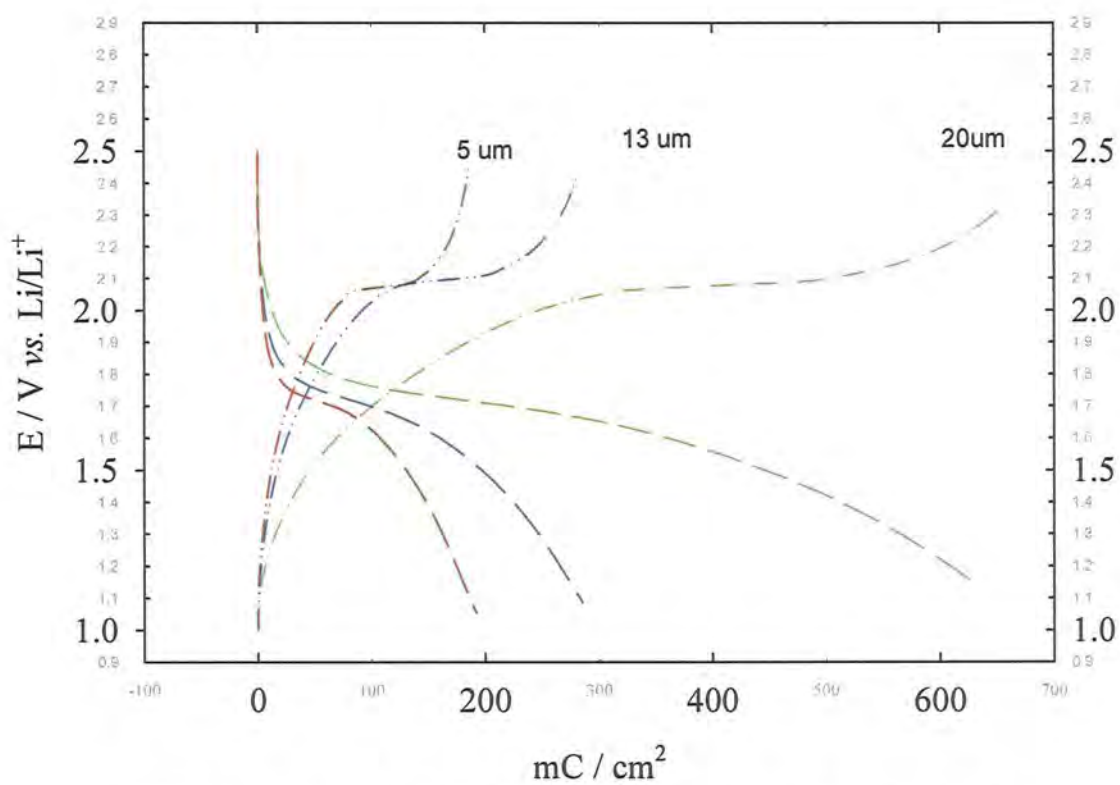
Figure 5.4.29: PVDF Aldrich 12 nm Nanoparticles Thin films at 3 Ag^{-1}.
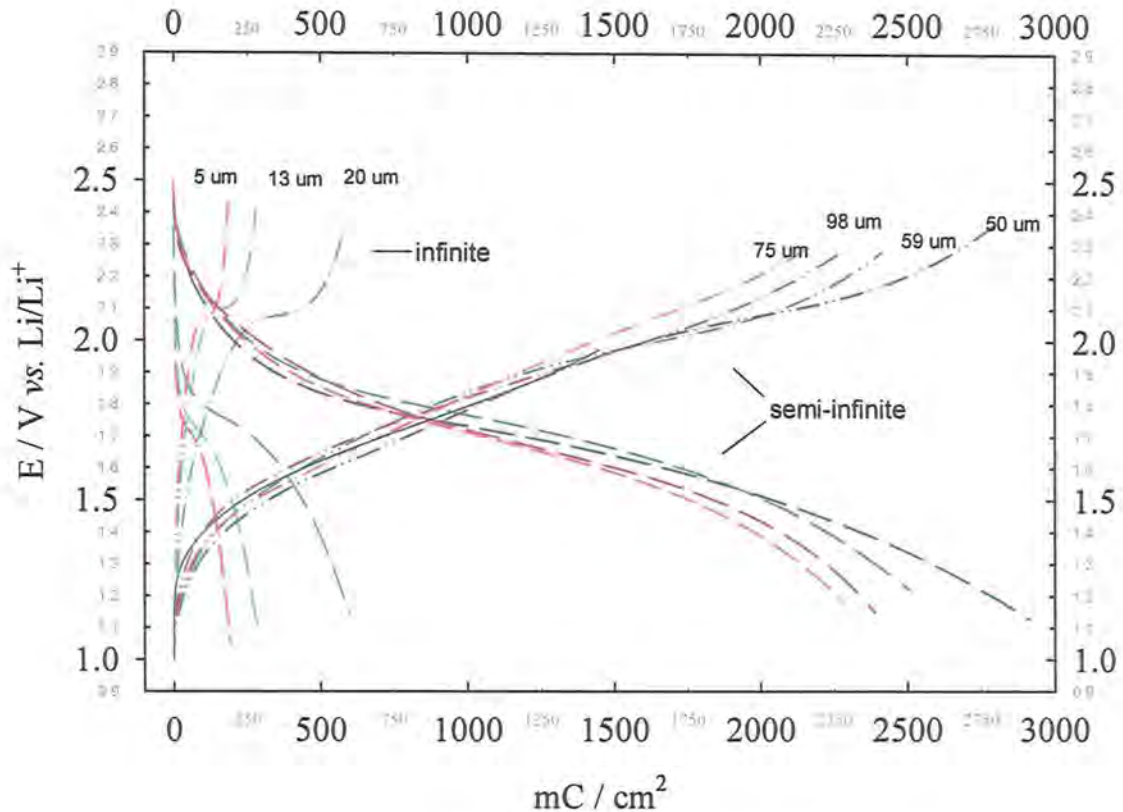
Figure 5.4.30: A comparison of thin (PVDF) and thick (PTFE) films at 3 A g^{-1} showing the transition between finite and semi-infinite boundary conditions.

The comparison transition between the finite and semi-infinite boundary condition is displayed in Figure 5.4.30. The transition between 20 μm and 45 μm is clearly observed, unfortunately the mechanical stability of roll milled PTFE (thick) films is limited to > 45 μm. The thinner films fabricated with PVDF using a doctor blading technique which does not allow a direct comparison. This is especially relevant as the density of these PVDF films is typically less than 1 g cm^{-3}, whilst the PTFE films ~ 1.5-1.8 g cm^{-3} (as discussed in the experimental). This means more electrolyte is contained within the electrode and ions should have a less tortuous path. A further difference is that considerably more ACB is needed for electronic percolation, as well as more binder to hold the electrode together. As a result, the active material loading is much lower than for PTFE films, so the geometric current density is much lower.

With a thin film in the finite boundary condition, we can recalculate the Diffusion coefficient for extraction of lithium in the solid state. The maximum value of q.i obtained for a 5 μm should be used to calculate $D_{solid\ state}$.

For 5 μm at 3 Ag^{-1} q.i => 2050 C^{2}g^{-2}s^{-1}

$$D = \frac{qi}{k_m^2} = D_{solid\ state} = (2050\ C^2g^{-2}s^{-1}/\ 3.88\ x\ 10^{22})\ x10000 = \underline{5.28\ x\ 10^{-16}\ cm^2\ s^{-1}}$$

This result is half order of magnitude higher than for the thick film that highlights the predicted over estimate obtained from the thick film.($1.06\ x\ 10^{-16}\ cm^2\ s^{-1}$). The macroscopic diffusion coefficient obtained with chronoamperometry on CVD films was found to be $2\ x\ 10^{-15}\ cm^2\ s^{-1}$ for insertion and $6\ x\ 10^{-15}\ cm^2\ s^{-1}$ for extraction.[127] This is significantly smaller than those obtained for single crystalline anatase: $2\ x\ 10^{-13}cm^2\ s^{-1}$ for insertion and $6\ x\ 10^{-13}\ cm^2\ s^{-1}$ for extraction.[136]

Some predictions can be made about relaxation times for a nanostructured electrode: Where:

$$r_{wall}^2/D_{solid\ state};$$

For 6 nm wall thickness $= 6\ x10^{-7}$ cm:

$3.6\ x10^{-13}\ cm^2/\ 5.28\ x\ 10^{-16}\ cm^2\ s^{-1} => 681$ s the time to discharge a 6 nm wall or a 12 nm particle. This can be described as the transition time τ between case 1 and case 3. If the electrode can reach the finite condition within $\sim$700 s then case 3 (solid-state diffusion) could be measured; if not the effect of the electrode diffusion limitation is measured depending on the ratio of:

$$r^2/D_{solid\ state} : d^2/D_{electrode}$$

For the thick films τ solid state $< \tau$ electrode. This transition will depend on parameters such as particle size, solid-state diffusion coefficient. As well as the effective diffusion coefficient of Li in the electrode composite:

$$D_{electrode} = \sigma_{electrolyte} / C_v\ active\ mass$$

$D_{electrode}$ is increased by decreasing active material loading, reducing electrode-packing density, or simply by changing the intrinsic conductivity of the electrolyte.

To demonstrate, the transition between the two limiting factors described above, both thick and thin films with differing conductivity electrolytes; 12 nm anatase particles in 95 μm and 13 μm films were prepared. An active material loading $\sim$9 mg and 0.5 mg cm^{-2} respectively, obviously the latter had a much lower film density (prepared by PVDF method). Both were cycled with the standard electrolyte LiPF$_6$ in EC:DMC (approx. conductivity 12 mS cm^{-1}) and a less conductive electrolyte LiBF$_4$ in

PC (approx. conductivity 3 mS cm^{-1}). The effect of the differing electrolytes is clearly visible in Figure 5.4.30:
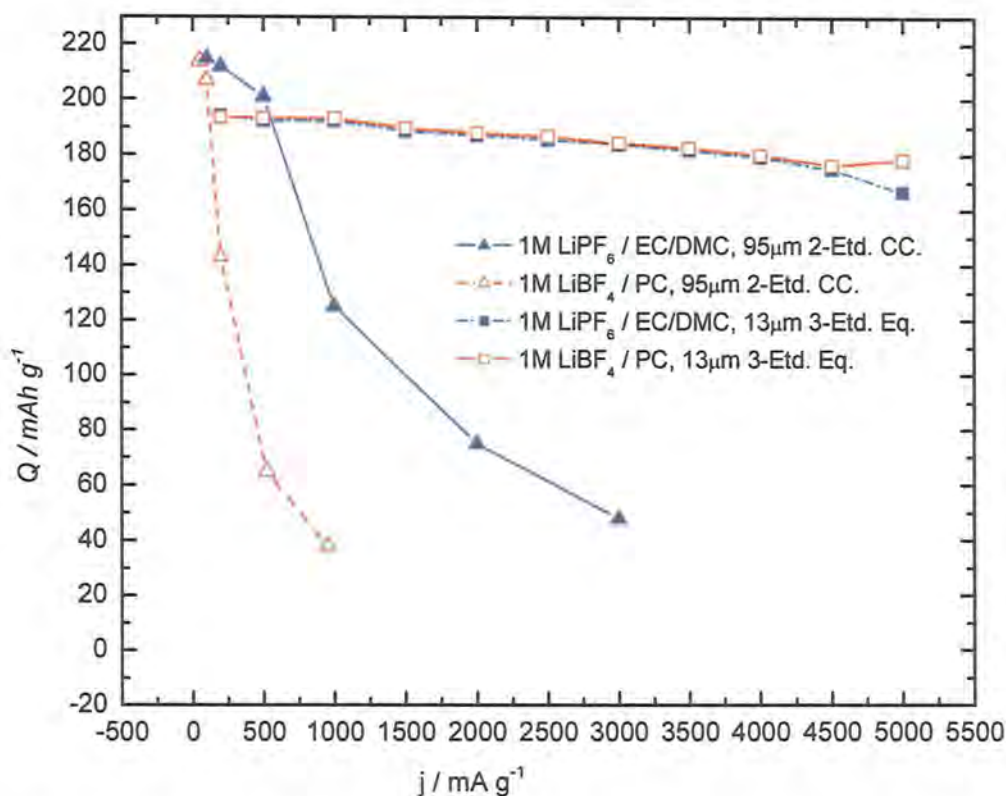
Figure 5.4.31: Plot of extraction capacity *vs.* current density(rate) to show electrode effect by varying electrolyte conductivity for 2 different films: *Thick film*: 92 μm (9 mg cm^{-2}); *Thin film*: 13 μm (0.52 mg cm^{-2});Active material was anatase nanoparticles; 12 nm; BET 180 m^2 g^{-1}; 2-electrode cell, CC cycling.

For the thick film indicating that diffusion through the electrode is the limiting factor. However, for the low-density thin film it is clear that the capacity obtained had no bearing on the electrolyte; the entire electrode was accessed at extremely high current densities. This is clear evidence that the diffusion of ions through the electrode matrix determines the rate of discharge for thick or dense films.
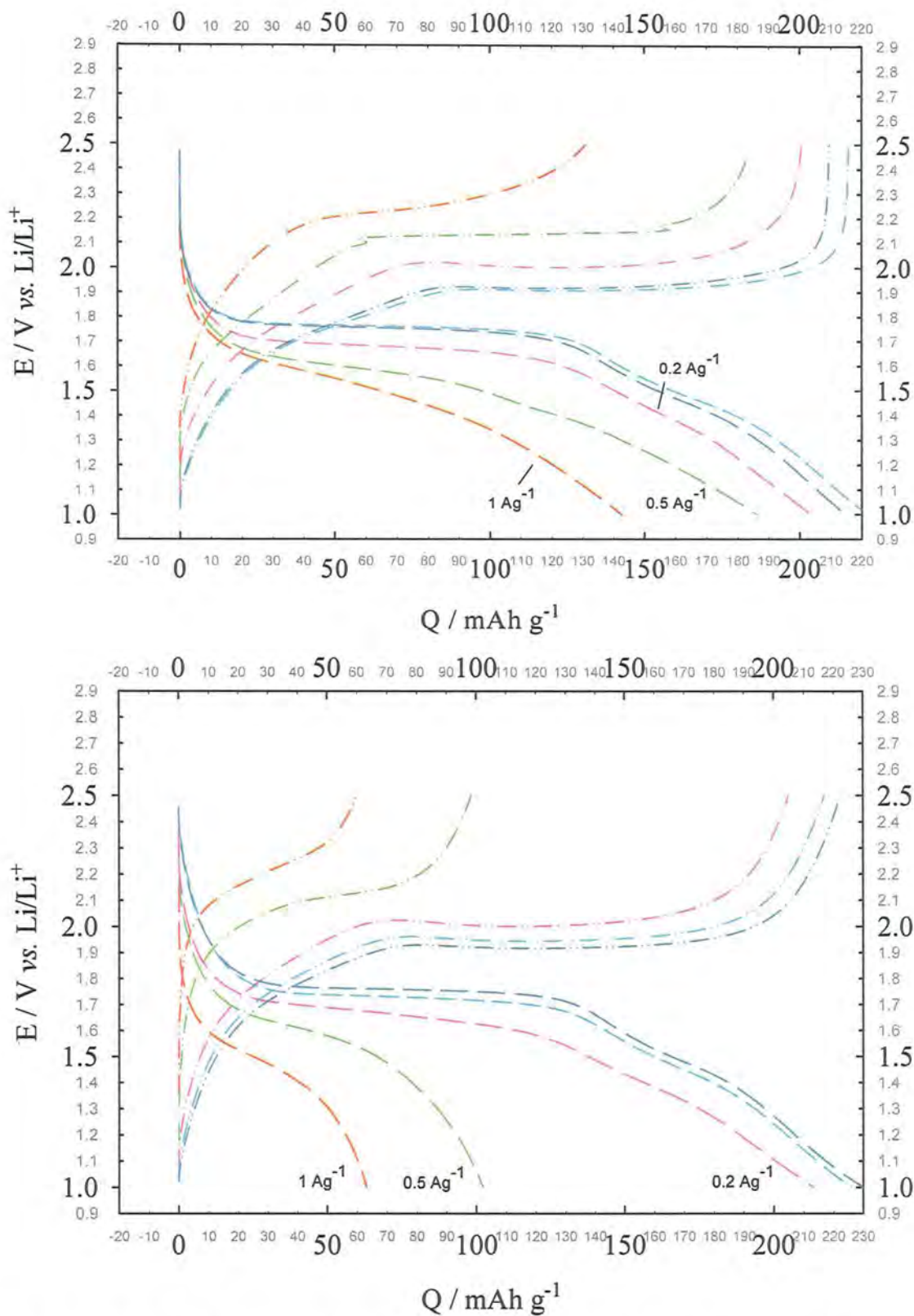
Figure 5.4.32: Plot of voltage profiles to show electrode effect by varying electrolyte conductivity;. Top:1 M LiPF$_6$ in EC:DMC (~12 mS / cm); Bottom: 1 M LiBF$_4$ in PC (~3 mS / cm). NP film; 92 μm (~9 mg cm^{-2}), nanoparticles 12 nm BET 180 m^2 g^{-1}, 2-electrode cell, CC cycling.

The shape of contrasting discharge profiles for the thick films is displayed in Figure 5.4.32. Although there is a difference in the ir drop this does not have a major bearing on the capacity difference obtained from the cycling. The thermodynamic capacity of the electrode is achieved for both electrolytes at low rates 0.05, 0.1 A g^{-1} and is even broadly similar for 0.2 A g^{-1}, at these rates up to ~1 C the 100 μm electrode is in the finite-boundary condition. Once a rate in excess of 0.5 A $g^{-1}$is used the conductivity of the electrolyte, infused within the electrode matrix becomes apparent. The voltage profile for the LiPF$_6$ in EC:DMC shows a slight compression due to the increased resistance, and indeed this result is predicted in Figure 5.4.33. An increased slope for discharge is explained by the lower conductivity LiBF$_4$ in PC (~3 mS / cm) as the charge-voltage profile becomes even steeper, indicating an increased resistance. The increased resistance cannot explain the sharp tailing off at the end of discharge, and premature polarisation indicates the depletion of Li$^+$ ions in the electrode matrix.
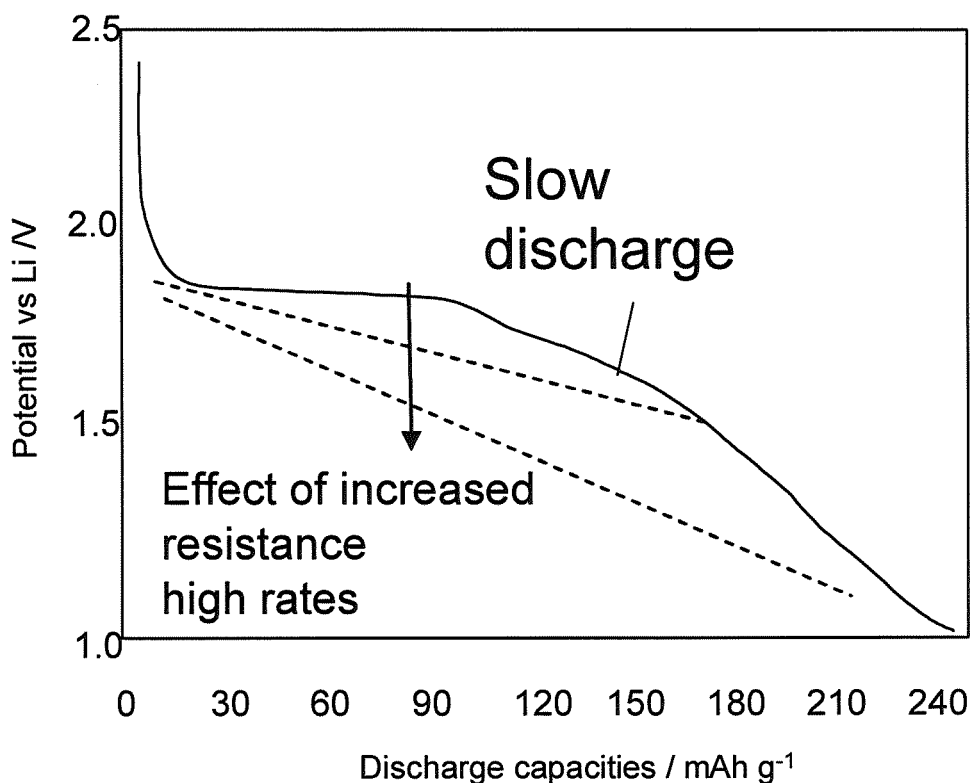
Figure 5.4.33: The expected result for the charge-voltage profile for Nanostructured TiO$_2$ with increased current density.

This depletion is accentuated at high rates, higher mass loading and thicker films as a result of the electrode having little time to equilibrate due to the fast continuous cycling.

For many applications, it may be necessary to charge and discharge the electrode continuously. However, as identified above at high rates, the time constant of the Li^+ ion diffusion is not enough for equilibration of the internal concentration profile within the electrode (or in the solid state). This effect, which becomes increasingly important for thick films, may also contribute to the lower values we have calculated for diffusion coefficients.

5.4.7   Constant Current Cycling with Equilibration

There are a few limitations of the CC cycling method (on which previous discussion is based) that must be considered. Firstly the extraction of lithium begins the instant the insertion stops, meaning no time to equilibrate the concentration profile within the solid state/particle/electrode. Indeed, for thick films the electrolyte was depleted completely at high rates. Secondly, the electrode is discharged from different starting points, i.e. the extraction at 3 Ag^{-1} is not a measure of the ability to extract the total inserted charge from the material but how much is extracted from what was originally inserted at 3 A g^- ₁.

5.4.7.1   Development of new method

To solve these problems a modified cycling procedure was developed. On the first discharge lithium was inserted until it reached the expected charge limit (250 mA g^{-1} allowing for some characteristic reversible charge on the first cycle), by holding the cell at the voltage limit 1 V *vs*. Li. This achieved a fully charged electrode, whilst the electrode also had time to resolve its concentration profile. The extraction would then be held at 2.5 V until the expected 220 mA h g^{-1} had been extracted, and so on at 220 mA h g^{-1} for subsequent charge/discharge cycles.

This procedure however had some problems that yielded poor cycling performance. Firstly, it was not always possible to obtain maximum capacity expected from the electrode; consequently, the cell remained at the potential limits for some hours. A huge increase in cell resistance was observed (and confirmed via AC Impedance) and can be attributed to consumption of the electrolyte and the build up of SEIs on the active electrode. Subsequently, a modified procedure yielded much improved cycling data. The cycling limits were shifted from 1- 2.5 V *vs*. Li, to 1.2- 2.7 V *vs*. Li, to reduce consumption of electrolyte and to reduce the build up of SEIs. A

second modification meant that instead of waiting for the electrode to reach a pre-calculated capacity the cell was held at voltage limits until a small residual current value was reached (~0.02 mA). This meant the cell was no longer subject to extreme voltages for long periods, but still had sufficient time to equilibrate with broadly the same amount of charge stored in the electrode. This method was known as the Constant Current with Equilibration method (CCE).
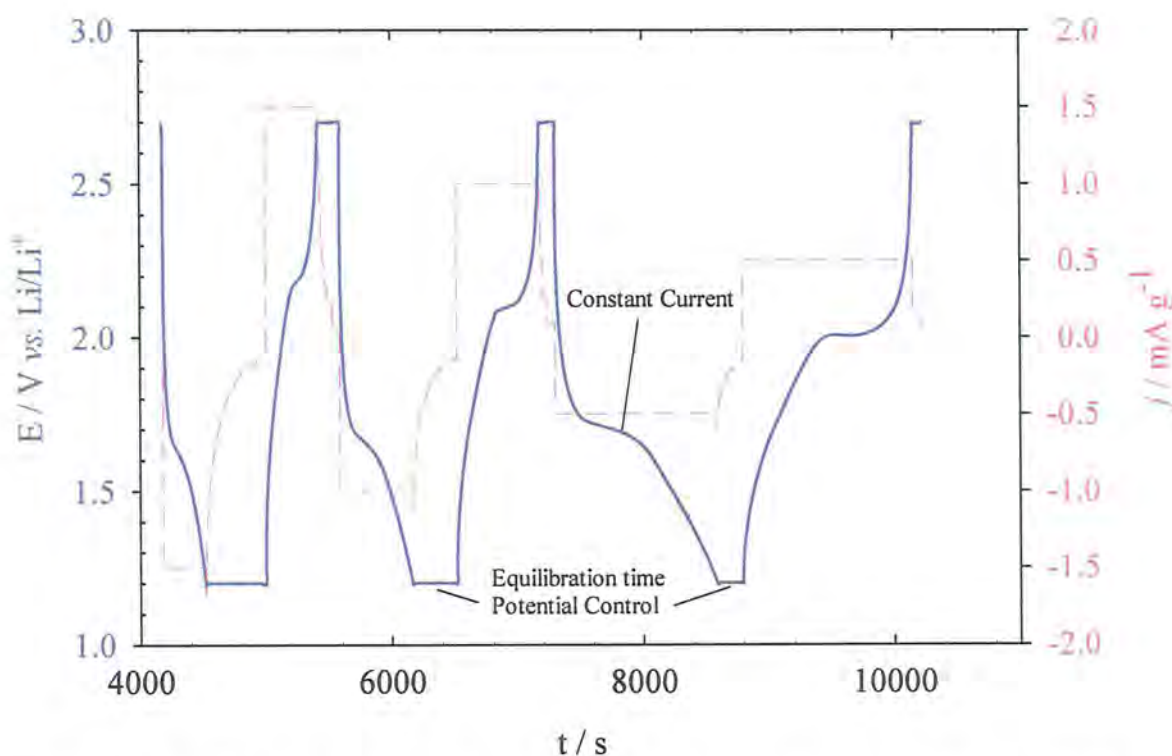
Figure 5.4.34 The modified cycling method constant current with equilibration (CCE)

Figure 5.4.34 shows the first few cycles of a typical procedure. Only one charge discharge for each cycle was obtained for each current density rather than four for each in the continuous-cycling (CC) method. The result of a 50 μm nanostructured TiO$_2$ which has been subject to the CCE cycling regime can be seen in Figure 5.4.35
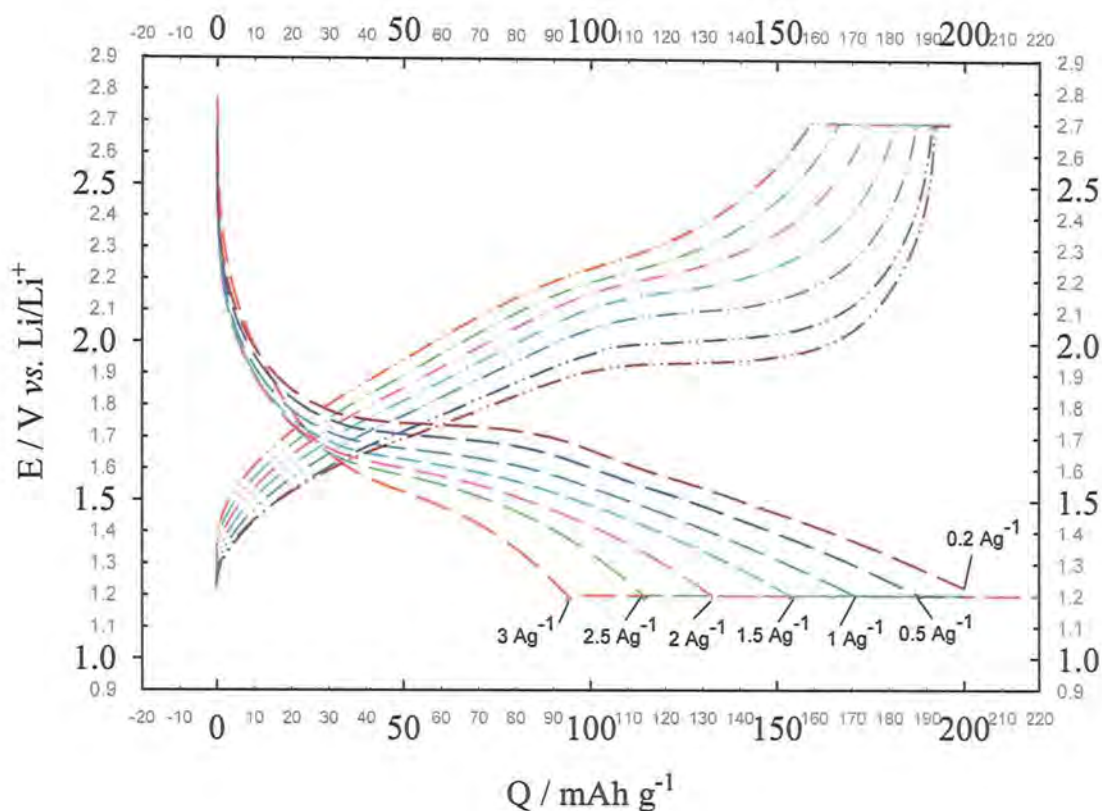
Figure 5.4.35: Constant Current Cycling with Equilibration (CCE) of NS TiO₂ 145 m^2g^{-1}, 60 μm, , 2.88 mg, 0.5 cm^{-2} (KS4_B2).The cell is was equilibrated by adding charge to 200 mA h g^{-1} under potential control. Potential limits $1.2 - 2.7$ V vs. Li/Li⁺.

The first thing to notice is that the insertion (discharge) is more affected by the increased current density than the extraction (charge). This can be partially explained by the fact the discharge is quite sloped and the upward shirt of the lower voltage limit to 1.2 V had cut off a region where further charge can be inserted. The upper voltage limit has been shifted to 2.7 V from 2.5 V, this has less of an effect as the last part of the charge is quite vertical as the electrode become polarised at the upper limit. The CCE method permits extraction of 160 mA h g^{-1} of a total of 200 mA h g^{-1} inserted 80 per cent of the thermodynamic capacity. It is clear that extraction of lithium from the electrode is much faster than insertion (also observed by Wakizaka with a LiFePO₄ composite electrode)[73]. This would suggest that the lithium ions can escape the electrode matrix faster than they are incorporated, and that there are no problems with electrolyte salt (LiPF₆) accumulation at these rates. This would occur at high rates if Lithium were expelled from the particle faster than it could diffuse to the bulk; so much so that the solubility limit was reached for the solvent.
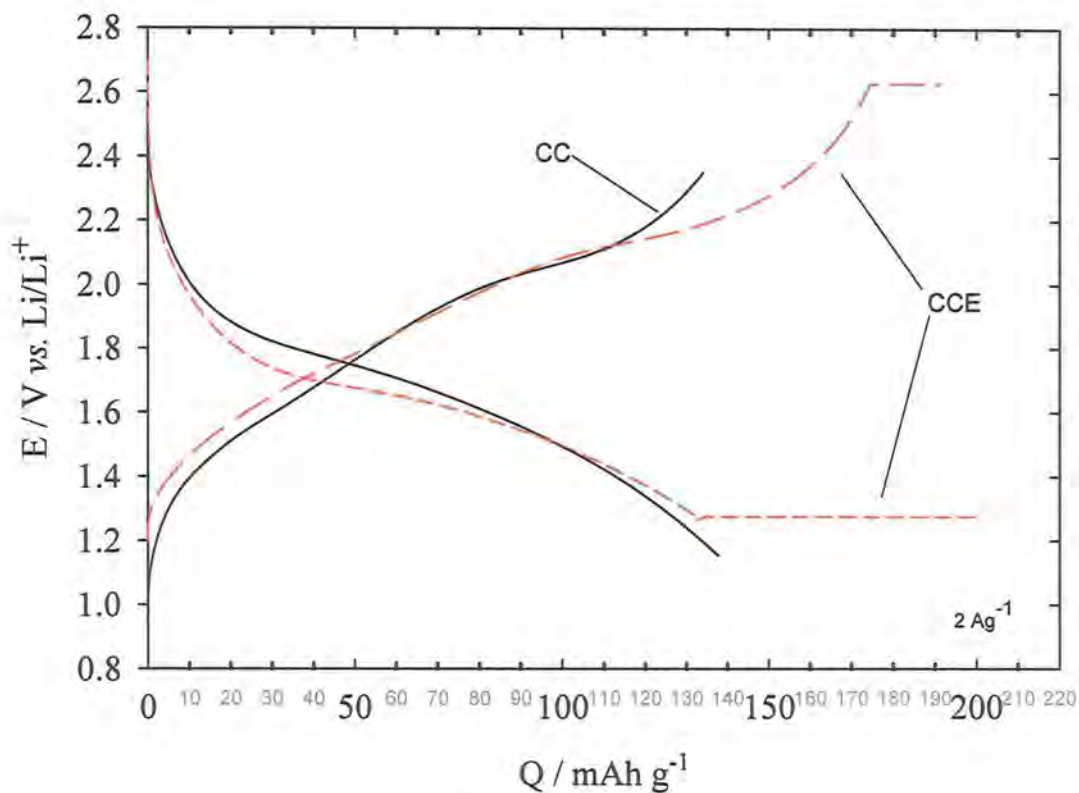
Figure 5.4.36: CCE method *vs.* CC method for nanostructured TiO_2 145 m^2 g^{-1}, 60 μm thick film.

A comparison between two electrodes cycled by the CCE method and the former CC method are presented in Figure 5.4.36. For an electrode of this thickness ~60 μm it shows the voltage profile is fairly similar (the profiles have been adjusted for ir drops). This result suggests that at this high rate 2 Ag^{-1}, the electrode or particle has had enough time for the concentration profile to equilibrate. The 60 μm electrode is typical for this study, however this effect would become increasingly significant for thicker electrodes.
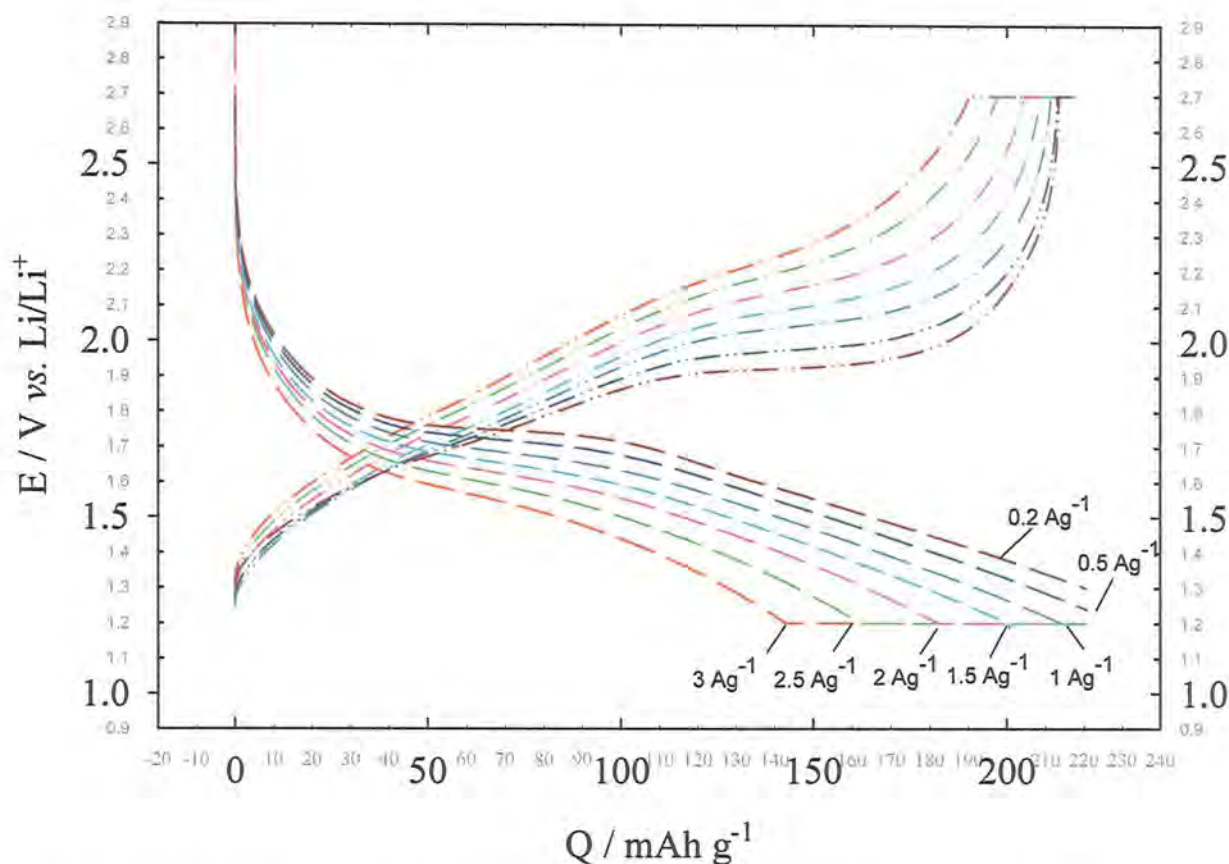
Figure 5.4.37: Constant Current Cycling with Equilibration (CCE) for 55 μm NP TiO$_2$, (BET 180 m^2 g^{-1}, 5.21 mg cm^{-2}). Cell is discharged and charged each time equilibrated by adding charge to 220 mA g^{-1} under potential control. Potential limits were1.2 – 2.7 V *vs.* Li/Li$^+$, 3 electrode Teflon cell TiO$_2$/ Li in 1 M LiPF6 in 1:1 EC:DMC.

The nanoparticles show similar profiles to the nanostructured material. Characteristically, the nanoparticles show more thermodynamic capacity than our prepared material therefore the electrodes are equilibrated up to a maximum of 220 mAh g^{-1}. Because of the slightly higher intrinsic capacity, at high rates (15 C) 190 mAh g^{-1} is extracted at relating to Li$_{0.6}$TiO$_2$ or 86 % of the inserted charge. The CCE method has less effect on the thin low-density PVDF electrodes as their time constant for relaxation is much less. The charge-voltage profile is less affected as the electrode is already in the finite condition and the profiles fall almost on top of each other over a broad distribution of specific current densities. A further observation from Figure 5.4.38 is that the normal thermodynamic capacity is not realised. This may be due to dislocated areas of material for such a thin film. It is also possible that for such a low mass loading that, a small error in active material weight could lead to error estimating the capacity per gram.
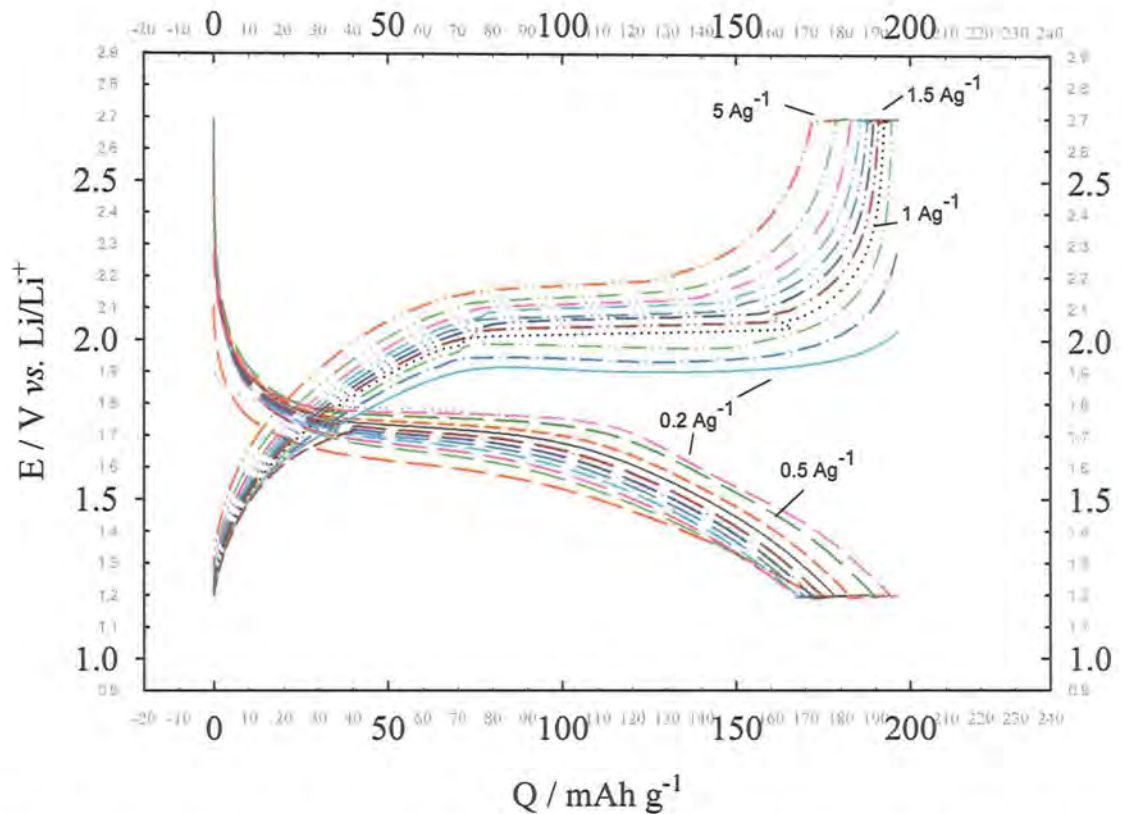
Figure 5.4.38: Current Cycling with Equilibration (CCE) for 13 μm NP TiO$_2$ film, prepared via PVDF Doctor Blade. (0.52 mg cm^{-2}, 0.88 g cm^{-3}, BET 180 m^2 g^{-1}). Cell was equilibrated on charge/discharge until current reached = 0.02 mA. . Potential limits were1.2 – 2.7 V *vs.* Li/Li$^+$, 3 electrode Teflon cell TiO$_2$/ Li in 1 M LiPF6 in 1:1 EC:DMC.

5.4.8   A study of voltage profiles.

The last part of this chapter is an attempt to explain the shape of the voltage profiles over a range of current densities. According to the sand equation[*137*]:

$$C_{surface} = C^o_{surface} + k\, i_a\, t^{1/2}.$$

Eq. 5.4.6

Where $C_{surface}$ is the concentration at the interface e.g. particle surface, and $C^o_{surface}$ is the initial concentration, and i$_a$ is current per area.

Eq. 5.4.6 should apply for the early part of the discharge profile whilst charge is less than half of the thermodynamic capacity. Under constant current this equation can be transformed to:

$$C_{surface} = C^o_{surface} + k\, q_a^{1/2}$$

Eq. 5.4.7

Where q_a is charge per area to produce a straight line whose gradient is proportional to current. A set of charge discharge curves for a 98 μm composite electrode appears in Figure 5.4.39 with the charge presented per geometric electrode area.
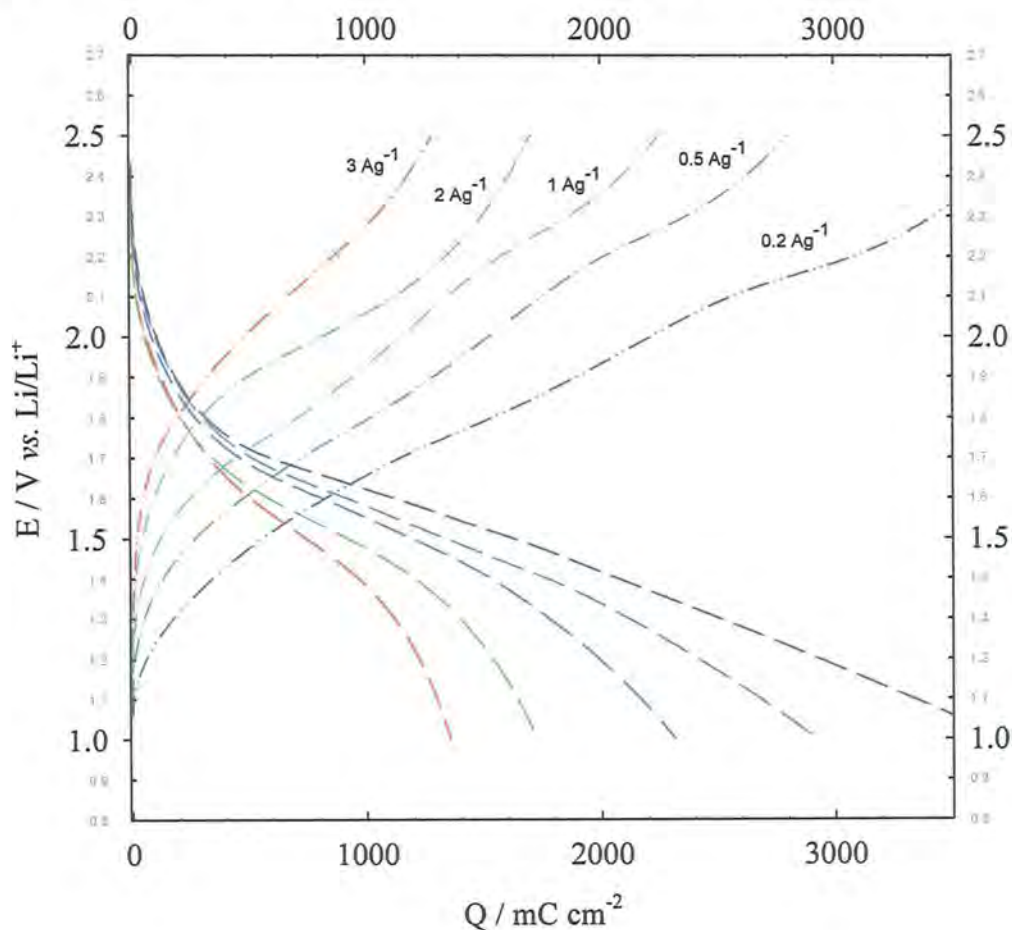
Figure 5.4.39: Plot of charge (per geometric area) *vs.* voltage for a 98 μm film of NS TiO$_2$ at different current densities 3, 2, 1, 0.5, 0.2 ,0.1 A g^{-1} for the CC method in a 2-electrode cell. 1 M LiPF$_6$ in 1:1 EC:DMC.
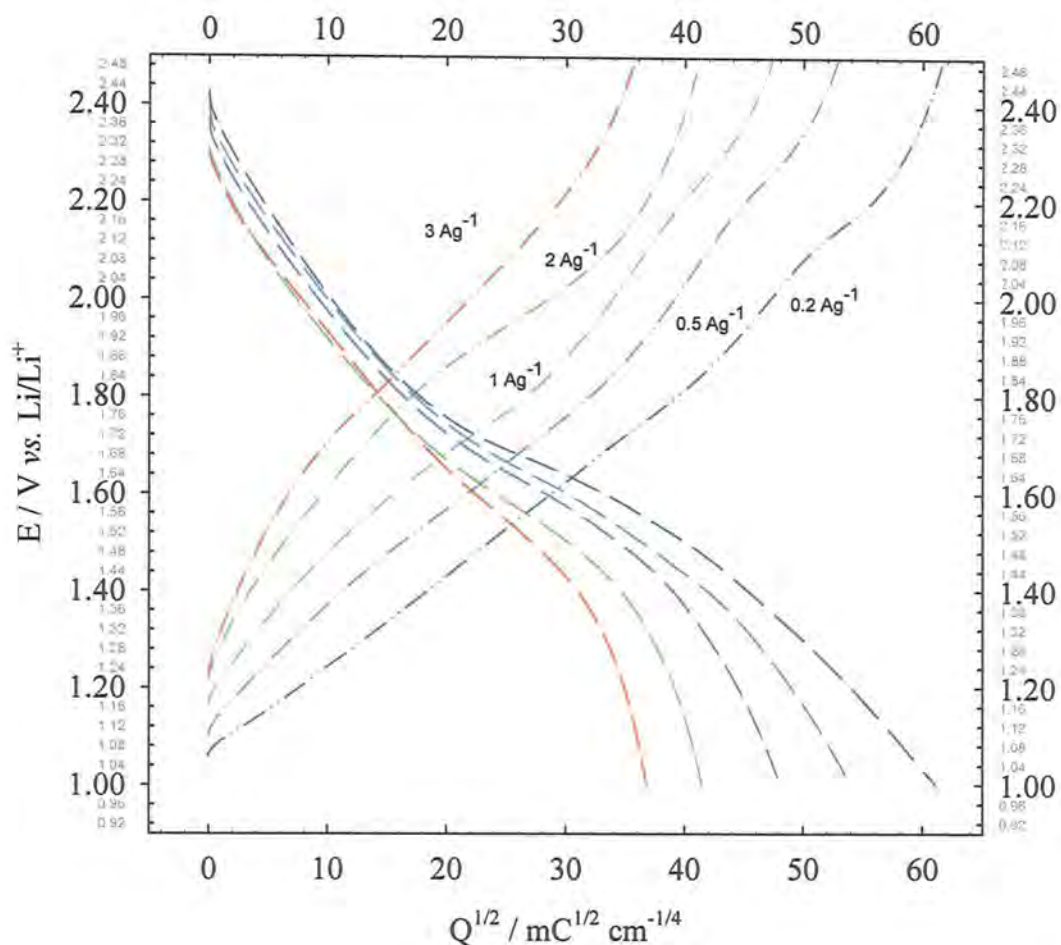
Figure 5.4.40 Plot of $Q^{1/2}$ (geometric area) *vs.* voltage for a 98 μm film of NS TiO$_2$ at different current densities: 3, 2, 1, 0.5, 0.2 ,0.1 A g^{-1} for the CC method in a 2-electrode cell. 1 M LiPF$_6$ in 1:1 EC:DMC.

The effect of different current rates for a thick electrode is evident from Figure 5.4.40 which shows the plot of Q normalised as the $Q^{1/2}$ according to Eq. 5.4.7. The early part of the extraction shows the expected linear dependence with the gradient proportional to the increasing current rate. For the insertion however, there seems to be no kinetic limitation (at these rates), with the gradients independent of current density. This is unexpected but the early part of the insertion is into a solid solution region of anatase and this can explain the fast kinetics for lithium insertion. The kinetic limitation for higher rates is evident once the two-phase region is reached, and continues into the last part of the insertion. The interpretation of the voltage profiles is made more difficult by the complex and particle size dependent chemistry of lithium insertion in TiO$_2$. An initial solid solution region followed by a two-phase insertion, before a final insertion into poorly defined surface phases at low voltage, as discussed in detail in section 5.4.2.

Another complication is the reproducibility of the nanostructure of our material. A simple two-phase insertion compound such as $LiFePO_4$ would make such analysis simpler and should be considered a good candidate for further work, even a 1-phase material such as $LiNiO_2$ would allow a much simpler interpretation of the charge-voltage profiles.

5.5 Conclusions and Further Work

TiO_2 with micron sized particles containing an internal nanostructure have been characterised electrochemically. These micron particles have demonstrated extended capacity for Li insertion, attributed to their high surface area. An impressive 300 mAh g^{-1} corresponding to a stoichiometry of $Li_{0.9}TiO_2$ is inserted on the first discharge with 240 mAh g^{-1} on the first charge ($Li_{0.7}TiO_2$); this confirms some additional reduction beyond the $Li_{0.5}TiO_2$ reported for anatase. The material also shows impressive cyclability; 200 mAh g^{-1} is extracted after 50 cycles at C/4.

The affect of particle size clearly has an effect on the electrochemical properties; our particles also demonstrate impressive rate performance with up to 190 mAh g^{-1} with discharge at 15 C-rate. This value compares favourably to nanowires[70] and nanoparticles in composite electrodes[116]. Therefore, our material has the advantage that it is mechanically processed as a micron size particle, with the electrochemical rate performance of nano size material. This ability to achieve composite electrodes with less binder and conductive additive means improved volumetric energy density and power density. It should also provide improved cyclability as less material should become dislocated on cycling, as the larger particles should maintain electronic contact.

When cycling the material at high rate a thickness limitation due to slow diffusion through the composite electrodes was observed. The benefit of large surface areas and short solid-state diffusion distance is negated if the species in solution facilitating the reaction are not able to move rapidly to the reaction sites within the electrode. Therefore, electrodes must also have a composite structure capable of facilitating rapid diffusion. For films >30 μm diffusion of Li through the composite electrode determines the discharge rate of the material. This is not a definitive transition point but will depend on the ratio of the relaxation times according to Eq. 5.5.1:

$$r^2/D_{solid\ state} : d^2/D_{electrode}$$

Eq. 5.5.1

For the thick films τ solid state $<\tau$ electrode; the transition between rate limitations will depend on parameters such as particle size and solid-state diffusion coefficient, as well as the effective diffusion coefficient of Li in the electrode composite:

$$D_{electrode} = \sigma_{electrolyte} / C_v \text{ active mass}$$

$D_{electrode}$ is increased by reducing the tortuousity in the composite; this may be achieved by decreasing active material loading, reducing electrode-packing density, or simply by changing the intrinsic conductivity of the electrolyte.

A modified form of the sand equation was used to estimate the diffusion coefficient for the possible rate limitations within the composite electrode structure. The value $\sim 10^{-16}$ cm^{2}s^{-1} for solid state diffusion of lithium in anatase is likely to be an underestimate because of the electrode limitation discussed above. Furthermore, other previous calculations of solid state diffusion coefficients derived from composite electrodes are also likely to be subject to this problem.

Equilibration in cycling allows increased relaxation time for thicker films or particles when their time constants are higher than the time scale of the experiment, but should be less significant for thin films or small particles with fast relaxation time.

Any attempt to interpret the voltage profiles using the sand equation is made more difficult by the complex and particle size dependent chemistry of lithium insertion in TiO_2. Another complication is the reproducibility of the nanostructure of our material. Nanostructured TiO_2 has a combination of two-phase and one-phase regions: an initial solid-solution region followed by a two-phase insertion, before a final insertion into poorly defined surface phases at low voltage, as discussed in detail in 5.4.2. A uniquely one-phase or two-phase material would make the interpretation easier for example; the charge-voltage profiles for a one-phase material as the voltage change is directly related to composition or concentration. The voltage during discharge changes because the chemical potential changes with composition, for example $Li_{1-x}CoO_2$ over the range $0 < x < 0.5$ where the composition varies continuously within a single phase the discharge occurs between 4.3 and 3.6 V. However, a two-phase material such as $LiFePO_4$ would make such analysis simpler as they undergo discharge by conversion between two phases of different stoichiometry. In this case a constant potential is predicted because of the constant chemical potential for phase equilibrium. These two materials should be used to investigate the electrode thickness effect in a more systematic study.

Chapter 6

Thesis Conclusions and Further Work

Nanostructured materials have attracted attention for application in energy storage devices[*120*], especially for those with high charge/discharge current rates such as lithium ion batteries[*2, 3*]. The initial objective of this thesis was to find an electrode pair capable of performing as a high rate device.

Previous work by Nelson on thin films of mesoporous nickel had demonstrated high rate performance in alkaline electrolyte by cycling the $Ni(OH)_2$/NiOOH redox couple.[*77*] Attempts to import this electrode in to lithium battery electrolyte proved futile due to the inability of converting the NiOOH into $LiNiO_2$ by ion-exchange. The hypothesis was that the corrosion by anionic components of the aprotic lithium electrolytes led to destruction of the Ni-O bonds, and a breakdown of mesoporous structure preventing the ion-exchange process. Incorporation of Phosphorous into Ni was known to have beneficial corrosion resistance[*89, 138*], so the thesis began in Chapter 2 by attempting to incorporate Phosphorous into first Ni and Mesoporous Ni films.

Deposition of the first nanostructured Ni-P alloy films was demonstrated, and Ni-P alloy films have shown an increase the corrosion resistance compared to pure Ni in lithium battery electrolytes, shifting the pitting potential (E_P) from ~3.2 V *vs.* Li , to 4.75 V *vs.* Li in an optimised Ni-P alloy. The Nanostructured deposits do not show significantly higher corrosion currents than their non-templated equivalents in either HCl, or the $LiPF_6$ salt. This is unexpected due to their intrinsic surface roughness however; this could be due to increased passivation through extra P incorporated via the templating method. Further work should involve improved analysis of the corrosion in lithium electrolytes, to use more agitating salts and different solvents to determine the versatility of the corrosion resistance of the Ni-P alloy. An optimised plating bath should be investigated to try to improve the plating efficiency (only~10 %) of mesoporous Ni-P.

The ion-exchanged MiNiP did yield significantly higher electrochemical activity than those reported for MNi in previous work by Nelson[*87*], however despite this, the ion exchange reaction was only 22 % complete. This implies that the diffusion of Li ions through the MNiP structure is still slow, and may be due to the disordered structure of the gamma phase of NiOOH, limiting the extent to which ion-exchange can occur. Neither the MNi or MNiP electrodes showed significant activity as a positive electrode in Lithium electrolytes. Therefore, the search for a nanostructured electrode pair moves

back to the alkaline system in chapter 4; with the attempt to find an aqueous negative electrode to partner the mesoporous Ni electrode with similarly fast kinetics.[77]

Nanostructured TiO_2 films deposited by dip coating are investigated in Chapter 4, as an alternative to hydrogen storage electrodes in alkaline cells for battery and super capacitor applications. The advantage would be a much higher current density given by a nanostructured electrode filled with a highly conducting electrolyte, as compared with a normal microparticulate electrode in which the discharge rate is limited by solid state diffusion.[74]

Prior to electrochemical characterisation in chapters 4 and 5, chapter 3 reported the synthesis and structural characterisation of a series of mesoporous cubic and hexagonal titania films and powders; using the complementary techniques of TEM, powder X-ray diffraction and N_2 adsorption/desorption isotherms. A multi-dip method was used to produce films of 0.5 μm and 1.3 μm, which were homogeneous in cross section as well as in surface profile and show good adhesion to their FTO substrate. Two different surfactants Brij ®78 and the Pluronics F127 demonstrate the ability to design different structures H_I templated TiO_2 from Brij ®78 shows a periodicity 5-8 nm, the larger surfactant F127 in the I_I cubic phase has a greater periodicity and indeed the 15-18 nm agrees broadly with that seen from AFM and TEM. Problems arose due on scale up as thicker films were subject to cracking and exfoliation to reveal the underlying substrate.

BET of titania powder prepared with I_I F127 gave the highest surface area 220 m^2g^{-1}, the pore size analysis shows an array of 7-12 nm pores which equates to a pore volume fraction of 0.3. Many attempts were made to improve quality and uniformity of the mesoporous structure throughout the mass of the powder. However, despite changing many parameters, it was not possible to improve the surface area of powders reproducibly, and typically, BET gave a surface area of 100-220 m^2g^{-1}. XRD data for both titania powder and commercially obtained 12 nm anatase particles showed a low degree of crystallinity, predominantly anatase. For the nanostructured material a large distribution of particle sizes and shapes were observed; with a characteristic length of about 10 μm from the sides to the centre of the particles for the majority of the sample. By contrast, the agglomerates of the nanopowders were much smaller, and characterised by corresponding lengths of about 0.5 μm. The powder size is significant when material processing is considered; the internally structured nanoparticles can be treated

as micron sized particles, which are safer and much easier to handle than nanoparticulates.

Chapter 4 demonstrated the effect of the nanostructure of TiO_2 on its electrochemical reactivity in water. Nanostructured TiO_2 films formed by the surfactant template method, unlike films prepared without surfactant, have been found to be reduced when cathodically polarised in aqueous lithium hydroxide. The result is attributed to accelerated lithium ion diffusion within the porous nanostructure, allowing a rapidly reversible insertion of lithium ions forming Li_xTiO_2 with x as high as 0.25, corresponding to a charge capacity of 127 $mCcm^{-2}$ in a 1.3 μm thick film. This insertion may be facilitated by the extension of a solid solution region recently reported[*139*] for high surface area anatase, which has faster interstitial dynamics and also occurs at a lower overpotential for hydrogen evolution. Self-discharge is slower than expected, with half-life of a few minutes under oxygen-free conditions.

The potential difference of 2 V between lithiated TiO_2 and NiOOH (also nanostructured using a liquid crystal template[*75*]) is close to the maximum possible potential range in an aqueous solution. An all-mesoporous supercapacitor is demonstrated by coupling these electrodes in an aqueous lithium hydroxide electrolyte. An open circuit potential of 1.75 V is observed, with an average cell potential of 1.6 V well in excess of Ni/MH and Ni/Cd systems which discharge between 1.0 and 1.3 V respectively.[*110*] A specific energy of 90 Wh kg^{-1} can be calculated, based on the mass of the charged electrodes, albeit a modest energy for a battery, this would be an outstanding value for a supercapacitor, especially if accompanied by the high power densities indicated in these preliminary results. However, further work is required to establish whether the storage times can be increased to acceptable values.

The chemistry of the thin films were also examined in aprotic electrolytes, although a higher degree of lithiation was achieved it is slower than from the aqueous electrolyte. There were also concerns that the SnO_2 may have been subject to lithium insertion at lower voltages and slow scan rates. Further work on thin films should focus on finding a substrate inert to lithium insertion and with a higher overpotential for hydrogen evolution; this will improve self-discharge times. Despite the excellent power density, to achieve an energy density comparable to batteries it is essential to increase film thickness. Synthesising films of a thickness great enough to be utilised in a battery or ultra capacitor device was however, ultimately unsuccessful; to achieve higher material

loadings the nanostructured TiO$_2$ had to be investigated in a composite electrode film. The internally nanostructured micro powers compared showed an extra capacity to insert lithium and impressive rate performance, characteristic of high surface area titanates and compared favourably with other nano-scale titanates such as anatase nanoparticles[139] and TiO$_2$ nantubes and wires[124].

Chapter 5 also identified the importance of the method in testing nanomaterials at high rates; many previous reports may be simply a function of experimental technique rather than intrinsic material properties. A three-electrode cell was developed to reduce the experimental ir drop and passivation resistance due to the lithium counter electrode. An experimental testing regime with time built in for equilibration of the concentration profile within the composite/ particle was also demonstrated.

Perhaps the most interesting result in Chapter 5 was the effect of electrode thickness on rate performance. Nanomaterials were producing different capacities on cycling at high rates, with little systematic correlation; until a correlation was noticed between electrode thickness and observed electrode capacity. Further study revealed that the diffusion of ions through the electrode matrix was the limiting factor for nanomaterials in thick composite electrodes, which remained in the semi-infinite condition, as the diffusion front failed to penetrate to the back of the electrode, leaving much of the electrode material unutilised. A transition to finite boundary condition (the back of the electrode is accessed) was achieved by reducing the active material loading either by reducing the electrode thickness, or lowering the density of the composite electrode structure. In this work for films >30 μm diffusion of Li through the composite electrode affected the discharge of the material rather than purely diffusion in the solid state. This is not a definitive value but will depend on the ratio of relaxation time according to:

$$r^2/D_{\text{solid state}} : d^2/D_{\text{electrode}}$$

For the thick films τ solid state < τ electrode, the transition between rate limitations will depend on parameters such as particle size, solid-state diffusion coefficient, as well as the effective diffusion coefficient of Li in the electrode composite.

If we assume that the rapid charge/discharge process is complete within one minute and that D is of the order of 10^{-16} cm^{2}s^{-1} in the solid state[140], particles with a size of 2r should be about 2 nm. This concept has been shown to hold for nanoporous TiO$_2$ by

Zhou *et al.* where a two-dimensional hexagonal mesostructure containing uniform pores with a diameter of 4 nm and 5 nm-wide pore walls of nanocrystalline anatase, showed high specific capacity (about 260 mAh/g) at high current density (10 A/g). Similar results have also been observed with a diameter of 6 nm by Jiang[2]. High capacity values were achieved by changing parameters in the electrode structure rather than by active materials design, the former by using an intricate self-ordered, crystalline-glass nanocomposite.[*141*] Both methods involved composite electrode structures with < 45 % active material which acts to artificially reduce the specific current density and increase the effective electrolyte conductivity within the composite, the volumetric energy density will obviously give an artificially high value as values refer only to the active material..

Nanomaterials are now subject to relaxation times of less than 1 minute, therefore the composite or microstucture of the battery must also operate on this time scale. As has been clearly demonstrated in this work conventional composite electrode structures used in commercial battery electrodes, do not. If characteristic electrode thickness > 100 μm for commercial application are to facilitate high rates, significant efforts must now focus on optimisation of the microstructure of batteries, in tandem with continued efforts on more uniform nanostructured materials.

7
Appendix

7.1 Composition of Composite Electrodes

A series of pellet/films and composition. Thickness measurements made with a micrometer to $^+/_-$ 2μm; μm$_1$ is bulk film thickness, μm$_2$ is pellet thickness,(both measured). Weight (Wt.) is the total electrode mass and is used to calculate density (ρ) from the electrode size and thickness. Theoretical density (ρ_{Thero}) was calculated from the individual components of the electrode (active material, carbon and binder) The difference between the two values was used to calculate Volume Fraction (free space in the composite electrode matrix). μm$_{calc}$ is the electrode thickness calculated using the density values and mass for each electrode. And AM loading is the amount of active material per composite electrode and the value used for calculations involving charge and current density.

Table 7.1.

Film	PTFE	ACB	AM	Pellet	film	pellet	Wt.	ρ	ρ, Theroy	Vol Frac	μm calc	AM loading
	wt. %			No.	μm	μm	mg	$\dfrac{g}{cm^{-3}}$		%		$\dfrac{mg}{cm^{-2}}$
KS4	5	15	80	1	110	110	16.2	1.55	2.44	36.4	118.5	12.96
	5	15	80	2	110	120	16.4		2.44		120.0	13.12
	5	15	80	3	110	120	17		2.44		124.4	13.60
	5	15	80	4	110	120	16.2		2.44		118.5	12.96
	5	15	80	5	110	120	16		2.44		117.1	12.80
	5	15	80	6	110	120	16.3		2.44		119.3	13.04
	5	15	80	7	110	120	16.4		2.44		120.0	13.12
	5	15	80	8	110	120	16.2		2.44		118.5	12.96
KS4 B	5	20	75	1	55	55	9.03		2.40		59.3	6.77
	5	20	75	2	55	55	8.37	1.60	2.40	34.3	55.0	6.28
	5	20	75	3	55	55	7.97		2.40		52.4	5.98
	5	20	75	4	55	55	8.14		2.40		53.5	6.11
	5	20	75	5	55	55	8.37		2.40		55.0	6.28
	5	20	75	6	55	61	8.51		2.40		55.9	6.38
	5	20	75	7	55	61	8.5		2.40		55.8	6.38
	5	20	75	8	55	59.5	8.14		2.40		53.5	6.11
KS19	10	25	65	1	95	95	16.46	1.53	2.33	37.1	94.9	10.70
	10	25	65	2	95	95	16.48		2.33	37.0	95.1	10.71
	10	25	65	3	55	55	11.66	1.88	2.33	23.0	55.0	7.58
	10	25	65	4	55	64	11.3	1.82	2.33	25.4	62.0	7.35
	10	25	65	5	55	64	11.12		2.33	26.6	61.0	7.23
	10	25	65	6	75	79	15.08	1.73	2.33	27.0		9.80
	10	25	65	7	75	73	14.08		2.33	31.8		9.15
	10	25	65	8	75	78	14.7		2.33	28.8		9.56
	10	25	65	9	50	50	9.69	1.72	2.33	29.6		6.30
	10	25	65	10	50	50	9.44		2.33	31.4		6.14
	10	25	65	11	50	48	9.07		2.33	34.1		5.90
												0.00

Film	PTFE wt. %	ACB	AM	Pellet No.	film µm	pellet µm	Wt. mg	ρ g cm⁻³	ρ, Theroy	Vol Frac %	µm calc	AM loading mg cm⁻²
KS19 B	5	20	75	1	95	95	16.5	1.54	2.40	36.9	98.0	12.38
	5	20	75	2	95	98	16.37		2.40	37.4	98.0	12.28
	5	20	75	3	95	96	16.48		2.40	37.0	96.0	12.36
	5	20	75	4	95	95	17.33		2.40	33.7		13.00
	5	20	75	5	75	71.5	12.64	1.49	2.40	38.8	73.1	9.48
	5	20	75	6	75	75	13.19		2.40	36.1	76.2	9.89
	5	20	75	7	75	71.5	12.37		2.40	40.1	71.5	9.28
	5	20	75	8	50	50	9.36	1.66	2.40	32.0	53.1	7.02
	5	20	75	9	50	50	8.33		2.40	39.5	47.2	6.25
	5	20	75	10	55	55	9.69	1.56	2.40	36.0	55.0	7.27
Film	**PTFE** wt. %	**ACB**	**AM**	**Pellet No.**	**film** µm	**pellet** µm	**Wt.** mg	**ρ** g cm⁻³	**ρ, Theroy**	**Vol Frac** %	**µm calc**	**AM loading** mg cm⁻²
KS19_ C	10	25	65	4	55	64	9.22	1.76	2.33	27.6	64.0	5.99
	10	25	65	5	55	64	9.22	1.76	2.33	27.6	64.0	5.99
	10	25	65	6	75	79	12.36	1.73	2.33	28.8	79.0	8.03
	10	25	65	7	75	73	11.54		2.33	33.5	73.0	7.50
	10	25	65	8	75	78	12.17	1.71	2.33	29.9	78.0	7.91
	10	25	65	11	50	48	7.48	1.57	2.33	35.4	50.0	4.86
KS19_ D	5	20	75	2	95	98	13.55	1.50	2.40	38.4	98.0	10.16
	5	20	75	3	95	96	13.53	1.50	2.40	38.5	96.0	10.15
	5	20	75	5	75	72	10.3	1.45	2.40	40.7	72.0	7.73
	5	20	75	7	75	71.5	10.14		2.40	41.6	71.5	7.61
	5	20	75	10	50	55	7.89	1.66	2.40	31.8	55.0	5.92
												0.00
121205 Aldrich	5	15	72	A	55	55	7.45	1.43	3.07	41.5	58.5	5.36
	5	15	72	B	55	52	6.62	1.27	3.07	48.0	52.0	4.77
	5	15	72	C	55	55	7.35	1.41	3.07	42.3	57.7	5.29
	5	15	72	D	55	55	6.98	1.34	3.07	45.2	54.8	5.03
	5	15	72	E	55	60	7.28	1.39	3.07	42.8	57.2	5.24
	5	15	72	F	55	60	7.54	1.44	3.07	40.8	59.2	5.43
	5	15	72	G	55	55	7.17	1.37	3.07	43.7	56.3	5.16
	5	15	72	H	55	55	7	1.34	3.07	45.0	55.0	5.04
	5	15	72	I	55	55	6.83	1.31	3.07	46.4	53.6	4.92
	PVDF	ACB	AM									
30206 Aldrich	15	25	60	A	5	5	0.503	1.06	3.01	56.5	4.7	0.30
	15	25	60	B	5	5	0.593	1.25	3.01	48.8	5.6	0.36
	15	25	60	C	5	5	0.533	1.12	3.01	53.9	5.0	0.32
	15	25	60	A	13	13	0.923	0.75	3.01	69.3	11.0	0.55
	15	25	60	B	13	13	1.133	0.92	3.01	62.3	13.5	0.68
	15	25	60	C	13	13	1.09	0.88	3.01	63.8	13.0	0.65
	15	25	60	D	13	13	0.883	0.71	3.01	70.7	10.5	0.53
	15	25	60	E	13	13	1.233	1.00	3.01	59.0	14.7	0.74
	15	25	60	A	20	20	1.713	0.90	3.01	63.0	20.1	1.03
	15	25	60	B	20	20	1.173	0.62	3.01	74.7	13.8	0.70
	15	25	60	C	20	20	1.303	0.69	3.01	71.9	15.3	0.78
	15	25	60	D	20	20	1.713	0.90	3.01	63.0	20.1	1.03

7.2 Preparation of TiO$_2$ powders

Sample KS	Detail	Solvent	Average D Spacing	BET
			A	m^{2}g^{-1}
1	HCl (Conc)	HPLC MeOH	107.70	114.2
2	HNO$_3$ (Conc)	HPLC MeOH	150.20	220
3	7M HCl	HPLC MeOH	117.71	143
4	HNO$_3$ (Conc)	HPLC MeOH	110.34	151.3
5	HCl (Conc)	HPLC MeOH		145.3
6	7M HCl	HPLC MeOH	104.46	131.9
7	HNO$_3$ (Conc)	HPLC MeOH		101.3
10	HNO$_3$ (Conc)	HPLC MeOH	103.50	112.7
13	HNO$_3$ (Conc)	BuOH	99.79	87.7
18	HCl (Conc)	HPLC MeOH		96.3
19	7M HCl	HPLC MeOH		146.4
20	HNO$_3$ (Conc)	HPLC MeOH		94.9
25	7M HCl	HPLC MeOH		127
26	7M HCl	HPLC MeOH		136

Table 7.2.1 Preparation Conditions for different TiO$_2$ precursor solution. BET and X-ray periodicity for the corresponding powders and dipping solutions. KS stands for Ken Series.

Sample 25		
Calincation Temp	BET Area	% Carbon
300	88.1	8.03
350	122.0	7.77
400	114.2	5.80
450	90.2	0.09

Sample 26		
Calincation Temp	BET Area	% Carbon
325	131.7	16.24
350	134.3	8.27
375	135.0	8.72

Table 7.2.2 Affect of Calcination Temperature on BET surface area % carbon determined by mass loss from a Thermal Gravimetric Analysis (TGA), where residual surfactant was burned away using a butane torch in a ceramic crucible..

References

1.   J. Maier, *Nature Materials* **4**, 805 (NOV, 2005).

2.   C. H. Jiang, E. Hosono, H. S. Zhou, *Nano Today* **1**, 28 (Nov, 2006).

3.   C. R. Sides, N. C. Li, C. J. Patrissi, B. Scrosati, C. R. Martin, *Mrs Bulletin* **27**, 604 (Aug, 2002).

4.   A. S. Arico, P. Bruce, B. Scrosati, J. M. Tarascon, W. Van Schalkwijk, *Nature Materials* **4**, 366 (May, 2005).

5.   G. Soler-Illia, E. L. Crepaldi, D. Grosso, D. Durand, C. Sanchez, *Chemical Communications*, 2298 (2002).

6.   D. A. Doshi *et al.*, *Journal of the American Chemical Society* **125**, 11646 (Sep 24, 2003).

7.   T. J. Barton *et al.*, *Chemistry of Materials* **11**, 2633 (OCT, 1999).

8.   M. K. Nazeeruddin *et al.*, *Journal of the American Chemical Society* **115**, 6382 (JUL 14, 1993).

9.   D. R. Rolison, B. Dunn, *Journal of Materials Chemistry* **11**, 963 (2001).

10.   R. K. Iler, *The Chemistry of Silica* (Wiley, New York, 1979), pp. 578-599.

11.   D. B. Le *et al.*, *Journal of the Electrochemical Society* **143**, 2099 (JUL, 1996).

12.   M. E. Davis, R. F. Lobo, *Chemistry of Materials* **4**, 756 (JUL-AUG, 1992).

13.   P. B. Moore, J. Shen, *Nature* **306**, 356 (1983).

14.   C. M. Zicovichwilson, A. Corma, P. Viruela, *Journal of Physical Chemistry* **98**, 10863 (OCT 20, 1994).

15.   I. D. Robb, *Anionic Surfactants, Physical Chemistry of Surfactant Action*. E. H. Lucassen-Reynders, Ed., Surfactant Science (Marcel Dekker, New York, 1981), pp. Chapter 3.

16.   P. Spegt, V. Luzzati, *Nature* **215**, 701 (1967).

17.   L. E. Scriven, *Nature* **263**, 123 (1976).

18.   N. H. Hartshorne, *The Microscopy of Liquid Crystals* (Microscope Publications Ltd., London, 1974), pp.

19.   J. N. Israelachvili, D. J. Mitchell, B. W. Ninham, *Journal of the Chemical Society-Faraday Transactions Ii* **72**, 1525 (1976).

20.   D. J. Mitchell, G. J. T. Tiddy, L. Waring, T. Bostock, M. P. Mcdonald, *Journal of the Chemical Society-Faraday Transactions I* **79**, 975 (1983).

21. N. R. B. Coleman, University of Southampton (1999).

22. R. G. Laughlin, *The Aqueous Phase Behaviour of Surfactants* (Academic Press, London, 1996), pp.

23. K. Mortensen, W. Brown, E. Jorgensen, *Macromolecules* **28**, 1458 (FEB 27, 1995).

24. R. Ivanova, B. Lindman, P. Alexandridis, *Langmuir* **16**, 9058 (NOV 14, 2000).

25. R. Ivanova, B. Lindman, P. Alexandridis, *Advances in Colloid and Interface Science* **89**, 351 (JAN 29, 2001).

26. P. Holmqvist, P. Alexandridis, B. Lindman, *Macromolecules* **30**, 6788 (NOV 3, 1997).

27. P. Holmqvist, P. Alexandridis, B. Lindman, *Journal of Physical Chemistry B* **102**, 1149 (FEB 12, 1998).

28. T. Iwanaga, M. Suzuki, H. Kunieda, *Langmuir* **14**, 5775 (SEP 29, 1998).

29. H. Kunieda, K. Shigeta, M. Suzuki, *Langmuir* **15**, 3118 (APR 27, 1999).

30. R. Ivanova, P. Alexandridis, B. Lindman, *Colloids and Surfaces a-Physicochemical and Engineering Aspects* **183**, 41 (JUL 15, 2001).

31. P. Alexandridis, U. Olsson, B. Lindman, *Langmuir* **14**, 2627 (MAY 12, 1998).

32. G. Wanka, H. Hoffmann, W. Ulbricht, *Macromolecules* **27**, 4145 (JUL 18, 1994).

33. C. N. R. Rao, A. K. Cheetham, *Journal of Materials Chemistry* **11**, 2887 (2001).

34. C. T. Kresge, M. E. Leonowicz, W. J. Roth, J. C. Vartuli, J. S. Beck, *Nature* **359**, 710 (OCT 22, 1992).

35. J. S. Beck *et al.*, *Journal of the American Chemical Society* **114**, 10834 (DEC 30, 1992).

36. C.-Y. Chen, H.-X. Li, M. E. Davis, *Microporous Materials* **2**, 17 (1993/12, 1993).

37. C.-Y. Chen, S. L. Burkett, H.-X. Li, M. E. Davis, *Microporous Materials* **2**, 27 (1993/12, 1993).

38. G. S. Attard, J. C. Glyde, C. G. Goltner, *Nature* **378**, 366 (Nov 23, 1995).

39. A. Corma, *Chemical Reviews* **97**, 2373 (SEP-OCT, 1997).

40. P. T. Tanev, T. J. Pinnavaia, *Science* **267**, 865 (FEB 10, 1995).

41. N. Coustel, F. Direnzo, F. Fajula, *Journal of the Chemical Society-Chemical Communications*, 967 (APR 21, 1994).

42.   P. D. Yang, D. Y. Zhao, D. I. Margolese, B. F. Chmelka, G. D. Stucky, *Nature* **396**, 152 (Nov 12, 1998).

43.   G. D. Stucky *et al.*, *Chemistry of Materials* **11**, 2813 (Oct, 1999).

44.   G. Soler-Illia, A. Louis, C. Sanchez, *Chemistry of Materials* **14**, 750 (Feb, 2002).

45.   E. L. Crepaldi *et al.*, *Chemistry of Materials* **14**, 3316 (Aug, 2002).

46.   E. L. Crepaldi *et al.*, in *Nanoporous Materials Iii*. (ELSEVIER SCIENCE BV, Amsterdam, 2002), vol. 141, pp. 235-242.

47.   D. Grosso, F. Babonneau, G. Soler-Illia, P. A. Albouy, H. Amenitsch, *Chemical Communications*, 748 (2002).

48.   E. L. Crepaldi *et al.*, *Journal of the American Chemical Society* **125**, 9770 (Aug 13, 2003).

49.   F. Bosc, A. Ayral, P. A. Albouy, C. Guizard, *Chemistry of Materials* **15**, 2463 (Jun 17, 2003).

50.   G. Soler-Illia, E. L. Crepaldi, D. Grosso, C. Sanchez, *Current Opinion in Colloid & Interface Science* **8**, 109 (Mar, 2003).

51.   G. S. Attard, C. G. Goltner, J. M. Corker, S. Henke, R. H. Templer, *Angewandte Chemie-International Edition in English* **36**, 1315 (Jul 4, 1997).

52.   G. S. Attard *et al.*, *Science* **278**, 838 (Oct 31, 1997).

53.   J. M. Elliott *et al.*, *Chemistry of Materials* **11**, 3602 (Dec, 1999).

54.   G. S. Attard, N. R. B. Coleman, J. M. Elliott, in *Mesoporous Molecular Sieves 1998*. (ELSEVIER SCIENCE PUBL B V, Amsterdam, 1998), vol. 117, pp. 89-94.

55.   G. S. Attard, *Journal of New Materials for Electrochemical Systems* **2**, 239 (Oct, 1999).

56.   S. Guerin, G. S. Attard, *Electrochemistry Communications* **3**, 544 (Oct, 2001).

57.   P. N. Bartlett, P. N. Birkin, M. A. Ghanem, P. de Groot, M. Sawicki, *Journal of the Electrochemical Society* **148**, C119 (FEB, 2001).

58.   P. N. Bartlett, P. R. Birkin, M. A. Ghanem, *Chemical Communications*, 1671 (2000).

59.   I. Nandhakumar, J. M. Elliott, G. S. Attard, *Chemistry of Materials* **13**, 3840 (Nov, 2001).

60.   I. S. Nandhakumar, G. S. Attard, *Abstracts of Papers of the American Chemical Society* **221**, 415 (Apr 1, 2001).

61.   L. M. Huang *et al.*, *Chemistry of Materials* **14**, 876 (Feb, 2002).

62.   J. M. Elliott, L. M. Cabuche, P. N. Bartlett, *Analytical Chemistry* **73**, 2855 (JUL 1, 2001).

63.   W. Cheng, E. Baudrin, B. Dunn, J. I. Zink, *Journal of Materials Chemistry* **11**, 92 (2001).

64.   K. H. Cheng, A. J. Jacobson, M. S. Whittingham, *Abstracts of Papers of the American Chemical Society* **180**, 151 (1980).

65.   K. H. Cheng, A. Jacobson, M. S. Whittingham, *Journal of the Electrochemical Society* **127**, C404 (1980).

66.   M. Mamak, N. Coombs, G. A. Ozin, *Chemistry of Materials* **13**, 3564 (OCT, 2001).

67.   M. Mamak, G. A. Ozin, N. Coombs, *Abstracts of Papers of the American Chemical Society* **222**, U627 (AUG, 2001).

68.   D. Fattakhova, L. Kavan, P. Krtil, *Journal of Solid State Electrochemistry* **5**, 196 (Apr, 2001).

69.   A. R. Armstrong, G. Armstrong, J. Canales, R. Garcia, P. G. Bruce, *Advanced Materials* **17**, 862 (Apr 4, 2005).

70.   A. R. Armstrong, G. Armstrong, J. Canales, P. G. Bruce, *Angewandte Chemie-International Edition* **43**, 2286 (Apr 19, 2004).

71.   L. Kavan, J. Rathousky, M. Gratzel, V. Shklover, A. Zukal, *Journal of Physical Chemistry B* **104**, 12012 (Dec 21, 2000).

72.   L. Kavan, P. Krtil, D. Fattakhova, S. Burnside, M. Gratzel, *Solid State Ionics* **135**, 101 (Nov, 2000).

73.   Y. Wakizaka, University of Southampton (2007).

74.   G. S. Attard, J. M. Elliott, P. N. Bartlett, A. Whitehead, J. R. Owen, *Macromolecular Symposia* **156**, 179 (Jul, 2000).

75.   P. A. Nelson, J. M. Elliott, G. S. Attard, J. R. Owen, *Journal of New Materials for Electrochemical Systems* **5**, 63 (Jan, 2002).

76.   A. H. Whitehead, J. M. Elliott, J. R. Owen, G. S. Attard, *Chemical Communications*, 331 (Feb 21, 1999).

77.   P. A. Nelson, J. M. Elliott, G. S. Attard, J. R. Owen, *Chemistry of Materials* **14**, 524 (Feb, 2002).

78.   A. Stein, S. W. Keller, T. E. Mallouk, *Science* **259**, 1558 (MAR 12, 1993).

79.   M. Figlarz *et al.*, *Solid State Ionics* **43**, 143 (NOV, 1990).

80. J. N. Reimers, E. W. Fuller, E. Rossen, J. R. Dahn, *Journal of the Electrochemical Society* **140**, 3396 (DEC, 1993).

81. G. G. Amatucci, J. M. Tarascon, D. Larcher, L. C. Klein, *Solid State Ionics* **84**, 169 (APR, 1996).

82. J. Maruta, H. Yasuda, M. Yamachi, *Journal of Power Sources* **90**, 89 (SEP, 2000).

83. M. Ratzker, D. S. Lashmore, *Journal of Metals* **37**, A1 (1985).

84. T. M. Harris, Q. D. Dang, *Journal of the Electrochemical Society* **140**, 81 (JAN, 1993).

85. R. L. Zeller, U. Landau, *Journal of the Electrochemical Society* **139**, 3464 (DEC, 1992).

86. M. Saitou, Y. Okudaira, W. Oshikawa, *Journal of the Electrochemical Society* **150**, C140 (MAR, 2003).

87. P. A. Nelson, University of Southampton (2003).

88. A. Brenner, D. E. Couch, E. K. Williams, *J. Research NBS* **44**, 109 (1950).

89. M. Ratzker, D. S. Lashmore, K. W. Pratt, *Plating and Surface Finishing* **73**, 74 (SEP, 1986).

90. T. Mimani, S. M. Mayanna, *Surface & Coatings Technology* **79**, 246 (FEB, 1996).

91. R. B. Diegle, N. R. Sorensen, C. R. Clayton, M. A. Helfand, Y. C. Yu, *Journal of the Electrochemical Society* **135**, 1085 (MAY, 1988).

92. S. S. Zhang, T. R. Jow, *Journal of Power Sources* **109**, 458 (JUL 1, 2002).

93. B. P. Zhang *et al.*, *Corrosion Science* **32**, 433 (1991).

94. B. P. Zhang, H. Habazaki, A. Kawashima, K. Asami, K. Hashimoto, *Corrosion Science* **33**, 667 (MAY, 1992).

95. M. Morita, T. Shibata, N. Yoshimoto, M. Ishikawa, *Electrochimica Acta* **47**, 2787 (JUL 5, 2002).

96. E. M. Shembel *et al.*, *Journal of Power Sources* **54**, 416 (APR, 1995).

97. E. M. Shembel *et al.*, *Journal of Power Sources* **54**, 421 (APR, 1995).

98. P. Poizot, S. Laruelle, S. Grugeon, L. Dupont, J. M. Tarascon, *Nature* **407**, 496 (SEP 28, 2000).

99. L. Kavan, M. Zukalova, M. Kalbac, I. Exnar, M. Graetzel, *Chemistry of Materials* **17**, 1248 (Mar 8, 2005).

100. T. J. Gordon-Smith, University of Southampton (2003).

101. R. Hengerer, L. Kavan, P. Krtil, M. Gratzel, *Journal of the Electrochemical Society* **147**, 1467 (Apr, 2000).

102. M. Gratzel, *Journal of Sol-Gel Science and Technology* **22**, 7 (Sep, 2001).

103. L. Kavan, J. Rathousky, M. Gratzel, V. Shklover, A. Zukal, *Microporous and Mesoporous Materials* **44**, 653 (Jun, 2001).

104. P. H. E. Stephen Brunauer, Edward Teller, *Journal of the American Chemical Society* **60**, p309 (1938).

105. K. H. Reiman *et al.*, *Electrochemistry Communications* **8**, 517 (APR, 2006).

106. S. Y. Choi, M. Mamak, N. Coombs, N. Chopra, G. A. Ozin, *Advanced Functional Materials* **14**, 335 (Apr, 2004).

107. R. Schumacher, *Berichte Der Bunsen-Gesellschaft-Physical Chemistry Chemical Physics* **84**, 125 (1980).

108. L. Kavan *et al.*, *Chemistry of Materials* **16**, 477 (Feb 10, 2004).

109. W. Li, W. R. McKinnon, J. R. Dahn, *Journal of the Electrochemical Society* **141**, 2310 (Sep, 1994).

110. R. M. Dell, D. A. J. Rand, *Understanding Batteries* (The Royal Society of Chemistry, ed. 1st., 2001), pp. 172.

111. P. C. A. Alberius *et al.*, *Chemistry of Materials* **14**, 3284 (Aug, 2002).

112. M. Wagemaker, D. Lutzenkirchen-Hecht, A. A. van Well, R. Frahm, *Journal of Physical Chemistry B* **108**, 12456 (Aug 19, 2004).

113. Y. G. Guo, Y. S. Hu, J. Maier, *Chemical Communications*, 2783 (2006).

114. M. Manickam, P. Singh, T. B. Issa, S. Thurgate, R. De Marco, *Journal of Power Sources* **130**, 254 (MAY 3, 2004).

115. A. B. Yuan, Q. L. Zhang, *Electrochemistry Communications* **8**, 1173 (JUL, 2006).

116. G. Sudant, E. Baudrin, D. Larcher, J. M. Tarascon, *Journal of Materials Chemistry* **15**, 1263 (2005).

117. G. Armstrong, A. R. Armstrong, J. Canales, P. G. Bruce, *Chemical Communications*, 2454 (2005).

118. M. Wagemaker, A. A. van Well, G. J. Kearley, F. M. Mulder, *Solid State Ionics* **175**, 191 (Nov 30, 2004).

119. M. Wagemaker, A. P. M. Kentgens, F. M. Mulder, *Nature* **418**, 397 (JUL 25, 2002).

120. P. Balaya *et al.*, *Journal of Power Sources* **159**, 171 (SEP 13, 2006).

121. M. Wagemaker, W. J. H. Borghols, F. M. Mulder, *Journal of the American Chemical Society* **129**, 4323 (2007).

122. P. Krtil, L. Kavan, D. Fattakhova, *Journal of Solid State Electrochemistry* **1**, 83 (Jul, 1997).

123. http://www.durston.co.uk/prod-m-minimill.htm.

124. A. R. Armstrong, G. Armstrong, J. Canales, P. G. Bruce, *Journal of Power Sources* **146**, 501 (Aug 26, 2005).

125. L. Kavan *et al.*, *Journal of the Electrochemical Society* **150**, A1000 (Jul, 2003).

126. M. Zukalova *et al.*, *Nano Letters* **5**, 1789 (Sep, 2005).

127. H. Lindstrom *et al.*, *Journal of Physical Chemistry B* **101**, 7710 (SEP 25, 1997).

128. M. Wagemaker *et al.*, *Advanced Materials* **18**, 3169 (Dec 4, 2006).

129. M. Wagemaker, R. van de Krol, A. P. M. Kentgens, A. A. van Well, F. M. Mulder, *Journal of the American Chemical Society* **123**, 11454 (NOV 21, 2001).

130. M. Wagemaker, R. van de Krol, A. A. van Well, *Physica B-Condensed Matter* **336**, 124 (Aug, 2003).

131. J. M. Elliott, J. R. Owen, *Physical Chemistry Chemical Physics* **2**, 5653 (2000).

132. A. J. Bard, L. R. Faulkner, Electrochemical Methods (Wiley, New York, 1980), pp.104

133. A. A. Andriiko, P. V. Rudenok, L. I. Nyrkova, *Journal of Power Sources* **72**, 146 (1998/4/21, 1998).

134. R. de Levie, *Electrochimica Acta* **8**, 751 (1963/10, 1963).

135. R. de Levie, *Electrochimica Acta* **9**, 1231 (1964/9, 1964).

136. L. Kavan, H. Pelouchova, P. Janda, J. Weber, *Journal of Electroanalytical Chemistry* **566**, 73 (May 1, 2004).

137. P. G. Bruce, *Solid state electrochemistry*. B. Dunne, Ed., Chemistry of Solid Sate Materials (Cambridge University Press, 1995), pp. 225.

138. A. Krolikowski, P. Butkiewicz, *Electrochimica Acta* **38**, 1979 (OCT, 1993).

139. C. Jiang *et al.*, *Journal of Power Sources* **166**, 239 (2007/3/30, 2007).

140. M. Winter, J. O. Besenhard, M. E. Spahr, P. Novak, *Advanced Materials* **10**, 725 (Jul 9, 1998).

141. H. S. Zhou, D. L. Li, M. Hibino, I. Honma, *Angewandte Chemie-International Edition* **44**, 797 (2005).